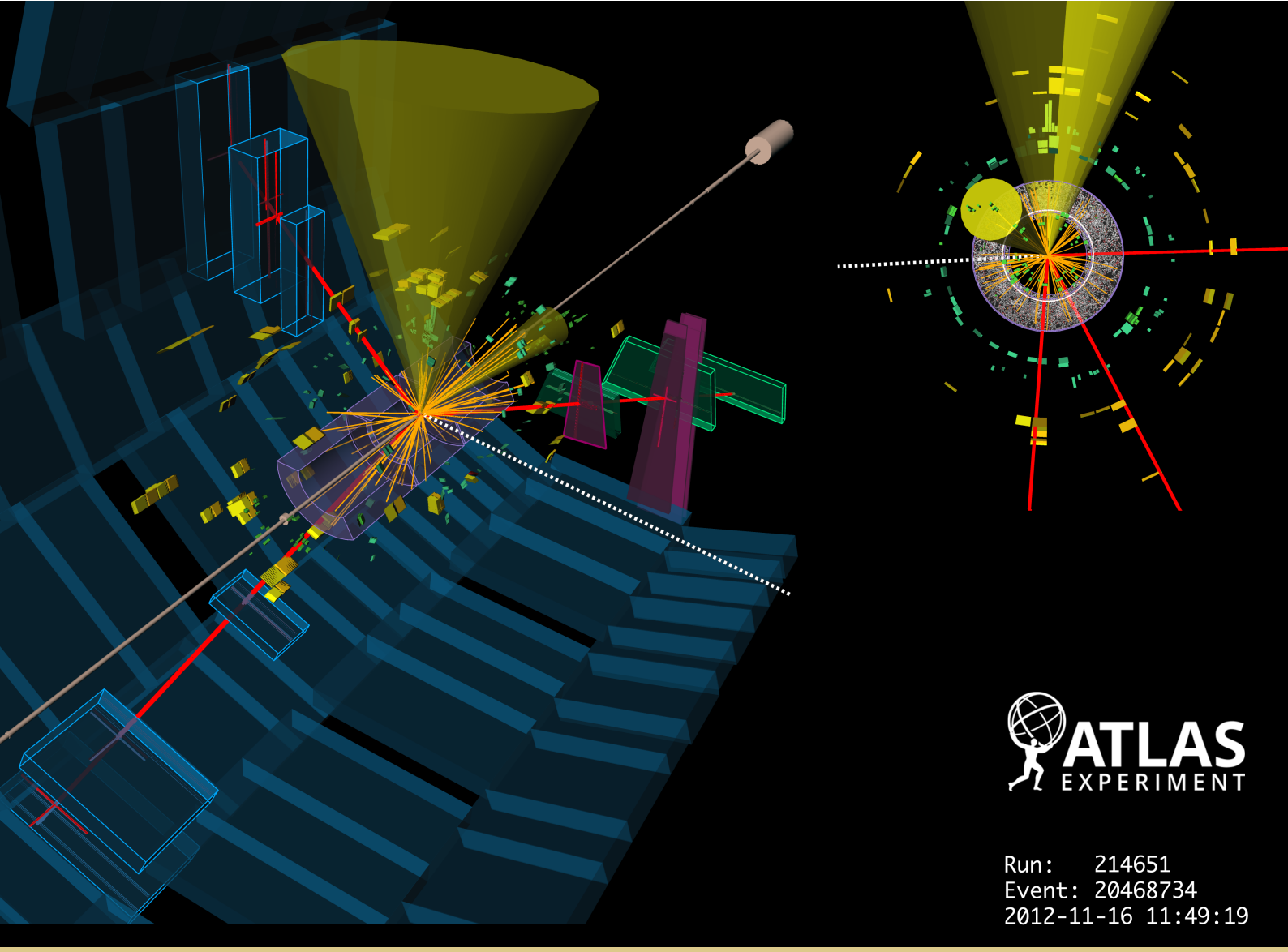

Bruno Miguel Leonardo Galhardo

MEASUREMENT OF RARE TOP QUARK DECAYS IN ATLAS/LHC

Tese de Doutoramento em Física, Ramo de Física Nuclear e das Partículas, orientada pelos Professores Doutores Filipe Veloso e António Onofre e apresentada ao Departamento de Física da Faculdade de Ciências e Tecnologia da Universidade de Coimbra

Outubro de 2016

· U C ·

Universidade de Coimbra

Measurement of rare top quark decays in ATLAS/LHC

Bruno Miguel Leonardo Galhardo

Department of Physics of the Faculty of Science and Technology

University of Coimbra

Supervisors: Prof. Dr. Filipe Veloso and Prof. Dr. António Onofre

Doutoramento em Física

2016

Cover figure: Event display of a $t\bar{t} \to bWqZ$ candidate event, selected with the analysis described in Chapter 5 (run = 214651, event = 20468734) with two opposite-sign muons (p_{T} = 69 GeV and p_{T} = 46 GeV), a third muon (p_{T} = 55 GeV), one light jet (p_{T} = 65 GeV), one b-tagged jet (p_{T} = 43 GeV), $E_{\mathrm{T}}^{\mathrm{miss}}$ = 91 GeV, $m_{\ell_a\ell_b}^{reco}$ = 89 GeV, $m_{\ell_c\nu}^{reco}$ = 96 GeV, $m_{j_a\ell_a\ell_b}^{reco}$ = 173 GeV, $m_{j_b\ell_c\nu}^{reco}$ = 151 GeV and $\chi^2 = 1.5$. Taken from [1]

Abstract

In this thesis, a search for the flavour-changing neutral-current decay $t \to qZ$ is presented. Data collected by the ATLAS detector during 2012 from proton–proton collisions at the Large Hadron Collider (LHC) with a centre-of-mass energy of $\sqrt{s} = 8$ TeV, corresponding to an integrated luminosity of 20.3 fb^{-1}, are analysed. Top-quark pair-production events with one top quark decaying through the $t \to qZ$ ($q = u, c$) channel and the other through the dominant Standard Model mode $t \to bW$ are considered as signal. Only the decays of the Z boson to charged leptons and leptonic W boson decays are used. No evidence for a signal is found and an observed (expected) upper limit on the $t \to qZ$ branching ratio of 6.7×10^{-4} (7.7×10^{-4}) is set at a 95% confidence level (CL). The expected sensitivity for the $t \to qZ$ channel at the high-luminosity phase of the LHC is also derived, along with the expected sensitivity for the $t \to q\gamma$ channel. The expected limits at 95% CL for both channels are in the range between 10^{-5} and 10^{-4} for an integrated luminosity of 3 ab^{-1}. The study of the stability and linearity of the ATLAS hadronic calorimeter (TileCal) photomultipliers is also presented. The methods described aim to monitor the performance of the photomultipliers and identify possible problematic channels.

Resumo

Nesta tese é apresentada uma análise dedicada à pesquisa do decaimento do quark top via correntes neutras com troca de sabor, $t \to qZ$. Os dados analisados foram recolhidos pelo detetor ATLAS durante 2012 em colisões protão–protão no Grande Colisor de Hadrões (LHC), a uma energia de centro de massa de $\sqrt{s} = 8$ TeV e que correspondem a uma luminosidade integrada de 20.3 fb^{-1}. Acontecimentos produzidos com pares de quarks top, no qual um quark top decai no canal $t \to qZ$ ($q = u, c$) e o outro pelo decaimento dominante de acordo com o Modelo Padrão $t \to bW$, são considerados como sinal. Apenas são considerados os decaimentos do bosão Z para leptões carregados e os decaimentos leptónicos do bosão W. Não tendo sido encontrada nenhuma evidência da existência do sinal, foi calculado um limite superior observado (esperado) para a fração do decaimento $t \to qZ$ de 6.7×10^{-4} (7.7×10^{-4}) com um nível de confiança de 95%. A sensibilidade esperada para o canal $t \to qZ$ é também derivada para a fase de alta luminosidade do LHC, juntamente com a sensibilidade esperada para o canal $t \to q\gamma$. Os limites esperados com um nível de confiança de 95% para ambos os canais são da ordem de 10^{-5} e 10^{-4} para uma luminosidade integrada de 3 ab^{-1}. Também é apresentado o estudo da estabilidade e linearidade dos fotomultiplicadores do calorímetro hadrónico, TileCal, do detetor ATLAS. Os métodos descritos visam a monitorização do desempenho dos fotomultiplicadores e a identificação de possíveis canais problemáticos.

Acknowledgements

First, I would like to thank Filipe Veloso, for all the continued support, dedication and patience. His expertise and guidance were invaluable during the course of this work. Also, a thanks to António Onofre for the contagious enthusiasm towards particle physics and everything he has taught me.

I would also like to thank João Carvalho, for his help during the work in TileCal, and to Claudio Santoni who, during my stays at CERN, was always a supporting figure, available to help whenever needed.

I would like to express my gratitude to LIP for all the institutional support and the Portuguese ATLAS group, in particular to Amélia Maio and Patricia Conde Muiño for the amazing work they have done as group leaders.

As a member of the ATLAS Collaboration I wouldn't be able to fully realise the goals of the analyses without all the Top Working Group, the Top Properties Subgroup and the LASER group members, thanks for all the discussions and feedback. Especially to Nuno Castro for accompanying the development of the analysis work and for always being promptly available to give a helping hand.

A warm and sincere thanks to my colleagues: Juanpe, Susana and Miguel for all the work related discussions and the continued friendship.

Thanks to all my friends for their fellowship and encouragement during this journey. A special thank you to Fátima for her true friendship and for always being at my side these past years.

Last, but certainly not the least, a thank you to my family for their unconditional love and support; without them, I wouldn't be where I am today. Thanks to my parents, Fernanda and Herminio, to my sister Joana and also to my uncle António José.

This work was funded by the Fundação para a Ciência e a Tecnologia, through the grant SFRH/BD/51401/2011, and by the project "Colaboração na experiência ATLAS no CERN", with Ref. CERN/FP/116346/2010 and CERN/FIS-NUC/0005/2015.

Contents

List of Figures

LIST OF FIGURES

List of Tables

List of Acronyms

ALICE A Large Ion Collider Experiment

ATLAS A Toroidal LHC ApparatuS

BR branching ratio

CERN European Organisation for Nuclear Research

CIS Charge Injection System

CMS Compact Muon Solenoid

CR Control Region

CSC Cathode Strip Chambers

DD Data-Driven

EF Event Filter

FCal Forward Calorimeter

FCNC Flavour-Changing Neutral Currents

FSR final state radiation

GRL good runs list

HEC Hadronic Endcap Calorimeter

ID Inner Detector

ISR initial state radiation

JER jet energy resolution

JES jet energy scale

LHC Large Hadron Collider

LHCb Large Hadron Collider beauty

LS1 Long Shutdown 1

MC Monte Carlo

MDT Monitored Drift Tubes

MM matrix method

PD Photodiode

PDF parton distribution function

pdf probability density functions

PMT photomultiplier tube

PS Proton Synchrotron

PSB Proton Synchrotron Booster

QCD Quantum Chromodynamics

QFT Quantum Field Theory

ROB Read-Out Buffer

ROD Read-Out Driver

ROS Read-Out Sub-system

RPC resistive plate chambers

SCT SemiConductor Tracker

SFI Sub-Farm Input

SM Standard Model of Particle Physics

SPS Super Proton Synchrotron

SR Signal Region

TGC Thin Gap Chambers

TileCal Tile Calorimeter

TRT Transition Radiation Tracker

1

Introduction

The Standard Model of particle physics has so far successfully explained almost all experimental results and precisely predicted many phenomena. Nevertheless, there are some phenomena like gravity or dark matter, for example, that it does not successfully describe. One way to probe for physics beyond the Standard Model is through the study of the top-quark since its large mass, significantly higher than all the other known elementary particles, makes it a good probe of possible evidences of new physics at the current accessible energies. Discovered in 1995 by the Tevatron experiments at the Fermilab, the top-quark has since been heavily studied by those collaborations and now on the LHC. During 2011 and 2012, about 15 million top-quarks were produced by the LHC in proton–proton collision. This high number of events make possible not only more precise measurements of its properties but also to probe the more rare decay modes, in particular to search for flavour changing neutral currents (FCNC) interactions. These are highly suppressed in the Standard Model, nonetheless they can be highly enhanced by several models of new physics. Therefore, any significant signal of top quark FCNC decays will indicate the existence of new particles or interactions. In this thesis, the search for the FCNC decay of the top-quark into a Z boson and a light-quark is described, using data collected by the ATLAS detector at the LHC. These events are searched for in $t\bar{t}$ production with one top-quark decaying through the FCNC mode and the other one through the Standard Model dominant decay to a b-quark and a W boson, with both W and Z decaying leptonically.

This thesis comprises the work developed in three different topics, required for a complete understanding of FCNC in top-quark physics. In the first topic, technical

work was performed with the apparatus used to collect the data for the analysis. Here, calibration work was done in the ATLAS detector, one of the LHC experiments. The stability and linearity of the photomultipliers (PMTs) from the hadronic calorimeter of the ATLAS detector was studied using its LASER calibration system. The second topic consisted in developing the analysis of the search for FCNC $t \to qZ$ decays in data from proton–proton collisions with a centre-of-mass energy of $\sqrt{s} = 8$ TeV, and a total integrated luminosity of 20.3 fb^{-1}. On the third topic of the doctorate work, the future prospects of the FCNC top-quark decays searches were tested for the high-luminosity LHC, which will deliver an expected luminosity of 3 ab^{-1}, significantly higher than the current statistics. Limits were derived performing a similar analysis to the 8 TeV data, taking into account the higher centre-of-mass energy and high-luminosity conditions, giving an idea of what can be expected to be reached with the future experiments.

The outline of the thesis is as follows. Chapter 2 gives an introduction to the Standard Model, with emphasis on the top-quark properties and the models in which some rare decays might be enhanced. An overview of the LHC and the ATLAS detector, along with a description of each of the various sub-systems is presented in Chapter 3. A description of the TileCal calibration systems, with particular attention to the LASER system, are presented in Chapter 4. It includes the description of the stability and linearity studies performed with the TileCal PMTs. Chapter 5 is devoted to the search of the FCNC top-quark decay to qZ on the 8 TeV LHC data sample, with a description of the background and signal samples used, an overview of the strategy to control and measure the backgrounds, an outline of the systematics involved in the analysis and, finally, the calculation of the limit on the FCNC decay branching ratio. Future prospects for FCNC searches are studied in Chapter 6, in view of the High-Luminosity LHC phase for a centre-of-mass energy of 14 TeV and a luminosity of 3 ab^{-1}. Sensitivities for the FCNC top-quark decays into qZ and $q\gamma$ are estimated. In the end, in Chapter 7, the final conclusions are presented.

Throughout this thesis, natural units will be used ($\hbar = c = 1$) and energies, masses and momenta will be expressed in GeV.

2

Theoretical framework

Over the course of the past century, observations and discoveries led to the conclusion that all matter is made of twelve fundamental particles that interact via four fundamental forces. Our present understanding of all known fundamental particles and three of their interactions (electromagnetic, strong and weak) is described within a single theoretical framework called the Standard Model (SM) of Particle Physics. The model was finalised in the mid 1960s and, since then, many of its predictions have been successfully tested and confirmed by experiments.

This chapter presents a brief introduction to the SM, with emphasis on the top quark properties and production.

2.1 The Standard Model of particle physics

The SM [2–5] is a theory that unifies the weak interaction with electromagnetism and describes the strong interaction. Furthermore, it classifies all elementary particles into two categories: the "force carrier" bosons and the building blocks of all matter, the fermions. It uses a mathematical formalism known as quantum field theory (QFT) [6]. Its Lagrangian, $\mathcal{L}_{\text{SM}}$, can be divided into the following four sectors:

$$\mathcal{L}_{\text{SM}} = \mathcal{L}_{\text{gauge}} + \mathcal{L}_{\text{matter}} + \mathcal{L}_{\text{Higgs}} + \mathcal{L}_{\text{Yukawa}}, \tag{2.1}$$

that describes the behaviour of gauge bosons and of fermions, the Higgs mechanism and the Yukawa interactions between the fermions and the Higgs field.

2.1.1 Gauge groups

The SM is a gauge theory whose Lagrangian is invariant under continuous internal transformations of the groups $SU(2)_L \otimes U(1)_Y$ and $SU(3)_C$. These gauge symmetries describe the behaviour and interactions of the spin-1 vector bosons ("force carriers"). On one hand, the $SU(3)$ theory, named quantum chromodynamics (QCD), describes the strong interactions [5]. The generators of this group correspond to eight gauge bosons called gluons, that carry colour charge and therefore allow gluon-gluon interactions. On the other hand, the $SU(2)_L \otimes U(1)_Y$ describes the electro-weak interactions [2–4], with the group generators $\{T^{\pm}, T^3, Y\}$ being the weak isospin and the weak hypercharge of the $U(1)_Y$ group. The symmetry is spontaneously broken into an $U(1)_{\mathrm{EM}}$ group, giving rise to the electromagnetic interaction (quantum electrodynamics [7–10]), and the massive W and Z bosons and the massless photon (γ).

2.1.2 Matter

In the SM, matter is described by fermionic fields, which are associated to spin 1/2 particles called leptons or, if they experience strong interactions, quarks. Several flavours of quarks (up u, down d, charm c, strange s, top t and bottom b) and leptons (electron e^-, muon μ^-, tau τ^-, electronic neutrino ν_e, muonic neutrino ν_μ and taonic neutrino ν_τ) are known, each one with a corresponding anti-particle. The weak interactions are known to violate parity and this is included in the theory by making the charged $W^{\pm}$ bosons couple only to left-handed (right-handed) fermions (anti-fermions). Hence, the fields associated to the fermions are described in terms of the chirality components – doublets of left-handed components and singlets of right-handed components. The fermions can be organised in generations, presented in Table 2.1 along with their weak isospin, hypercharge, electric charge (defined as $Q_{\mathrm{EM}} = T_3 + Y/2$) and colour quantum numbers. The three generations appear to have identical properties, differing only in their masses and flavours.

The various particles interact in different ways. Neutrinos only interact via the weak force whereas the charged leptons also interact electromagnetically. Quarks, in addition to the other quantum numbers, also have colour charge (*red*, *green* or *blue*) allowing them to interact through the strong force. One characteristic of quarks is that they are always bound in order to form colourless states, a phenomena known

Table 2.1: Quantum numbers of the SM fermionic field content are shown. The fermions can be divided into coloured quarks and colourless leptons, and grouped into three generations ordered by increasing masses. Left- and right-handed quarks fall into different $SU(2)_L$ representations, a doublet and two singlets respectively. A similar structure is obeyed by the leptons, but the SM assumes the absence of right-handed neutrinos. The electric charges, Q, defined as $Q_{\mathrm{EM}} = T_3 + Y/2$, are normalised to the positron charge. In addition, for each particle there is a corresponding antiparticle grouped in right-handed doublets and left-handed singlets, with opposite Q, T^3, Y and corresponding anti-color.

	Families			T	T^3	Y	Q	C
	1^{st}	2^{nd}	3^{rd}					
leptons	$\begin{pmatrix}\nu_e\\ e^-\end{pmatrix}_L$	$\begin{pmatrix}\nu_\mu\\ \mu^-\end{pmatrix}_L$	$\begin{pmatrix}\nu_\tau\\ \tau^-\end{pmatrix}_L$	$\begin{pmatrix}1/2\\ 1/2\end{pmatrix}$	$\begin{pmatrix}+1/2\\ -1/2\end{pmatrix}$	$\begin{pmatrix}-1\\ -1\end{pmatrix}$	$\begin{pmatrix}0\\ -1\end{pmatrix}$	—
	e_R^-	μ_R^-	τ_R^-	0	0	-2	-1	—
quarks	$\begin{pmatrix}u\\ d\end{pmatrix}_L$	$\begin{pmatrix}c\\ s\end{pmatrix}_L$	$\begin{pmatrix}t\\ b\end{pmatrix}_L$	$\begin{pmatrix}1/2\\ 1/2\end{pmatrix}$	$\begin{pmatrix}+1/2\\ -1/2\end{pmatrix}$	$\begin{pmatrix}+1/3\\ +1/3\end{pmatrix}$	$\begin{pmatrix}+2/3\\ -1/3\end{pmatrix}$	$\begin{pmatrix}r,g,b\\ r,g,b\end{pmatrix}$
	u_R	c_R	t_R	0	0	$+4/3$	$+2/3$	r,g,b
	d_R	s_R	b_R	0	0	$-2/3$	$-1/3$	r,g,b

as "confinement" [11]. Thus, individual quarks cannot be isolated and are observed in composite particles like baryons (three-quarks particles, like the proton or the neutron), mesons (quark/anti-quark particles like the pion), pentaquarks (four-quarks and one anti-quark particle, recently announced by the LHCb collaboration at the LHC [12]) or conceivably other colourless combinations of quarks. When free quarks or gluons are created, they combine with quark and anti-quark pairs spontaneously created from the vacuum, a phenomenon known as hadronisation.

2.1.3 Brout–Englert–Higgs mechanism and Yukawa interaction

Both the gauge and the fermionic sector of the theory are not allowed to have mass terms in the Lagrangian, since such type of terms would break the gauge invariance. In order to give rise to the masses of the particles, a four-component scalar field, the Higgs field, can be introduced in the Lagrangian. The Higgs field has an infinite number of degenerate ground-states and through the choice of any (arbitrary) value for this ground-state, the symmetry is spontaneously broken. After the symmetry breaking, besides the three massive gauge bosons, a massive scalar field appears, that corresponds to the Higgs boson. This is known as the Brout–Englert–Higgs mechanism [13–15]. The fermions gain mass through this mechanism by means of a Yukawa interaction term that couples the left- and right-chiral fermions to the new scalar field. Neutrinos are massless in this model since they do not have the right-handed chirality component.[1] To get the mass of the particles from the Yukawa terms, it is necessary to redefine the fields, changing from flavour states, d'_L, to mass states, d_L, by introducing unitary matrices $V^{d,u,\ell}_{L,R}$:

$$d_{L,R} = V^{d}_{L,R} d'_{L,R}, \quad u_{L,R} = V^{u}_{L,R} u'_{L,R}, \quad \ell_{L,R} = V^{\ell}_{L,R} \ell'_{L,R}. \tag{2.2}$$

Furthermore, the left-handed quarks are transformed by different matrices, $V^d_L \neq V^u_L$ and consequently, in the mass eigenstate basis, the d, s, and b quarks are no longer the $SU(2)$ partners of u, c and t quarks, respectively. Instead, the $SU(2)$ doublets are:

$$(u, d''), \quad (c, s''), \quad (t, b''), \tag{2.3}$$

[1] Several experiments have since confirmed that neutrinos are massive particles [16–19], but this lies out of the scope of this thesis. For a recent review on the status of neutrino physics see Ref. [20].

where d'', s'', and b'' are linear combinations of the d, s, b quarks,

$$\begin{pmatrix} d'' \\ s'' \\ b'' \end{pmatrix} = V_{\text{CKM}} \begin{pmatrix} d \\ s \\ b \end{pmatrix} = \begin{pmatrix} V_{ud} & V_{us} & V_{ub} \\ V_{cd} & V_{cs} & V_{cb} \\ V_{td} & V_{ts} & V_{tb} \end{pmatrix} \begin{pmatrix} d \\ s \\ b \end{pmatrix} \tag{2.4}$$

The unitary matrix V_{CKM} is called Cabibbo–Kobayashi–Maskawa (CKM) [21] matrix and affects the couplings of the quarks to the charged W fields. The amplitude $|V_{ij}|^2$ is proportional to the probability of a quark with flavour i to decay into a quark of flavour j and a W boson. Therefore, the charged current, $\mathcal{L}_{CC}$, has couplings of quarks from one doublet to quarks in other doublets (quark mixing):

$$\mathcal{L}_{CC} \propto \bar{u}'_L \gamma^\mu d'_L + \text{h.c.} = \bar{u}_L \gamma^\mu V_L^{d\dagger} V_L^u d_L + \text{h.c.}, \tag{2.5}$$

where h.c. is the hermitian conjugate. Thus, the physical states couple with the charged currents through the matrix $V_{\text{CKM}} = (V_L^d)^\dagger (V_L^u)$. This is different for the neutral current sector where the same does not happen at leading-order:

$$\mathcal{L}_{NC} \propto \bar{u}' \gamma^\mu u' + \bar{d}' \gamma^\mu d' = \bar{u} \gamma^\mu u + \bar{d} \gamma^\mu d, \tag{2.6}$$

i.e., the flavour-changing neutral currents (FCNC) are suppressed at leading-order in the SM. At higher orders, loop contributions generate the following kind of term:

$$\sum_q \sum_{q' \neq q''} V_{qq'} V^*_{qq''} \bar{q}'' \left(\frac{i}{\not{p} - m_q} \right) q', \tag{2.7}$$

where $q = u, c, t$ and $q', q'' = d, s, b$. Due to the unitarity constraints of the CKM matrix, namely $\sum_k V_{ik} V^*_{jk} = 0$, these terms vanish when the masses of the quarks are equal. Since quarks do have different masses, a residual contribution can appear. This is known as Glashow–Iliopoulos–Maiani (GIM) mechanism [22].

2.1.4 Beyond the SM

The SM has been continually tested and has, so far, proven to be very successful at describing what is observed at the experiments. Several particles were predicted by the model before their discovery and many parameters have been measured, in agreement with the theory, most notably in LEP and SLAC [23, 24]. The compatibility between the parameters in the model and the measured electroweak observables, such as cross

sections, masses and various couplings has also been assessed by performing global SM fits to the electroweak data [25].

Nevertheless it is an incomplete theory since no consistent way to incorporate gravity has so far been found nor does it provide any candidate for dark matter or an explanation for the matter–antimatter asymmetry. Neutrinos are massless in the theory, but experiments have since confirmed the opposite. Moreover, it leaves many questions unanswered, since some features are included explicitly in the theory. For example, there is no prediction for the number of fermion generations or the mass hierarchy. Another issue is the "naturalness problem" concerning the low mass of the observed Higgs boson. Due to the quadratically divergent quantum corrections in the Higgs mass calculation, it should be expected a larger Higgs mass unless the parameters are carefully fine-tuned, which this is considered unnatural.

These are some of the unresolved problems that give motivation to formulate the various theories that go beyond the SM. Some include modifications to the SM that yield the same observed results but lead to possible new observables that can be tested with the experiments. In the next section some these theories are explored in order to motivate the search for SM inconsistencies, particularly in the FCNC decays.

2.2 The top quark

The top quark was discovered in 1995 by the CDF [26] and DØ [27] experiments in $p\bar{p}$ collisions with centre-of-mass energy of 1.8 TeV at Fermilab's Tevatron collider. It is the heaviest elementary particle known. The latest direct mass measurements are summarised in Figure 2.1. This large mass value, in comparison to the other quarks with masses ranging from 2 MeV to 4 GeV, indicates a strong Yukawa coupling to the Higgs, making it a good object to study the electroweak symmetry breaking mechanism. As a consequence of its large mass, its lifetime ($1/\Gamma \sim 5 \times 10^{-25}$ s [28]) is extremely small, about an order of magnitude shorter than the typical time scale of the strong interaction ($1/\Lambda_{\mathrm{QCD}} \sim 3 \times 10^{-24}$ s [28]), making it possible to decay before hadronisation can occur [29]. This allows the study of bare quarks by looking at information of the top-quark decay products. Additionally, it decays almost exclusively to bW ($|V_{tb}|^2$ close to unity) providing very specific signatures to look for (since the W boson can decay hadronically, $W \to q\bar{q}$, or leptonically, $W \to \ell\nu$, final top-quark

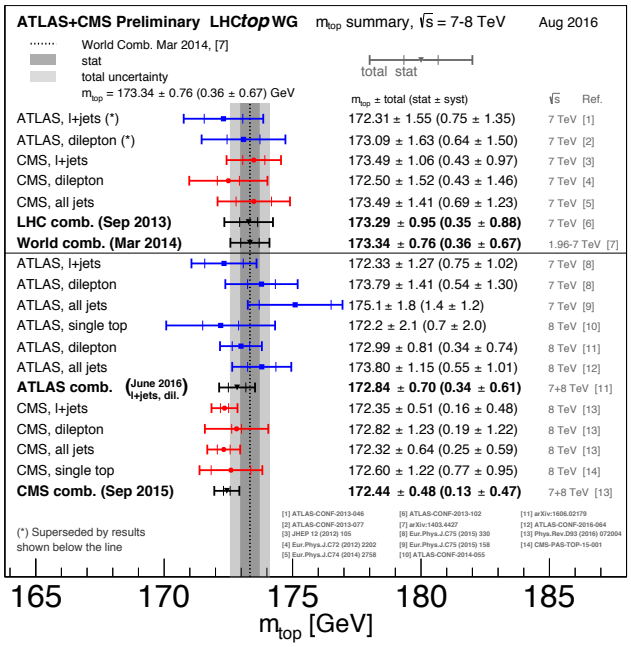

Figure 2.1: Summary of the ATLAS and CMS direct m_{top} measurements. The results are compared with the LHC and Tevatron+LHC m_{top} combinations. Taken from [30].

states can be $t \to Wb \to \{\ell\nu, q\bar{q}\}b$). The second most likely decays are to $t \to sW$ and $t \to dW$, which have branching ratios (BR) of around 1.6×10^{-3} and 7.1×10^{-5}, respectively [28]. All these properties make this particle a very interesting tool to test the SM and to look for new physics clues.

2.2.1 FCNC top-quark decays

Though absent at leading-order due to the GIM mechanism, FCNC top-quark decays can occur at loop-level, as mentioned in Section 2.1. The corresponding BRs are smaller than 10^{-12} [31–34], which is many orders of magnitude smaller than the dominant $t \to bW$ decay mode. Essentially this means that any measurable BR for these decays is an indication of new physics, since experimental sensitivities are significantly lower than the SM prediction, as can be seen in Table 2.3.

Some of these FCNC decays are enhanced in many models of new physics, leading to potentially measurable BRs by the current experiments. Even if those FCNC BRs are not measured, the experiments can test some of the models or constrain their

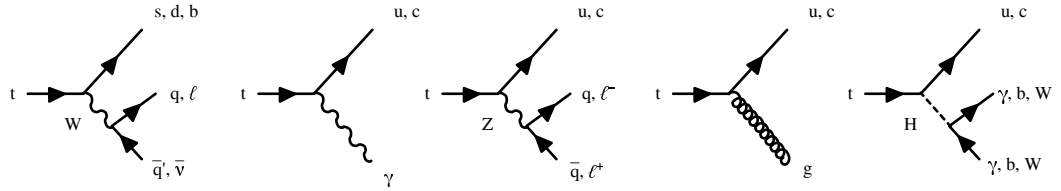

(a) (b) (c) (d) (e)

Figure 2.2: Top quark decays: (a) the dominant SM decay channel $t \to bW$ and the FCNC channels of SM extensions (b) $t \to q\gamma$, (c) $t \to qZ$, (d) $t \to qg$ and (e) $t \to qH$, with $q = u, c$. The subsequent most relevant W, Z and Higgs bosons decays are also represented.

parameters space. Leading order diagrams of FCNC top-quark decays are shown in Figure 2.2 along with the SM dominant decay; these include the decay into a photon, a Z boson, Higgs boson or a gluon.

Some extensions to the SM, can introduce exotic (vector-like) quarks [33, 35, 36] that are $SU(2)_L$ singlets (QS). In these models, the CKM matrix is no longer unitarity because, besides coupling to the down-type quarks, the up-type quarks can now couple to these new particles as well; as a consequence, the GIM mechanism becomes weaker. The neutral current sector also becomes non-diagonal, making it possible to the up- and down-type quarks to couple directly at leading-order to up- and down-type quarks from other generations. The FCNC top-quark BRs increase to about 10^{-4}, 10^{-7}, 10^{-9} and 10^{-5} for the $t \to qZ$, $t \to qg$, $t \to q\gamma$ and $t \to qH$ decay channels, respectively.

Extended electroweak symmetry breaking sectors with two Higgs-doublets (2HDM) [37–43] imply the existence of two complex scalar fields that, after the symmetry breaking, originate five types of Higgs bosons: three neutral (h, H, A) and a charged pair $(H^{\pm})$. Three types of 2HDM models exist depending on the coupling between the Higgs bosons and the fermions. In type I, up- and down-type quarks couple to the same Higgs doublet; in type II, they couple to different doublets and in type III they couple to both doublets. Types I and II are called Flavour Conserving 2HDM (FC 2HDM) and although the FCNC decays are forbidden at leading-order they are enhanced at loop-level reaching BRs of 10^{-10}, 10^{-4}, 10^{-7} and 10^{-3}, for the $t \to qZ$, $t \to qg$, $t \to q\gamma$ and $t \to qH$ decay channels, respectively. Type III allows FCNC decays at leading-order, resulting in BRs: 10^{-6}, 10^{-4}, 10^{-7} and 10^{-5}, for the $t \to qZ$, $t \to qg$, $t \to q\gamma$ and $t \to qH$ decay channels, respectively.

Another possible SM extension is supersymmetry (SUSY), which associates each of the known bosons and fermions to new particles, called super-partners. This model must be a broken symmetry so the super-partners have different masses than their counterparts, otherwise they would have already been found. A new quantum number associated to the new particles, R-parity, is defined as $R = (-1)^{3(B-L)+2S}$, where B, L and S are the baryon number, the lepton number and the spin, respectively. All SM particles have R-parity of $+1$ while supersymmetric particles have R-parity of -1. In minimal supersymmetric model (MSSM) [44–50] one Higgs-doublet is included into the SM, along with the corresponding supersymmetric partners, and it conserves R-parity. The super-parters add new contributions to the $t \to qZ$, $t \to qg$, $t \to q\gamma$ and $t \to qH$ FCNC decays at one-loop level increasing the BRs to about 10^{-7}, 10^{-7}, 10^{-8} and 10^{-5}, respectively. On models with R-parity violation ($\not{R}$ SUSY) [51, 52] top-quark decays may also be induced at one-loop level by baryon or lepton number-violating interactions, which can increase the BRs by an order of magnitude.

In Randall–Sundrum (RS) models [53, 54], the universe is believed to be a brane in a higher dimensional space-time and the SM particles can propagate in this extra dimension with profiles governed by the corresponding Yukawa couplings. FCNCs arise already at the tree level, due to flavour-violating couplings of the Kaluza-Klein modes (KK–partners that can carry momentum to the extra dimension) to the quark mass eigenstates. These couplings are largest for the top quark, whose profile typically has the most significant overlap with the KK modes. The BRs from FCNC processes such as $t \to qZ$ and $t \to qH$ can get values of 10^{-5} and 10^{-4}, respectively.

A summary of the maximum values for the BRs given by the different extensions to the SM is shown in Table 2.2, along with the SM ones. For reviews see Ref. [34, 55]. The experimental limits on the BRs established by experiments at the LEP [56–61], HERA [62–64], Tevatron [65–69] and LHC [70–72] colliders (before the work presented in this thesis was initiated) are shown in Table 2.3.

2.2.2 Effective model

These new interactions can manifest themselves at the current energy scale, through small deviations from the SM. Instead of looking into all the models, an effective Lagrangian [61, 73] can be used to parametrized how the new physics affects the low

Table 2.2: Maximum allowed FCNC BRs as predicted by several models (adapted from [34, 55]). Quoted values correspond to $q = c$, which have higher BRs than decays to an up-quark.

Model:	SM	QS	2HDM	FC 2HDM	MSSM	$\not{R}$ SUSY	RS
$t \to qZ$	10^{-14}	10^{-4}	10^{-6}	10^{-10}	10^{-7}	10^{-6}	10^{-5}
$t \to qg$	10^{-12}	10^{-7}	10^{-4}	10^{-8}	10^{-7}	10^{-6}	10^{-10}
$t \to q\gamma$	10^{-14}	10^{-9}	10^{-7}	10^{-9}	10^{-8}	10^{-9}	10^{-9}
$t \to qH$	10^{-15}	10^{-5}	10^{-3}	10^{-5}	10^{-5}	10^{-9}	10^{-4}

Table 2.3: Experimental 95% CL upper limits on the BRs of the FCNC top quark decay channels established by experiments at the LEP [56–60, 64] (combination of the ALEPH, DELPHI, L3 and OPAL collaborations), HERA [62–64] (best ZEUS and H1 results), Tevatron [65–69] and LHC [70–72] colliders in 2012 ($q = u, c$).

	LEP	HERA	Tevatron		LHC (7 TeV)	
			CDF	DØ	ATLAS	CMS
$t \to qZ$	7.8×10^{-2}	3.0×10^{-1} (uZ)	3.7×10^{-2}	3.2×10^{-2}	7.3×10^{-3}	2.1×10^{-3}
$t \to q\gamma$	2.4×10^{-2}	4.7×10^{-1} ($u\gamma$)	3.2×10^{-2}	—	—	—
$t \to ug$	1.7×10^{-1}	1.3×10^{-1}	3.9×10^{-4}	2.0×10^{-4}	5.7×10^{-5}	—
$t \to cg$			5.7×10^{-3}	3.9×10^{-3}	2.7×10^{-4}	—

energy observables. This new Lagrangian includes the effects of new physics at an energy scale, Λ, by adding dimension-six effective terms to the SM Lagrangian:

$$\mathcal{L} = \mathcal{L}_{\text{SM}} + \mathcal{L}^{\text{eff}} = \mathcal{L}_4 + \frac{1}{\Lambda^2}\mathcal{L}_6 + \ldots, \tag{2.8}$$

where $\mathcal{L}_4 = \mathcal{L}_{\text{SM}}$ and $\mathcal{L}_6$ contains operators with dimension-six. The rest of the terms contain operators of dimension higher than six and will be suppressed due to the associated factors $1/\Lambda^4$, etc. $\mathcal{L}_6$ can be written as a linear combination of dimension-six operators O_j:

$$\mathcal{L}_6 = \sum_j C_j O_j, \tag{2.9}$$

with C_j being complex constants. The O_j operators contain the fermion doublets and singlets, the gauge field tensors, the Higgs doublet and the covariant derivatives. For the scope of this thesis, this is used to generate the simulated signal samples used in the analysis, with the $t \to uZ$, $t \to cZ$, $t \to u\gamma$ and $t \to c\gamma$ decays. The most general Ztu, γtu, gtu and Htu vertices that arise from the dimension-six operators can be parametrised, including only γ^μ and $\sigma^{\mu\nu}q_\nu$ terms, [74] as:

$$\begin{aligned}
\mathcal{L}_{Ztu} =& -\frac{g}{2c_W}\bar{u}\gamma^\mu\left(X_{ut}^{\text{L}}P_{\text{L}} + X_{ut}^{\text{R}}P_{\text{R}}\right)tZ_\mu \\
&-\frac{g}{2c_W}\bar{u}\frac{i\sigma^{\mu\nu}q_\nu}{m_Z}\left(\kappa_{ut}^{\text{L}}P_{\text{L}} + \kappa_{ut}^{\text{R}}P_{\text{R}}\right)tZ_\mu + \text{h.c.}, && (2.10)\\
\mathcal{L}_{\gamma tu} =& -e\bar{u}\frac{i\sigma^{\mu\nu}q_\nu}{m_t}\left(\lambda_{ut}^{\text{L}}P_{\text{L}} + \lambda_{ut}^{\text{R}}P_{\text{R}}\right)tA_\mu + \text{h.c.}, && (2.11)\\
\mathcal{L}_{gtu} =& -g_s\bar{u}\lambda^a\frac{i\sigma^{\mu\nu}q_\nu}{m_t}\left(\zeta_{ut}^{\text{L}}P_{\text{L}} + \zeta_{ut}^{\text{R}}P_{\text{R}}\right)tG_\mu^a, && (2.12)\\
\mathcal{L}_{Htu} =& -\frac{1}{\sqrt{2}}\bar{u}\left(\eta_{ut}^{\text{L}}P_{\text{L}} + \eta_{ut}^{\text{R}}P_{\text{R}}\right)tH + \text{h.c.}, && (2.13)
\end{aligned}$$

where γ^μ are the gamma matrices, $\sigma^{\mu\nu}$ are the Pauli matrices, λ^a are the Gell-Mann matrices, g is the electroweak coupling, g_s is the strong coupling, e is the electric charge, c_W is the cosine of the weak mixing angle, u and t are the quark spinors, Z_μ, A_μ, G_μ^a and H are the boson fields, P_{L} (P_{R}) is the left-handed (right-handed) projection operator, m_Z is the Z boson mass, m_t is the top-quark mass, $q^\nu = p_t^\nu - p_u^\nu$ is the outgoing boson momentum. The Ztu vertex involves a minimum of four anomalous couplings $X_{ut}^{\text{L}}, X_{ut}^{\text{R}}, \kappa_{ut}^{\text{L}}, \kappa_{ut}^{\text{R}}$. The γtu, gtu and Htu vertices involve a minimum of two anomalous

couplings: $\lambda_{ut}^{\mathrm{L}}, \lambda_{ut}^{\mathrm{R}}$; $\zeta_{ut}^{\mathrm{L}}, \zeta_{ut}^{\mathrm{R}}$ and $\eta_{ut}^{\mathrm{L}}, \eta_{ut}^{\mathrm{R}}$, respectively. The Ztc, γtc, gtc and Htc vertices can be parametrised in a similar fashion.

2.2.3 Top-quark production

The top quark has been produced in particle colliders through two main mechanisms: pair production ($t\bar{t}$) and single production (single top), via the strong and weak interactions, respectively. Leading-order Feynman diagrams for $t\bar{t}$ and single-top production are shown in Figure 2.3 and Figure 2.4, respectively.

The top-quark pair production takes place through gluon fusion or $q\bar{q}$ annihilation. At the Large Hadron Collider (LHC) centre-of-mass energies of a few TeV, gluon fusion is expected to dominate $t\bar{t}$ production with a fraction of 87%, in comparison to the 13% fraction of the $q\bar{q}$ annihilation [75]. The predicted $t\bar{t}$ cross section in pp collisions at a centre-of-mass energy of $\sqrt{s} = 8$ TeV is $\sigma_{t\bar{t}} = 253^{+13}_{-15}$ pb for a top-quark mass of 172.5 GeV. The cross section has been calculated at next-to-next-to leading-order (NNLO) in QCD including resummation of next-to-next-to leading logarithmic (NNLL) soft gluon terms with `top++` 2.0 [76–81]. As detailed in Section 5.1.2, the uncertainty comes from the parton distribution function (PDF), the strong coupling (α_{S}) and the renormalisation/factorisation scale. The most recent public results from ATLAS and CMS collaborations on the $t\bar{t}$ production cross-section measurements are summarised in Figure 2.5.

The single-top production occurs at a lower rate through the t-channel exchange of a virtual W boson, the s-channel decay of a virtual W boson and the associated production of a top quark and a W boson (Wt-channel). The corresponding expected cross sections for pp collisions at a centre-of-mass energy of 8 TeV are $87.76^{+3.44}_{-1.91}$ pb [82], $5.61^{+0.22}_{-0.22}$ pb [83] and $22.37^{+1.52}_{-1.52}$ pb [84], respectively. The most recent public results from ATLAS and CMS collaborations on the single-top production cross-section measurements are summarised in Figure 2.6.

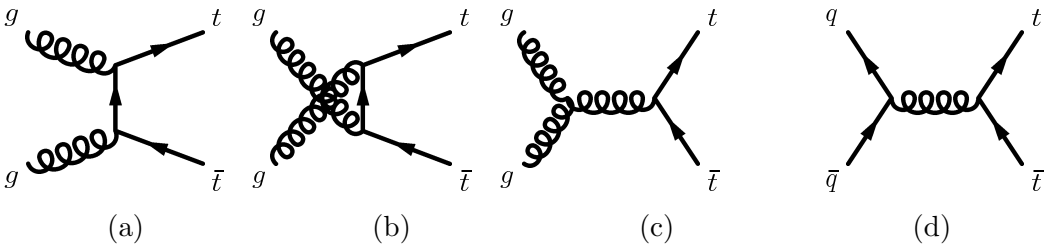

Figure 2.3: Leading-order Feynman diagrams of the $t\bar{t}$ production. Gluon scattering processes, (a), (b) and (c), are the dominant processes at LHC, while quark scattering, process (d), is the dominant one at Tevatron.

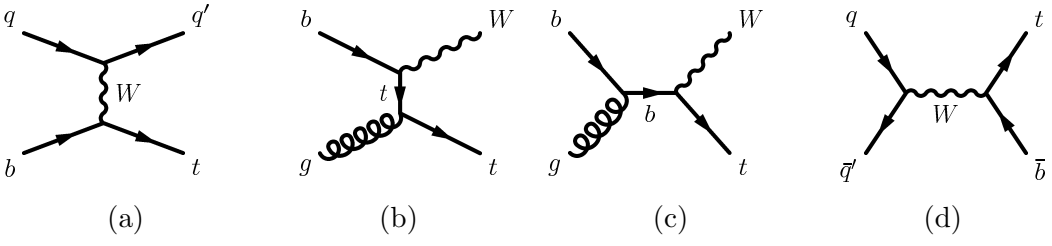

Figure 2.4: Leading-order Feynman diagrams of the single-top production, (a) t-channel, (b) and (c) Wt-channel and (d) s-channel.

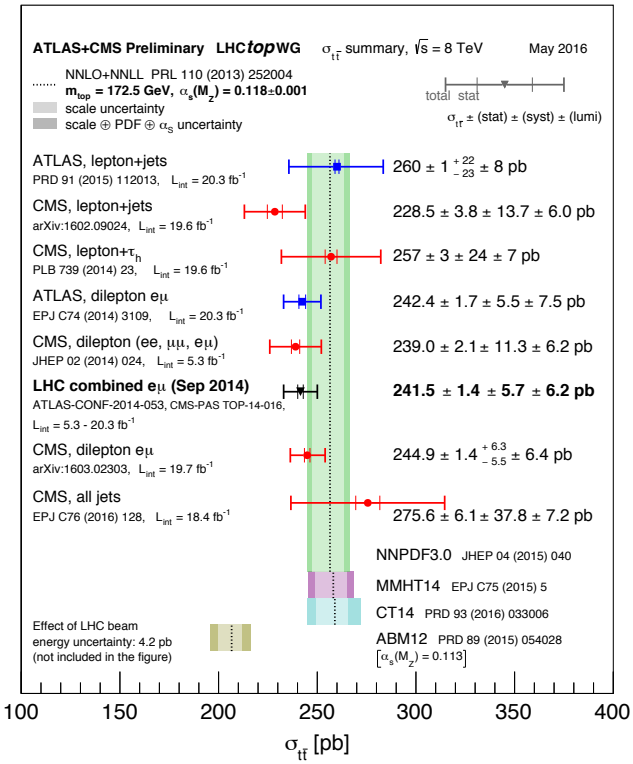

Figure 2.5: Summary of ATLAS and CMS measurements of the top-pair production cross-section at 8 TeV, compared to the NNLO QCD calculation complemented with NNLL resummation (`Top++` 2.0). The theory band represents uncertainties due to renormalisation and factorisation scale, PDFs and the strong coupling. The measurements and the theory calculation are quoted for m_{top} =172.5 GeV. Taken from [85].

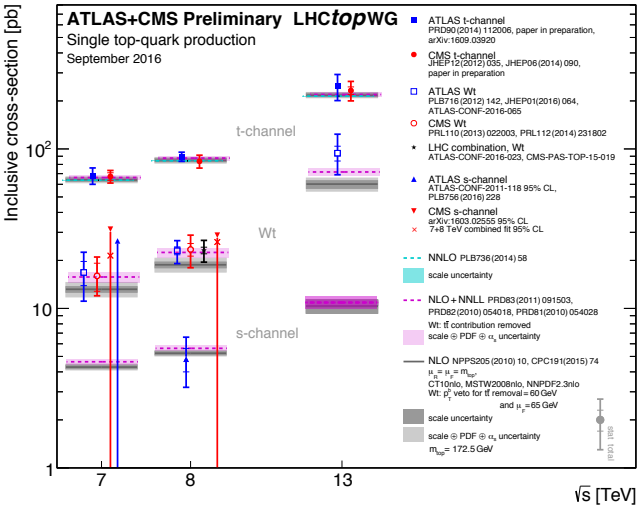

Figure 2.6: Summary of ATLAS and CMS measurements of the single-top production cross-sections in various channels as a function of the center of mass energy. The measurements are compared to theoretical calculations based on: NLO QCD, NLO QCD complemented with NNLL resummation and NNLO QCD (t-channel only). The measurements and the theory calculation are quoted for m_{top} =172.5 GeV. Taken from [86].

3

Experimental apparatus

"Indeed, the Standard Model, with all its brilliant successes, does not explain enough. It merely describes interactions among actors which Nature presents with many different properties for whose origin we presently have very few clues." [87]

In March of 1984, physicists attended a workshop in Lausanne and Geneva, to discuss the possibility of building an hadron collider housed in the LEP tunnel (still under construction at that time), at CERN. Such a collider would reach the TeV energies, relevant for electroweak physics, and provide data to explore some questions left open by the SM. Among these, were the origin of particle masses, origin of flavour and what kind of unification could exist beyond the SM.

In this chapter the CERN laboratory is described, focusing on the Large Hadron Collider and the ATLAS detector.

3.1 CERN

The European Organisation for Nuclear Research (CERN, derived from the french name *"Conseil Européen pour la Recherche Nucléaire"*) is the world's largest particle physics laboratory, located on the Franco-Swiss border, near Geneva. Founded in 1954, it was one of Europe's first joint ventures, aiming to motivate the collaboration in nuclear research between the member states [88], which would also allow them to share the increasing costs of nuclear physics facilities. Over the years, nuclear physics gave birth to particle physics, the main interest of CERN today. As of 2016, CERN has twenty-

two state-members and hosts over ten-thousand visiting scientists and engineers from international collaborations all over the world.

Since its inception, many important achievements in particle physics and computer science happened at CERN, namely the observation of neutral currents in the Gargamelle bubble chamber [89] (1973), the W and Z bosons discovery in the UA1 and UA2 experiments [90, 91] (1983); the determination of the number of neutrino families at the Large Electron–Positron Collider [23] (1989), the invention of the World Wide Web (1989) [92], the discovery of direct CP violation in the NA48 experiment [93] (1999) and the observation of a new particle consistent with the SM Higgs boson [94, 95] (2012).

3.2 Large Hadron Collider

The Large Hadron Collider (LHC) [96] is a two-ring superconducting hadron accelerator and collider, installed in the 26.7 km tunnel constructed for the LEP accelerator at CERN. It lies at depths of 50 m to 175 m below the French and Swiss countryside.

The main goal is to accelerate protons to high energies and collide them, though it can also work with lead-ions. To accomplish this, an injection and acceleration chain, shown in Figure 3.1, is needed. Protons are produced in bunches by applying an electric field to a bottle of hydrogen gas thus stripping the atoms of their electrons. The first step in the acceleration chain is the Linac 2 where the protons reach the energy of 50 MeV. The beam is then injected into the Proton Synchrotron Booster (PSB) which accelerates the protons to 1.4 GeV, then to the Proton Synchrotron (PS) further accelerating them to 25 GeV and next to the Super Proton Synchrotron (SPS), where they reach 450 GeV. Finally, two counter-rotating beams are injected into the LHC.

The path of the tunnel is not a perfect circle, instead, it consists of eight arc sections (22 km) separated by eight long straight sections (5 km). The four LHC experiments are located in straight sections where beam crossing occurs: ATLAS (A Toroidal LHC ApparatuS), CMS (Compact Muon Solenoid), ALICE (A Large Ion Collider Experiment) and LHCb (A Large Hadron Collider beauty Experiment). The four remaining straight sections do not have beam crossing and contain utility insertions.

The beam pipe itself is comprised of 1232 superconducting dipole magnets to bend the beams and keep them on course, 392 main quadrupole magnets to keep the beams

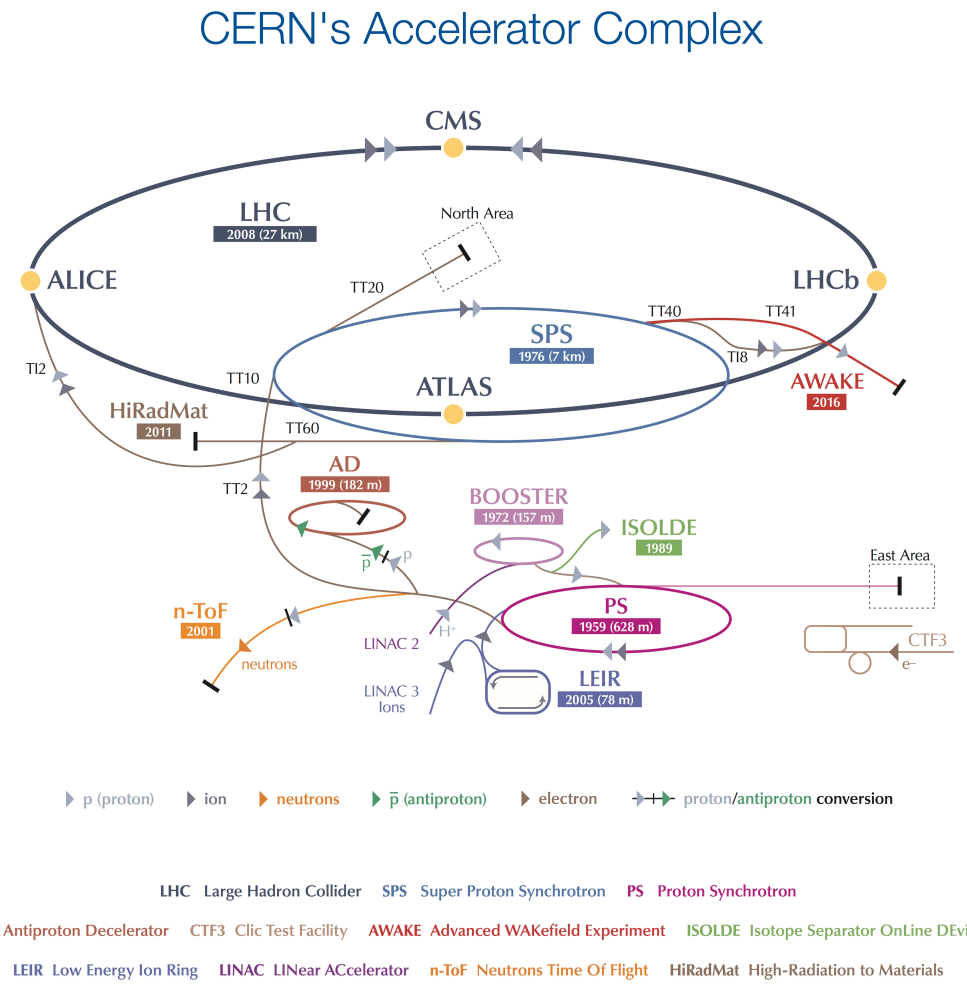

Figure 3.1: Schematic view of the LHC injection and acceleration chain at the CERN's accelerator complex. Adapted from [97].

focused and additional higher order magnetic multipoles to further correct the beam trajectory. These are type-II superconducting magnets, made of niobium-titanium that operate at an average temperature of 1.9 K. This is possible due to a constant flow of liquid helium circulating in a cryogenic ring, right beside the main pipe. The cross section of an LHC dipole is represented in Figure 3.2 where the two beam pipes can be seen with the superconductor coils around them.

Special quadrupole magnets focus the particle beams to reach highest densities at their interaction points in the centre of the experiments. To be sensitive to rare events, the main design goals for the LHC were set so that the experiments would get high beam intensity with centre-of-mass energies above 1 TeV. Since protons are composite particles made of quarks and gluons, the minimum beam energy should be higher, because only a fraction of the total beam energy is involved in a particular collision; thus the design value of 7 TeV per beam was chosen. The number of events (N) that are produced is given by the product of the event cross-section, σ, and the instantaneous luminosity of the delivered beams, $\mathcal{L}$:

$$N = \sigma \int \mathcal{L} dt = \sigma L, \tag{3.1}$$

with L the so-called integrated luminosity. For a Gaussian beam distribution, $\mathcal{L}$ can be written as [98]:

$$\mathcal{L} = \frac{N_1 N_2 f N_b}{4\pi\sigma_x\sigma_y}, \tag{3.2}$$

where N_1 and N_2 are the number of protons per bunch, f the revolution frequency, N_b the number of bunches and $\sigma_{x,y}$ the transversal size of the bunches at the interaction point. Beams with 2808 bunches (with 1.15×10^{11} protons each), spaced 25 ns apart, are needed to reach the goal luminosity of 10^{34} cm^{-2}s^{-1}. Also, a field of 8.3 T, produced by the superconducting magnet dipoles, is required to reach the design energy value.

The first high-energy collisions took place on the 30$^{\text{th}}$ of March 2010 with a centre-of-mass energy of $\sqrt{s} = 7$ TeV and continued during the rest of 2010 and in 2011. In 2012, from April to November, the beam energy was increased to 4 TeV, with the superconducting dipole magnets producing a magnet field of 4.8 T. The beams consisted of around 1374 bunches, with an average of 1.6 to 1.7×10^{11} protons, spaced 50 ns from one another [99].

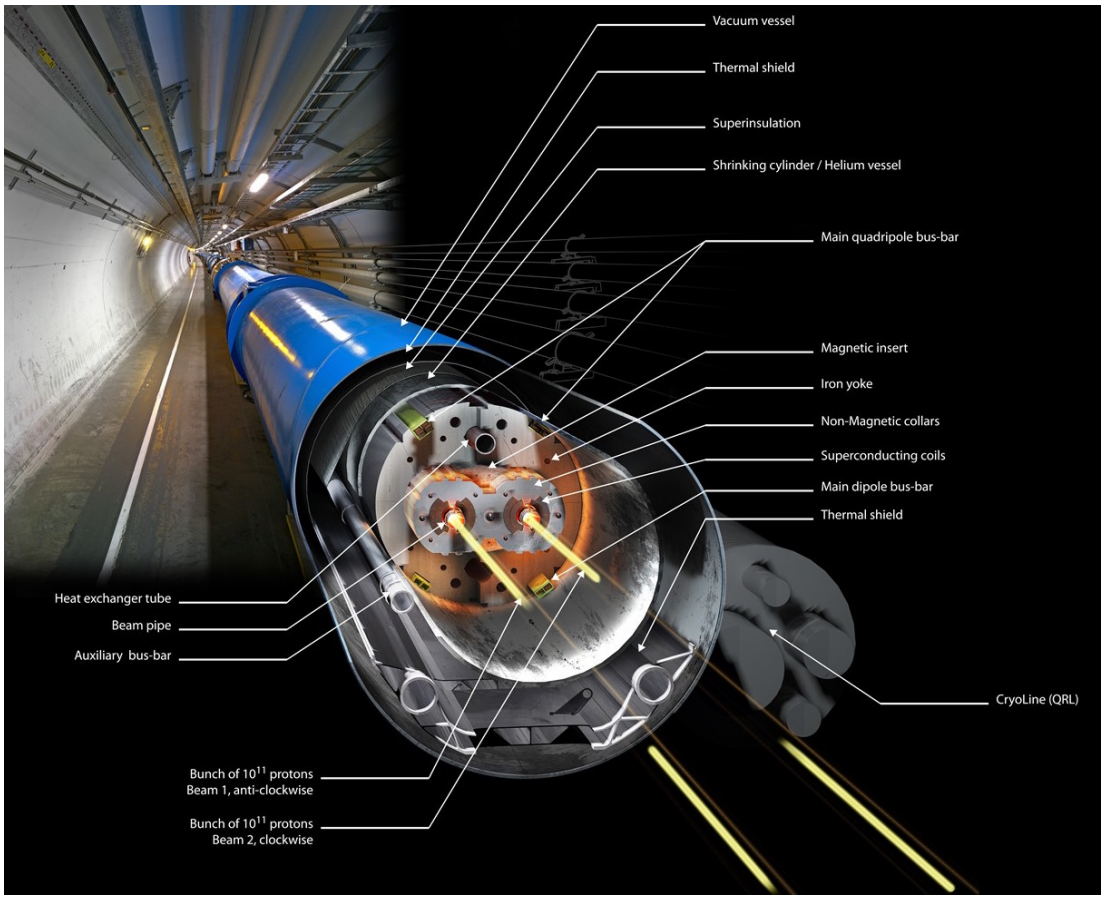

Figure 3.2: Cross section of an LHC dipole in the tunnel. Taken from [100].

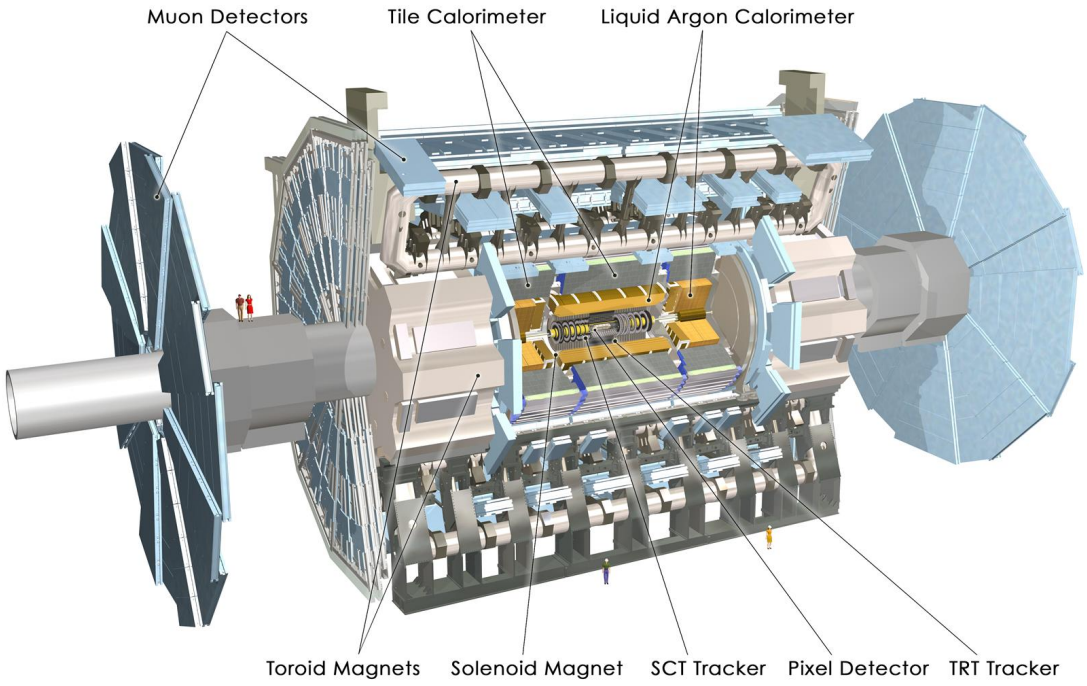

Figure 3.3: Cut-away view of the ATLAS detector. Taken from [102].

3.3 ATLAS detector

The ATLAS detector [101], depicted in Figure 3.3, is one of the two general-purpose detectors at the LHC, the other one being the CMS detector. Although they have the same goals, they apply different technical solutions and different magnet-system designs. Measuring 44 m long and 25 m high, ATLAS consists of several cylindrical layers of sub-detectors around the beam pipe and two endcaps, in order to cover the highest possible solid angle around the interaction point. Each one of these sub-detectors is designed to measure specific properties or particles, such as the tracking device (called "Inner Detector") to reveal the path of electrically charged particles, calorimeters that absorb and measure the energy of the particles (LAr, TileCal, ...) and a detector to identify muons (muon system). By gathering the information given by the different type of detectors it is possible to deduce what kind of event was registered at the moment of the collision. The signatures left in the detector by different types of particles are represented in Figure 3.4. All the different ATLAS components are described in the following sub-sections.

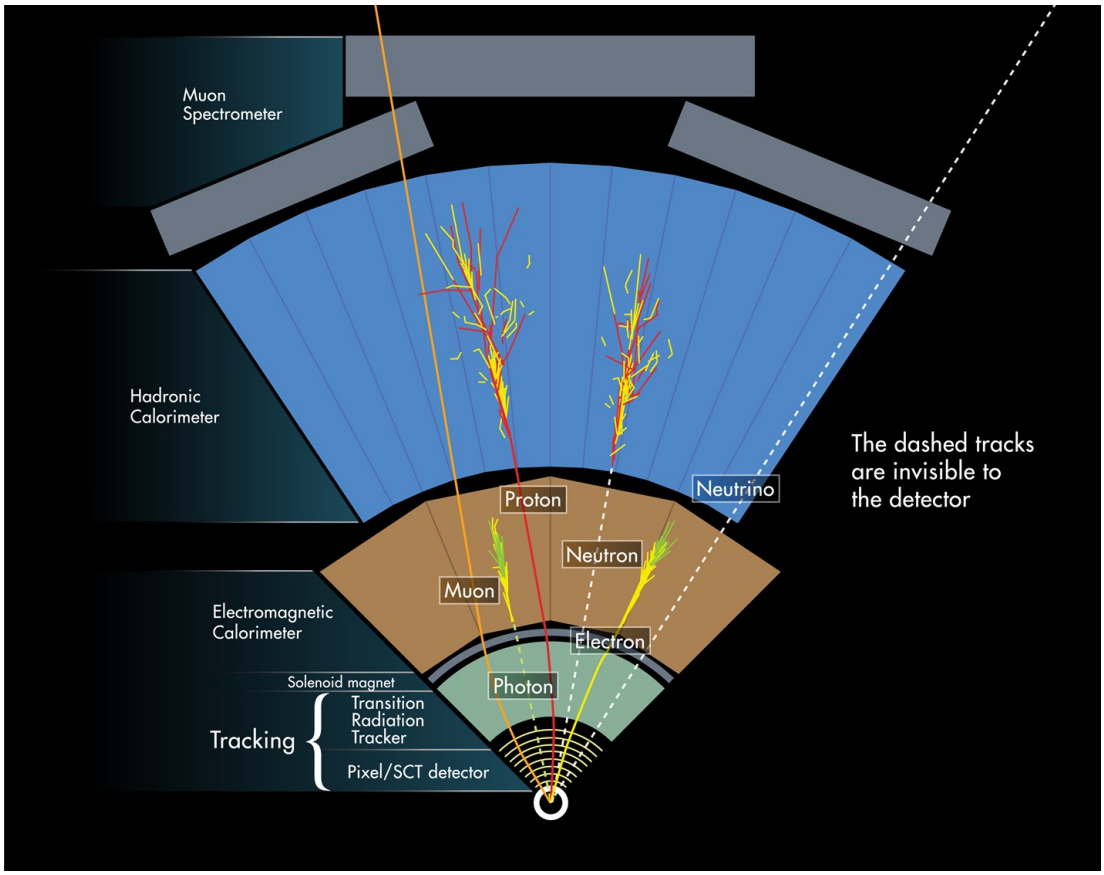

Figure 3.4: A schematic view representing how ATLAS detects particles. Taken from [103].

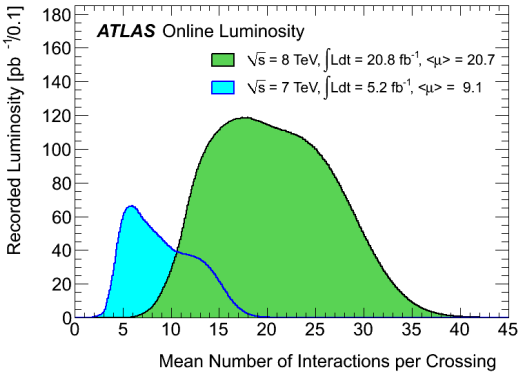

Figure 3.5: Luminosity-weighted distribution of the mean number of interactions per beam crossing for the 2011 and 2012 data. The mean number of interactions per beam crossing corresponds to the mean of the Poisson distribution on the number of interactions per beam crossing calculated for each bunch. More details on this can be found in Ref. [105]. Taken from [106].

One of the challenges presented to the detector is the high luminosity provided by the LHC. Using Equation 3.1 and the total cross-section value of around 10^8 nb [104], 10^9 events/s are expected at the design instantaneous luminosity. Hence, every rare candidate event of new physics will be accompanied, on average, by 25 "pile-up" events. To illustrate this, the mean number of interactions per bunch-crossing, for the 7 TeV and 8 TeV data, is shown in Figure 3.5 and an example of a high pile-up event is shown in Figure 3.6.[1]

To overcome this, several requirements are fulfilled by the detector, namely a very good electromagnetic calorimeter for electron and photon measurements complemented by full-coverage hadronic calorimetry for accurate jet and missing transverse energy measurements, efficient tracking at high luminosity and standalone precision muon-momentum measurements. In addition it must have fast response, otherwise it would accumulate many bunch crossings (this requires fast, radiation resistant electronics). The general ATLAS detector performance goals are summarised in Table 3.1.

During the Run I phase of the operations, the ATLAS detector recorded more than 26 fb^{-1} of data with each subsystem operating with efficiency above 95%. Figure 3.7

[1]Note that the average number of interactions is different from the design value since several design performance goals (namely the spacing between bunches which was 50 ns instead of 25 ns) were not yet reached for the 2011/2012 data taking periods.

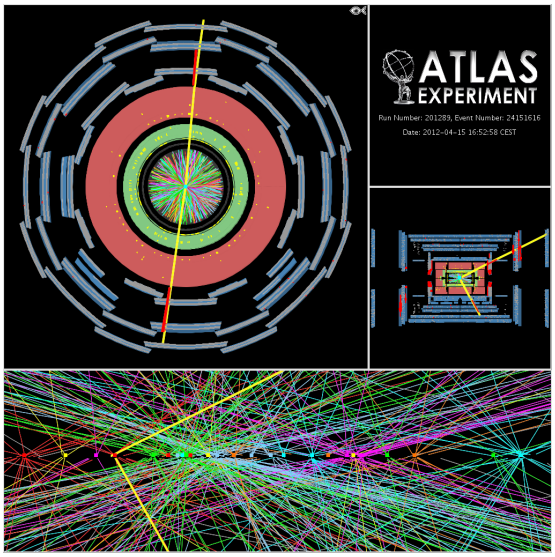

Figure 3.6: A candidate Z boson event in the di-muon decay with 25 reconstructed vertices. This event was recorded on April 15$^{\text{th}}$ of 2012 and demonstrates the high pile-up environment in the 2012 data taking period. For this display the track p_{T} threshold is 0.4 GeV and all tracks are required to have at least 3 Pixel and 6 SCT hits. Taken from [107].

shows the cumulative luminosity delivered by the accelerator (green) and recorded by ATLAS (yellow) as a function of time, during stable beams (for pp collisions) at centre-of-mass energies of 7 TeV in 2011 and 8 TeV in 2012.

3.3.1 Coordinate system

ATLAS uses a right-handed coordinate system, depicted in Figure 3.8, with its origin at the nominal interaction point in the centre of the detector and with the z-axis along the beam pipe. The x-axis points from the interaction point to the centre of the LHC ring, and the y-axis points upward. As usual, ϕ is the azimuthal angle around the beam pipe (measured in relation to the x-axis) and the polar angle, θ, is the angle measured from the positive z-axis. The pseudorapidity, η, relates with θ by:

$$\eta = -\ln\left(\tan\left(\theta/2\right)\right). \tag{3.3}$$

The xy (or $r\phi$) plane is called the transverse plane and quantities such as transverse momentum (p_{T}) or transverse energy (E_{T}) are measured with respect to this plane.

Table 3.1: General performance goals of the ATLAS detector. Note that, for high-p_{T} muons, the muon-spectrometer performance is independent of the inner-detector system. The units for E and p_{T} are GeV. Taken from [101].

Detector component	**Required resolution**	**η coverage**	
		Measurement	Trigger
Tracking	$\sigma_{p_{\mathrm{T}}}/p_{\mathrm{T}} = 0.05\%\ p_{\mathrm{T}} \oplus 1\%$	± 2.5	
EM calorimetry	$\sigma_E/E = 10\%\ /\ \sqrt{E} \oplus 0.7\%$	± 3.2	± 2.5
Hadronic calorimetry (jets)			
barrel and endcap	$\sigma_E/E = 50\%\ /\ \sqrt{E} \oplus 3\%$	± 3.2	± 3.2
forward	$\sigma_E/E = 100\%\ /\ \sqrt{E} \oplus 10\%$	$3.1 < \lvert\eta\rvert < 4.9$	$3.1 < \lvert\eta\rvert < 4.9$
Muon spectrometer	$\sigma_{p_{\mathrm{T}}}/p_{\mathrm{T}} = 10\%$ at $p_{\mathrm{T}} = 1$ TeV	± 2.7	± 2.4

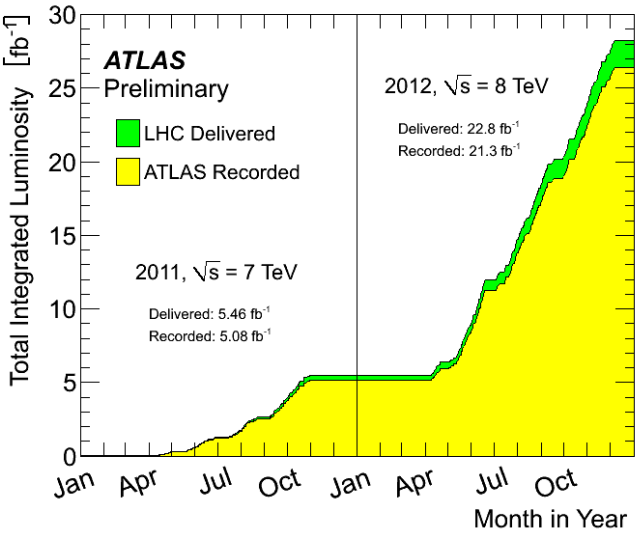

Figure 3.7: Cumulative luminosity delivered by the LHC (green), and recorded by ATLAS (yellow) as a function of time, during stable beams for pp collisions at centre-of-mass energy of 7 TeV in 2011 and 8 TeV in 2012. Taken from [108].

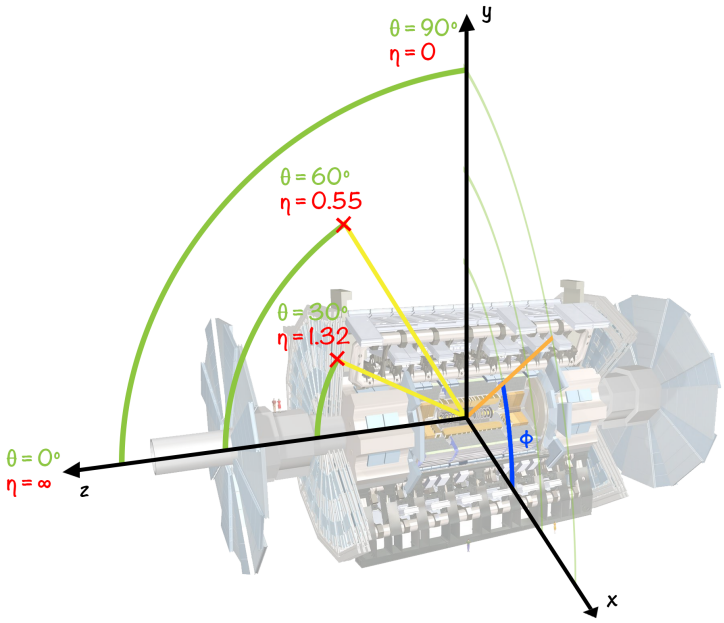

Figure 3.8: ATLAS coordinate system. Adapted from [102].

The ΔR distance is defined as:

$$\Delta R = \sqrt{(\Delta\eta)^2 + (\Delta\phi)^2}. \tag{3.4}$$

3.3.2 Magnet system

The magnet system [109], depicted in Figure 3.9 is composed of four large superconducting magnets (the barrel toroid, the endcap toroids and the central solenoid), 26 m long and with a diameter of 20 m.

The barrel toroid and the two endcap toroids provide a toroidal magnetic field of about 0.5 T and 1 T, respectively, for the muon detectors. The barrel toroid is 25.3 m long with an inner diameter of 9.4 m and an outer diameter of 20.1 m. The solenoid, located around the inner detector, provides a 2 T axial magnetic field. It has an inner diameter of 2.46 m, an outer diameter of 2.56 m and is 5.8 m long. Liquid helium is used to cool down and maintain the superconducting magnets at the operating temperature of 4.5 K.

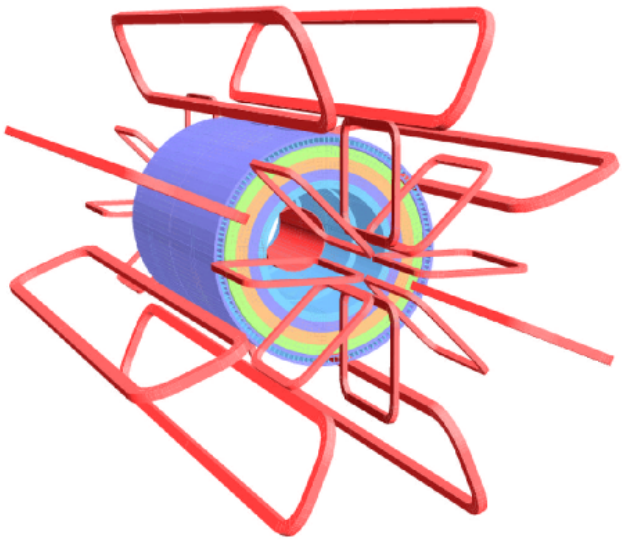

Figure 3.9: Geometry of the ATLAS magnet system components and the tile calorimeter steel. The eight barrel toroid coils, with the endcap coils interleaved, are visible. The solenoid winding lies inside the calorimeter volume. Taken from [101].

3.3.3 Inner detector

The ATLAS Inner Detector (ID) [110–112], with the layout shown in Figure 3.10, is the system closest to the beam pipe, designed to yield an excellent momentum resolution and both primary and secondary vertex measurements for charged tracks within $|\eta| < 2.5$. It also provides electron identification over $|\eta| < 2.5$. As it is inside the 2 T magnetic field, produced by the solenoid, the trajectories of charged particles are deflected, making possible the measurement of their momenta. The ID is composed of three different sub-detectors described in more detail in the next paragraphs: the pixel detector, the semiconductor tracker (SCT) and the transition radiation tracker (TRT), outer from the beam pipe. For each track, the pixel detector contributes typically with three tracking space points, the SCT with four and the TRT with 36.

The pixel detector consists in three cylindrical silicon-pixel layers (three barrels, and three disks on each side) with a total of total 1744 pixel modules, 63×19 mm^2, with 47232 pixel elements per module. When a charged particle goes through the silicon of the module, it liberates electrons that move creating a current through one or more pixel elements, giving away the original particle position. These 80 million individual pixels cover an area of 1.7 m^2. Due to the location (5 cm to 12 cm from the beam

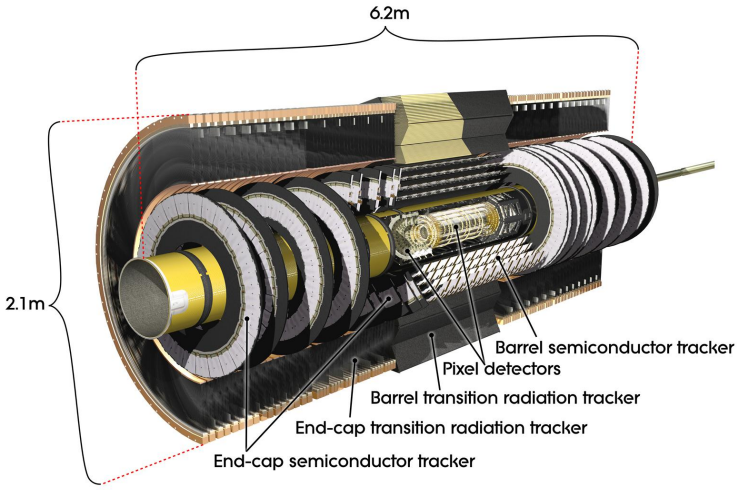

Figure 3.10: Cut-away view of the ATLAS inner detector. Taken from [101].

pipe) these are very resistant to radiation. It mostly determines the impact parameter resolution and the ability of the ID to find short-lived particles such as b-hadrons.

At 30 cm to 50 cm from the beam pipe, the SCT works in a way similar to the pixel detector. It has 4088 silicon modules arranged to form four barrels and 18 disks (nine at each end). Each silicon module, 6.36×6.40 cm^2, consists of one or two pairs of single-sided microstrip detectors glued back-to-back at a 40 mrad stereo angle to provide two-dimensional hit information. There are 6.3 million silicon strip readout channels, with 1536 channels per module. The SCT contributes to the measurement of momentum, impact parameter and vertex position.

Spanning 55 cm to 108 cm away from the beam pipe, the TRT consists of a central barrel and three endcaps on either side. It comprises many layers of straw tube, 4 mm in diameter and 144 cm long, interleaved with transition radiation material. Each straw is filled with gas that becomes ionised when a charged particle passes through it, producing a signal in a wire at the straw centre. In between the straws, materials with widely varying indices of refraction cause ultra-relativistic charged particles to produce transition radiation and leave much stronger signals. Xenon gas is used to increase the number of straws with strong signals. This allows to identify electrons which have much larger energy deposition (6 keV) as compared to the few hundred eV deposited by other ionising particles. The TRT has about 350 thousand readout channels.

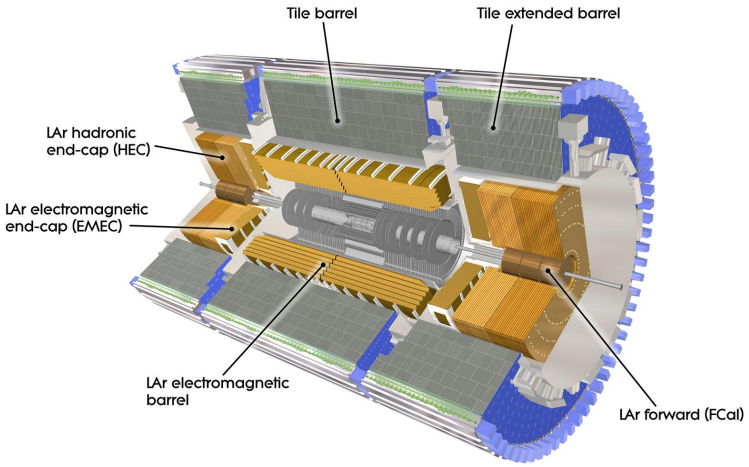

Figure 3.11: Cut-away view of the ATLAS calorimetry system. Taken from [101].

3.3.4 Calorimetry

ATLAS has two calorimeters to measure the energy of both charged and neutral particles. The electromagnetic calorimeter [113–115], used mainly to measure the energy of electrons and photons, and the hadronic calorimeter [113, 116, 117] responsible for measuring the energy of hadrons and mesons. The ATLAS calorimetry system can be seen in Figure 3.11.

The electromagnetic calorimeter is a sampling calorimeter made of lead absorbers, with thickness ranging from 1.1 mm to 2.2 mm, bent to an accordion-geometry shape and immersed in a liquid-argon bath at a temperature of 87 K. It is divided into a barrel part ($|\eta| < 1.475$) and two endcap components ($1.375 < |\eta| < 3.2$), each housed in its own cryostat. The barrel is made of two cylindrical halves, 3.2 m long and 53 cm thick, each divided into 16 modules, with 3424 readout channels per module. When the electrons or photons interact with the lead layers they radiate, producing a shower of low energy electrons, positrons and photons. The shower of low energy particles passes through the liquid-argon and ionises its atoms, creating more electrons and positive ions. Due to a electric field, the electrons drift to the electrodes located in the gaps between the absorbers and produce currents proportional to the energy deposited. From the amount of charge deposited on the electrodes in its path, the energy of the original electron or photon that entered the electromagnetic calorimeter

can be measured.

The hadronic calorimeter consists of three components: the tile calorimeter (TileCal), the liquid-argon hadronic endcap calorimeter (HEC) and the liquid-argon forward calorimeter (FCal). The TileCal is located behind the liquid-argon electromagnetic calorimeter and contains a long central barrel (divided in LBA and LBC) covering the region $|\eta| < 1.0$, and two extended barrels (EBA and EBC) in the range $0.8 < |\eta| < 1.7$. These four partitions are divided into 64 modules along the azimuthal direction. It is a sampling calorimeter, using steel as the absorber and scintillating tiles as the active material. Two sides of the scintillating tiles are read out by wavelength shifting fibres into two separate photomultiplier tubes (PMTs). There are a total of 5184 readout cells, comprising 9856 channels. When a high energy hadron passes through the steel it interacts with the atomic nuclei. These nuclear reactions produce more particles that initiate further interactions, creating a shower of particles. When the particle shower enters the scintillator, ultraviolet light, in an amount proportional to the incident energy, is radiated into the fibres, which subsequently converts it to visible light. The energy of the incident particle can then be inferred from the PMTs measurement of the light intensity.

The HEC and FCal cover the regions of $1.5 < |\eta| < 3.2$ and $3.1 < |\eta| < 4.9$, respectively. As a consequence of the increased radiation at these angles, these calorimeters have a similar design to the liquid-argon electromagnetic calorimeter. The main difference is that in HEC the lead plates are replaced by copper plates. In FCal there are three modules in depth: one electromagnetic module that uses copper as absorbing material and two hadronic ones that use tungsten. Both HEC and FCal share the same cryostats as the electromagnetic calorimeter liquid-argon endcaps.

3.3.5 Muon system

Muons are the only known charged particles that can travel through all of the calorimeters material and reach the outer layer. The ATLAS muon system [118, 119] is designed to measure their momenta with a high precision independently of the ID, but under the same principle, based on the magnetic deflection of the tracks. Over the range $|\eta| < 1.4$, magnetic bending is provided by the large barrel toroid, for $1.6 < |\eta| < 2.7$, muon tracks are bent by two smaller endcap magnets, while over $1.4 < |\eta| < 1.6$, the magnetic deflection is provided by a combination of the two.

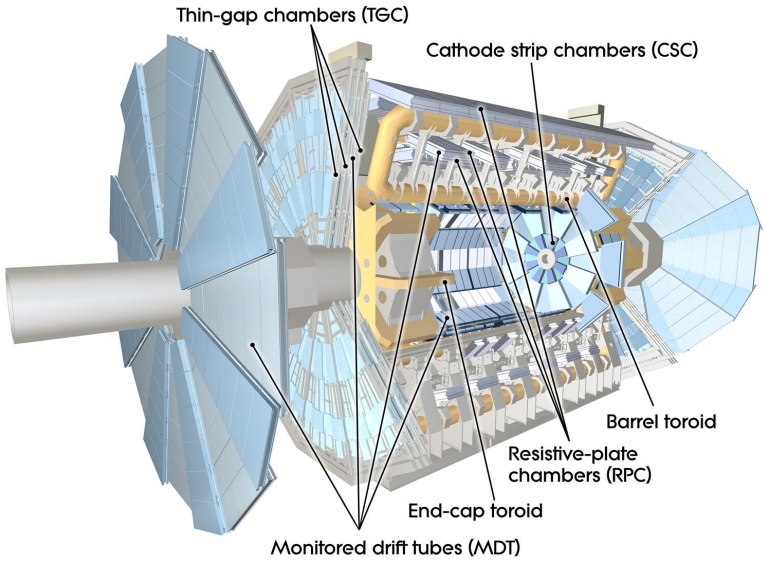

Figure 3.12: Cut-away view of the ATLAS muon system. Taken from [101].

With the layout shown in Figure 3.12, the system is arranged in three layers, both in the barrel (with radii of 5 m, 7.5 m and 10 m) and in the three endcap wheels mounted perpendicular to the beam axis (at the distances of 7.4 m, 14 m and 21.5 m). They consist of monitored drift tubes (MDT) and cathode strip chambers (CSC), designed for precision momentum measurement up to $|\eta| < 2.7$, and resistive plate chambers (RPCs) and thin gap chambers (TGCs) for triggering in barrel and endcap, respectively ($|\eta| < 2.4$ for the combination).

The 1171 MDT chambers (around 355 thousand individual drift tubes) cover most of the detector with each layer giving around 6 to 8 hits per track. When a muon passes in a tube, the gas inside is ionised, creating pairs of electrons and ions. Due to the electric field, the electrons drift towards the wire (in the centre). Close to the wire they get sufficient kinetic energy from the electric field to free new electrons creating an avalanche. The distance between the particle and the wire is determined by measuring the time that electrons, created during the primary ionisation process, take to drift towards the wire (this time is measured by the RPC and TGC). To reconstruct a track segment, the various drift radii from each MDT hit are connected by a tangent line to each drift circle.

3.3.6 Trigger and data acquisition system

The ATLAS trigger system [120–122] is composed of three levels of event selection, Level-1 (L1), Level-2 (L2) and event filter (EF), designed to reduce the event rate from the LHC nominal bunch-crossing of 40 MHz, down to 200 Hz (an average of 700 Hz [123] was achieved during 2010–2012, reduced from a 20 MHz bunch-crossing rate), rejecting 99.9995% of the events. These three levels are schematically represented in Figure 3.13.

The L1 trigger performs initial selection based on reduced-granularity information from the muon system and calorimeters. It searches for signatures from high-p_{T} muons, electrons/photons and τ-leptons decaying into hadrons or jets. It also selects events with large missing transverse energy and large total transverse energy. It requires about 2 μs (100 nominal bunch-crossings) to reach its decision after the bunch-crossing. About 1 μs of this time is spent in the signal propagation delays on cables between the detector and the underground counting room. All the information from the detector (around 1.5 MB) must be stored in pipeline memory until the L1 decision is available. The design event rate after L1 is about 75 kHz. When an event is accepted by L1, data from each detector is transferred by the read-out drivers (RODs) to dedicated detector read-out buffers (ROBs) hosted in the readout sub-system (ROS) computers.

For each event accepted by L1, a list of the regions of interest is given to L2 with the positions of all interesting objects found by the L1. The L2 then accesses the appropriate ROSs to pull out and analyses data from the ROBs corresponding to the regions of interest. In this way, the L2 only needs to access about 2% of the full event data in order to make its decision. The L2 trigger reduces the event rate to below 3.5 kHz, with a latency of 40 ms.

Finally, Sub-Farm Input (SFI) nodes collect all event information from the ROSs. Upon request, the SFIs provide fully assembled events to the event filter which is a processing farm that uses offline analysis procedures to further select events down to a rate that can be recorded for subsequent offline analysis. It reduces the rate to about 200 Hz, with an average latency of 4 s. The accepted events are sent into the Sub-Farm Output (SFO) nodes which indexes the events into different files, according to each event's trigger path, before they are moved to the central mass storage facility at CERN. Depending on the type of trigger, events are organised into four primary

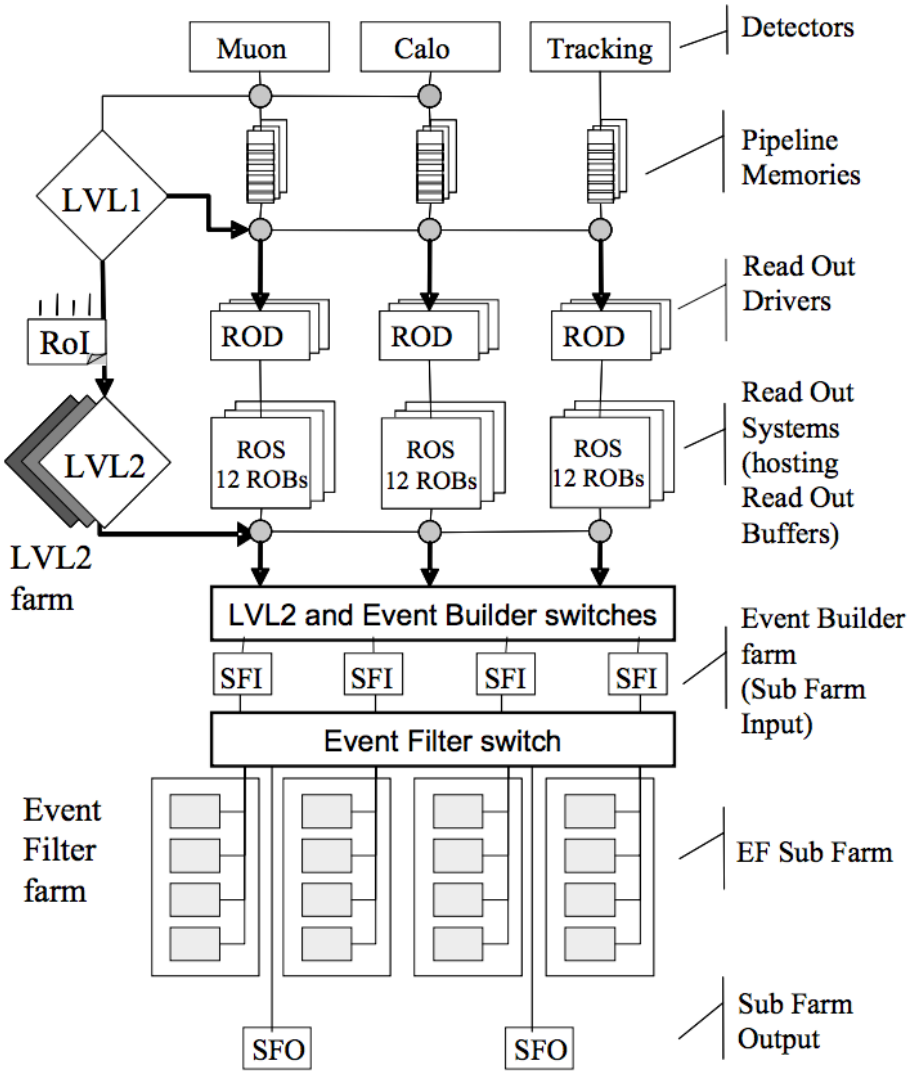

Figure 3.13: The ATLAS Trigger and Data Acquisition system. Taken from [120].

different physics streams (Egamma, Muon, JetTauEt-miss and MinBias) plus several other additional calibration streams.

3.3.7 Worldwide LHC Computing Grid

In 1999, CERN started to plan a computer system for data analysis of the LHC experiments. However, it became clear that the computing power required was far beyond the one CERN could provide, given the funding. Nevertheless, each of the laboratories and universities collaborating with the experiments already had access to their own computing facilities. These resources were integrated into a single computing service, the Worldwide LHC Computing Grid, which now links thousands of computers and storage all over the world.

The computing grid is composed of four tiers, each made up of several computing centres. Between them, the tiers process, store and analyse all data from LHC. ATLAS alone, in full operation, provides about 4 PB of data every year, to which the participating scientists will access worldwide. Tier 0 is CERN's data centre located in Geneva, Switzerland and also in Budapest, Hungary (at the Wigner Research Centre for Physics), over 1200 km away. The two sites are connected by two dedicated 100 Gbit/s data links. All data from LHC passes through the central CERN hub. It is responsible for the safekeeping of raw data and performs its first reconstructing into meaningful information. It subsequently distributes the raw data and the reconstructed output through optical-fibres working at 10 Gbit/s to Tier 1 centres, and reprocesses data when the LHC is not running. These Tier 1 consist of 13 computer centres spread worldwide, large enough to store LHC data and make it available to more than 150 Tier 2 centres, each consisting of one or several collaborating computing facilities. They provide sufficient storing and computing power for the specific analysis tasks and handle a proportional share of the production and reconstruction of simulated events. Individual scientists can access the Grid through local cluster computing resources (Tier 3) [124, 125].

4

TileCal LASER calibration and monitoring system

The LASER system is an important component of the ATLAS TileCal calibration and monitoring framework. It simultaneously illuminates all the 9852 PMTs with light pulses of known intensity, allowing to monitor their properties such as stability and linearity and to calibrate them when necessary. In this chapter it is described a study of the stability and linearity behaviour of the PMTs along with ways of identifying the ones presenting problems.

4.1 Introduction

The ATLAS TileCal (see Section 3.3.4) is a sampling calorimeter made of steel plates (absorber) and scintillating tiles (active medium). It has a cylindrical structure (shown in Figure 3.11) divided into three sections: the middle long barrel divided into two partitions (LBA and LBC) and two extended barrels (EBA and EBC). Each of the four partitions is further divided in ϕ by 64 modules. Within the modules, the light from the scintillating tiles is transported by wavelength shifting optical fibres to PMTs (depicted in Figure 4.1) and converted into electric signals that are digitised and passed to the ATLAS readout system. Each cell is read out by two PMTs.

In order to achieve the best performance, the difference between the energy of the particle and the energy reconstructed by the detector should be as small as possible. To minimise this difference one has to carefully monitor and calibrate the entire optical

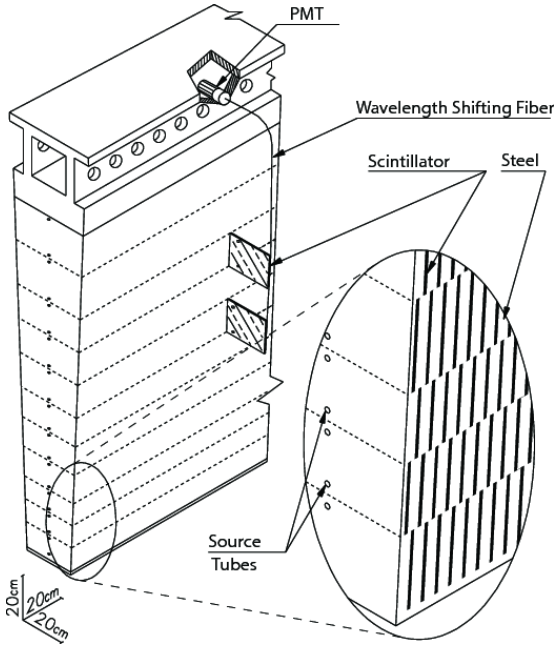

Figure 4.1: Structure of a TileCal module. Taken from [126].

and electronics chain.

There are three main components in the TileCal calibration scheme (Figure 4.2): the Cesium system (Cs), the LASER system and the charge injection system (CIS). With these three systems a complete calibration of the hardware chain is achieved, from the active modules to the read-out electronics. The system is also designed to be able to diagnose potential issues throughout the physics read-out path. For example, if both the Cs and the LASER systems report issues in the calibration data, whereas on the CIS side no issues are raised, then the problem might be in the PMT. Thus, comparing the results of all systems, one can disentangle the effects coming from different parts of TileCal and understand where are the sources of problems: electronics, PMTs or the tiles and wavelength shifting fibres themselves.

4.1.1 Cesium system

The first level of calibration is provided by the Cesium system [117, 127, 128]. Approximately once a month, a Cesium run is taken in which an ^{137}Cs γ-source is sent throughout TileCal, along the detector calibration tubes. While the source passes through the scintillating tiles, the PMTs responses are read-out (in Figure 4.3 is a

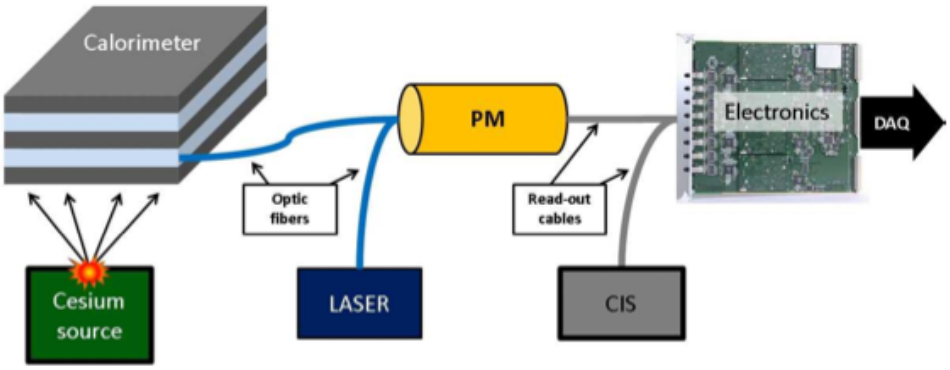

Figure 4.2: Overview of the calibration systems used in TileCal. Taken from [126].

schematic representation of the source passing through the tiles and the corresponding signal as measured by the PMTs). The γ-source emits photons with a energy of 0.662 MeV allowing to test the scintillators and fibres optical quality and, at the same time, providing an overall energy calibration. In order to correct for changes in PMTs and electronics between two Cesium runs, LASER and CIS runs are taken more frequently (weekly).

4.1.2 LASER system

The LASER system [117, 129] is the next in the chain and was designed to calibrate and monitor the PMTs response with an accuracy better than 0.5%. The LASER pulse produces a PMT response similar to a signal generated by a particle in the TileCal. The major difference is that the initial energy of the light pulse is known precisely (with an accuracy better than 1%, according to the LASER manufacturer). This enables accurate monitoring of PMT gains and linearity. Moreover, during physics data taking, the LASER system sends light pulses in the gaps of particle crossings (empty bunches) with a frequency of 1 Hz, so the status of the PMTs can be checked during actual data acquisition runs.

4.1.3 Charge injection system

Finally, to fully calibrate the hardware chain, the CIS [117, 130] is used, as the LASER calibration runs cannot differentiate changes in the PMT from the ones due to the

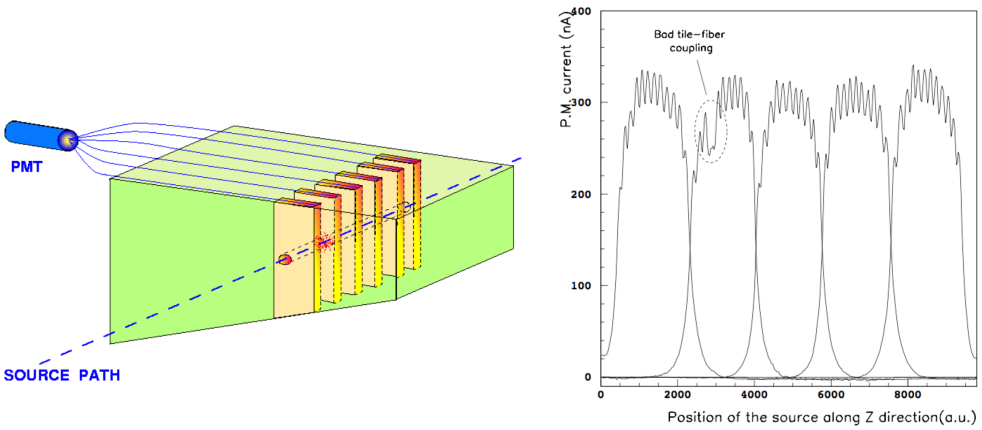

(a) (b)

Figure 4.3: On the left is depicted a schematic view of the Cesium system with the ^{137}Cs source passing through the tiles of the calorimeter. On the right the current measured in five PMTs is shown as a function of the source position along the rod. Taken from [128].

electronics. Here, charge pulses of known amplitude are injected into the readout electronics chain, mimicking the PMT signal, and leading to a precise estimation of the electronics noise and linearity. The CIS runs are taken weekly. Also, in physics runs, for calibration purposes, a fixed amplitude charge is injected outside particles crossings.

4.2 PMT performance studies

The two main characteristics of the PMTs that must be monitored are stability and linearity. The stability concerns the ability to measure the same output over time for the same input energy, while the linearity refers to the proportionality between the output signal and the increase of energy or, in other words, by increasing the LASER output signal intensity the PMT must yield an increased proportional response. During Run I the first version of the LASER system (LASER I) was installed in the ATLAS cavern and the studies performed with it let to a better understanding of the system and where it could improve. During the technical stop of 2013–2014 a new system (LASER II) was developed and installed in time for Run 2. The following results describe the studies performed with both versions of the system.

Table 4.1: Filter wheel attenuation factors used in LASER I [131].

Position	1	2	3	4	5	6	7	8
Attenuation	1050	103	32	10	1	3.1	103	330

4.2.1 LASER I

The LASER system is divided into two main parts: the LASER box and the light distribution system. The LASER box (depicted in Figure 4.4) contains not only the LASER head, but also two PMTs used for triggering and monitoring purposes, four Si PIN photodiodes (PDs) (inter-calibrated by an ^{241}Am source) used for the measurement of the absolute light intensity emitted by the LASER, and the optical components necessary for changing the LASER beam intensity. The humidity and temperature in the box are constantly monitored and controlled. The LASER light is transmitted to the PDs via four optical fibres. One of them (the one linked to PD number 1) receives the light collected directly in the LASER box, whereas the other three are getting information at another level of the system. PD 1 and the two PMTs (which are similar to the PMTs installed in the TileCal) receive light after reflection in a semi-reflecting mirror. The light not reflected by the mirror passes through a filter wheel with eight positions. One of them is empty (position 5) and the others contain filters that attenuate the beam with a factor 3 to 1000. The catalogue values of the filter attenuations are shown in Table 4.1. These filters were chosen to provide full coverage of the entire TileCal dynamic range, from a few hundred MeV to around 1 TeV.

For safety reasons, a shutter is also installed in the LASER box and is closed when the LASER is not in use. It can be used to make tests without sending light to the TileCal. If a LASER pulse is emitted when the shutter is open, the light leaves the LASER box and enters into a 1 m long liquid light guide. It links the LASER box output to the beam expander (also known as "Coimbra box", depicted schematically in Figure 4.5), the first component of the light distribution system, which is a system composed of two lenses that increase the beam diameter. It also has a diffuser in order to attenuate the speckles due to LASER light coherence. The beam expansion in turn sends the primary beam toward a bunch of 384 fibres (128 for each endcap barrel and 128 for the long barrel).

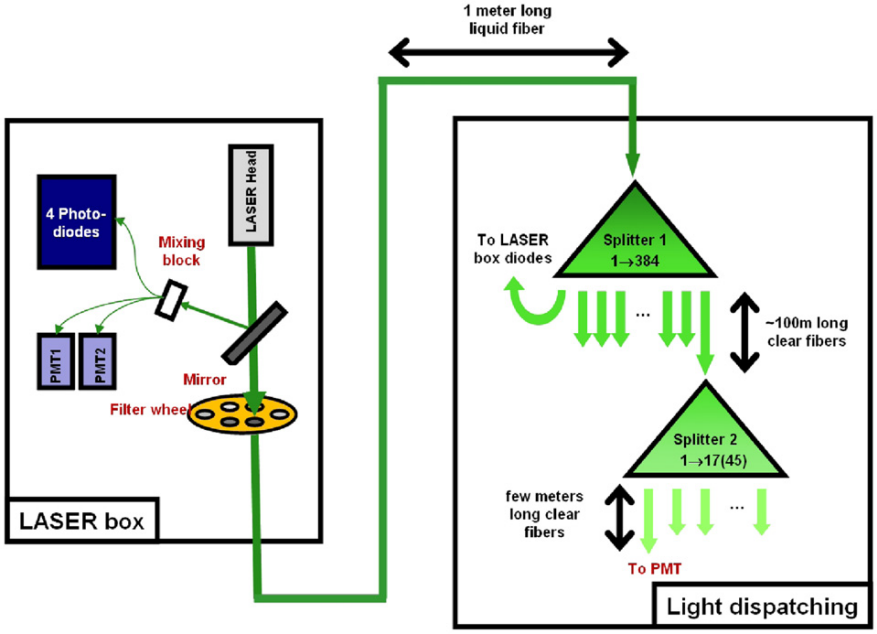

Figure 4.4: Schematic representation of the components inside the LASER I box and the path of the light to the TileCal channels. Taken from [129].

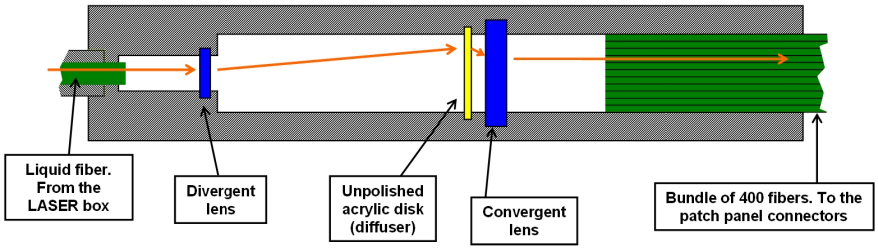

Figure 4.5: Schematic representation of the beam expander principle. Taken from [131].

Each fibre is glued to an adjustable connector that is held in a large patch panel located immediately behind the LASER box. The role of the connectors is to equalise the light sent by all the fibres to the TileCal, so that the PMTs receive roughly the same amount of light, simplifying the calibration work. On the other side of the connectors, long fibres take the light individually to TileCal drawers where they are split a last time in order to reach all the PMTs. Each extended barrel is fed by two fibres (17 PMTs per fibre) and each barrel module (two partitions) is fed by two fibres (45 PMTs per fibre). This is summarised in Figure 4.4. Once again, not all the fibres coming out of the beam expander box go to the TileCal: around 20 fibres are either kept as spares, or used to feed the three remaining PDs in the LASER box.

When a monitoring run is taken, a LASER pulse of fixed intensity is sent to all TileCal PMTs through the optical fibres, usually until ten thousand events are recorded. Runs with different intensities are obtained either by changing the filter (using the filter wheel) or the LASER output intensity. Each PD in the LASER box covers a dedicated energy range. Since the PDs are known to be linear at the 0.5% level [132], PMT linearity could, in principle, be easily measured comparing its response to the ones from the PDs. However, in the LASER I system there was a constraint to this procedure as the light measured by one PD was strongly affected by light on the other PDs, a phenomena known as optical crosstalk effect [133]. The ratio between PD1 and a LASER box PMT, with the shutter closed (no light on the PD2, 3 and 4), was measured to be different from the one with the shutter open. This effect quickly rises as the signal increases. This is not an issue for a stability analysis but becomes a serious problem in linearity studies, since it affects the PD linearity itself. To keep the same settings used for the stability analysis[1] the PDs can only be used over a limited energy range, like, for instance, the range covered individually by each PD, and in each data taking run, two of the PD are disconnected from the patch panel in order to minimize the effect of the crosstalk (PD1 cannot be disconnected).

There are three ways of studying the linearity. One is to keep the same filter and take several runs for different LASER light outputs. The second one is to keep the LASER output constant and change the filter wheel position inside the LASER box, changing the attenuation of the LASER light. And finally use both, by changing the

[1]The LASER system was not accessible for hardware modifications during Run 1. It was only by the 2013 LHC shutdown period that the LASER system could be upgraded.

output signal of the LASER and the attenuation filter. With the LASER I system, only the first two were used, in order to minimise systematic effects. Whether using the first or the second method, a linear fit using two parameters is performed to the signal measured by the PMTs in different intensity runs as compared to the signal measured by a PD.

Moreover, the TileCal PMTs do not all measure the same signal in a single run as each light mixer introduces additional systematic variations. Figure 4.6 shows a histogram with the signals of all the TileCal PMTs, the mean signal for all fibres and a distribution comparing the signal of the TileCal fibres (after the beam expander) for the low gain (LG) and high gain (HG) range of the digitised signals. The signal of a given PMT will depend on the light transmitted by the fibre. This means that fibres transmitting lower light intensity (probably placed further from the central region on the beam expander), will lead to lower signals sent to the corresponding PMTs. Additionally, there are other sources of systematic uncertainties between two consecutive runs, for instance the movement of the filter wheel, temperature, and so on. Thus a direct comparison between the fit results (slope and offset) obtained for the different runs is not possible. For these reasons, the residuals of each point are used to compare the results, instead of looking to the fits results themselves. The relative residuals are computed according to:

$$\text{Relative Residual} = \frac{\text{Fit Result - Signal}}{\text{Fit Result}}, \text{ with Fit} = a \times \text{PD} + b, \tag{4.1}$$

where a and b are the fit parameters, slope and offset, respectively. After fitting all PMTs, a distribution is computed and the mean and standard deviation calculated. In principle the distributions should be narrow, symmetric and centred at zero. Deviations indicate linearity problems.

4.2.1.1 LASER runs with fixed filter wheel position, changing LASER intensity

The runs are taken with seven different filter wheel positions (1, 2, 3, 4, 5, 6 and 8). For each filter wheel position, 10000 events are recorded for five LASER intensities (18k, 22k, 26k, 28k and 30k, in arbitrary units). Saturation of the reconstructed signal starts at around 700 pC [133], so signals higher than that are discarded. PD 4 is used

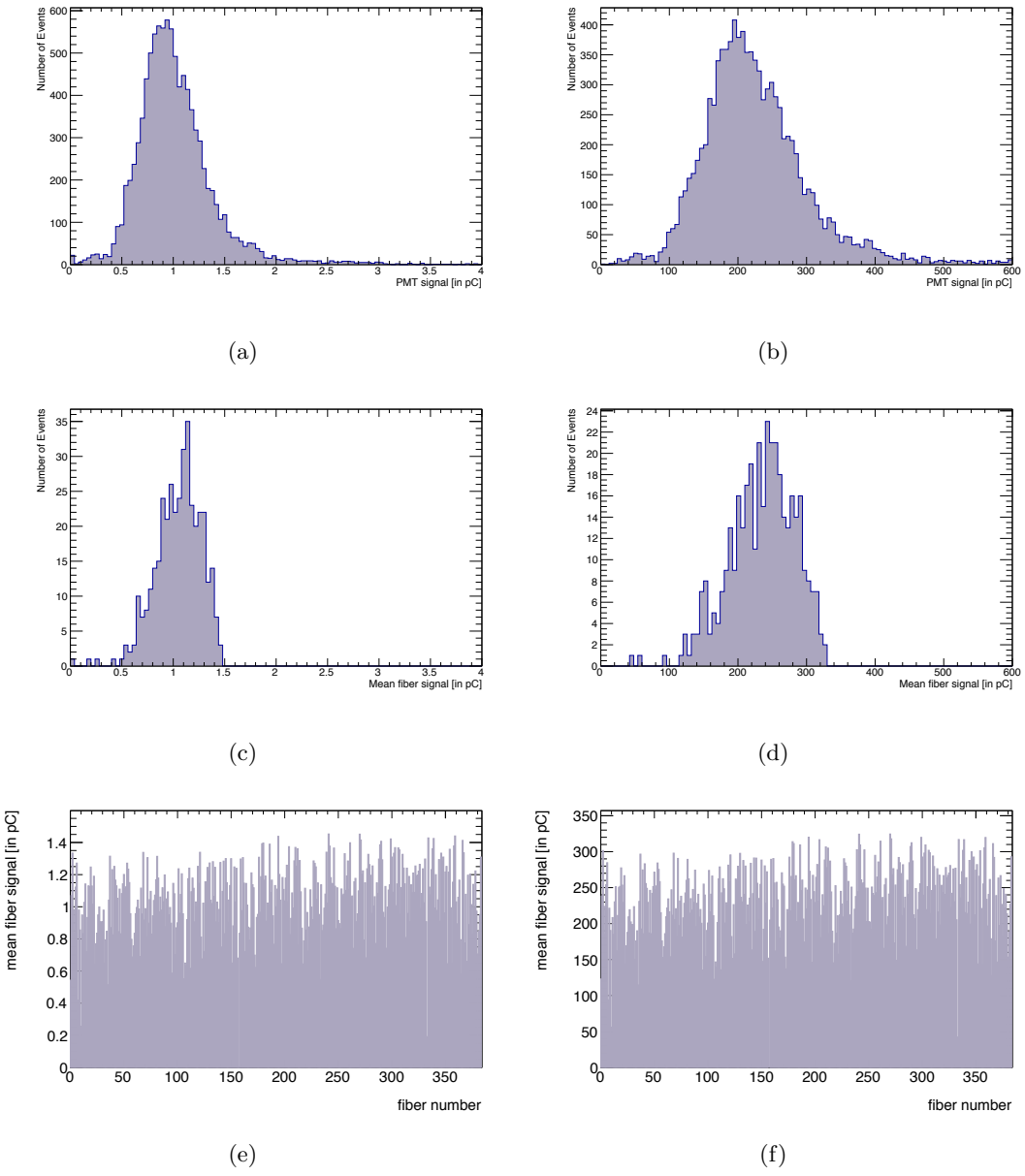

Figure 4.6: PMT Signal distribution for (a) HG and (b) LG. Mean fibre signal distribution for (c) HG and (d) LG. Mean fibre signal versus the fibre number for (e) HG and f) LG. These distributions were obtained with a 23k LASER intensity and filter wheel position 6 and 8 for LG and HG, respectively.

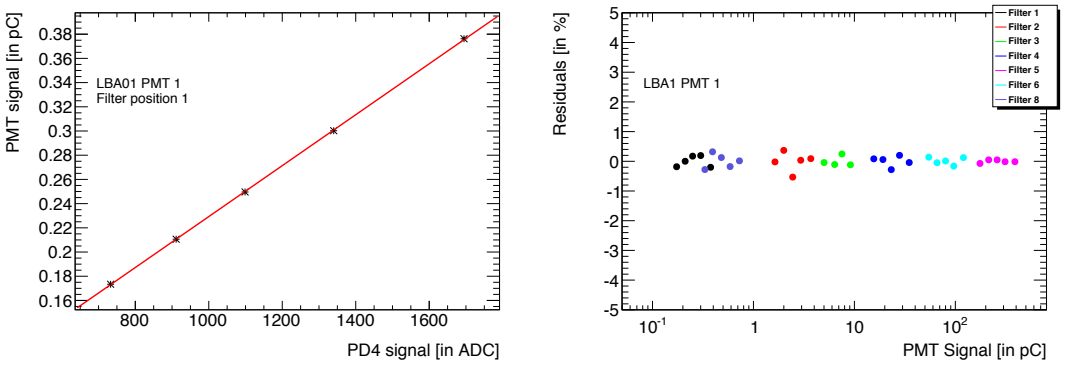

(a) (b)

Figure 4.7: (a) an example of a linear fit with two parameters using the first PMT in the TileCal LBA01 module. Runs with different LASER intensities, 18k, 22k, 26k, 28k and 30k, are used with the first filter wheel position. (b) the residuals of each fit (in percentage), for the same PMT.

as a reference since it receives light after the beam expander, thus being more closely related to the light being sent to the different PMTs of TileCal. The dynamical range of the PD4 is changed accordingly (for each filter wheel position) so it does not saturate for the different LASER intensities. An example of the fit is shown in Figure 4.7 along with the residuals from each fit.

Combining the fits from all PMTs for the different filter wheel positions, the mean residuals taken from the residual distribution of all PMTs can be obtained, as a function of the mean PMT signal for each LASER intensity and filter wheel position (examples of these residuals are shown in Figure 4.8 for the first filter and the mean residuals as a function of the signal is shown in Figure 4.9). A residual range of about $\sim$0.5% is observed. The filter wheel position 3 covers the range where there is a change of gains. At around 10 pC, PMT signals can be readout by the high gain or low gain circuits and the events are split into two samples. Consequently, the fits change and the errors increase.

4.2.1.2 LASER runs with LASER intensity constant, changing filter wheel position

Considering the runs taken keeping the LASER intensity fixed while changing the filter wheel position, for each of the six LASER intensities (23k, 24k, 26k, 27k, 28k and 30k)

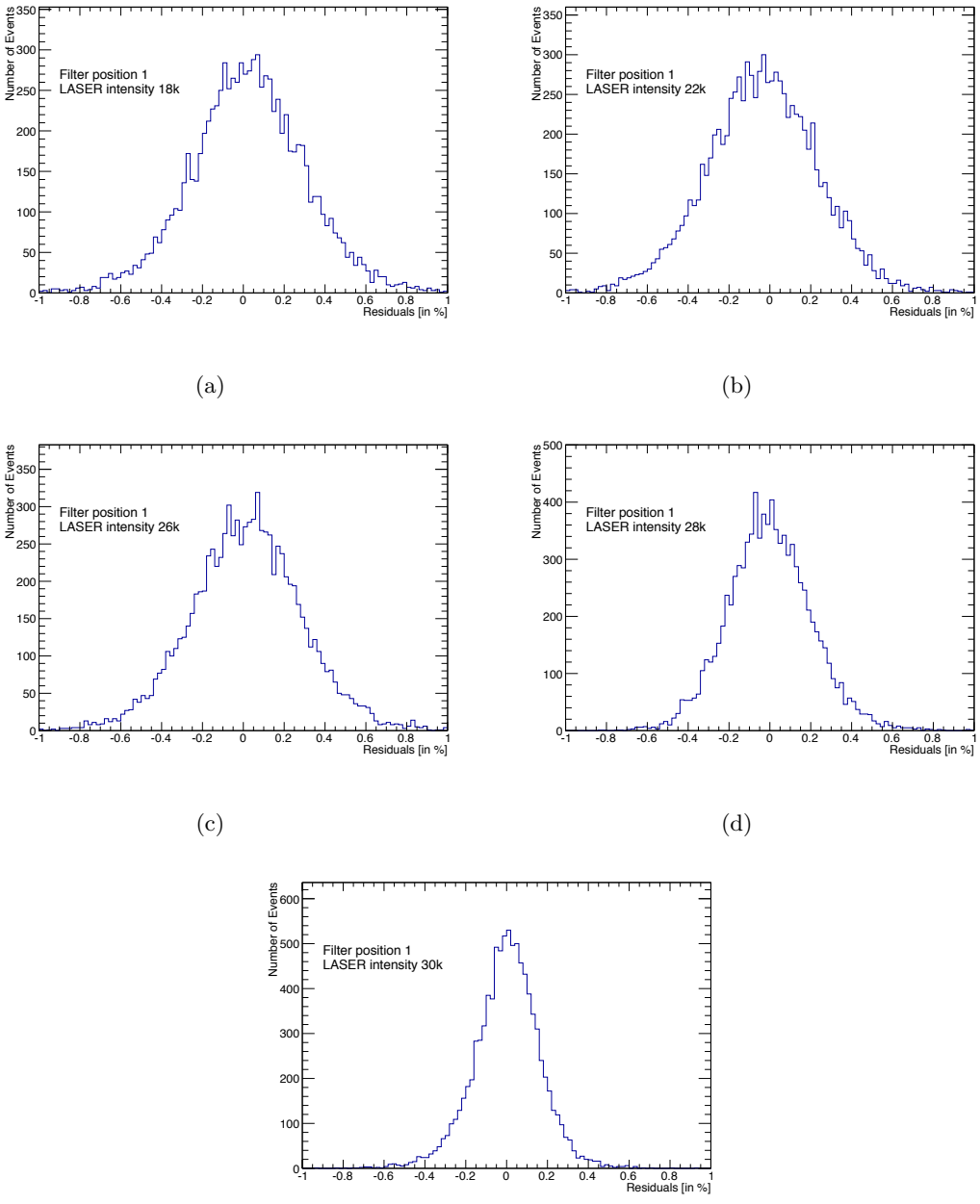

Figure 4.8: Examples of the relative residuals distributions for the points obtained with filter position 1 and the LASER intensities (a) 18k, (b) 22k, (c) 26k, (d) 28k and (e) 30k.

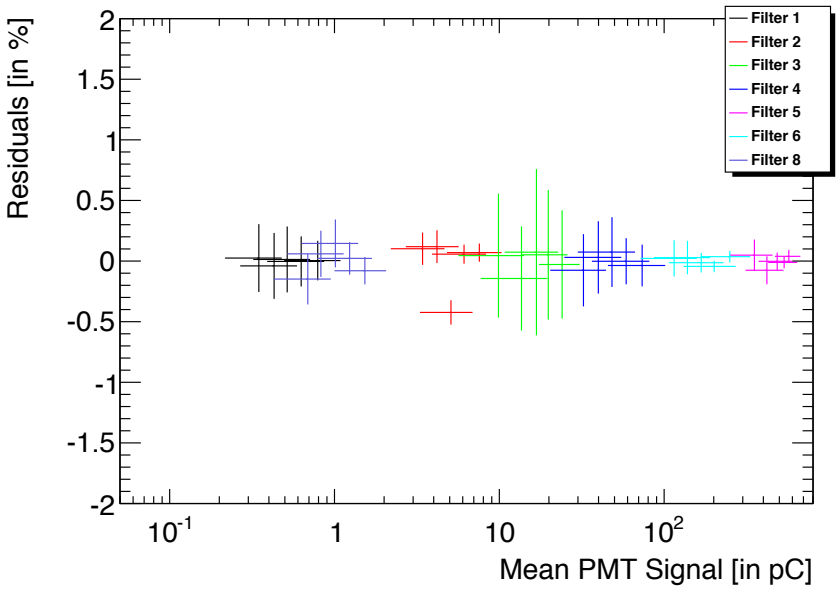

Figure 4.9: Mean relative residuals from all the PMTs of TileCal versus the mean PMT signal from all PMTs for each LASER intensity/filter combination, keeping the filter wheel position fixed, using a two parameter fit. The error bars correspond to the standard deviation of the distributions.

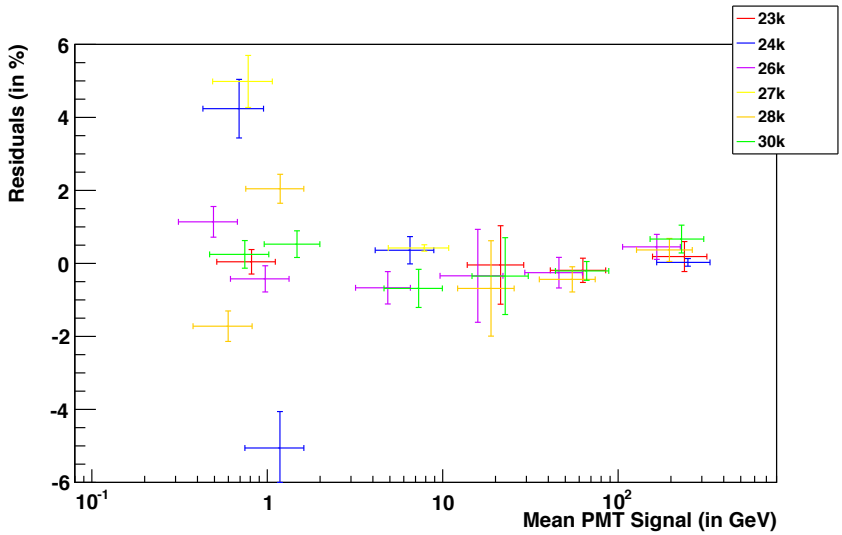

Figure 4.10: Mean residuals from all the PMTs of the TileCal versus the mean PMT signal for all PMTs for each LASER intensity/filter combination, keeping the LASER intensity constant, using a two parameter linear fit. The error bars correspond to the standard deviation of the distributions.

the filter wheel is rotated and the events recorded for six positions (1, 2, 3, 4, 6 and 8). PD3 (that measures the light after the beam expander) is used as reference with its dynamical range changed in each run. The results are summarised in Figure 4.10 and it can be seen that they are worse than those obtained with the fixed filter wheel. Since this fit is performed over an increased range, the cross-talk effect due to PD1 could be playing a larger role than with the previous conditions.

4.2.2 LASER II

With the limitations of the LASER I system in mind, the system was upgraded [134, 135] and the shortcomings of the optical part have been solved. Among the improvements were, for instance, a PD crosstalk greatly reduced and the number of PDs increased to ten and placed at three different stages of the light chain within the LASER box. Moreover, the dynamical range of the PDs was increased allowing multiple for runs over a multitude of intensities to be used with a single reference. The new filter wheel attenuation factors are in Table 4.2.

To measure the stability of a given PMT, the ratio between its signal and a reference

Table 4.2: Filter wheel attenuation factors used in LASER II [135].

Position	1	2	3	4	5	6	7	8
Attenuation	10	1.6	2.5	333	1	3.2	33	100

LASER PD response is compared as a function of time. LG calibration LASER runs taken twice a week using filter 6 are used. Since the PMTs may be recalibrated after TileCal's cesium runs, only LASER runs taken between two consecutive cesium runs are used. Here, the runs taken between 12 November 2015 and 9 December 2015 were chosen to be presented. An example of distributions obtained with all PD using these runs is shown in Figure 4.11.

A fit of data to a constant ($y = p_0$) can be made since the behaviour of the ratios is expected to be flat. The standard deviation of the signal measured by the PMTs and the PDs is taken as the uncertainty in the fit. The fits are also computed without the standard deviations (i.e. all points have weights equal to 1) to ensure that cases where large uncertainties could lead to good χ^2 are also taken into consideration.

The PMT output also depends on its HV power supply with many signal jumps being directly correlated to jumps in the HV. Since the HV usually fluctuates, values closer than 2 V are clustered. If more than one HV is found, independent fits are performed, and the overall χ^2 is considered. The HV power supply is classified as "jump" if more than one peak is found, "fat" if the width of at least one peak is larger than 5 V or "good" otherwise. Figures 4.12 (b) and (c) show the PMTs HV distribution and PMTs HV peak widths, respectively, while Figure 4.13 shows an example of a PMT with more than one HV peak. The χ^2 distributions of the fits with (χ^2_{u0}) and without taking into account the standard deviations (χ^2_{u1}) are shown in Figures 4.12 (d) and (e).

The PDs that measure the light after the beam expander (PD 6–9) have a behaviour more similar to the TileCal PMTs. As can be seen in Figures 4.12 (a), (d) and (e), the best PDs to assure the PMTs stability are PD 6 and PD 9. PD 6 is used as reference for the PMT / PD ratio since its fibre is the one closer to the centre of the beam expander and PD 9 filter was changed (together with the ones of PD 5 and PD 8) in the beginning of September 2015, thus causing a time series break. The plane with both χ^2 information obtained with PD 6 is shown in Figure 4.12 (f). From this χ^2

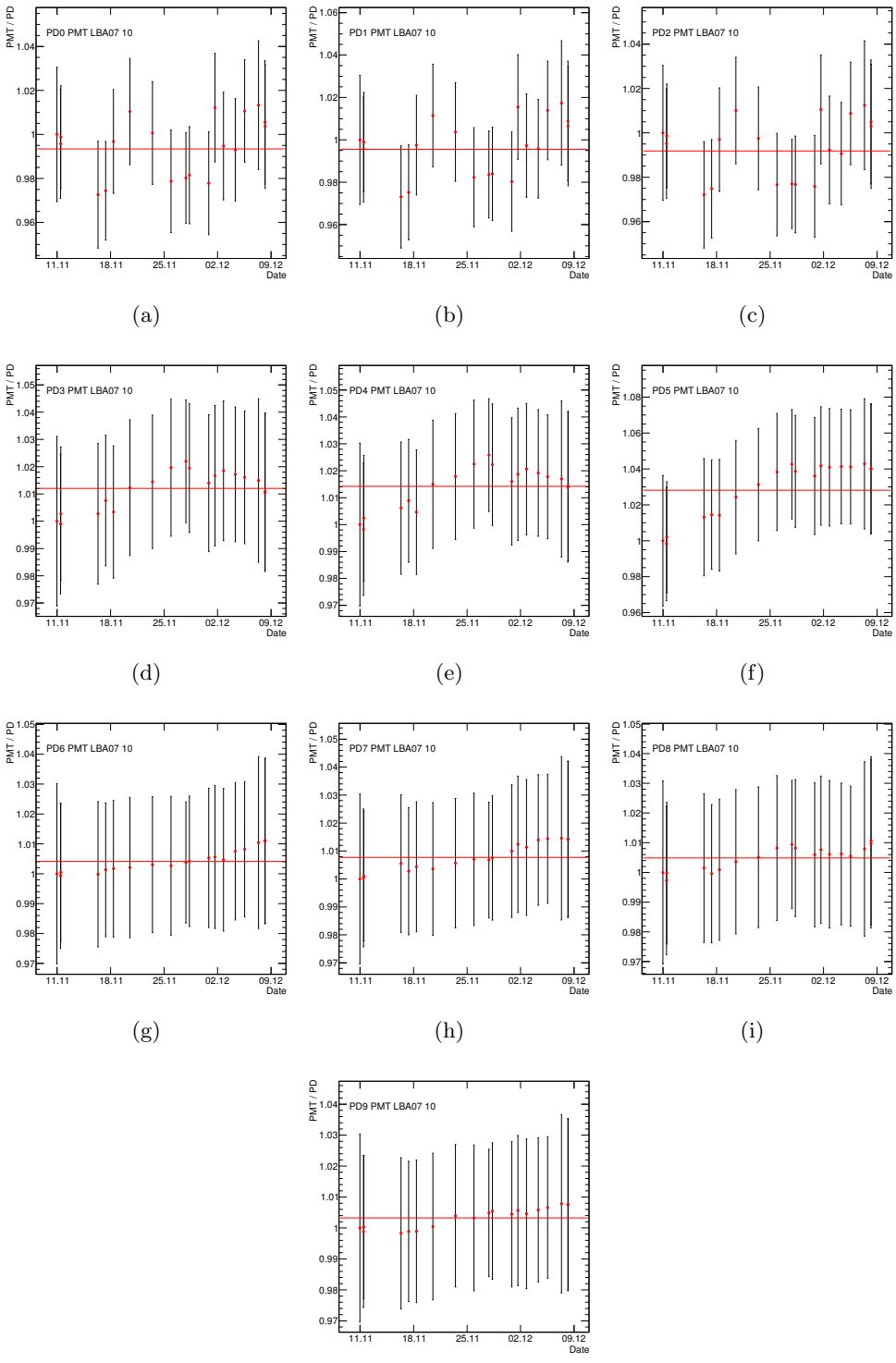

Figure 4.11: Distribution of the ratio between the signals measured by PMT 10 of LBA 7 and the PD (a) 0, (b) 1, (c) 2, (d) 3, (e) 4, (f) 5, (g) 6, (h) 7, (i) 8 and (j) 9 as a function of time. The ratios are normalised to the first event and the error bars represent the standard deviation of each ratio.

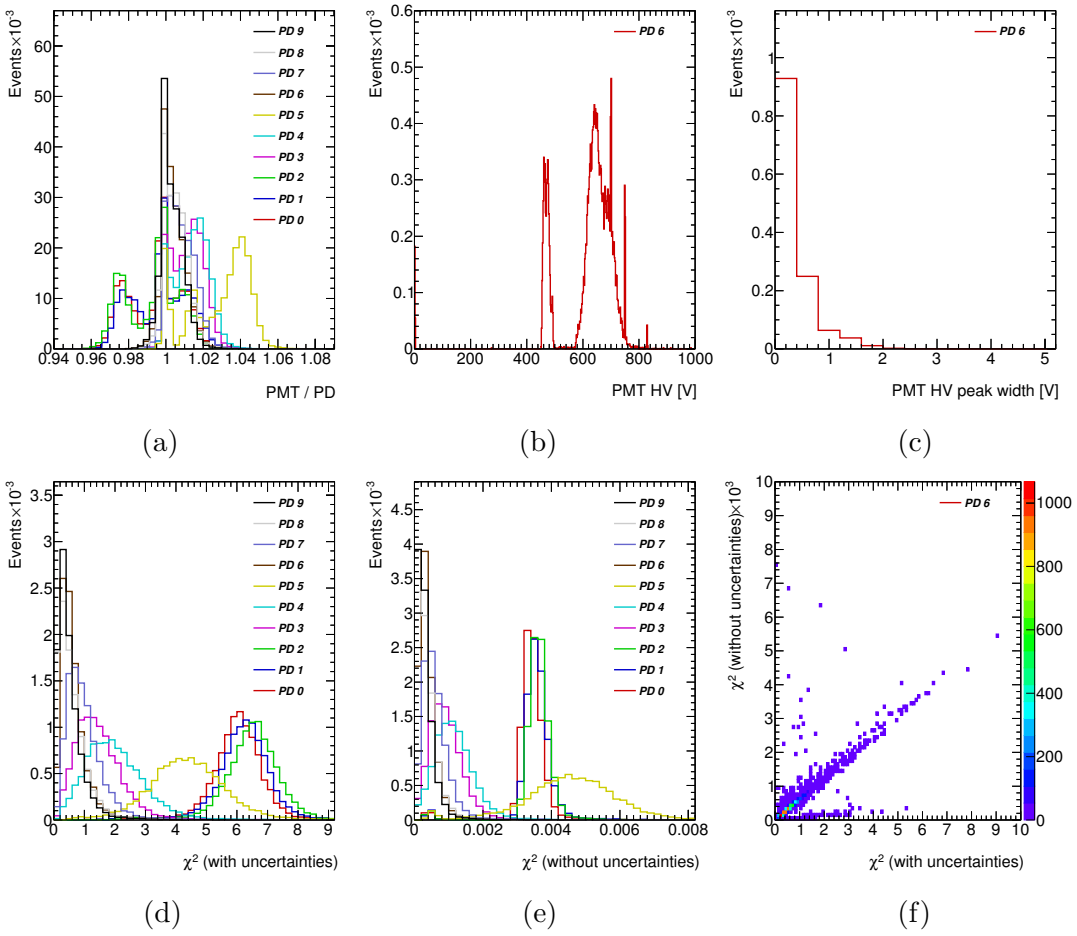

Figure 4.12: Distribution of the (a) mean PMT / PD ratios for all PMTs, PDs and runs; (b) PMTs HV for all PMTs and runs; (c) PMTs HV peak widths for all PMTs and runs; (d) χ^2 of the fits taking into account the uncertainties for all PMTs and PDs; (e) χ^2 of the fits without taking into account the uncertainties for all PMTs and PDs and (f) χ^2 of the fits with uncertainties versus the χ^2 of the fits without the uncertainties for all PMTs and PD 6.

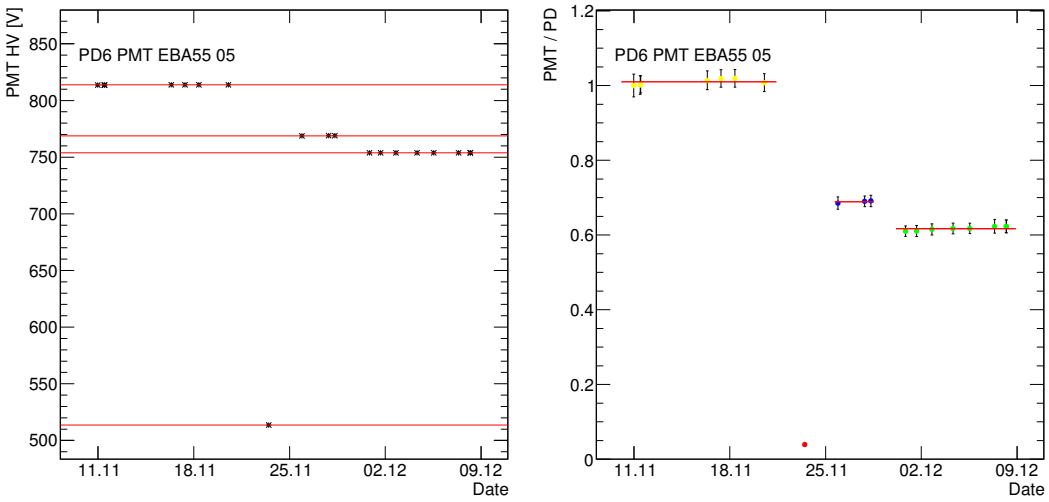

(a) (b)

Figure 4.13: Example of a PMT (PMT 5 of EBA 55) with four HV peaks: (a) PMT HV and (b) PMT / PD ratio for PD 6, both as a function of the run date.

plane it can be seen that both informations are useful to identify deviations from stable behaviour. PMTs are then classified as:

- **good**: both χ^2 values are in the first 3% percentiles;
- **regular**: one of the χ^2 values lies between the first and the last 3% percentiles and the other one is not in the last 3% percentile;
- **bad**: one of the χ^2 values lies between the last 3% and the last 1% percentiles and the other one is not in the last 1% percentile;
- **ugly**: one of the χ^2 values is in the last 1% percentile;
- **ndf**: if, independently of the definitions above, there is at least one null data point.
- **dead**: if, independently of the definitions above, there are only null data points.

The "good" tag shows the optimal PMT behaviour, whereas the "bad" and "ugly" are used to identify and troubleshoot possibly problematic ones. The "ndf" tag identifies PMTs that, for any sort of reason, do no seem to work during some runs, while

Table 4.3: Summary of the PMT stability results.

	HV good	HV jump	HV fat	total
ndf	3	0	0	3
good	22	2	0	24
regular	8986	262	0	9248
bad	275	46	0	321
ugly	117	18	1	136
dead	120	0	0	120
total	9523	328	1	9852

"dead" PMTs are the ones from turned off TileCal modules. Table 4.3 presents the number of PMTs classified as above, while Table 4.4 shows the correlation between the tags used in the PMT stability survey described here and the ones in TileCal bad channel list from the COOL database. Illustrative distributions of PMTs classified with the different tags are presented in A.1.

Table 4.4: Correlation between the tags used in the stability analysis and the ones in the COOL database.

COOL database tag	Good	Regular	Bad	Ugly
ADC masked	0	22	6	9
Bad CIS calibration	0	14	7	10
Bad cesium calibration	0	2	0	2
Bad laser calibration	0	43	3	7
Bad timing	0	2	1	1
Channel masked	0	2	0	10
Data corruption	0	4	0	0
No CIS calibration	0	1	0	0
No cesium calibration	0	2	0	1
Severe stuck bit	0	3	1	6
Stuck bit	0	12	0	1
Untagged	0	0	310	113

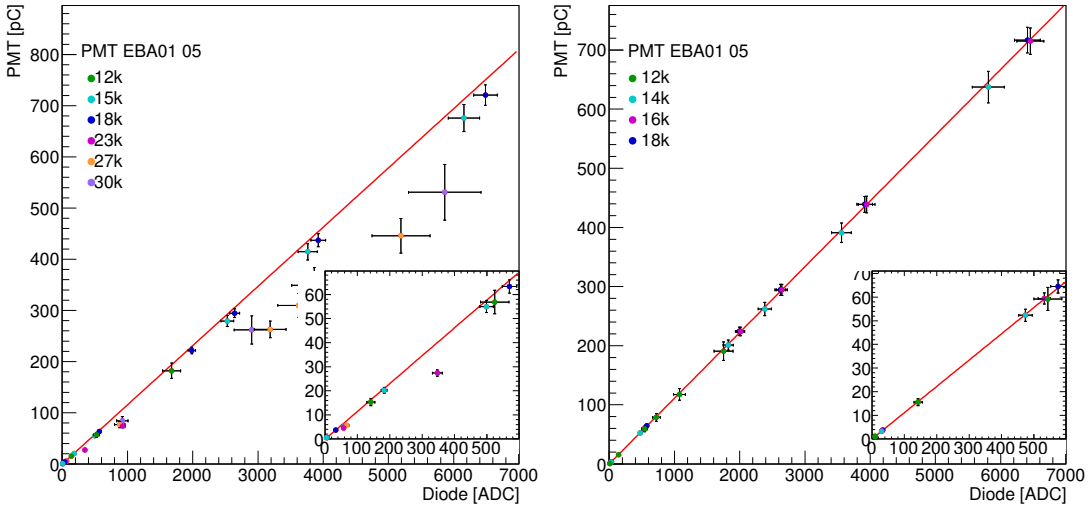

Figure 4.14: Distribution of the signals measured by PD 6 versus PMT 1 of EBA 05 using LASER runs with intensities of (a) 12k to 30k and (b) 12k to 18k. The red lines show the resulting fits.

To check the PMTs linearity, a two parameter line is once again used to fit a set of data. With the LASER II system it is no longer required to manually adjust the range of the PD since a single one can be used over the full PMT signal window; for this reason a combination of different filter/intensities can be used simultaneously in the same fit. An example distribution of the PMT signal response as a function of the PD 6 response is shown in Figure 4.14. From the figure it is clear that there is an effect in the slope for intensities larger than 18k. The calibration LASER runs used throughout the remainder of this section include intensities of 12k, 14k, 16k and 18k with 1, 2, 3, 5, 6 and 8 filter wheel positions.

It is a known feature of the PMTs that they loose linearity shortly before the saturation point. This behaviour can be observed in the TileCal PMTs that receive enough light. Figure 4.15 shows an example of such behaviour. In average, PMTs start to loose linearity above $\sim$ 750 pC and reach saturation at $\sim$ 850 pC, as can be seen in Figure 4.16 (a), which shows the distribution of the minimum non-linear data point for each PMT.

For each data point, a linear fit to it and all below it is performed and the total

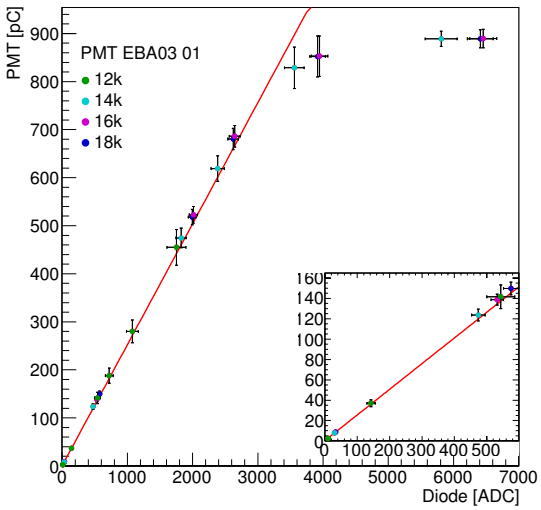

Figure 4.15: Example of a PMT reaching saturation (PMT 1 of EBA03).

number of points within one standard deviation is evaluated. The fit that comprises most points is chosen as final. The lowest point not included in the fit is the first non-linear value. In this way, the best linear fit can be selected without being affected by outliers. Nevertheless, these outliers are selected as non-linear points and used for troubleshooting. The slopes and resulting χ^2 distributions of the linear fits to the TileCal PMTs response as a function of PD 6 signal are shown in Figure 4.16 (b) and (c).

Deviation from linearity is computed as the ratio between the area delimited by the intersection of the joint data points and the linear fit and the integral of the linear fit, which corresponds to the the ratio between the grey area and the fit function integral between x_0 and x_1, as shown in Figure 4.17. This deviation from the linearity is then used to classify the different PMTs as:

- **regular**: the minimum non-linear point (if it exists) is above 750 pC (exluding "good" and "dwarf" PMTs);
- **good**: at least one non-linear data point above 750 pC and deviation from linearity below 0.6%;
- **dwarf**: maximum linear point below 150 pC and no non-linear point below 750 pC;

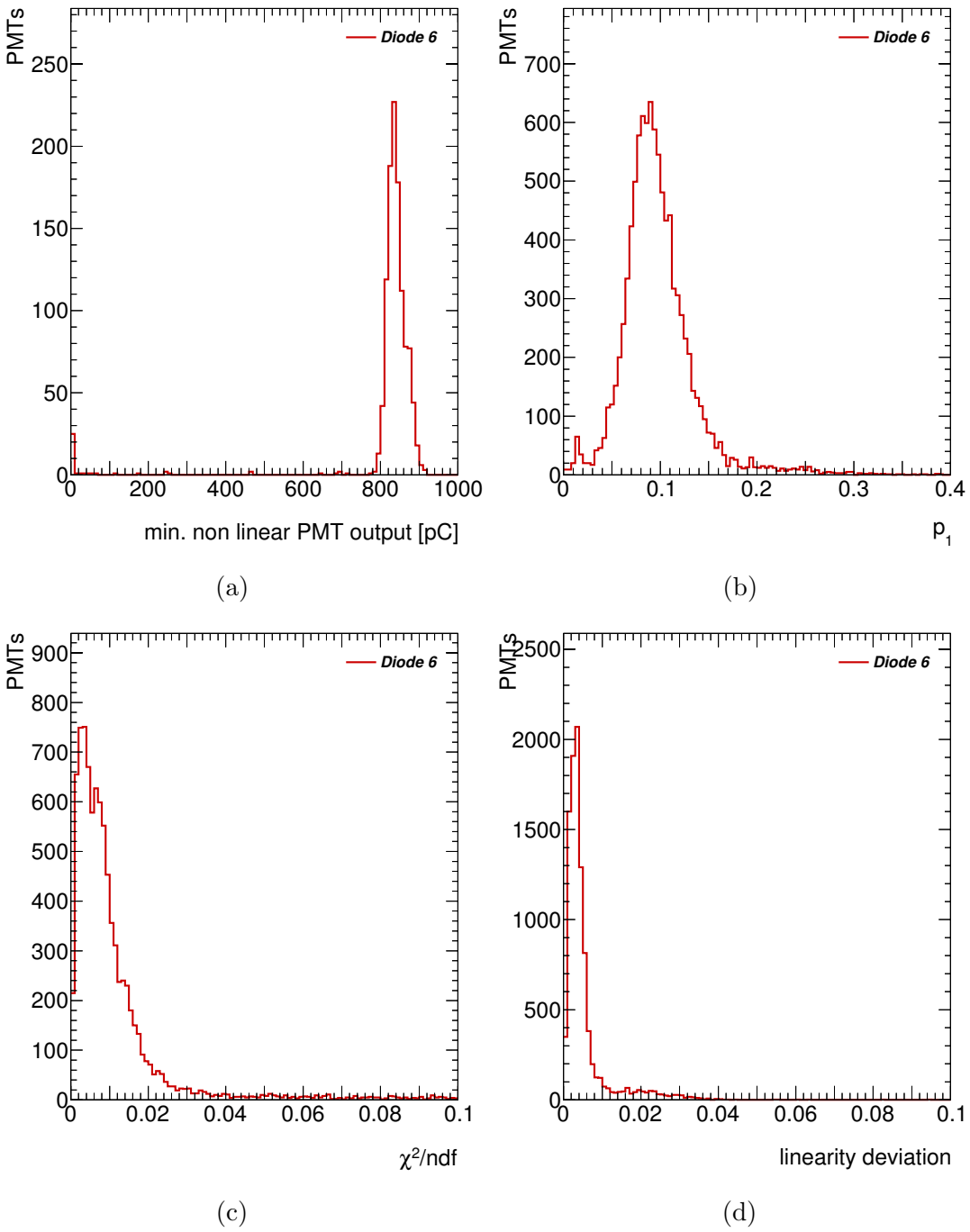

Figure 4.16: Distributions of (a) the minimum non-linear point (PMTs without non linearity behaviour are not represented); (b) fit slope; (c) fit χ^2 and (d) deviation from linearity. All distributions were computed using data from PD 6.

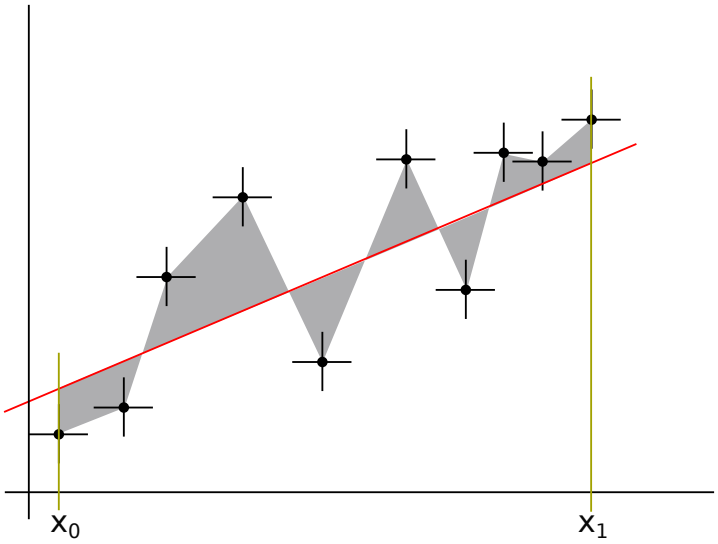

Figure 4.17: Schematic representation of the area obtained by intercepting the joint data points and the fit function. Deviation from linearity is then calculated as the ratio between the grey area and the integral of the fit function integral between x_0 and x_1.

- **bad** : the minimum non-linear point is below 750 pC (excluding "ugly" PMTs);
- **ugly**: the minimum non-linear point is below 750 pC, additionally the deviation from linearity is above 3% (or negative) or the maximum linear point is below 20 pC.

The "good" tag shows the optimal PMT behaviour, with at least one non-linear point to reflect the largest range coverage, including the transition from linearity to non-linearity; whereas the "bad" and "ugly" are used to identify and troubleshoot possibly problematic ones. The "dwarf" tag identifies PMTs that, due to the optical chain of the LASER system, receive low LASER signals and thus do not have enough information to correctly check their linearity over a large range. Note that "good" and "dwarf" would be subsets of "regular" if they were not excluded explicitly in the definitions. The same applies to "bad" and "ugly". With these definitions there are 10 good, 9647 regular, 13 bad, 35 ugly and 147 dwarves PMTs. Looking at the deviation from linearity, 95.1% of the PMTs are within 2%, as shown in Figure 4.16 (d) and in Table 4.5.

Table 4.5: Percentage of PMTs within the given deviation from linearity.

deviation	percentage of PMTs
1%	89.9%
2%	95.1%
3%	98.6%
4%	99.7%
5%	99.8%
11%	99.9%

Table 4.6 shows a summary of the comparison of the PMT linearity survey described in this note with the TileCal bad channel list information registered in the COOL database. It can be seen that the majority of the PMTs classified as ugly or bad are already tagged in the COOL database with at least one problem. Although some of the good or regular PMTs are listed in the TileCal bad channel list, the reported problems do not affect their linearity response. Illustrative distributions of PMTs classified with the different tags are presented in A.2.

4.3 Conclusion

A method to measure the linearity of the PMTs started with LASER I and culminated with the results shown with the upgraded LASER II. The TileCal PMT stability and linearity survey presented here is able to identify the problematic channels. Such information can be used to improve the TileCal description in the ATLAS simulation software. Running this analysis periodically will also allow to ensure the evolution of all TileCal PMTs linearity.

Table 4.6: Correlation between the tags used in the linearity analysis and the ones in the COOL database.

COOL database tag	Good	Regular	Bad	Ugly	Dwarf
ADC masked	0	25	7	10	1
Bad CIS calibration	0	26	8	12	0
Bad cesium calibration	0	6	1	1	2
Bad laser calibration	0	35	1	2	16
Bad timing	0	4	0	0	0
Channel masked	0	7	1	8	2
Data corruption	0	1	0	0	0
Large HF noise	0	11	0	0	0
No CIS calibration	0	3	0	2	0
No cesium calibration	0	36	1	7	0
No laser calibration	0	0	0	7	1
Severe stuck bit	0	1	1	9	0
Stuck bit	0	12	0	3	0
Untagged	0	0	4	7	0

5

Search for FCNC top-quark decays to qZ

With a detector providing high efficiency and good geometrical acceptance, the discovery of new physics depends not only on the cross section of the signal in question, the amount of SM processes for proton–proton collisions masking such signal, but also on the efficiency of a given analysis to find such events. A summary of several SM production cross-section measurements are presented in Figure 5.1. From the figure, it can be seen that new physics is probed at small cross-sections (below 10 pb), comparing to the many other processes occurring at the colliders. Thus, finding rare events implies removing from data most of the more common SM background processes without affecting too much the signal events or, in other words, increasing the analysis efficiency. This is performed by testing the analysis strategy on simulated samples and comparing to data.

The subject of the analysis described in this thesis is an FCNC top-quark decay that, as mentioned in Chapter 2, would be evidence for new physics. It can be studied directly by searching for final states with the corresponding decay particles. The considered signal events are $t\bar{t}$ decays, with one of the top-quarks decaying through the dominant $t \to bW$ mode and the other one through the FCNC $t \to qZ$ channel. Furthermore, only the leptonic decays of the W and Z bosons are considered which, although it accounts for only a fraction $\mathrm{BR}(W^{\pm} \to \ell^{\pm}\nu) \times \mathrm{BR}(Z \to \ell^{+}\ell^{-}) = 3.304\%$ [28] of the whole signal, these leptonic decays lead to cleaner signatures as opposed to those based only on jets and missing transverse momentum. This is also why the search for this

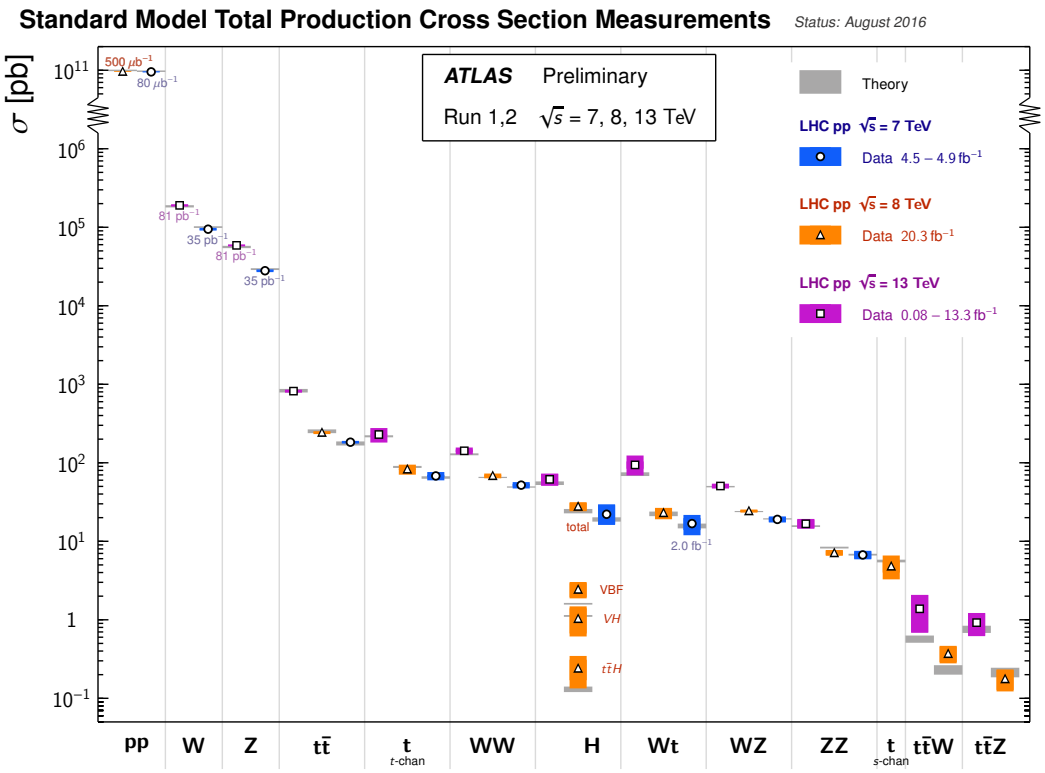

Figure 5.1: Summary of several Standard Model total production cross-section measurements, corrected for leptonic BR, compared to the corresponding theoretical expectations. All theoretical expectations are calculated at NLO or higher. The W and Z vector-boson inclusive cross-sections are measured with 35 pb^{-1} of integrated luminosity from the 2010 dataset. All other measurements are performed using the 2011, 2012, or 2015 datasets. Taken from [136].

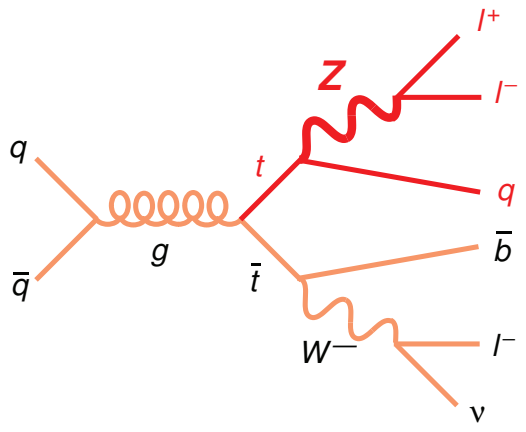

Figure 5.2: Dominant Feynmam diagram of the signal topology. One top-quark decays into the dominant decay mode $t \to bW$ and the other one through the FCNC $t \to qZ$ decay channel. The W and Z boson decays considered are the leptonic ones. Taken from [137].

FCNC process is performed in the decay instead of the $qZ \to t$ production.

The signatures of the signal, $t\bar{t} \to bWqZ \to b\ell\nu q\ell\ell$ are then: three leptons, two quarks that hadronise and form jets, and missing transverse momentum from the undetected neutrino – this specific signature is called the topology of the signal and the corresponding dominant leading order Feynman diagram is shown in Figure 5.2.

The strategy of the analysis is described in the following sections. It consists in the reconstruction of the particles involved in the $t\bar{t}$ decay, both in data and in simulated samples, and a measurement of the process BR if a discovery is claimed, otherwise derive upper limits on it.

5.1 Data and simulated samples

This section outlines the details of the 2012 ATLAS data set and Monte Carlo simulations used in the analysis.

5.1.1 Data samples

The full 2012 dataset from pp collisions at $\sqrt{s} = 8$ TeV, and collected with the ATLAS detector between April 4th and December 6th, is used. After data taking, raw data from the data acquisition system is processed. Sophisticated algorithms are applied to

raw data to identify and reconstruct physics objects, namely particle tracks. As data is comprised of independent events, parallel applications can process several events at the same time. This first processing of raw data is done at ATLAS Tier-0 site. Subsequent reprocessing is done to improve the quality of the reconstructed data using the Worldwide LHC Computing Grid resources [138].

Not all recorded data is considered valid for physics analysis. Events are required to fulfil standard data quality requirements corresponding to a good physics run, meaning that all ATLAS detector components are required to be functioning normally. Data events recorded when a sub-system is offline or temporarily failing are rejected by comparing them to a "good runs list" (GRL) that essentially keeps track of the data quality flags of each sub-systems. Table 5.1 lists information about the data taking periods, the luminosity delivered by the LHC during stable beams, the luminosity recorded by ATLAS and the luminosity after applying the GRL. The corresponding integrated luminosity used for the analysis is then 20.3 fb^{-1} with an uncertainty of $\pm 2.8\%$. This uncertainty is derived, following the same methodology as that detailed in Ref. [139], from a preliminary calibration of the luminosity scale derived from beam-separation scans performed in November 2012. Event level vetoes are also applied, removing incomplete data events or data events with corrupt or bad calorimeter information.

Additionally, events selected for this analysis are also required to have fired a single lepton trigger. A lower threshold single lepton trigger with an isolation requirement and a higher threshold one without an isolation requirement were applied. From the index given by event filter (see Section 3.13), the events considered can either be from the Egamma (electrons) or Muon stream. An event selected from the Egamma stream must have fired the `EF_e24vhi_medium1` or the `EF_e60_medium1` trigger. An event selected from the Muon stream must have fired the `EF_mu24i_tight` or the `EF_mu36_tight` trigger. The number in the trigger tag's represents the lower p_{T} threshold for which the trigger is 95% efficient and the "`i`" indicates if an isolation requirement was applied. The efficiency is computed with respect to offline electron or muon candidates, which are required to pass either the "medium" or "tight" quality requirements described in Section 5.2.

Table 5.1: Data taking periods of the full 2012 dataset are A-L (Apr 4 - Dec 6). The integrated luminosity over all stable beam periods is 22.83 fb^{-1} and the integrated luminosity recorded by ATLAS is 21.28 fb^{-1}. The final luminosity, after applying the quality requirements, is also shown. The F and K periods correspond to data taking without LHC collisions, hence are not shown.

Period	Date range	Int. lum. [fb^{-1}]	Int. ready lum. [fb^{-1}]	Int. lum. after GRL [fb^{-1}]
A	05 Apr – 20 Apr	0.91	0.84	0.79
B	01 May – 18 Jun	5.69	5.30	5.10
C	01 Jul – 24 Jul	1.64	1.54	1.41
D	24 Jul – 23 Aug	3.60	3.37	3.29
E	23 Aug – 17 Sep	2.86	2.70	2.53
G	26 Sep – 08 Oct	1.40	1.30	1.28
H	13 Oct – 26 Oct	1.66	1.56	1.45
I	26 Oct – 02 Nov	1.15	1.06	1.02
J	02 Nov – 27 Nov	2.94	2.72	2.60
L	30 Nov – 06 Dec	0.98	0.89	0.84
Total	04 Apr – 06 Dec	22.83	21.28	20.31

5.1.2 Simulated samples

Samples of simulated events are used to validate the software used for the event reconstruction and, when data is available, to compare data with the theory predictions. Software packages, called event generators, incorporate the knowledge of the physics behind a given process and, by using Monte Carlo (MC) statistical techniques, generate samples[1] of events for a chosen process. The generator is responsible for modelling all the sub-processes that take place in a collision: the hard process, initial and final state radiation, hadronisation and decays of unstable hadrons. An example of a collision with these processes is depicted in Figure 5.3. Since factorisation of the event into these well-defined steps is generally possible, these individual processes/states are calculated separately [140]. Some of them may be handled by other packages that are interfaced with the main generator.

The collision between the protons can be treated as collisions between the partons (the quarks and gluons) inside [141], each carrying a fraction of the total momentum of the proton. The protons macroscopic properties can be described by the valence up and down quarks; however, they are also composed by many quark–antiquark pairs, called the sea quarks, as well as gluons. These sea quarks can, in general, have any flavour, although the chance to find the heavier quarks is reduced. The probability of finding a certain flavour, i, of a parton (quark, antiquark or gluon) with a momentum fraction x of the proton is given by parton distribution functions (PDFs), $f_i(x, Q^2)$, for a given scale determined by the squared momentum of the exchange boson, Q^2. Due to limitations of perturbative QCD, these PDFs cannot be calculated from first principles, involving quarks, gluons and their QCD interactions. They are instead derived from fits to experimental data from deep-inelastic scattering and jet production at colliders [142], most notably from HERA and Tevatron. PDFs for other x and Q^2 can be obtained by solving DGLAP (Dokshitzer-Gribov-Lipatov-Altarelli-Parisi) evolution equations [143–145]. Figure 5.4 shows the (Q^2, x) plane and the coverage by various experiments, and a sample PDF of the proton showing valence quarks (u_v, d_v) with, on average, larger momentum than sea quarks (S) and the gluon contribution dominating for $x < 0.1$.

Using the PDFs to describe the incoming protons, the event generation starts by calculating the hard process at some fixed order perturbation theory (e.g. LO, NLO

[1] Throughout the rest of the text, the simulated samples are labeled "MC samples" or just MC for simplicity.

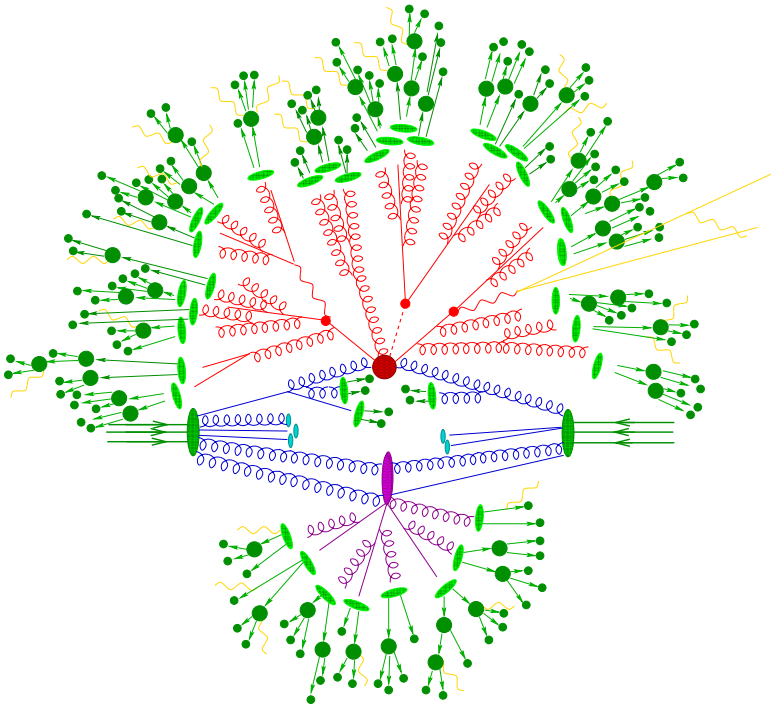

Figure 5.3: Representation of a $t\bar{t}H$ event as produced by an event generator. The hard interaction (big red blob) is followed by the decay of both top quarks and the Higgs boson (small red blobs) with additional QCD radiation produced (parton showers). A secondary interaction (underlying event) can also take place (purple blob). The free partons hadronise (light green blobs) and decay (dark green blobs). QED bremsstrahlung takes place at any stage (yellow). Taken from [140].

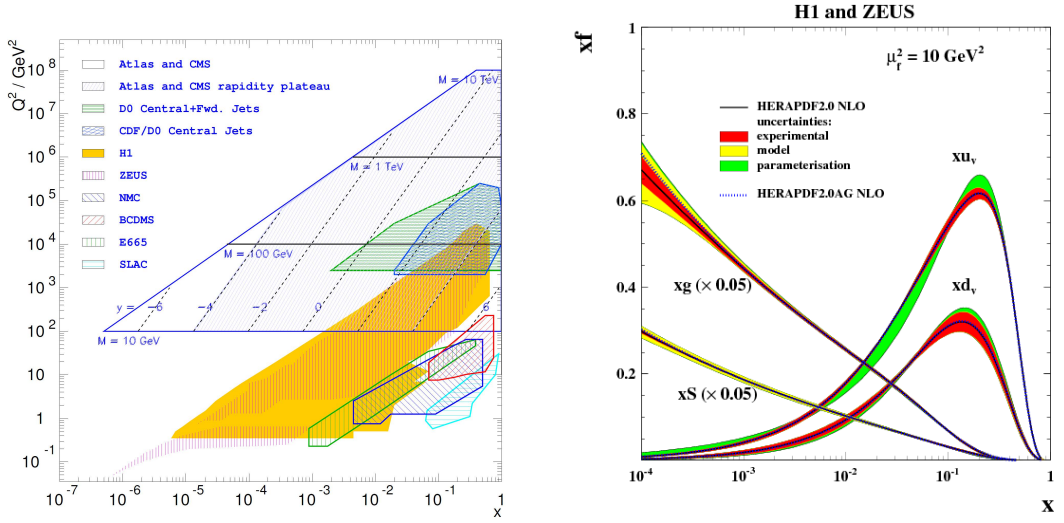

(a) (b)

Figure 5.4: On the left, the kinematic coverage of the fixed target deep-inelastic scattering experiments and HERA compared to $p\bar{p}$ and pp colliders, the Tevatron and LHC respectively. Taken from [146]. On the right, the parton distributions of the proton, measured by the HERA collaborations [147]. The probability xf to find a parton of a given momentum fraction x is plotted against the momentum fraction x. Valence quarks (u_v, d_v) have, on average, larger momentum than sea quarks (S). The gluon and sea distributions are scaled down by a factor 20.

or higher levels). This consists in evaluating the corresponding matrix element that describes the two interacting partons. Since the partons have color, they radiate gluons which, in turn, can spontaneously produce more gluons and quark-antiquark pairs. This leads to the formation of parton showers and, if this gluon radiation originates from the initial state partons, it is called initial state radiation (ISR), if it comes from the outgoing hard process particles it is called final state radiation (FSR). Photon emission can also occur from the electrically charged particles involved that, in this case, can lead to the production of electron-positron pairs. At a certain energy scale, the parton showering is cutoff and the gluons and quarks are grouped into color neutral particles. These primary hadrons are heavy and unstable and so they decay into lighter stable particles that can be observed in detectors. Aside from the interacting partons that form the hard process (relevant for the analysis in question), other partons in the same proton might also interact, which is usually referred as the underlying event. This is distinct from the pile-up that relates to collisions happening simultaneously involving other protons.

At this stage the generator has simulated all the information of the final decay products (which particles have decayed into the final particles, the four-momentum of them, etc.). The next step is to send this information to the detector simulator. This software simulates the passage of particles through the detector material, ionisations, Compton scattering, etc. Extra particles may appear here as a result of these effects. Finally the detector hits and outputs are simulated from the particle hits and energy depositions as they would be read out by the electronics. Then the information can be reconstructed like real data would be.

In the end, some shortcomings from the MC simulation are corrected with scale factors. For instance, the MC simulation can be produced at LO, if there is no significant impact in the kinematics of the event, and then the total event cross-section can be rescaled to the NLO value using the so called k-factors. MC samples also need to be rescaled to match the total integrated luminosity of data. The samples are further rescaled in bins of the average number of interactions per bunch crossing to match the number of interaction seen in data. Other corrections are applied to the MC that depend on the reconstructed objects. These are described in Section 5.2. Once this is complete the MC simulated samples can be treated as real data and used in the various analyses.

Table 5.2: Scale factors applied to the events before the analysis chain to extrapolate the $t\bar{t}$ cross section from LO to NLO.

$p_{\mathrm{T}^{t\bar{t}}}$ [GeV]	$\frac{1}{\sigma}\frac{d\sigma}{dp_{\mathrm{T}^{t\bar{t}}}}$ [10^{-3} GeV^{-1}]	SF
$[0, 40[$	14.1	1.14
$[40, 170[$	3.0	0.86
$[170, 340[$	0.25	0.84
$[340, 1000]$	0.008	3.70

5.1.2.1 Signal samples

The simulation of signal events is performed with PROTOS 2.2 [148, 149], which includes the effects of new physics using an effective Lagrangian (see Section 2.2.2). The four anomalous couplings $X_{ut}^L, X_{ut}^R, \kappa_{ut}^L, \kappa_{ut}^R$, are set to 0.01 each (see Equation 2.10). A comparison of the different coupling values was done by setting a coupling to 0.01 and turning off the other three. From the impact on the p_{T}, η, E and masses of the generated particles, shown in Figures B.1 to B.13 in Appendix B, it can be seen that the coupling choice does not affect the kinematics of the event.

Since PROTOS generates massless c-quarks, a valid approximation due to the much larger top quark mass, no impact in the kinematics is seen by comparing the $bWuZ$ and $bWcZ$ processes and the latter is used as reference. Only decays of the W and Z bosons involving charged leptons are generated at the matrix-element level by PROTOS ($Z \to e^+e^-, \mu^+\mu^-, \tau^+\tau^-$ and $W \to e\nu, \mu\nu, \tau\nu$). The CTEQ6L1 [150] leading-order PDF is used. To account for higher-order contributions in the signal production, the events are reweighted according to the measured $t\bar{t}$ differential cross section as a function of the transverse momentum of the $t\bar{t}$ system $(1/\sigma)(\mathrm{d}\sigma/\mathrm{d}p_{\mathrm{T}}^{t\bar{t}})$ [151]. The scale factors used are shown in Table 5.2 and are applied to the events before the analysis chain. Hadronisation is handled by PYTHIA 6.426 [152] with the Perugia2011C [153] set of tuned parameters and τ decays are processed with TAUOLA [154].

The top-quark mass is set to $m_t = 172.5$ GeV. To study the effect of the uncertainties on the top-quark mass, samples with different central values are generated (top quark masses of 170 GeV and 175 GeV are considered). Also, additional simulations with different parton shower parameterisations[1] are used to estimate the systematic

[1]The following PYTHIA parameters are used for less (more) radiation: PARP(67) = 0.75(1.75), PARP(64) = 4.08(1.02), PARP(72) = 0.150(0.425) and PARJ(82) = 1.66(0.5).

uncertainties on the amount of ISR/FSR.

Simulation of the ATLAS detector and trigger are performed using fast simulation with ATLFASTII [155, 156]. The fast simulation uses full simulation for the ID and muon system and FastCaloSim [157] in the calorimetry. In total 300 000 signal events are generated for each of the simulated signal samples described.

5.1.2.2 Background samples

Several SM processes have final-state topologies similar to the signal. These include events with three prompt leptons, namely from diboson (WZ, ZZ), $t\bar{t}W$, $t\bar{t}Z$ and $t\bar{t}WW$, Higgs ($t\bar{t}H$, ggH, ZH, WH), tZ and triboson (WWW, ZWW and ZZZ) production. Additionally, events with non-prompt leptons or in which at least one jet (including jets from heavy-flavour decays) is misidentified as an isolated charged lepton (labelled as "fake leptons" throughout this thesis) can also fulfil the event selection requirements. These events comprise Z+jets, $Z + \gamma$, $t\bar{t}$ and single-top, and are estimated from a data-driven (DD) method using a parametrisation of the true- and fake-lepton efficiencies (explained in Section 5.4.2). Samples of simulated events of these backgrounds with fake leptons are used to cross-check the DD estimation. The Z+jets simulations include Z production in association with heavy-flavour quarks.

Diboson events (WZ, WW and ZZ where Z means Z/γ^*) are produced using SHERPA (Simulation of High-Energy Reactions of PArticles) [140] version 1.4.3 with the PDF set CT10 [158]. They contain up to three additional partons and are filtered for leptons with $p_{\mathrm{T}} > 5$ GeV and $m_{\ell\ell} > 0.1$ GeV for the Z/γ^*. Additionally, ALPGEN and HERWIG (Hadron Emission Reactions With Interfering Gluons) diboson samples are used for comparison. The HERWIG v6.5 [159] samples use the default set of tuned parameters AUET2 (ATLAS Underlying Event Tune 2) [160] to the ATLAS data and the PDF set CTEQ6L1. These samples are filtered for one lepton with $p_{\mathrm{T}} > 10$ GeV, $|\eta| < 2.8$. The samples generated with ALPGEN 2.14 [161] use the CTEQ6L1 PDF and are interfaced with HERWIG to add the parton shower with the AUET2 set of tuned parameters. Up to five additional partons from the matrix element are simulated.

Events with $t\bar{t}W$, $t\bar{t}Z$ and $t\bar{t}WW$ production (the collection of these samples is labelled $t\bar{t}V$ throughout this thesis, where V stands for vectorial boson), including those with extra jets in the final state as well as triboson samples (WWW, ZWW and ZZZ) and tZ with up to one additional parton, are generated using MADGRAPH 5 [162]

version 1.3.33 with CTEQ6L1 PDF. Parton showering is added using PYTHIA 6.426 with the AUET2B set of tuned parameters. The Higgs samples $t\bar{t}H$, WH, ZH are generated with PYTHIA 8.165 [163] using CTEQ6L1 PDF and AU2 [164] set of tuned parameters. The sample ggH is generated with POWHEG BOX (Positive Weight Hardest Emission Generator) [165] + PYTHIA with CT10 PDF and AU2 set of tuned parameters.

Two Z+jets ALPGEN samples are compared with hadronisation from PYTHIA or HERWIG. ALPGEN + PYTHIA use the CTEQ6L1 PDF and P2011C set of tuned parameters. These samples include Z boson production in association with heavy flavour quarks with dileptons in the invariant mass range of 30 GeV $< m_{\ell\ell} <$ 1 TeV. The overlap between the samples are corrected for by the Heavy Flavor Overlap Removal Tool (HforTool) [166]. Samples generated with ALPGEN + HERWIG use the PDF CTEQ6L1 and the AUET2 set of tuned parameters with $m_{\ell\ell} >$ 60 GeV. Up to five additional partons are simulated. Again, additional samples for Z production in association with heavy flavour quarks are generated and the overlap removed with HforTool. Samples for the low mass region 10 GeV $< m_{\ell\ell} <$ 60 GeV are also used.

$Z\gamma$ background events are generated with SHERPA 1.4.1 with the CT10 PDF. $W\gamma$ samples are generated with ALPGEN + HERWIG using the AUET2 set of tuned parameters and the CTEQ6L1 PDF.

For $t\bar{t}$, the events are generated with POWHEG BOX + PYTHIA 6.426 with P2011C. For single top (s-channel and Wt-channel), events are generated using the MC@NLO generator v4.03 [167] with the CT10 PDF. The parton shower and the underlying event are added using the HERWIG generator with the AUET2-CT10 set of tuned parameters. Single top t-channel events are generated with AcerMC [168] and hadronised with PYTHIA using the CTEQ6L1 PDF and AUET2B set of tuned parameters.

Detailed simulation of the ATLAS detector and trigger is performed with GEANT4 (GEometry ANd Tracking) [155, 169] for all described samples. Table 5.3 summarises the information about the generators, parton shower and parton distribution functions used to simulate the different event samples considered in the analysis. The number of events, cross-sections and k-factors of the individual samples are detailed in appendix C.

Table 5.3: Generators, parton shower, parton distribution functions and parameter tune for hadronisation used to produce simulated samples used in this analysis.

Sample	Generator	Parton shower	PDF	Tune
Samples of backgrounds with at least three prompt leptons:				
$t\bar{t} \to bWqZ$	PROTOS 2.2 [148]	PYTHIA 6.426 [152]	CTEQ6L1 [150]	Perugia2011C [153]
WZ	SHERPA 1.4.3 [140]	SHERPA 1.4.3	CT10 [158]	—
WZ	ALPGEN 2.14 [161]	HERWIG 6.520.2 [159]	CTEQ6L1	AUET2 [160]
ZZ	SHERPA 1.4.3	SHERPA 1.4.3	CT10	—
ZZ	HERWIG 6.5	HERWIG 6.5	CTEQ6L1	AUET2
$t\bar{t}V$, tZ, tribosons	MADGRAPH 5 1.3.33 [162]	PYTHIA 6.426	CTEQ6L1	AUET2B
$t\bar{t}H$, WH, ZH	PYTHIA 8.163 [163]	PYTHIA 8.163	CTEQ6L1	AU2 [164]
ggH	POWHEG BOX 2 [165]	PYTHIA 8.163	CT10	AU2
Samples of other backgrounds:				
WW	SHERPA 1.4.3	SHERPA 1.4.3	CT10	—
Z+jets (30 GeV $< m_{\ell\ell} <$ 1 TeV)	ALPGEN 2.14	PYTHIA 6.426	CTEQ6L1	Perugia2011C
Z+jets (10 GeV $< m_{\ell\ell} <$ 60 GeV)	ALPGEN 2.14	HERWIG 6.520.2	CTEQ6L1	AUET2
$Z\gamma$	SHERPA 1.4.1	SHERPA 1.4.1	CT10	—
$t\bar{t} \to bWbW$	POWHEG BOX 2	PYTHIA 6.426	CTEQ6L1	Perugia2011C
Single top (s, Wt channel)	MC@NLO 4.03 [167]	HERWIG 6.520.2	CT10	AUET2
Single top (t channel)	AcerMC 3.8 [168]	PYTHIA 6.426	CTEQ6L1	AUET2B

5.2 Object reconstruction

The primary physics objects considered in this search are electrons, muons, missing transverse momentum, jets and b-tagged jets. Tau leptons are not explicitly reconstructed, although the τ decay products are reconstructed as electrons, muons or jets and as an additional contribution to the missing transverse momentum. A summary of the main reconstruction methods and identification criteria applied to each object is given below.

5.2.1 Electrons

Electron candidates are reconstructed [170] from energy deposits (clusters) in the electromagnetic calorimeter, which are then matched to reconstructed charged-particle tracks in the inner detector. MC-based corrections are applied at cluster level to account for energy loss due to absorption in the passive material and external leakage outside the cluster. In the end, overall electron response in data is calibrated using $Z \to e^+e^-$ events, to match the expectation from simulation.

The candidates are required to have a transverse energy E_{T} greater than 15 GeV and a pseudorapidity of the calorimeter cluster associated with the electron candidate $|\eta_{\mathrm{cluster}}| < 2.47$. Candidates in the transition region between the barrel and endcap calorimeters with $1.37 < |\eta_{\mathrm{cluster}}| < 1.52$ are excluded. Electron candidates in this analysis must satisfy tight quality requirements on the electromagnetic cluster and associated track which provide discrimination between isolated electrons and jets. In order to suppress multi-jet backgrounds, it is also required that there is little activity in the space surrounding the electron. Two isolation variables are employed: the energy deposited around the electron in the calorimeter in a cone of size $\Delta R = 0.2$ and the p_{T} sum of tracks around the electron in a cone of size $\Delta R = 0.3$. Cuts on these two quantities are used to select isolated electrons; the cuts provide a 90% isolation efficiency in Z boson decays to e^+e^- events from the full 2012 dataset. Additionally, the longitudinal impact parameter $|z_0|$ of the electron track with respect to the selected primary vertex of the event is required to be less than 2 mm. The closest jet if separated by $\Delta R < 0.2$ from the selected electron is removed from the event. The electron candidate is discarded if an additional selected jet is found with $\Delta R < 0.4$. A looser

electron selection, used for the estimation of backgrounds with fake leptons, is defined by removing the isolation requirements.

A correction factor is applied to the simulated samples to account for the differences with respect to data. It depends on the reconstruction efficiency to find a cluster in the electromagnetic calorimeter and match it to a reconstructed charged particle track, on the identification efficiency relative to reconstructed electron objects and on the trigger efficiency with respect to all reconstructed and identified electron candidates. The trigger efficiency is defined as the fraction of identified offline electrons that fire a given trigger. Clean samples of electrons are used to measure these efficiencies from the decays: $Z \to e^+e^-$, $W \to e\nu$ (with high kinematic coverage) and $J/\Psi \to e^+e^-$ (for lower transverse energies) [171]. Finally, using the same $Z \to e^+e^-$ sample used to correct the electron energy scale in data, it is observed that the energy resolution is slightly worse than in the simulation so corrections are derived and applied to simulation to match real data. Figure 5.5 shows the identification, reconstruction and trigger efficiencies, as well as electron energy resolution, for 8 TeV data.

5.2.2 Muons

The muon candidate reconstruction [175] is performed independently in the ID and MS. Depending on the signature, the muon reconstruction can be categorized into four types:

- Standalone muons (SA), when the muon trajectory is reconstructed only in the MS and to extend the range to $2.5 < |\eta| < 2.7$, a region not covered by the ID;
- Combined (CB) muon, when the track is reconstructed independently both in the ID and MS, and then combined (this is the main type of reconstruction);
- Segment-tagged (ST) muons, when a track in the ID can be extrapolated to the MS and associated to, at least, one track in the MDT or CSC chambers (used to increase acceptance of low p_{T} muons that cross only one layer);
- Calorimeter-tagged (CaloTag) muons, if a track in the ID can be associated to a energy deposit in the calorimeter, compatible with an ionizing particle.

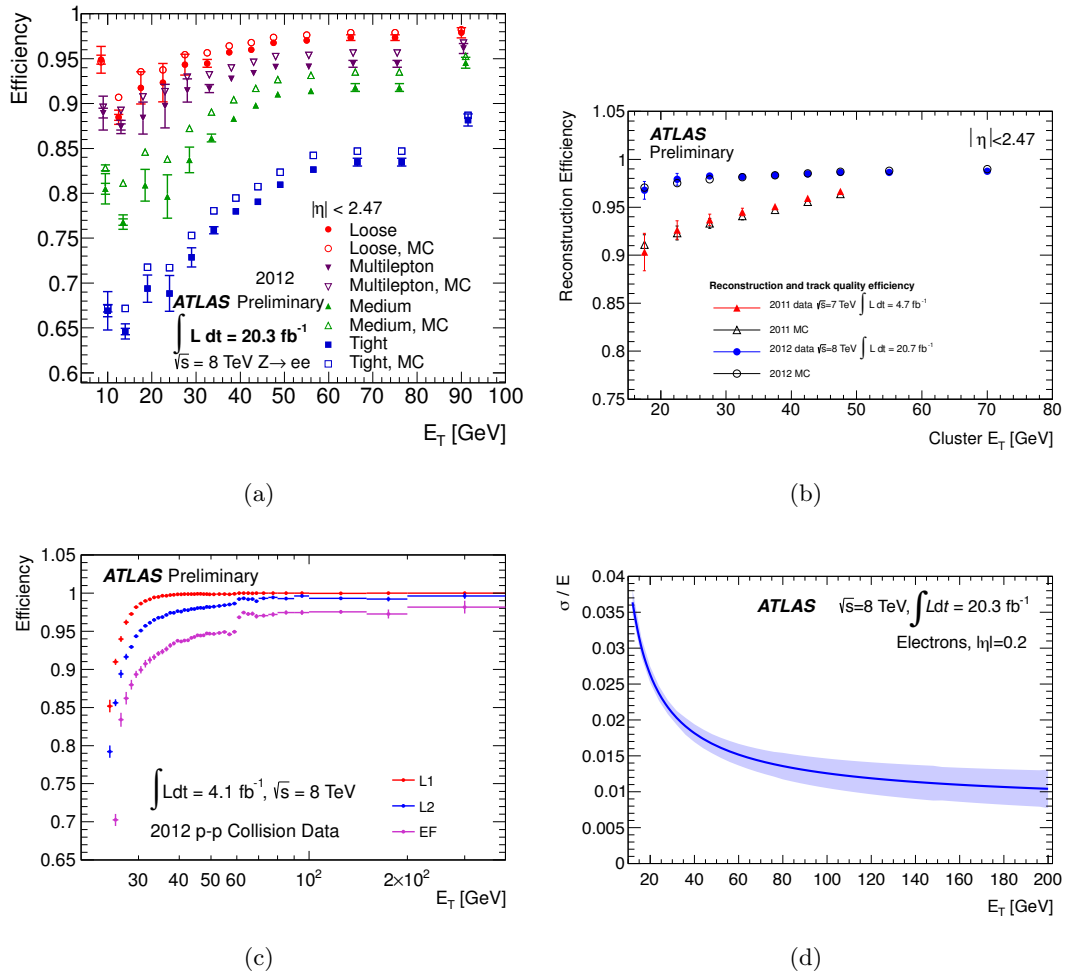

Figure 5.5: Distributions for (a) electron identification efficiency vs. E_{T} from real data and MC, using 2012 data, [172] for the different working points, (b) electron reconstruction efficiency vs. E_{T} from 2011 and 2012 data [173], respectively, (c) L1, L2 and EF trigger efficiencies as a function of the offline-reconstructed electron E_{T} for the single electron triggers used for ATLAS physics analyses [174], and (d) the resolution curve and its uncertainty as a function of E_{T} for electrons with $|\eta| = 0.2$ [170].

Muon reconstruction efficiency is shown in Figure 5.6(a) for the different types of muon reconstruction, as a function of η. In most regions it is above 99%. CB candidates have the highest muon purity and are used in this analysis. Still, the other types are taken into account in missing transverse momentum calculations. The CB muon track segments are built in MS from segments that typically start from the outer and middle chambers and are extrapolated to the inner chambers. The identified muons are then matched with tracks reconstructed in the ID. The candidates are refitted using the complete track information from both detector systems, and are required to satisfy $p_{\mathrm{T}} > 15$ GeV, $|\eta| < 2.5$ and to be separated by $\Delta R > 0.4$ from any selected jet. The hit pattern in the inner detector is required to be consistent with a well-reconstructed track [175] and the $|z_0|$ of the muon track is required to be less than 2 mm. Additionally, the sum of the momenta of tracks inside a cone around the muon candidate, with variable size such that it is smaller for higher muon p_{T} [176], must be less than 5% of the muon energy.

Correction factors are applied to the simulated samples to account for the differences with respect to the real data. Muon reconstruction and trigger efficiencies as well as muon energy-scale and resolution are corrected in simulation to match data, and the factors are extracted using samples with $Z \to \mu\mu$ and $J/\Psi \to \mu\mu$ events [123, 175]. Figure 5.6 shows the muon reconstruction and trigger efficiencies as well as muon resolution.

5.2.3 Jets

Jets are associations of several particle trajectories that originate from a single object at parton or lepton level, due to hadronisation and can be seen in the detector as tracks in the ID and energy deposition of the jet particles in the calorimeters. Jets are reconstructed [177] from topological clusters of neighbouring calorimeter cells with significant energy deposits using the anti-k_t algorithm [178] with a radius parameter $R = 0.4$. Prior to jet finding, a local calibration scheme is applied to correct the topological cluster energies for the non-compensating response of the calorimeter, dead material, and energy leakage. The corrections are obtained from simulations of charged and neutral particles. The jets are then calibrated to the hadronic energy scale using p_{T}- and η-dependent correction factors in four steps. First, the average additional energy due to pile-up is subtracted from the energy measured in the calorimeters. Then, the

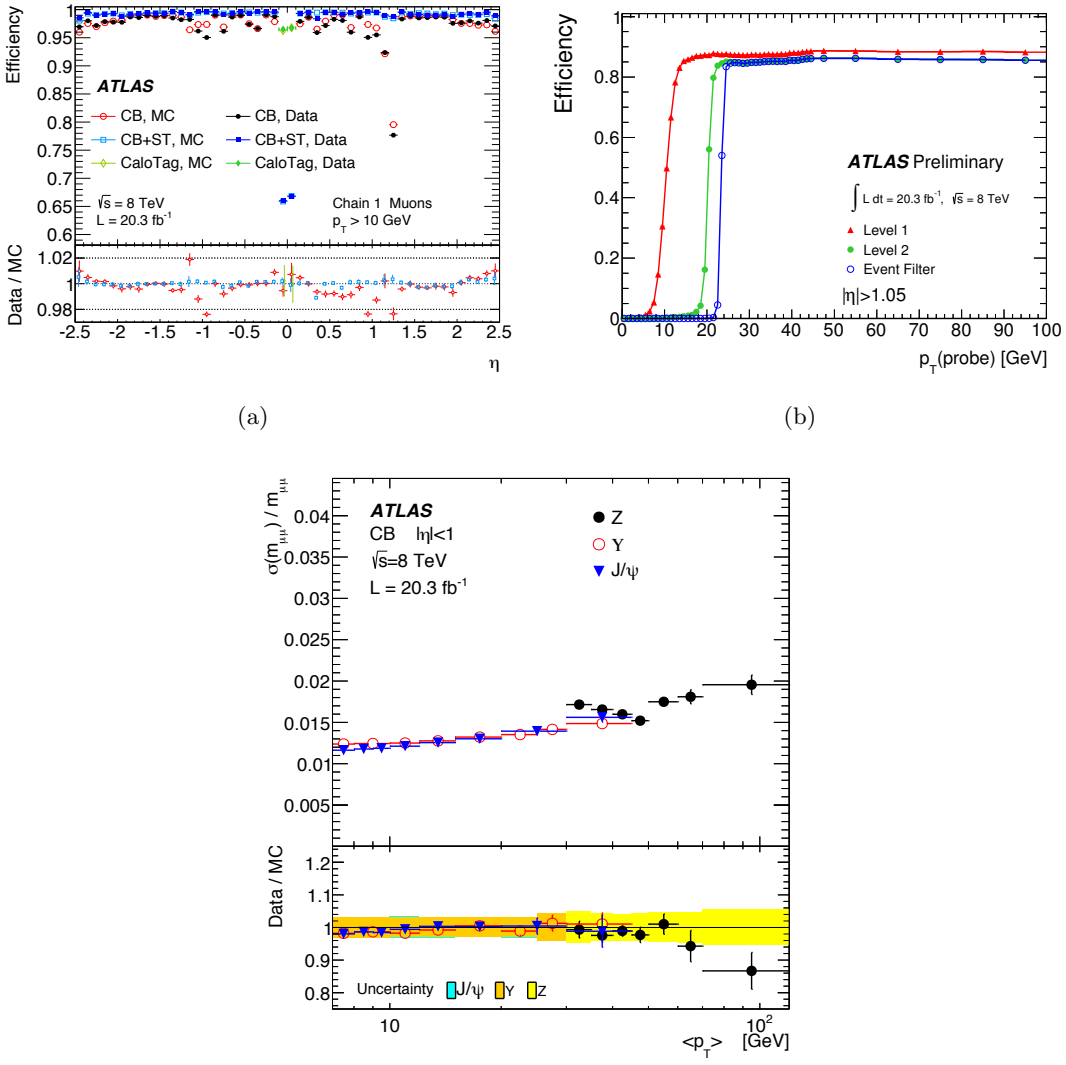

(a) (b)

(c)

Figure 5.6: Distributions for (a) the muon reconstruction efficiency as a function of η, measured in $Z \to \mu\mu$ events for muons with $p_{\mathrm{T}} > 10$ GeV, and for different muon reconstruction types [175], (b) the muon efficiency of passing either the `mu24i` or `mu36` trigger as function of the muon p_{T}, for the three trigger levels [123] and (c) the Z, Y and J/ψ dimuon invariant mass resolution for CB muons as a function of the average transverse momentum for $|\eta| < 1$ [175].

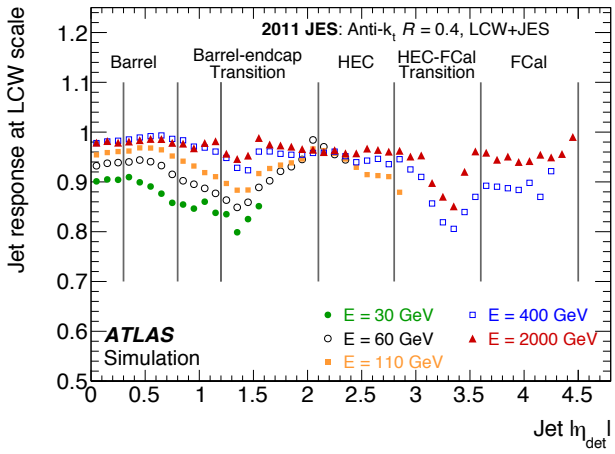

Figure 5.7: Average response of simulated jets formed from topo-clusters (which corresponds to the inverse of the average jet energy scale correction). The response is shown separately for various truth-jet energies as function of the uncorrected (detector) jet η. Also indicated are the different calorimeter regions [177].

direction of the jet is corrected so, instead of originating in the geometric centre of the detector, it instead originates from the main primary vertex of the interaction. The jet energy and direction are corrected, by comparing the kinematics of the reconstructed jets and those of the truth jets (reference jets in MC). The average energy response is shown in Figure 5.7 and corresponds to the inverse of the average jet energy scale correction. Finally, residual data/MC corrections (in η and p_{T}) are applied only to data.

Dedicated requirements are applied to remove the negligible fraction of events (less than 0.01%) where a jet is incorrectly reconstructed from a few noisy calorimeter cells [179]. The jets used in the analysis are required to have $p_{\mathrm{T}} > 25$ GeV and $|\eta| < 2.5$. To reduce the number of selected jets that originate from secondary pp interactions (pile-up), for jets with $p_{\mathrm{T}} < 50$ GeV and $|\eta| < 2.4$, the scalar sum of the p_{T} of tracks matched to a jet and originating from the primary vertex must be at least 50% of the scalar sum of the p_{T} of all tracks matched to the jet.

Jets containing b-hadrons are identified ('b-tagged') [180] using an algorithm (MV1 tagger) that uses multivariate techniques to combine information from the impact parameters of displaced tracks as well as topological properties of secondary and tertiary decay vertices reconstructed within the jet. It is determined with simulated $t\bar{t}$ events

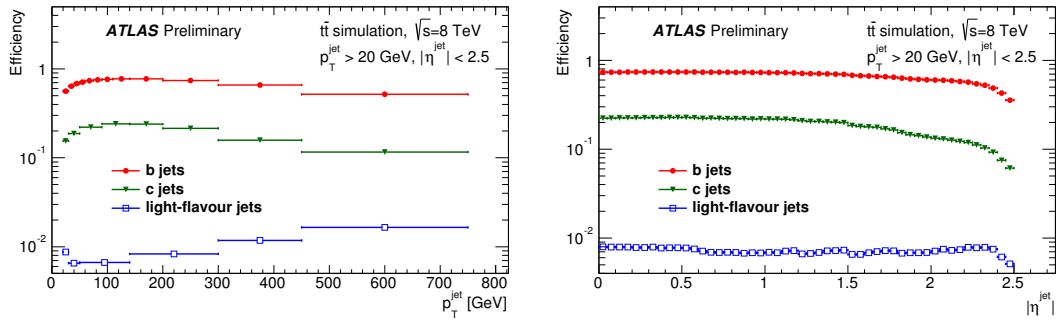

(a) (b)

Figure 5.8: Efficiency of the MV1 algorithm to tag b-, c-, and light-quark jets as b jets, as a function of the jet (a) p_{T} and (b) η [181].

that, for the chosen working point, the tagging efficiency for b-jets with $p_{\mathrm{T}} > 20$ GeV is 70%, while the rejection factors for light-quark or gluon jets (light jets), charm jets and τ leptons are 137, 5 and 13, respectively. Figure 5.8 shows the efficiency of the MV1 algorithm to tag b-, c-, and light-quark jets as b jets, as a function of jet p_{T} and η.

5.2.4 Missing transverse momentum

The missing transverse momentum (with magnitude $E_{\mathrm{T}}^{\mathrm{miss}}$) is based [182, 183] on the energy deposits in the calorimeter and muons reconstructed in the muon spectrometer. In the $E_{\mathrm{T}}^{\mathrm{miss}}$ calculation, reconstructed and calibrated physics objects are used as well as the energy deposits not associated with any of the reconstructed objects. These are calibrated according to their energy sharing between the electromagnetic and hadronic calorimeters. The $E_{\mathrm{T}}^{\mathrm{miss}}$ reconstruction includes terms from:

$$E_{x(y)}^{\mathrm{miss}} = E_{x(y)}^{\mathrm{miss},e} + E_{x(y)}^{\mathrm{miss},\gamma} + E_{x(y)}^{\mathrm{miss},\tau} + E_{x(y)}^{\mathrm{miss,jets}} + E_{x(y)}^{\mathrm{miss,SoftTerm}} + E_{x(y)}^{\mathrm{miss},\mu}. \tag{5.1}$$

Each term is calculated as the negative sum of the calibrated reconstructed objects, projected onto the x and y directions. $E_{x(y)}^{\mathrm{miss},e}$, $E_{x(y)}^{\mathrm{miss},\gamma}$ and $E_{x(y)}^{\mathrm{miss},\tau}$ are reconstructed from cells in clusters associated to electrons, photons and τ-jets from hadronically decaying τ-leptons, respectively. $E_{x(y)}^{\mathrm{miss,jets}}$ is reconstructed from cells in clusters associated to jets with calibrated $p_{\mathrm{T}} > 20$ GeV. $E_{x(y)}^{\mathrm{miss,SoftTerm}}$ is calculated from clusters and tracks

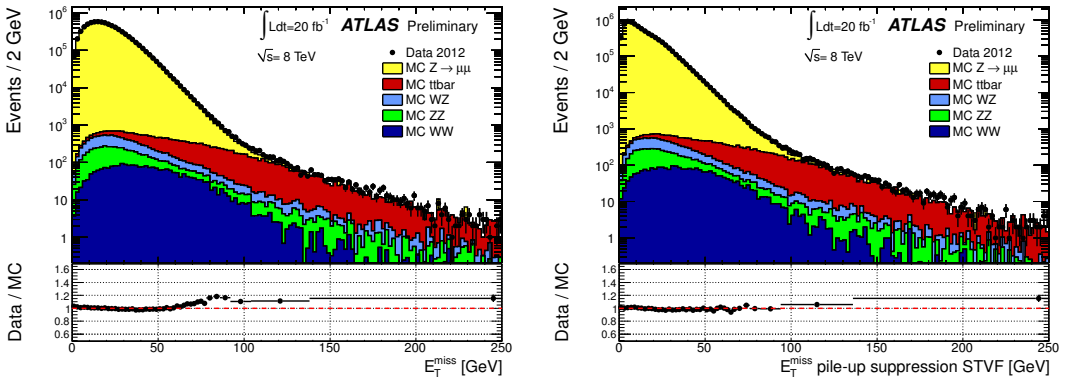

(a) (b)

Figure 5.9: $E_{\mathrm{T}}^{\mathrm{miss}}$ distribution as measured in a data sample of $Z \to \mu\mu$ events (a) without pile-up correction and (b) with pile-up corrections [183].

not associated to high-p_{T} objects (including jets with $p_{\mathrm{T}} < 20$ GeV). The $E_{x(y)}^{\mathrm{miss},\mu}$ term is calculated from the momenta of muon tracks reconstructed with $|\eta| < 2.7$ as $-\sum_{\mathrm{muons}} p_{x(y)}^{\mu}$. The value of the $E_{\mathrm{T}}^{\mathrm{miss}}$ is then calculated as:

$$E_{\mathrm{T}}^{\mathrm{miss}} = \sqrt{\left(E_x^{\mathrm{miss}}\right)^2 + \left(E_y^{\mathrm{miss}}\right)^2}. \tag{5.2}$$

Figure 5.9 shows the $E_{\mathrm{T}}^{\mathrm{miss}}$ distribution with and without pile-up correction on $Z \to \mu^+\mu^-$ events in 8 TeV data. The MC after pile-up correction agrees very well with data over a large $E_{\mathrm{T}}^{\mathrm{miss}}$ range.

5.3 Event selection

Events in the signal region (SR) must pass the single-lepton trigger (electron or muon) and the lepton that triggers the event must match a reconstructed lepton (same flavour and with $p_{\mathrm{T}} > 25$ GeV) within a cone of size $\Delta R < 0.15$. The trigger efficiencies for the leptons are approximately 93% for electrons, 70% for muons with $|\eta| < 1.05$ and 86% for muons with $1.05 < |\eta| < 2.4$ [123, 184]. Events are required to have at least one primary vertex with more than four associated tracks, each with $p_{\mathrm{T}} > 400$ MeV. The primary vertex chosen is the one with highest $\sum p_{\mathrm{T}}^2$ over all associated tracks. Leptons from cosmic rays are rejected by removing muon pairs with large, oppositely signed transverse impact parameters ($|d_0| > 0.5$ mm) and consistent with being back-to-back in the $r - \phi$ plane. Events containing noise bursts and readout errors in the LAr calorimeter are also rejected [185].

Exactly three leptons coming from the same vertex are required. The three leptons must have $|\eta| < 2.5$ and $p_{\mathrm{T}} > 15$ GeV, and two of the leptons are required to have the same flavour, opposite charge and their reconstructed mass be within 15 GeV of the known Z boson mass (m_Z) [28]. If more than one lepton-pair is found, the one with the reconstructed mass closer to the known Z boson mass is chosen as the Z boson candidate.

According to the signal topology, the events are then required to have $E_{\mathrm{T}}^{\mathrm{miss}} > 20$ GeV and two jets (although an additional third jet from initial- or final-state radiation is allowed). All jets are required to have $p_{\mathrm{T}} > 35$ GeV and $|\eta| < 2.5$. One or two of the jets must be b-tagged. Although only one b-tagged jet is expected in the signal events, a second one can arise from a misidentified c-jet associated with the FCNC decay of the top quark. Allowing for the additional b-tagged jet increases the signal efficiency without compromising the signal-to-background ratio.

Events with fake leptons used in the analysis are estimated using a DD method called "Matrix Method" (MM) (explained in Section 5.4.2.1). The reason to use a DD method instead of the MC to describe the fake leptons, is due to the high level of precision required in the modelling of QCD. Namely, the precision of the fragmentation and hadronisation models, the description of interactions with matter and hadronic activity and the estimation of the cross-sections. Nevertheless, the MM is compared and cross-checked with results obtained using MC simulation for the corresponding

backgrounds that would yield the fake leptons such as Z+jets, $Z\gamma$+jets, $t\bar{t}$, single top and WW. Throughout the remainder of this section these two methods are compared and designated as MM and MC, for simplicity.

A C++ program, LipCbrAnalysis [186, 187], using the `ROOT` [188] framework and developed for previous analysis of the Portuguese ATLAS top-quark group, was updated. It loops through all the events of each data and simulated samples and applies the topological cuts, event reconstruction and other tests described in this section.

5.3.1 Preselections

As will be explained in Section 5.4.2.1, the MM requires measurement of parameters in a dedicated control region (CR). As such, one can only look at yields for the fake leptons in selections including the requirements of that CR. Therefore, the two fake-lepton estimation approaches (MM and MC) are validated at two different levels (labeled as MC preselection and MM preselection). For the MC preselection it is required, additionally to the quality cuts already described, the presence of exactly three leptons with two of them having the same flavour and opposite charge and a reconstructed mass within 15 GeV of the Z boson mass. With just these requirements, a sample with high statistics can be analysed and a good agreement is found between the prediction given by the MC and data. The distributions of p_{T} and η of the three leptons, the jet multiplicity and $E_{\mathrm{T}}^{\mathrm{miss}}$ are shown in Figure 5.10. The p_{T} and mass of the reconstructed Z boson is also shown at this level in Figure 5.11. The MC prediction for the number of events is consistent with data, as can be seen in Table 5.4.

In addition to the MC preselection, the MM preselection requires at least one jet with $p_{\mathrm{T}} > 35$ GeV and $|\eta| < 2.5$, at least one b-tagged jet and $E_{\mathrm{T}}^{\mathrm{miss}} > 20$ GeV. For comparison, both the MM and MC methods for fake-lepton estimations are shown at this level. Distributions of p_{T} and η of the three leptons, the jet multiplicity and $E_{\mathrm{T}}^{\mathrm{miss}}$ are depicted in Figure 5.12 and the p_{T} and mass of the reconstructed Z boson in Figure 5.13 (Figures 5.14 and 5.15) for the MM (MC). Table 5.5 shows the predicted yields for both MM and MC. Both methods give a good agreement with data, within the statistical and systematic uncertainties. Table 5.18 summarises the selection requirements.

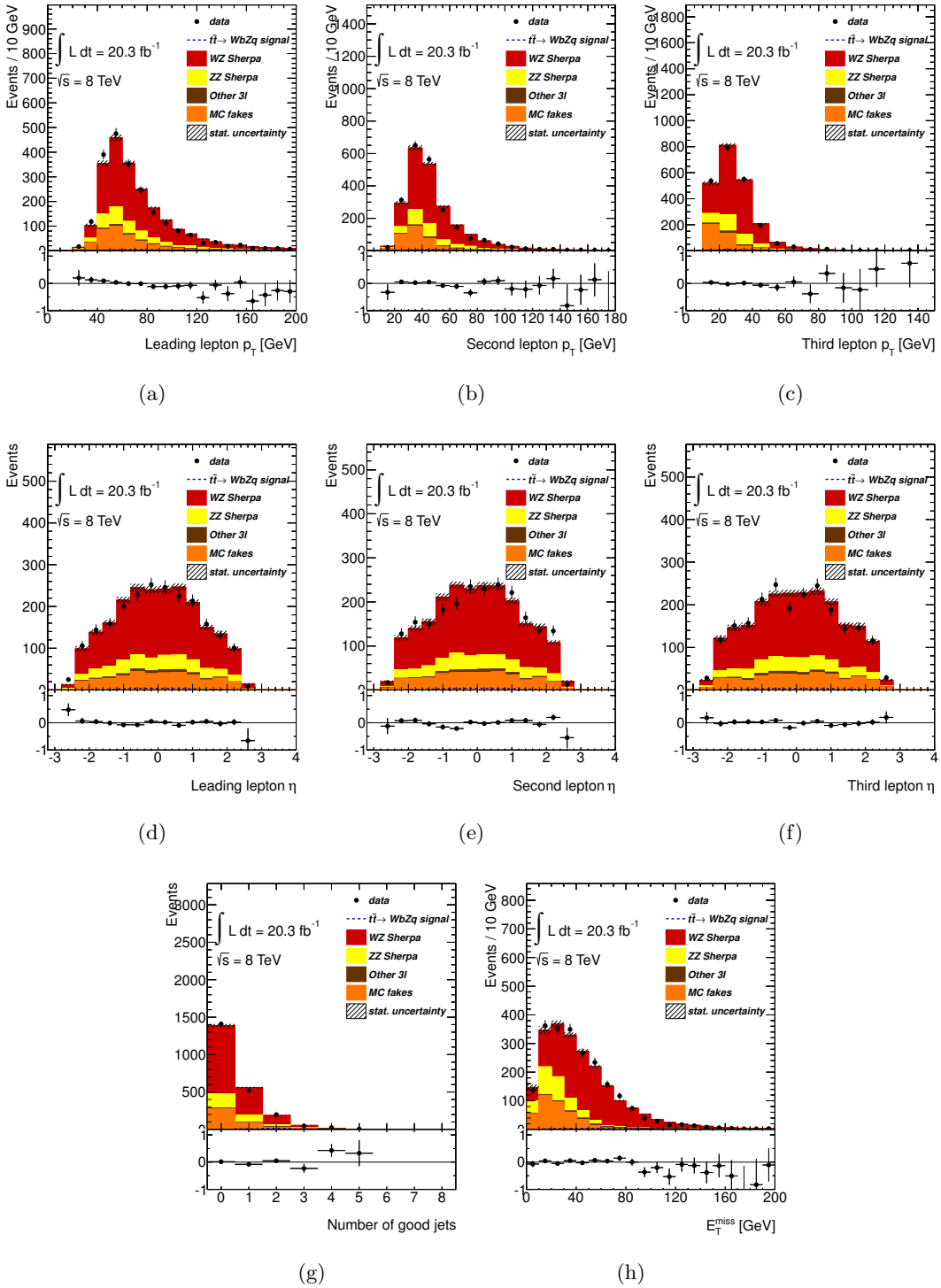

Figure 5.10: Expected and observed distributions obtained for the SR for (a) p_{T} of the leading lepton, (b) p_{T} of the second lepton, (c) p_{T} of the third lepton, (d) η of the leading lepton, (e) η of the second lepton, (f) η of the third lepton, (g) jet multiplicity and (h) $E_{\mathrm{T}}^{\mathrm{miss}}$, after preselection, using MC samples for the fake-lepton estimation. The $t\bar{t} \to qZ$ distributions are normalised to the observed limit.

Table 5.4: Expected number of background events, number of selected data events and signal efficiency (normalised to all decays of the W and Z bosons), after preselection using MC samples for fake-lepton estimation. Normalisations are applied as described in Section 5.4, and SHERPA samples are used for the dibosons and ALPGEN + PYTHIA for Z+jets backgrounds. For Z+jets, $Z\gamma$+jets, $t\bar{t}$ and single top samples a loose selection is applied as explained in Section 5.4 and then multiplied by the scale factors in Table 5.16 to account for the probability of loose leptons to enter the SR. The first uncertainty is the statistical one, associated with the number of events in the samples, the second one is systematic and is described in Section 5.5.

Sample	MC
WZ	$1446 \pm 11 \pm 269$
ZZ	$324 \pm 8 \pm 326$
Z+jets	$232 \pm 17 \pm 34$
$Z\gamma$+jets	$143 \pm 15 \pm 14$
$t\bar{t}V$	$22.6 \pm 0.4 \pm 6.8$
tZ	$16.8 \pm 0.3 \pm 8.5$
Higgs	$9.7 \pm 0.2 \pm 1.5$
$t\bar{t}$	$8 \pm 2 \pm 6$
Tribosons	$3.67 \pm 0.08 \pm 0.17$
Single top	$1.6 \pm 0.9 \pm 0.8$
WW	$0.11 \pm 0.05 \pm 0.09$
Total background	$2206 \pm 26 \pm 425$
Data	2196
Signal efficiency $[\times 10^{-3}]$	$3.86 \pm 0.03 \pm 0.23$

Table 5.5: Expected number of background events, number of selected data events and signal efficiency (normalised to all decays of the W and Z bosons), after preselection for the MM and MC. Normalisations are applied as described in Section 5.4, and `SHERPA` samples are used for the dibosons and `ALPGEN` + `PYTHIA` for Z+jets backgrounds. The fake-lepton component in the MC is the sum of the yields of Z+jets ($8.5 \pm 0.7 \pm 2.1$), $Z\gamma$+jets ($1.9 \pm 0.8 \pm 2.1$), $t\bar{t}$ ($3.6 \pm 0.7 \pm 2.3$), single top ($0.2 \pm 0.1 \pm 0.2$) and WW ($0.009 \pm 0.010 \pm 0.009$) samples. Also, for these samples, a loose selection is performed to improve statistics, and then multiplied by the scale factors in Table 5.16 to account for the probability of loose leptons to enter SR. The first uncertainty is the statistical one, associated with the number of events in the samples, the second one is systematic and is described in Section 5.5.

Sample	MM	MC
WZ	$32 \pm 2 \pm 6$	
Fake leptons	$17 \pm 2 \pm 10$	$14 \pm 1 \pm 4$
$t\bar{t}V$	$15.6 \pm 0.3 \pm 4.8$	
tZ	$8.7 \pm 0.2 \pm 4.4$	
ZZ	$2.9 \pm 0.8 \pm 3.7$	
Higgs	$0.90 \pm 0.07 \pm 0.19$	
Tribosons	$0.069 \pm 0.010 \pm 0.013$	
Total background	$76 \pm 2 \pm 14$	$74 \pm 2 \pm 11$
Data	67	
Signal efficiency [$\times 10^{-3}$]	$1.92 \pm 0.02 \pm 0.16$	

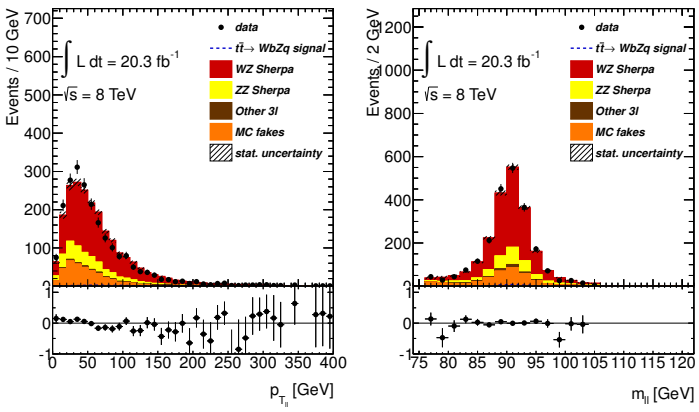

(a) (b)

Figure 5.11: Expected and observed distributions obtained for the SR for (a) p_{T} of the reconstructed Z boson and (b) reconstructed mass of the Z boson, after preselection, using MC samples for the fake-lepton estimation. The $t\bar{t} \to bWcZ$ distributions are normalised to the observed limit.

5.3.2 Kinematics and final selection

Several approaches are studied for the event reconstruction, not only to choose the one that maximises the signal efficiency but also to check the impact of the b-tag requirement. The selection, for these studies, requires exactly three leptons, with two of them of the same flavour, opposite charge and a reconstructed mass within 15 GeV of the Z boson mass and at least two jets with $p_{\mathrm{T}} > 25$ GeV and $|\eta| < 2.5$ for the leading two jets. These are the minimum requirements to select the signal topology under study (at this level, no $E_{\mathrm{T}}^{\mathrm{miss}}$ requirement is imposed to allow for higher statistics in the validations of the event reconstruction). Applying energy-momentum conservation, the kinematics of the top-quarks can be reconstructed from the corresponding decay particles. Since the neutrino from the SM semileptonic decay of the top quark ($t \to bW \to b\ell\nu$) is undetected, its four-momentum needs to be estimated. This can be done by assuming the $E_{\mathrm{T}}^{\mathrm{miss}}$ to be the neutrino transverse momentum. The longitudinal component of the neutrino momentum (p_z^{ν}) is then determined, together with the choice

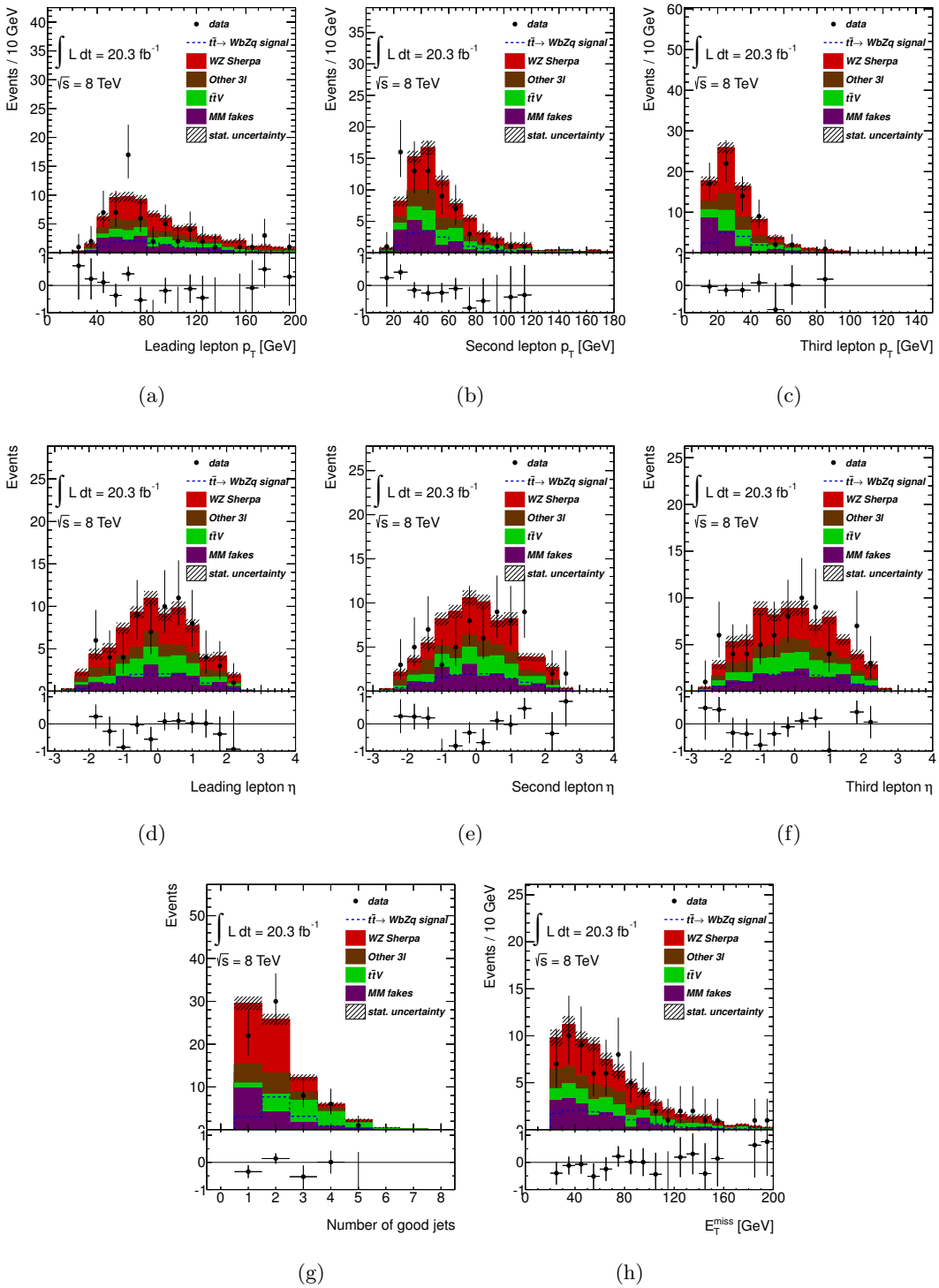

Figure 5.12: Expected and observed distributions obtained for the SR, after preselection, for (a) p_{T} of the leading lepton, (b) p_{T} of the second lepton, (c) p_{T} of the third lepton, (d) η of the leading lepton, (e) η of the second lepton, (f) η of the third lepton, (g) jet multiplicity and (h) $E_{\mathrm{T}}^{\mathrm{miss}}$, with fake-lepton estimation from MM. The $t\bar{t} \to bWcZ$ distributions are normalised to the observed limit.

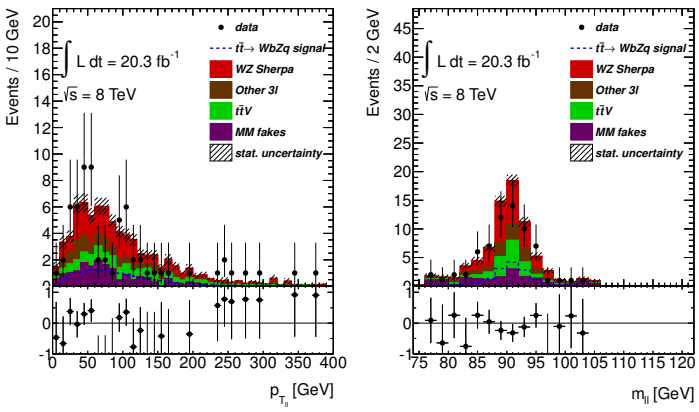

(a) (b)

Figure 5.13: Expected and observed distributions obtained for the SR, after preselection, for (a) p_{T} of the reconstructed Z boson and (b) reconstructed mass of the Z boson, with fake-lepton estimation from MM. The $t\bar{t} \to bWcZ$ distributions are normalised to the observed limit.

for the jet and lepton combination, by minimising the following expression:

$$\chi^2 = \frac{\left(m^{\mathrm{reco}}_{\mathrm{j}a\ell_a\ell_b} - m_{t_{\mathrm{FCNC}}}\right)^2}{\sigma^2_{t_{\mathrm{FCNC}}}} + \frac{\left(m^{\mathrm{reco}}_{\mathrm{j}_b\ell_c\nu} - m_{t_{\mathrm{SM}}}\right)^2}{\sigma^2_{t_{\mathrm{SM}}}} + \frac{\left(m^{\mathrm{reco}}_{\ell_c\nu} - m_W\right)^2}{\sigma^2_W} + \frac{\left(m^{\mathrm{reco}}_{\ell_a\ell_b} - m_Z\right)^2}{\sigma^2_Z} \tag{5.3}$$

where $m^{\mathrm{reco}}_{j_a\ell_a\ell_b}$, $m^{\mathrm{reco}}_{j_b\ell_c\nu}$, $m^{\mathrm{reco}}_{\ell_c\nu}$ and $m^{\mathrm{reco}}_{\ell_a\ell_b}$, are the reconstructed masses of the top quark decaying through the FCNC decay, the top quark with SM decay, the W boson from the top quark with SM decay and the reconstructed mass of the Z boson from the top quark FCNC decay, respectively.

The central value for masses and widths are taken from a Bukin fit[1] [189] to the reconstructed masses of the objects with the minimum ΔR with respect to the actual particles in the simulated signal samples generated by `PROTOS`. The longitudinal momentum of the neutrino is set to the p_z of the true generated particle (before hadronization). This represents the best detector resolution that can be achieved. These fits are shown in Figure 5.16 along with the mean values and standard deviations. The mean values and standard deviations used, that represent the best detector resolution possible, are

[1] This is a piecewise function with a Gaussian function in the center and two asymmetric tails.

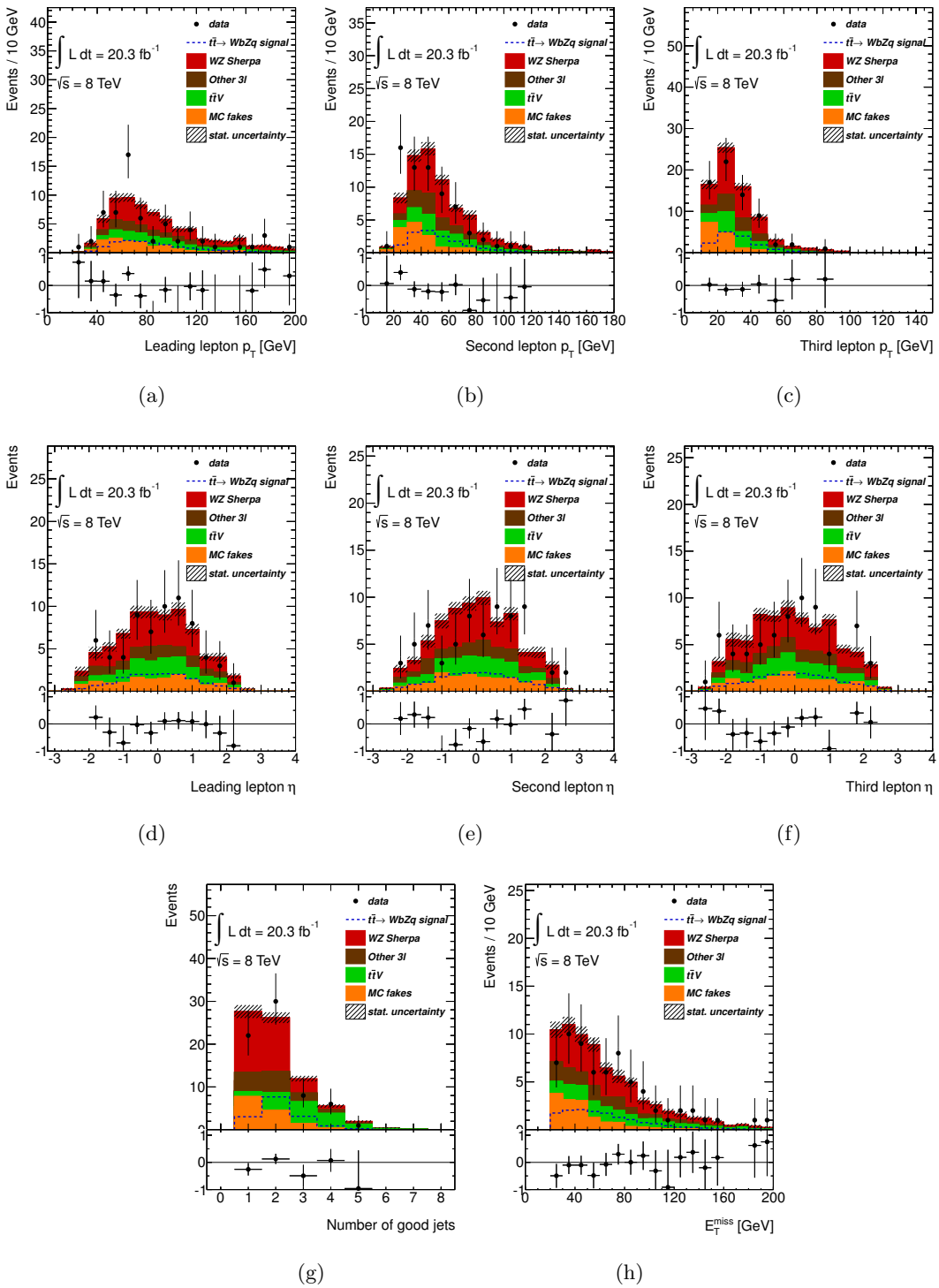

(a) (b) (c)

(d) (e) (f)

(g) (h)

Figure 5.14: Expected and observed distributions obtained for the SR, after preselection for (a) p_{T} of the leading lepton, (b) p_{T} of the second lepton, (c) p_{T} of the third lepton, (d) η of the leading lepton, (e) η of the second lepton, (f) η of the third lepton, (g) jet multiplicity and (h) $E_{\mathrm{T}}^{\mathrm{miss}}$, with fake-lepton estimation from MC. The $t\bar{t} \to bWcZ$ distributions are normalised to the observed limit.

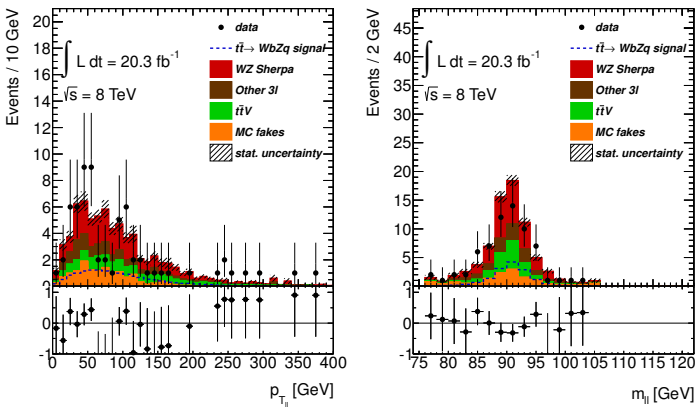

(a) (b)

Figure 5.15: Expected and observed distributions obtained for the SR, after preselection for (a) p_{T} of the reconstructed Z boson and (b) reconstructed mass of the Z boson, with fake-lepton estimation from MC. The $t\bar{t} \rightarrow bWcZ$ distributions are normalised to the observed limit.

$m_{t_{\mathrm{FCNC}}} = 173$ GeV, $m_{t_{\mathrm{SM}}} = 168$ GeV, $m_W = 82$ GeV, $m_Z = 91$ GeV, $\sigma_{t_{\mathrm{FCNC}}} = 10$ GeV, $\sigma_{t_{\mathrm{SM}}} = 23$ GeV, $\sigma_W = 15$ GeV and $\sigma_Z = 3$ GeV. As expected, the widths of the Z boson and the top-quark with the FCNC decay are smaller than the ones of the W boson and the other top-quark.

Several scenarios can be tested for reconstruction of the events, using the χ^2 in Expression 5.3, with and without including the b-tag requirement. The different tests are:

1. the χ^2 is calculated for the combinations of the two leading jets and the combinations of the three leptons;

2. the χ^2 is calculated for the combinations of the two leading jets and the lepton combination is fixed to from the combination found in preselection;

3. exactly one b-tagged jet is required and then the χ^2 is calculated for the combinations of the light quark (being one of the two jets with highest p_{T}) and the b-quark being set to the b-tagged jet. The lepton combination is fixed to the combination found in preselection;

4. the χ^2 is calculated for all combinations of jets and of three leptons;

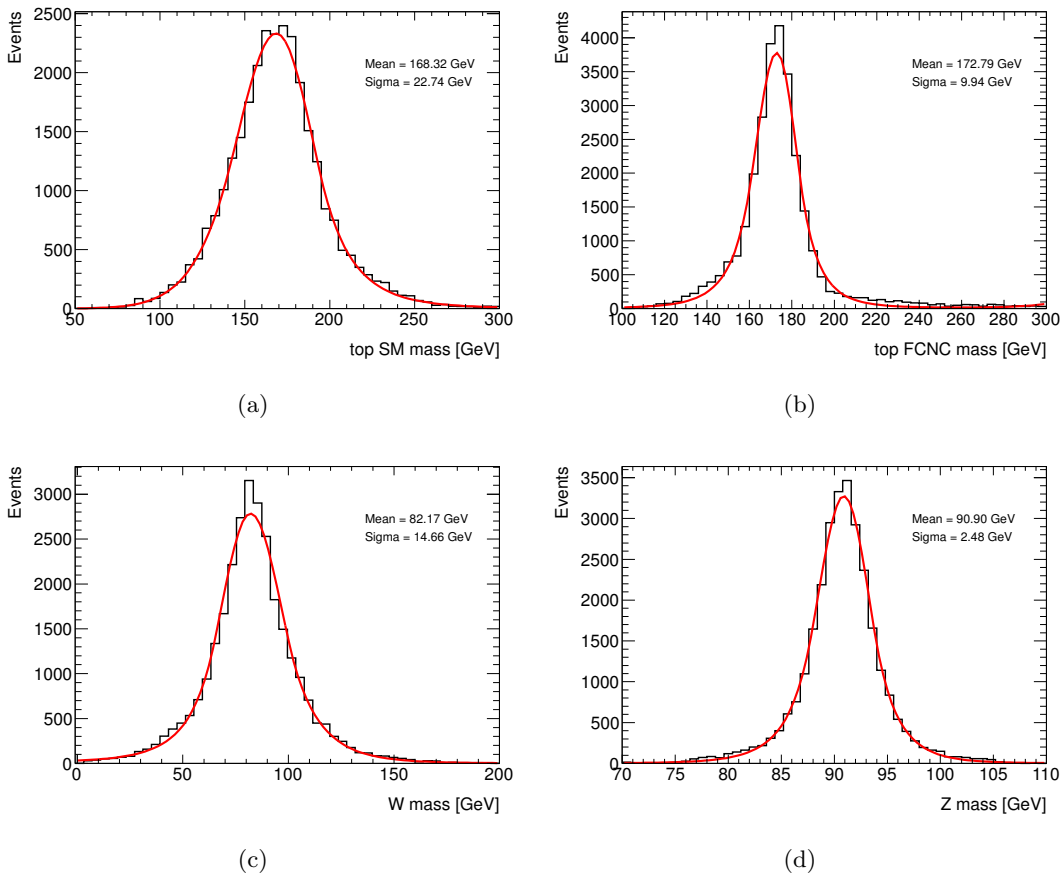

Figure 5.16: Reconstructed masses of the (a) top-quark coming from the SM decay, (b) top-quark coming from the FCNC decay, (c) W boson and (d) Z boson from the object with the minimum ΔR to the true particle generated by PROTOS.

5. the χ^2 is calculated without the Z term for all jet combinations. The lepton is set as the one not assigned to the Z at preselection;

6. exactly one b-tagged jet is required and set to the b-jet. The χ^2 is then calculated without the Z term for all jet combinations (except the b-tagged jet). The lepton is set as the one not assigned to the Z at preselection.

After the reconstruction, if a scenario does not require a b-tagged jet, then the requirement of a single b-tagged jet is applied, to check how the reconstruction efficiency changes. For each jet (and lepton, if that is the case) combination, the χ^2 minimisation gives the most probable value for p_z^ν. From all combinations, the one with the minimum χ^2 is chosen, along with the corresponding p_z^ν value. The jet associated to the top quark with the SM decay is labelled as the b-quark jet. The jet from the top quark with the FCNC decay is denoted as the light (q) quark jet.

For all combinations of χ^2 scenarios, both reconstructed top-quarks are compared with the truth top-quarks generated in the signal sample. The requirement for a match between the reconstructed object and the true particle generated by `PROTOS` is to be within a cone of $\Delta R < 0.4$ of each other.

The sixth χ^2 scenario yields the best efficiencies overall, with $\epsilon_{t_{\text{FCNC}}} = 79.9\%$ and $\epsilon_{t_{\text{SM}}} = 56.3\%$ and, for this reason, it is chosen for the event reconstruction. Tables 5.6 and 5.7 list the reconstructed efficiencies for each object in the events, with and without the b-tag requirement. It can be concluded that requiring a b-tagged jet not only increases the number of times the real b-quark is reconstructed, as expected, but also leads to a higher efficiency on the reconstruction of the light jet and, consequently, on both top-quarks.

As noted in Section 5.1.2.1, the coupling choice does not affect the kinematics of the event and the signal sample used only contains the uZ channel. Nevertheless, the cZ channel would contain more b-tagged jets than the samples used due to the larger c mis-tag rate. To account for this effect, the b-tag requirement of the event selection is relaxed to one or two b-tagged jets. For the case with two b-tagged jets in the event, an additional loop is done to choose the one yielding the lowest χ^2. The impact of this change in the reconstruction efficiencies is within the uncertainty for the chosen scenario.

Table 5.6: Reconstruction efficiencies, with the corresponding statistical uncertainty, for the objects in the event for the cases without the b-tag requirement.

	$\epsilon_{t_{\mathrm{FCNC}}}$ [%]	$\epsilon_{t_{\mathrm{SM}}}$ [%]	ϵ_W [%]	ϵ_Z [%]	ϵ_q [%]	ϵ_b [%]	ϵ_l [%]	ϵ_ν [%]
1	70.1 ± 0.6	39.3 ± 0.4	41.2 ± 0.4	96.4 ± 0.7	67.1 ± 0.6	59.0 ± 0.5	96.9 ± 0.7	25.8 ± 0.4
2	69.7 ± 0.6	39.1 ± 0.4	41.0 ± 0.4	96.4 ± 0.7	66.8 ± 0.6	58.8 ± 0.5	96.9 ± 0.7	25.7 ± 0.4
4	75.0 ± 0.6	41.7 ± 0.4	42.6 ± 0.5	96.9 ± 0.7	71.7 ± 0.6	60.8 ± 0.5	97.4 ± 0.7	27.1 ± 0.4
5	74.4 ± 0.6	41.3 ± 0.4	42.4 ± 0.4	96.4 ± 0.7	71.4 ± 0.6	60.6 ± 0.5	96.9 ± 0.7	27.0 ± 0.4

Table 5.7: Reconstruction efficiencies, with the corresponding statistical uncertainty, for the objects in the event after the b-tag requirement for all cases.

	$\epsilon_{t_{\mathrm{FCNC}}}$ [%]	$\epsilon_{t_{\mathrm{SM}}}$ [%]	ϵ_W [%]	ϵ_Z [%]	ϵ_q [%]	ϵ_b [%]	ϵ_l [%]	ϵ_ν [%]
1	70.1 ± 0.6	39.3 ± 0.4	41.2 ± 0.4	96.4 ± 0.7	67.1 ± 0.6	59.0 ± 0.5	96.9 ± 0.7	25.8 ± 0.4
2	69.7 ± 0.6	39.1 ± 0.4	41.0 ± 0.4	96.4 ± 0.7	66.8 ± 0.6	58.8 ± 0.5	96.9 ± 0.7	25.7 ± 0.4
3	69.6 ± 0.7	56.2 ± 0.6	43.1 ± 0.6	96.6 ± 0.8	69.2 ± 0.7	95.9 ± 0.8	97.0 ± 0.8	28.5 ± 0.5
4	75.0 ± 0.6	41.7 ± 0.4	42.6 ± 0.5	96.9 ± 0.7	71.7 ± 0.6	60.8 ± 0.5	97.4 ± 0.7	27.1 ± 0.4
5	74.4 ± 0.6	41.3 ± 0.4	42.4 ± 0.4	96.4 ± 0.7	71.4 ± 0.6	60.6 ± 0.5	96.9 ± 0.7	27.0 ± 0.4
6	79.9 ± 0.8	56.3 ± 0.6	43.2 ± 0.6	96.6 ± 0.8	78.6 ± 0.7	95.9 ± 0.8	97.0 ± 0.8	28.6 ± 0.5

Concluding, after the lepton requirements, two or three jets (with $p_{\mathrm{T}} > 35$ GeV and $|\eta| < 2.5$) are required, with the presence of one or two b-tagged jets and $E_{\mathrm{T}}^{\mathrm{miss}} > 20$ GeV, to reconstruct the event. Figure 5.19 shows the p_{T} and η distributions of the two leading jets. The p_z^ν is then determined, together with the choice for the light-quark jet and b-quark jet combination, by minimising expression 5.3 without the Z boson term. Figure 5.18 shows the resulting χ^2 after the reconstruction and Figure 5.17 the MV1 weight of the two leading jets and the reconstructed b-quark jet and light quark jet.

For the final selection the event is required to have a $\chi^2 < 6$ ($\chi^2 < 5$ for the fake-lepton estimates with the MC samples). The values for this requirement are the ones that minimise the expected limit as explained in Section 5.6. Figure 5.20 (Figure 5.21) shows the distributions of the third lepton p_{T}, the $E_{\mathrm{T}}^{\mathrm{miss}}$, and the reconstructed masses of the top quarks and the W and Z bosons, after the final selection, for the MM (MC). The number of observed data events, expected background yields and signal efficiency are shown in Tables 5.8 and 5.9, before the χ^2 cut and after the final selection, and the observations agree with both methods for the fake-leptons contribution.

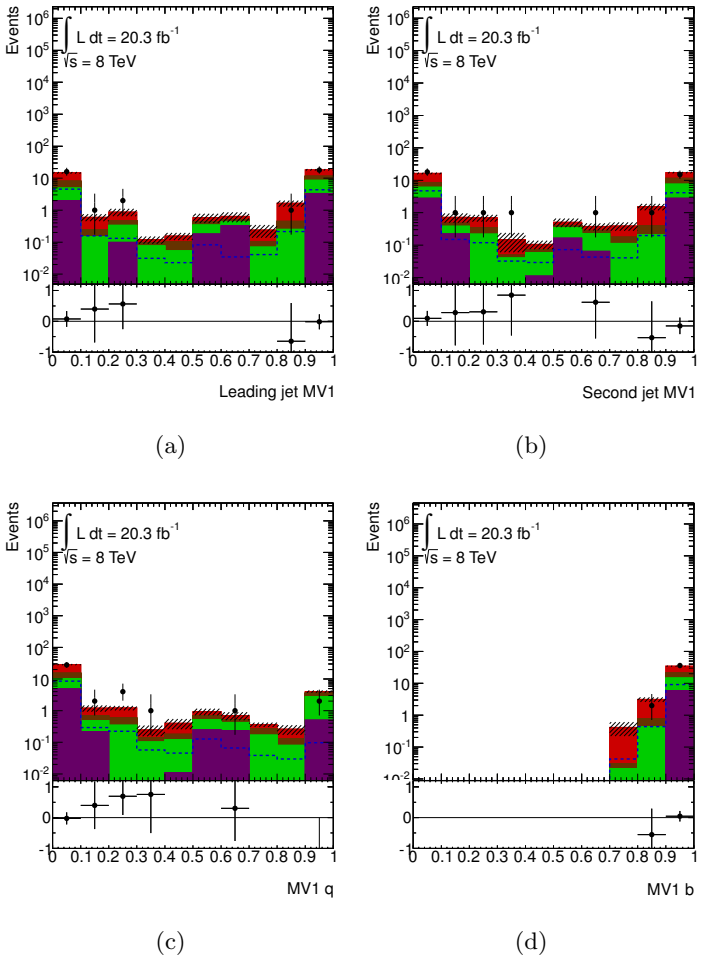

Figure 5.17: Distributions for the SR after the χ^2 reconstruction of the MV1 weight of the (a) leading jet, (b) second jet, (c) light quark jet and (d) b quark jet, using the MM for fake-lepton estimation. The $t\bar{t} \to bWuZ$ distributions are normalised to the observed limit.

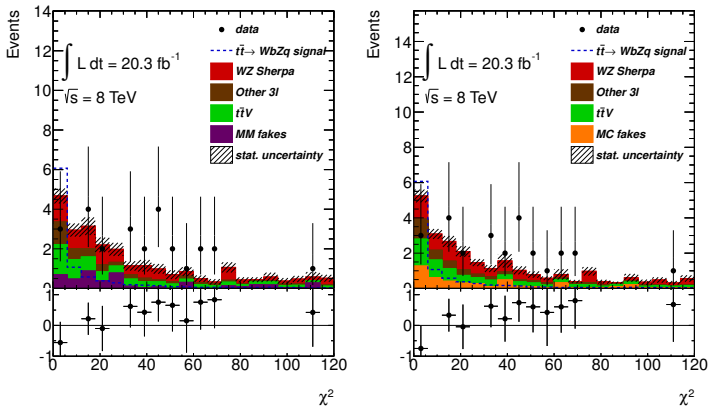

(a) (b)

Figure 5.18: χ^2 distributions for the SR for the fake-lepton estimation with (a) MM and (b) MC. The $t\bar{t} \rightarrow bWcZ$ distributions are normalised to the observed limit.

Table 5.8: Expected number of background events, number of selected data events and signal efficiency (normalised to all decays of the W and Z bosons), before the χ^2 cut for the MM and MC. Normalisations are applied as described in Section 5.4, and `SHERPA` samples are used for the dibosons and `ALPGEN` + `PYTHIA` for Z+jets backgrounds. The fake-lepton component in the MC is the sum of the yields of $Z\gamma$+jets ($1.1 \pm 0.6 \pm 2.7$), WW ($0.009 \pm 0.010 \pm 0.007$), $t\bar{t}$ ($1.3 \pm 0.3 \pm 0.8$) and single top ($0.05 \pm 0.04 \pm 0.16$) samples. Also, for these samples, a loose selection is performed to improve statistics, and then multiplied by the scale factors in Table 5.16 to account for the probability of loose leptons to enter SR. The first uncertainty is the statistical one, associated with the number of events in the samples, the second one is systematic and is described in Section 5.5.

Sample	MM	MC
WZ	$15.9 \pm 1.0 \pm 3.3$	
$t\bar{t}V$	$9.2 \pm 0.2 \pm 2.8$	
Fake leptons	$5.9 \pm 1.0 \pm 3.6$	$6.3 \pm 0.7 \pm 3.0$
tZ	$5.6 \pm 0.2 \pm 2.8$	
ZZ	$0.8 \pm 0.4 \pm 2.0$	
Higgs	$0.48 \pm 0.04 \pm 0.10$	
Tribosons	$0.019 \pm 0.005 \pm 0.004$	
Total background	$37.9 \pm 1.5 \pm 6.6$	$38.0 \pm 0.7 \pm 3.0$
Data	38	
Signal efficiency [$\times 10^{-3}$]	$1.38 \pm 0.02 \pm 0.12$	

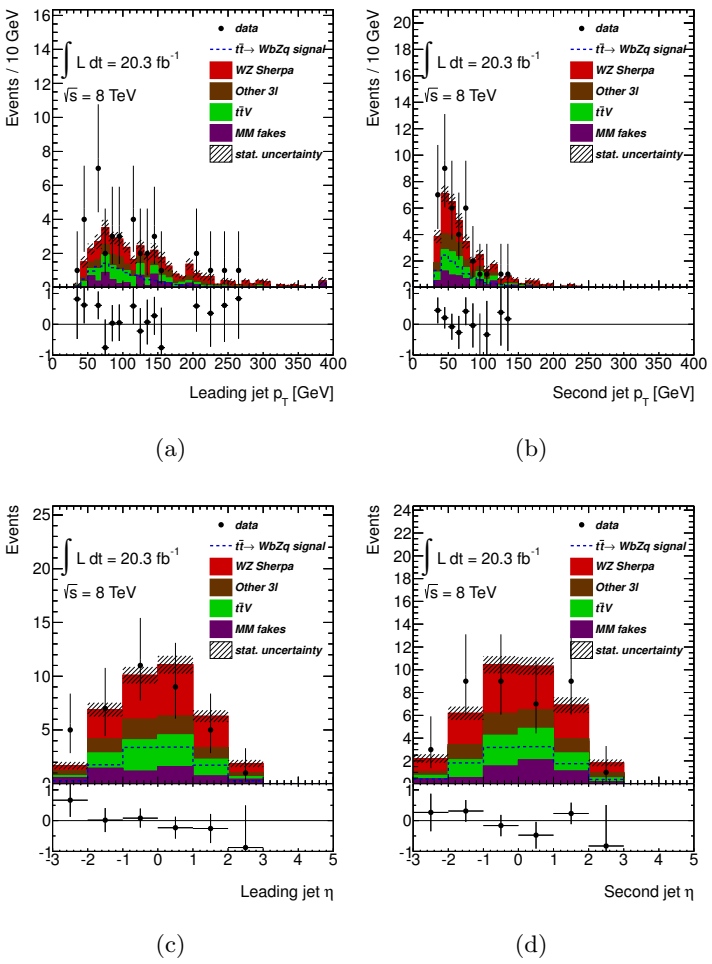

Figure 5.19: Jet distributions for the SR after the reconstruction for (a) p_{T} of the leading jet, (b) p_{T} of the second jet, (c) η of the leading jet and (d) η of the second jet. The $t\bar{t} \to bWcZ$ distributions are normalised to the observed limit. The fake-lepton estimation is from MM.

Table 5.9: Expected number of background events, number of selected data events and signal efficiency (normalised to all decays of the W and Z bosons), after the final selection for the MM and MC. Normalisations are applied as described in Section 5.4, and SHERPA samples are used for the dibosons and ALPGEN + PYTHIA for Z+jets backgrounds. The fake-lepton component in the MC is the sum of the yields of Z+jets ($0.8 \pm 0.2 \pm 0.3$), $t\bar{t}$ ($0.3 \pm 0.1 \pm 0.2$) and single top ($0.04 \pm 0.03 \pm 0.02$) samples. Also, for these samples, a loose selection is performed to improve statistics, and then multiplied by the scale factors in Table 5.16 to account for the probability of loose leptons to enter SR. The first uncertainty is the statistical one, associated with the number of events in the samples, the second one is systematic and is described in Section 5.5.

Sample	MM	MC
WZ	$1.3 \pm 0.2 \pm 0.6$	$1.1 \pm 0.2 \pm 0.5$
$t\bar{t}V$	$1.5 \pm 0.1 \pm 0.5$	$1.4 \pm 0.1 \pm 0.5$
tZ	$1.0 \pm 0.1 \pm 0.5$	$0.9 \pm 0.1 \pm 0.5$
Fake leptons	$0.7 \pm 0.3 \pm 0.4$	$1.1 \pm 0.2 \pm 0.4$
ZZ	$0.06 \pm 0.06 \pm 0.13$	$0.06 \pm 0.06 \pm 0.13$
Higgs	$0.08 \pm 0.02 \pm 0.02$	$0.06 \pm 0.01 \pm 0.02$
Tribosons	$0.0011 \pm 0.0011 \pm 0.0002$	$0.011 \pm 0.0011 \pm 0.0002$
Total background	$4.7 \pm 0.4 \pm 1.0$	$4.6 \pm 0.4 \pm 0.9$
Data	3	2
Signal efficiency [$\times 10^{-4}$]	$7.8 \pm 0.1 \pm 0.8$	$7.4 \pm 0.1 \pm 0.8$

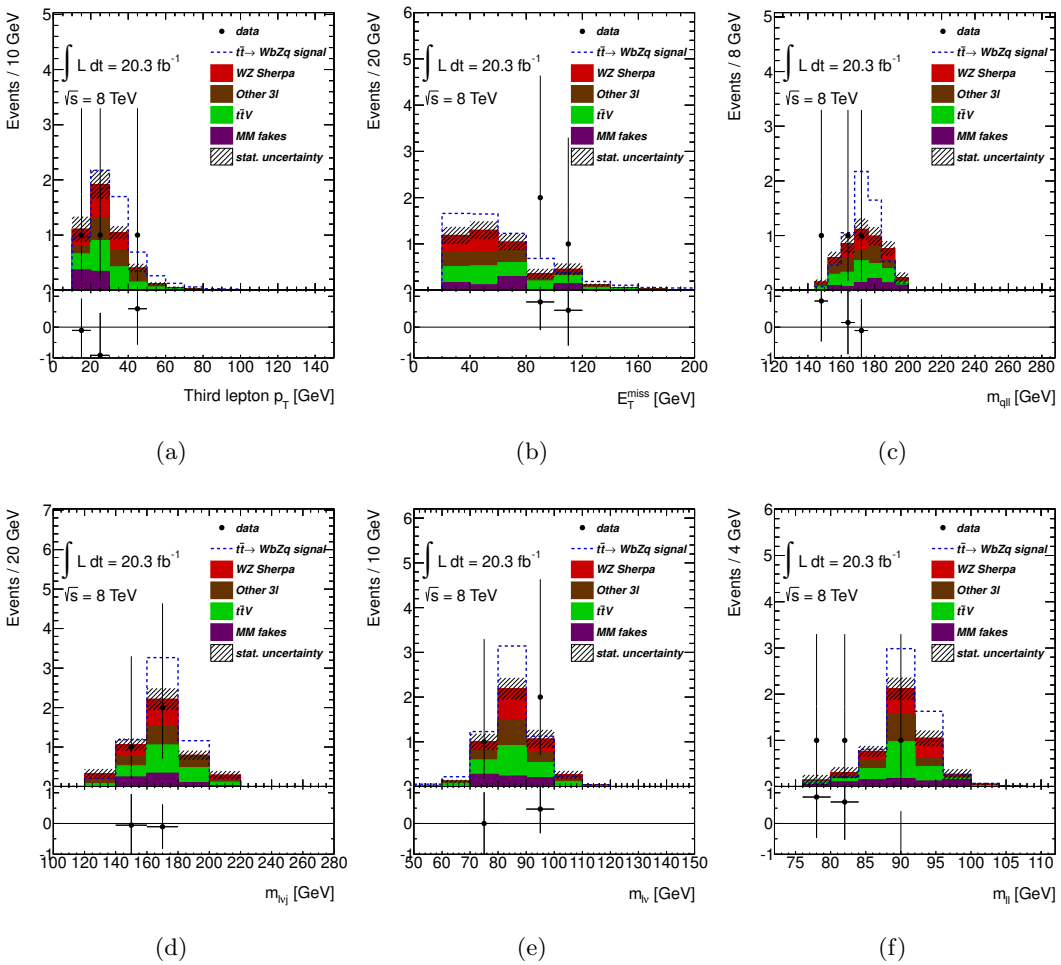

Figure 5.20: Expected and observed distributions for the SR after the final selection, for (a) p_{T} of the third lepton, (b) $E_{\mathrm{T}}^{\mathrm{miss}}$ and reconstructed masses of the (c) top quark from the FCNC decay, (d) top quark from the SM decay, (e) W boson and (f) Z boson with fake-lepton estimation from MM. The $t\bar{t} \to bWcZ$ distributions are normalised to the observed limit.

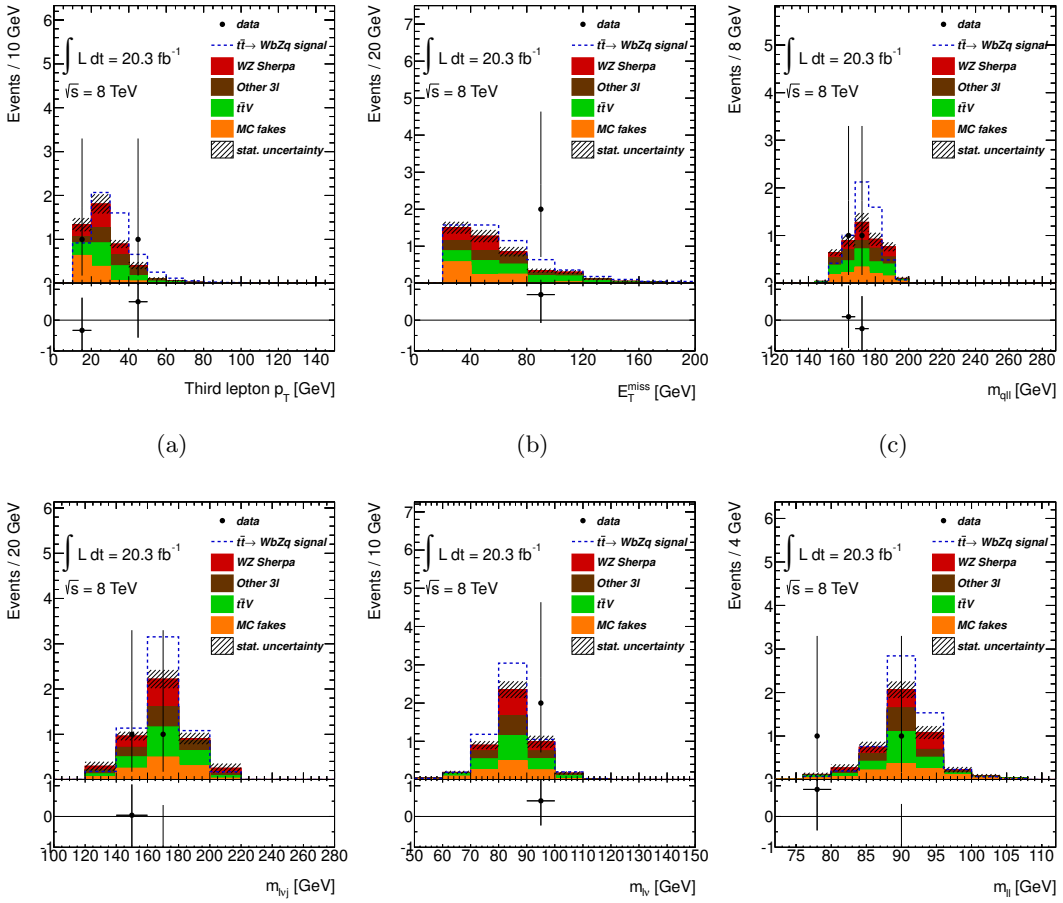

Figure 5.21: Expected and observed distributions for the SR, after the final selection for (a) p_{T} of the third lepton, (b) $E_{\mathrm{T}}^{\mathrm{miss}}$ and reconstructed masses of the (c) top quark from the FCNC decay, (d) top quark from the SM decay, (e) W boson and (f) Z boson, with fake-lepton estimation from MC. The $t\bar{t} \to bWcZ$ distributions are normalised to the observed limit.

5.4 Background evaluation

The backgrounds considered are the ones that also comprise three reconstructed leptons in the final state, which can be all three real leptons or including jets mis-reconstructed as leptons. In this section, the methods for estimating these backgrounds as well as a comparison between several available generators are described.

5.4.1 Backgrounds with three real leptons

Backgrounds that can produce three real leptons in the final states come primarily from dibosons (WZ and ZZ[1]), $t\bar{t}V(W, \mathrm{j})$, $t\bar{t}H$, $tZ(W)$ and triboson processes. These backgrounds are evaluated using MC samples as mentioned in Section 5.1.2.2. Three CRs are defined to check the agreement between data and MC of the ZZ, WZ and $t\bar{t}Z$ backgrounds. No scaling factors are derived from these CRs, however they are used to estimate the background modelling uncertainties described in Section 5.5. Additionally, three samples for diboson production are compared: `SHERPA`, `ALPGEN` and `HERWIG`.

The tZ contribution to the total background is expected to be smaller than the one from $t\bar{t}Z$ events [190] and, due to the similarity between this background and the signal, any definition for a tZ CR would have large signal contribution. For these reasons no CR is defined for the tZ background.

5.4.1.1 ZZ control region

Choosing a CR with two pairs of leptons with same flavour, opposite charge and $|m_Z - m_{\ell\ell}| < 15$ GeV, it is possible to select almost only ZZ events (no MC $Z\gamma$ events are selected). Table 5.10 shows the yields in this CR for each background for the three diboson generators. From Figures 5.22 (for the p_{T} of leading lepton), 5.23 (for the jet and b-jet multiplicity) and 5.24 (for the reconstructed mass of the ZZ system) it can be seen that `HERWIG` and `SHERPA` agree fairly well with data (taking into account both statistical and systematic uncertainties) as can be seen in Table 5.10. The `ALPGEN` samples do not agree in the number of events neither do they describe well the shape

[1]Events from ZZ decays can enter the SR in several ways: the dominant modes are four-lepton decays with one lepton not reconstructed, giving apparent $E_{\mathrm{T}}^{\mathrm{miss}}$, and $\tau^+\tau^-$ decays with one τ decaying to e or μ and two neutrinos, and the other tau decaying hadronically.

Table 5.10: Event yields in the ZZ CR for the three generators used: ALPGEN, HERWIG and SHERPA. The first uncertainty is the statistical one, associated with the number of events in the samples, the second one is systematic and is described in Section 5.5.

	ALPGEN	HERWIG	SHERPA
ZZ	$189 \pm 3 \pm 10$	$85 \pm 4 \pm 5$	$87 \pm 4 \pm 5$
$t\bar{t}\ V(W, \mathrm{j})$	$0.26 \pm 0.04 \pm 0.08$		
Tribosons	$0.125 \pm 0.010 \pm 0.011$		
Higgs	$0.07 \pm 0.03 \pm 0.02$		
$tZ(W)$	$0.025 \pm 0.005 \pm 0.014$		
Total background	$190 \pm 3 \pm 10$	$86 \pm 4 \pm 5$	$88 \pm 4 \pm 5$
Data	95		
Signal efficiency [$\times 10^{-8}$]	$5.6 \pm 4.3 \pm 0.8$		

of the distributions. The SHERPA sample is chosen because it has the best agreement with data in this CR.

5.4.1.2 WZ control region

To study the WZ background the following CR is tested: one pair of leptons with the same flavour, opposite charge and $|m_Z - m_{\ell\ell}| < 15$ GeV, at least one jet with $p_{\mathrm{T}} > 35$ GeV and no b-tagged jets with $p_{\mathrm{T}} > 35$ GeV. This selection is to distinguish it from the SR. Additionally, a requirement in the transverse W boson mass, $m_T^W > 50$ GeV, is performed to ensure the purity of the WZ samples. Table 5.11 shows the yields in this CR. When comparing the three generators, HERWIG does not describe well the normalisation as the other two do. ALPGEN describes reasonably well the normalisation and shape of the distributions, with the exception of the reconstructed mass of the Z boson. Of all generators, SHERPA seems to have the best description of both shape and yield and, for this reason, is chosen to be the generator used in this analysis. Figures 5.25 and 5.26 show the leading lepton p_{T} and reconstructed mass of the Z boson, respectively. Figures 5.27 and 5.28 show the reconstructed mass of the Z boson for the SR after the lepton requirements and after the reconstruction, respectively.

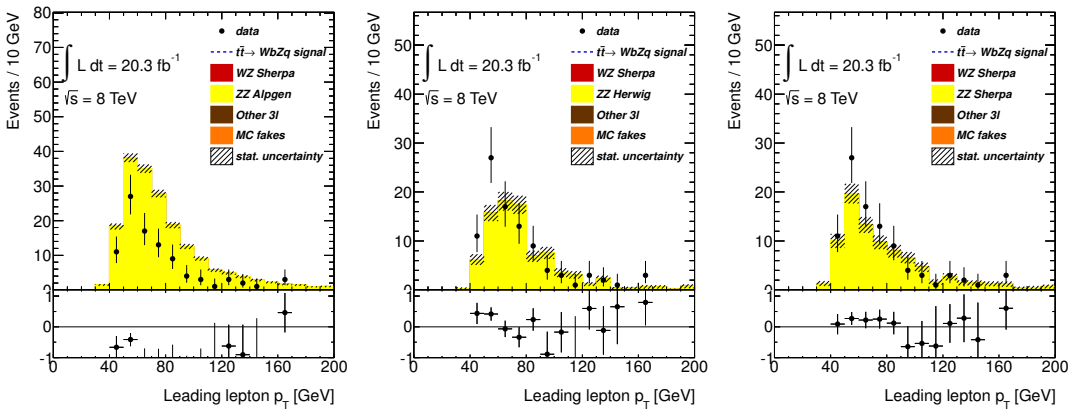

(a) (b) (c)

Figure 5.22: Expected and observed distributions in the ZZ CR, for the leading lepton p_{T} with (a) ALPGEN, (b) HERWIG and (c) SHERPA samples.

Table 5.11: Event yields in the WZ CR for the three generators used: ALPGEN, HERWIG and SHERPA. The first uncertainty is the statistical one, associated with the number of events in the samples, the second one is systematic and is described in Section 5.5.

	ALPGEN	HERWIG	SHERPA
WZ	$393 \pm 6 \pm 19$	$163 \pm 6 \pm 11$	$333 \pm 5 \pm 17$
ZZ		$35 \pm 3 \pm 6$	
$Z\gamma$+jets		$10 \pm 3 \pm 3$	
tZ		$3.9 \pm 0.2 \pm 2.0$	
$t\bar{t}V$		$3.7 \pm 0.2 \pm 1.3$	
Z+jets		$3.3 \pm 0.9 \pm 3.4$	
$t\bar{t}$ SM		$1.8 \pm 0.9 \pm 2.8$	
Higgs		$1.01 \pm 0.09 \pm 0.21$	
Tribosons		$0.94 \pm 0.04 \pm 0.34$	
WW		$0.035 \pm 0.025 \pm 0.002$	
Total background	$452 \pm 7 \pm 21$	$223 \pm 7 \pm 14$	$392 \pm 7 \pm 19$
Data		405	
Signal efficiency $[\times 10^{-4}]$		$9.8 \pm 0.1 \pm 1.0$	

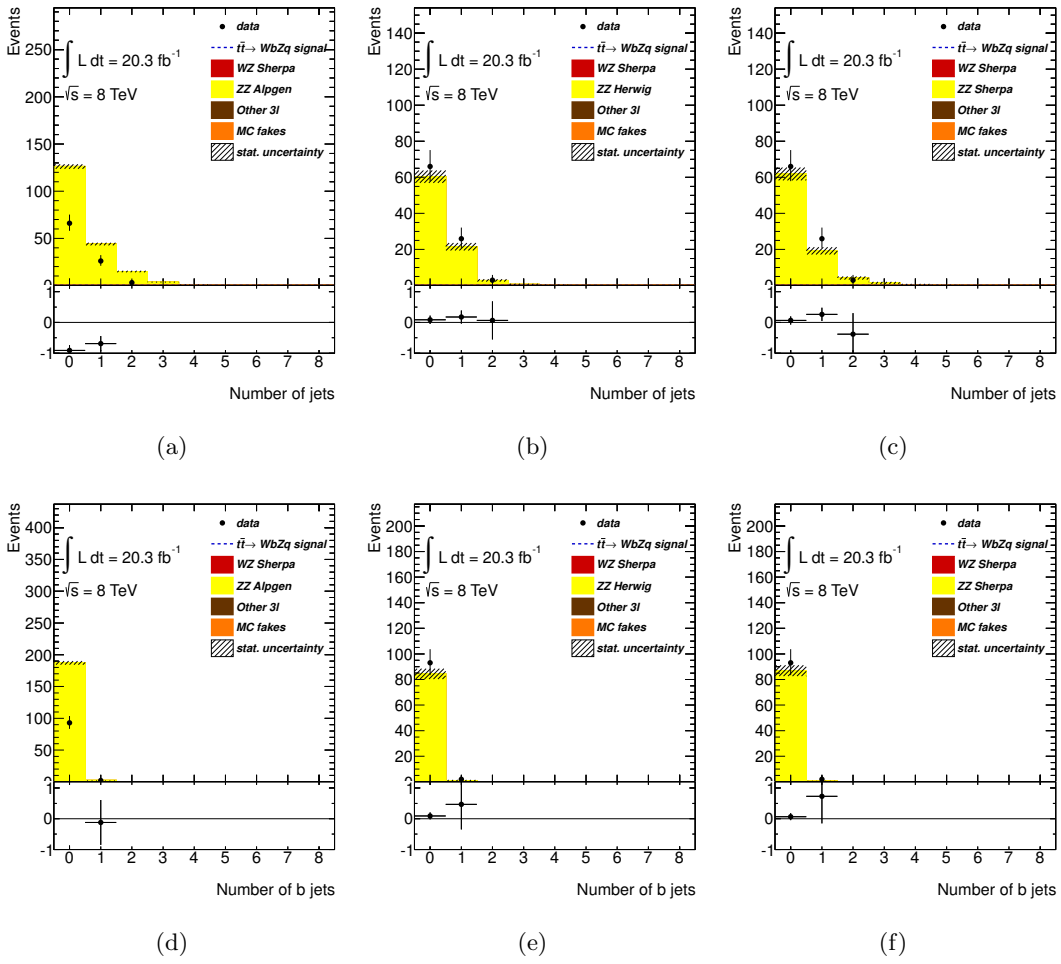

Figure 5.23: Expected and observed distributions in the ZZ CR, for jet multiplicity with (a) `ALPGEN`, (b) `HERWIG` and (c) `SHERPA` samples and for b-jet multiplicity with (d) `ALPGEN`, (e) `HERWIG` and (f) `SHERPA` samples.

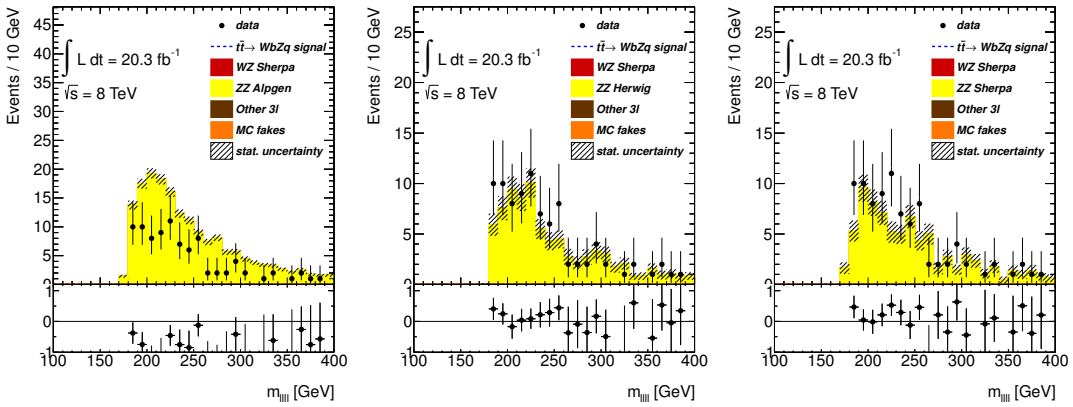

(a) (b) (c)

Figure 5.24: Expected and observed distributions in the ZZ CR, for reconstructed masses of the ZZ system with (a) `ALPGEN`, (b) `HERWIG` and (c) `SHERPA` samples.

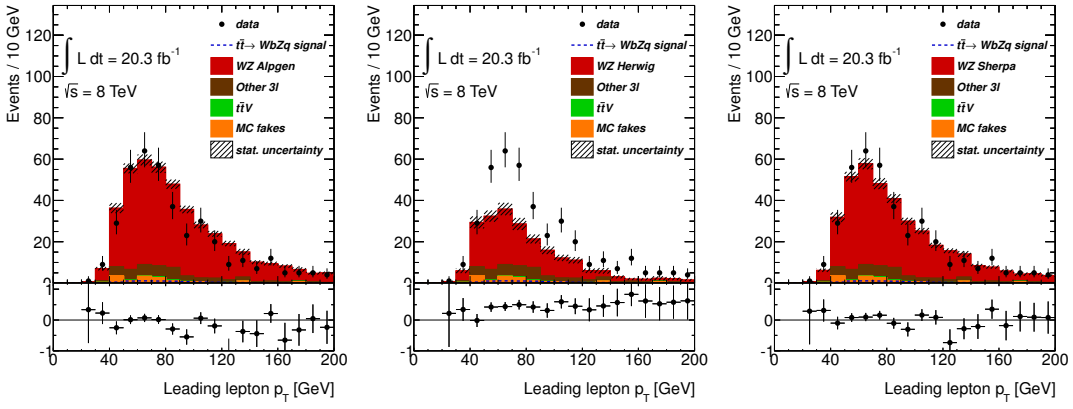

(a) (b) (c)

Figure 5.25: Expected and observed distributions in the WZ CR for the leading lepton p_{T} with (a) `ALPGEN`, (b) `HERWIG` and (c) `SHERPA` samples.

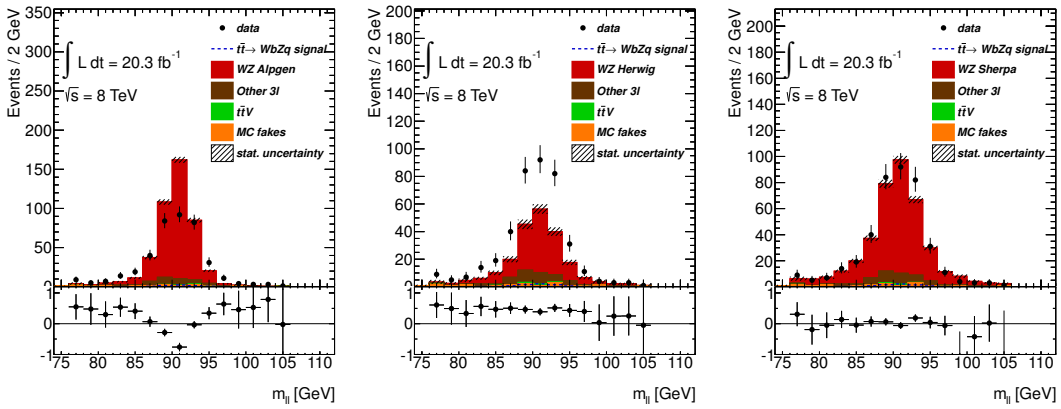

(a) (b) (c)

Figure 5.26: Expected and observed distributions in the WZ CR for reconstructed mass of the Z boson with (a) `ALPGEN`, (b) `HERWIG` and (c) `SHERPA` samples.

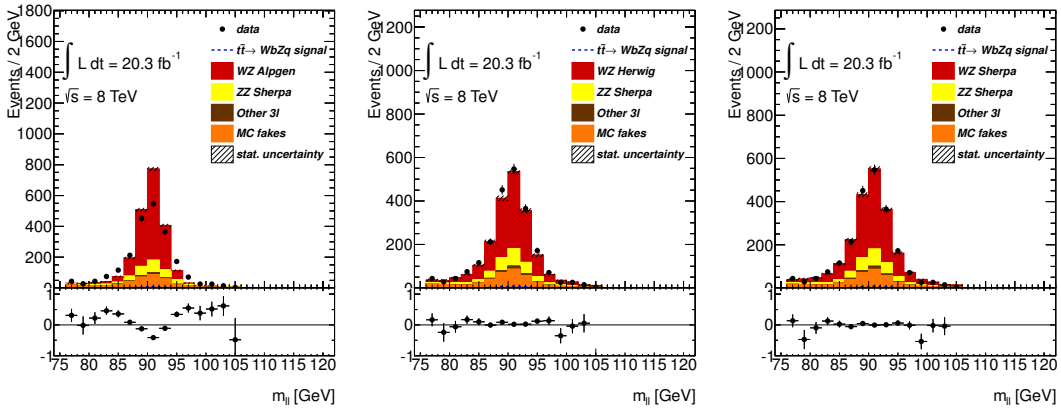

(a) (b) (c)

Figure 5.27: Expected and observed distributions for the SR after requiring exactly three leptons, with two of them of the same flavour, opposite charge and a reconstructed mass within 15 GeV of the Z boson mass, for the reconstructed mass of the Z boson. Left, center and right distributions are obtained with the diboson samples generated with `ALPGEN`, `HERWIG` and `SHERPA` respectively.

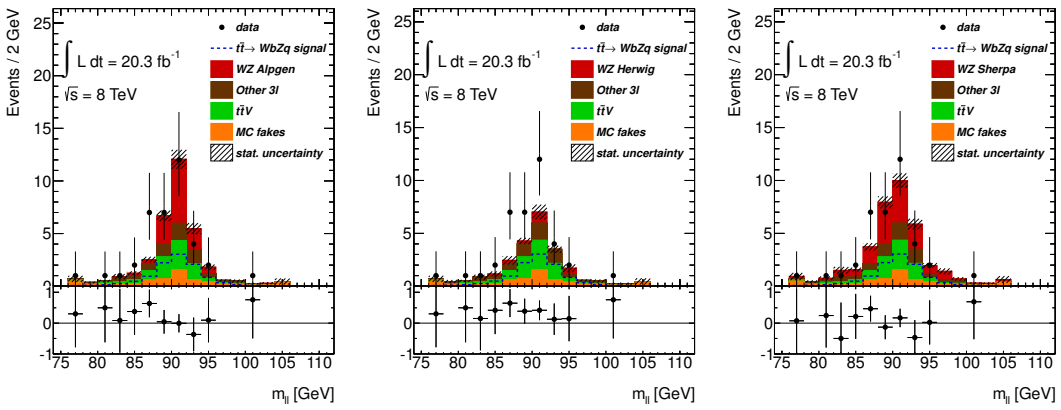

(a) (b) (c)

Figure 5.28: Expected and observed distributions for the SR after the reconstruction for the reconstructed mass of the Z boson. Left, center and right distributions are obtained with the diboson samples generated with `ALPGEN`, `HERWIG` and `SHERPA` respectively.

5.4.1.3 $t\bar{t}Z$ control region

Another significant background for the analysis comes from $t\bar{t}Z$ production and, for this reason, it is important to control the corresponding MC. The selection consists of requiring three or more leptons with one pair of leptons with the same flavour, opposite charge and $|m_Z - m_{\ell\ell}| < 15$ GeV, at least two jets with $p_{\mathrm{T}} > 25$ GeV and at least two b-tagged jets if there are three leptons in the event or at least one b-tagged jet if there are four or more leptons in the event. Table 5.12 shows the yields in this CR and the background agrees very well with data within the given uncertainty. Figure 5.29 shows the p_{T} distribution of the two leading leptons.

5.4.2 SM backgrounds with fake leptons

The background yields that contain at least one fake lepton are estimated from data using the "Matrix Method" and MC samples with the latter one serving as a crosscheck. These two methods are described below.

5.4.2.1 Matrix Method method based estimation

The so called matrix method is based on selecting two orthogonal sets of events. One with the "tight" selection requirement and another with the looser selection described

Table 5.12: Event yields in the $t\bar{t}Z$ CR. The fake-lepton contributions in the MC come from Z+jets ($0.5 \pm 0.2 \pm 0.2$) and $t\bar{t}$ SM ($0.3 \pm 0.2 \pm 0.1$) samples. The first uncertainty is the statistical one, associated with the number of events in the samples, the second one is systematic and is described in Section 5.5.

Sample	MC
$t\bar{t}V$	$8.3 \pm 0.2 \pm 2.7$
tZ	$2.0 \pm 0.1 \pm 1.0$
WZ	$1.8 \pm 0.3 \pm 0.4$
Fake leptons	$0.8 \pm 0.3 \pm 0.3$
ZZ	$0.6 \pm 0.3 \pm 0.6$
Higgs	$0.38 \pm 0.04 \pm 0.09$
Tribosons	$0.004 \pm 0.003 \pm 0.002$
Total background	$13.9 \pm 0.6 \pm 3.0$
Data	12
Signal efficiency $[\times 10^{-4}]$	$3.9 \pm 0.1 \pm 0.6$

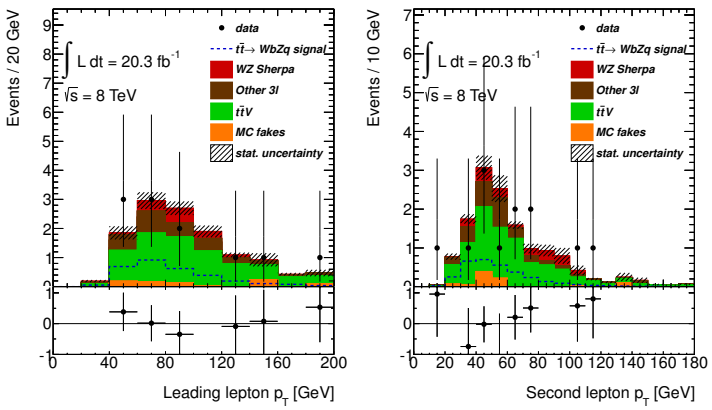

(a) (b)

Figure 5.29: Expected and observed distributions in the $t\bar{t}Z$ CR, for (a) p_{T} of the leading lepton and (b) p_{T} of the second lepton.

in Section 5.2 but without meeting tight selection requirements. For the single lepton case, the number of events which contain one tight lepton or, in other words, a loose lepton that passes the tight criteria, can be written as:

$$N_{\mathrm{T}} = \epsilon_{\mathrm{R}} N_{\mathrm{R}}^{\mathrm{loose}} + \epsilon_{\mathrm{F}} N_{\mathrm{F}}^{\mathrm{loose}}, \tag{5.4}$$

where $N_{\mathrm{R}}^{\mathrm{loose}}$ ($N_{\mathrm{F}}^{\mathrm{loose}}$) are the number of events containing real (fake) leptons that pass the loose lepton requirements, and ϵ_{R} (ϵ_{F}) the efficiency of a real (fake) loose lepton to pass the tight selection. These efficiencies are then defined as:

$$\epsilon_{\mathrm{R}} = \frac{N_{\mathrm{R}}^{\mathrm{tight}}}{N_{\mathrm{R}}^{\mathrm{loose}}} \quad \text{and } \epsilon_{\mathrm{F}} = \frac{N_{\mathrm{F}}^{\mathrm{tight}}}{N_{\mathrm{F}}^{\mathrm{loose}}}, \tag{5.5}$$

where $N_{\mathrm{R}}^{\mathrm{tight}}$ ($N_{\mathrm{F}}^{\mathrm{tight}}$) are the number of events containing real (fake) leptons that pass the tight lepton requirement. The number of events in which a loose lepton does not pass the tight lepton requirements is then the difference between the total number of loose leptons and tight leptons, and can be written in terms of real and fake leptons as:

$$N_{\mathrm{L}} = (1 - \epsilon_{\mathrm{R}}) N_{\mathrm{R}}^{\mathrm{loose}} + (1 - \epsilon_{\mathrm{F}}) N_{\mathrm{F}}^{\mathrm{loose}}. \tag{5.6}$$

Having the number of events passing the tight requirements and the number of events not passing the tight requirements, it is possible to write the following expression:

$$\begin{pmatrix} N_{\mathrm{T}} \\ N_{\mathrm{L}} \end{pmatrix} = \begin{pmatrix} \epsilon_{\mathrm{R}} & \epsilon_{\mathrm{F}} \\ 1 - \epsilon_{\mathrm{R}} & 1 - \epsilon_{\mathrm{F}} \end{pmatrix} \begin{pmatrix} N_{\mathrm{R}} \\ N_{\mathrm{F}} \end{pmatrix}. \tag{5.7}$$

Inverting this expression will yield the corresponding relation for the number of real (fake) leptons in terms of N_{T} and N_{L} for loose leptons:

$$\begin{pmatrix} N_{\mathrm{R}} \\ N_{\mathrm{F}} \end{pmatrix} = \frac{1}{\epsilon_{\mathrm{R}} - \epsilon_{\mathrm{F}}} \begin{pmatrix} 1 - \epsilon_{\mathrm{F}} & -\epsilon_{\mathrm{F}} \\ \epsilon_{\mathrm{R}} - 1 & \epsilon_{\mathrm{R}} \end{pmatrix} \begin{pmatrix} N_{\mathrm{T}} \\ N_{\mathrm{L}} \end{pmatrix}. \tag{5.8}$$

Since $N_{\mathrm{F}}^{\mathrm{tight}} = \epsilon_{\mathrm{F}} N_{\mathrm{F}}^{\mathrm{loose}}$, the relation for the number of fake tight leptons is:

$$N_{\mathrm{F}}^{\mathrm{tight}} = \frac{\epsilon_{\mathrm{F}}}{\epsilon_{\mathrm{R}} - \epsilon_{\mathrm{F}}} \left[(\epsilon_{\mathrm{R}} - 1) N_{\mathrm{T}} + \epsilon_{\mathrm{R}} N_{\mathrm{L}} \right]. \tag{5.9}$$

This method can be extrapolated from the single lepton case to the three lepton topology:

$$\begin{pmatrix} N_{\mathrm{TTT}} \\ N_{\mathrm{TTL}} \\ N_{\mathrm{TLT}} \\ N_{\mathrm{TLL}} \\ N_{\mathrm{LTT}} \\ N_{\mathrm{LTL}} \\ N_{\mathrm{LLT}} \\ N_{\mathrm{LLL}} \end{pmatrix} = M \begin{pmatrix} N_{\mathrm{RRR}} \\ N_{\mathrm{RRF}} \\ N_{\mathrm{RFR}} \\ N_{\mathrm{RFF}} \\ N_{\mathrm{FRR}} \\ N_{\mathrm{FRF}} \\ N_{\mathrm{FFR}} \\ N_{\mathrm{FFF}} \end{pmatrix} \tag{5.10}$$

In this case the corresponding matrix is the following:

$$M = \begin{pmatrix}
\epsilon_{\mathrm{R}_1}\epsilon_{\mathrm{R}_2}\epsilon_{\mathrm{R}_3} & \epsilon_{\mathrm{R}_1}\epsilon_{\mathrm{R}_2}\epsilon_{\mathrm{F}_3} & \epsilon_{\mathrm{R}_1}\epsilon_{\mathrm{F}_2}\epsilon_{\mathrm{R}_3} \\
\epsilon_{\mathrm{R}_1}\epsilon_{\mathrm{R}_2}(1-\epsilon_{\mathrm{R}_3}) & \epsilon_{\mathrm{R}_1}\epsilon_{\mathrm{R}_2}(1-\epsilon_{\mathrm{F}_3}) & \epsilon_{\mathrm{R}_1}\epsilon_{\mathrm{F}_2}(1-\epsilon_{\mathrm{R}_3}) \\
\epsilon_{\mathrm{R}_1}(1-\epsilon_{\mathrm{R}_2})\epsilon_{\mathrm{R}_3} & \epsilon_{\mathrm{R}_1}(1-\epsilon_{\mathrm{R}_2})\epsilon_{\mathrm{F}_3} & \epsilon_{\mathrm{R}_1}(1-\epsilon_{\mathrm{F}_2})\epsilon_{\mathrm{R}_3} \\
\epsilon_{\mathrm{R}_1}(1-\epsilon_{\mathrm{R}_2})(1-\epsilon_{\mathrm{R}_3}) & \epsilon_{\mathrm{R}_1}(1-\epsilon_{\mathrm{R}_2})(1-\epsilon_{\mathrm{F}_3}) & \epsilon_{\mathrm{R}_1}(1-\epsilon_{\mathrm{F}_2})(1-\epsilon_{\mathrm{R}_3}) \\
(1-\epsilon_{\mathrm{R}_1})\epsilon_{\mathrm{R}_2}\epsilon_{\mathrm{R}_3} & (1-\epsilon_{\mathrm{R}_1})\epsilon_{\mathrm{R}_2}\epsilon_{\mathrm{F}_3} & (1-\epsilon_{\mathrm{R}_1})\epsilon_{\mathrm{F}_2}\epsilon_{\mathrm{R}_3} \\
(1-\epsilon_{\mathrm{R}_1})\epsilon_{\mathrm{R}_2}(1-\epsilon_{\mathrm{R}_3}) & (1-\epsilon_{\mathrm{R}_1})\epsilon_{\mathrm{R}_2}(1-\epsilon_{\mathrm{F}_3}) & (1-\epsilon_{\mathrm{R}_1})\epsilon_{\mathrm{F}_2}(1-\epsilon_{\mathrm{R}_3}) \\
(1-\epsilon_{\mathrm{R}_1})(1-\epsilon_{\mathrm{R}_2})\epsilon_{\mathrm{R}_3} & (1-\epsilon_{\mathrm{R}_1})(1-\epsilon_{\mathrm{R}_2})\epsilon_{\mathrm{F}_3} & (1-\epsilon_{\mathrm{R}_1})(1-\epsilon_{\mathrm{F}_2})\epsilon_{\mathrm{R}_3} \\
(1-\epsilon_{\mathrm{R}_1})(1-\epsilon_{\mathrm{R}_2})(1-\epsilon_{\mathrm{R}_3}) & (1-\epsilon_{\mathrm{R}_1})(1-\epsilon_{\mathrm{R}_2})(1-\epsilon_{\mathrm{F}_3}) & (1-\epsilon_{\mathrm{R}_1})(1-\epsilon_{\mathrm{F}_2})(1-\epsilon_{\mathrm{R}_3})
\end{pmatrix}$$

$$\begin{pmatrix}
\epsilon_{\mathrm{R}_1}\epsilon_{\mathrm{F}_2}\epsilon_{\mathrm{F}_3} & \epsilon_{\mathrm{F}_1}\epsilon_{\mathrm{R}_2}\epsilon_{\mathrm{R}_3} & \epsilon_{\mathrm{F}_1}\epsilon_{\mathrm{R}_2}\epsilon_{\mathrm{F}_3} \\
\epsilon_{\mathrm{R}_1}\epsilon_{\mathrm{F}_2}(1-\epsilon_{\mathrm{F}_3}) & \epsilon_{\mathrm{F}_1}\epsilon_{\mathrm{R}_2}(1-\epsilon_{\mathrm{R}_3}) & \epsilon_{\mathrm{F}_1}\epsilon_{\mathrm{R}_2}(1-\epsilon_{\mathrm{F}_3}) \\
\epsilon_{\mathrm{R}_1}(1-\epsilon_{\mathrm{F}_2})\epsilon_{\mathrm{F}_3} & \epsilon_{\mathrm{F}_1}(1-\epsilon_{\mathrm{R}_2})\epsilon_{\mathrm{R}_3} & \epsilon_{\mathrm{F}_1}(1-\epsilon_{\mathrm{R}_2})\epsilon_{\mathrm{F}_3} \\
\epsilon_{\mathrm{R}_1}(1-\epsilon_{\mathrm{F}_2})(1-\epsilon_{\mathrm{F}_3}) & \epsilon_{\mathrm{F}_1}(1-\epsilon_{\mathrm{R}_2})(1-\epsilon_{\mathrm{R}_3}) & \epsilon_{\mathrm{F}_1}(1-\epsilon_{\mathrm{R}_2})(1-\epsilon_{\mathrm{F}_3}) \\
(1-\epsilon_{\mathrm{R}_1})\epsilon_{\mathrm{F}_2}\epsilon_{\mathrm{F}_3} & (1-\epsilon_{\mathrm{F}_1})\epsilon_{\mathrm{R}_2}\epsilon_{\mathrm{R}_3} & (1-\epsilon_{\mathrm{F}_1})\epsilon_{\mathrm{R}_2}\epsilon_{\mathrm{F}_3} \\
(1-\epsilon_{\mathrm{R}_1})\epsilon_{\mathrm{F}_2}(1-\epsilon_{\mathrm{F}_3}) & (1-\epsilon_{\mathrm{F}_1})\epsilon_{\mathrm{R}_2}(1-\epsilon_{\mathrm{R}_3}) & (1-\epsilon_{\mathrm{F}_1})\epsilon_{\mathrm{R}_2}(1-\epsilon_{\mathrm{F}_3}) \\
(1-\epsilon_{\mathrm{R}_1})(1-\epsilon_{\mathrm{F}_2})\epsilon_{\mathrm{F}_3} & (1-\epsilon_{\mathrm{F}_1})(1-\epsilon_{\mathrm{R}_2})\epsilon_{\mathrm{R}_3} & (1-\epsilon_{\mathrm{F}_1})(1-\epsilon_{\mathrm{R}_2})\epsilon_{\mathrm{F}_3} \\
(1-\epsilon_{\mathrm{R}_1})(1-\epsilon_{\mathrm{F}_2})(1-\epsilon_{\mathrm{F}_3}) & (1-\epsilon_{\mathrm{F}_1})(1-\epsilon_{\mathrm{R}_2})(1-\epsilon_{\mathrm{R}_3}) & (1-\epsilon_{\mathrm{F}_1})(1-\epsilon_{\mathrm{R}_2})(1-\epsilon_{\mathrm{F}_3})
\end{pmatrix}$$

$$\begin{pmatrix}
\epsilon_{\mathrm{F}_1}\epsilon_{\mathrm{F}_2}\epsilon_{\mathrm{R}_3} & \epsilon_{\mathrm{F}_1}\epsilon_{\mathrm{F}_2}\epsilon_{\mathrm{F}_3} \\
\epsilon_{\mathrm{F}_1}\epsilon_{\mathrm{F}_2}(1-\epsilon_{\mathrm{R}_3}) & \epsilon_{\mathrm{F}_1}\epsilon_{\mathrm{F}_2}(1-\epsilon_{\mathrm{F}_3}) \\
\epsilon_{\mathrm{F}_1}(1-\epsilon_{\mathrm{F}_2})\epsilon_{\mathrm{R}_3} & \epsilon_{\mathrm{F}_1}(1-\epsilon_{\mathrm{F}_2})\epsilon_{\mathrm{F}_3} \\
\epsilon_{\mathrm{F}_1}(1-\epsilon_{\mathrm{F}_2})(1-\epsilon_{\mathrm{R}_3}) & \epsilon_{\mathrm{F}_1}(1-\epsilon_{\mathrm{F}_2})(1-\epsilon_{\mathrm{F}_3}) \\
(1-\epsilon_{\mathrm{F}_1})\epsilon_{\mathrm{F}_2}(1-\epsilon_{\mathrm{R}_3}) & (1-\epsilon_{\mathrm{F}_1})\epsilon_{\mathrm{F}_2}(1-\epsilon_{\mathrm{F}_3}) \\
(1-\epsilon_{\mathrm{F}_1})(1-\epsilon_{\mathrm{F}_2})\epsilon_{\mathrm{R}_3} & (1-\epsilon_{\mathrm{F}_1})(1-\epsilon_{\mathrm{F}_2})\epsilon_{\mathrm{F}_3} \\
(1-\epsilon_{\mathrm{F}_1})(1-\epsilon_{\mathrm{F}_2})(1-\epsilon_{\mathrm{R}_3}) & (1-\epsilon_{\mathrm{F}_1})(1-\epsilon_{\mathrm{F}_2})(1-\epsilon_{\mathrm{F}_3})
\end{pmatrix} \tag{5.11}$$

The matrix can then be inverted to obtain $N_{\mathrm{RRR}}, \ldots, N_{\mathrm{FFF}}, \ldots$, from the measured $N_{\mathrm{TTT}}, \ldots, N_{\mathrm{LLL}}$. The inversion is done using a numerical method. The fake-lepton background contribution in the SR can then be computed as the contribution to N_{TTT} from terms involving $N_{\mathrm{RRF}}, \ldots, N_{\mathrm{FFF}}$.

Table 5.13: Efficiencies and fake rates of real electrons and muons, in seven p_{T} intervals (in GeV). These efficiencies are valid for lepton $p_{\mathrm{T}} > 15$ GeV, at least one b-tagged jet and $E_{\mathrm{T}}^{\mathrm{miss}} > 20$ GeV. Uncertainties in the values are under 50%; nevertheless, the impact is negligible in the total uncertainty of the event yields.

	$[15, 17]$	$]17, 20]$	$]20, 25]$	$]25, 30]$	$]30, 40]$	$]40, 45]$	> 45
$\epsilon_{\mathrm{R}}(e)$	0.78	0.88	0.78	0.78	0.77	0.74	0.78
$\epsilon_{\mathrm{F}}(e)$	0.04	0.06	0.08	0.01	0.04	0.06	0.13
$\epsilon_{\mathrm{R}}(\mu)$	0.80	0.81	0.83	0.90	0.96	0.98	0.99
$\epsilon_{\mathrm{F}}(\mu)$	0.03	0.07	0.07	0.14	0.12	0.18	0.13

The values used for ϵ_R and ϵ_F are taken from the dilepton fit described in [191, 192] using the electron and muon definitions considered in this analysis. The values for ϵ_{R} are measured in a CR requiring two leptons with the same flavour, opposite charge and $|m_Z - m_{\ell\ell}| < 10$ GeV and at least one b-tagged jet, while the values for ϵ_{F} are measured in a CR with two same charge leptons (if at least one of the leptons is an electron then $|m_Z - m_{\ell\ell}| > 10$ GeV is also required) and at least one b-tagged jet. They are shown in Table 5.13 as a function of the lepton p_{T}. These efficiencies are valid for leptons with $p_{\mathrm{T}} > 15$ GeV from events with at least one b-tagged jet and $E_{\mathrm{T}}^{\mathrm{miss}} > 20$ GeV (hence the requirements for the preselection MM in Section 5.3.1). A fake-lepton CR with three leptons ($p_{T_{\ell 1 \ell 2}} < 50$ GeV and $p_{T_{\ell 3}} < 30$ GeV), with two of them with the same flavour, opposite charge and $|m_Z - m_{\ell\ell}| < 15$ GeV, at least one b-tagged jet with $p_{\mathrm{T}} > 35$ GeV and $E_{\mathrm{T}}^{\mathrm{miss}} < 40$ GeV, is defined to test the agreement between the fake-lepton estimation derived and data. Figure 5.30 shows the correspondent distribution for the yields obtained using the MM and using the MC samples for backgrounds with fake leptons. The yields are shown in Table 5.14 and show a good agreement between both methods.

5.4.2.2 MC based estimation

As a crosscheck to the MM, MC samples with the fake-lepton contribution are used to estimate the yields. The background in which exactly one of the leptons is a fake lepton, is evaluated using a combination of data and MC samples. The dominant contribution in this category comes from Z+jets events, with a leptonic Z boson decay, in which one of the jets is misidentified as a third lepton. To evaluate this background a combined

Table 5.14: Event yields in the fake-lepton CR using the fake-lepton estimation from the MM and MC. The fake-lepton contribution in the MC is the sum of the $t\bar{t}$ ($1.0 \pm 0.6 \pm 2.7$), Z+jets ($7.6 \pm 0.9 \pm 1.3$) and $Z + \gamma$ ($0.6 \pm 0.6 \pm 0.6$) samples. The first uncertainty is the statistical one, associated with the number of events in the samples, the second one is systematic and is described in Section 5.5.

Sample	MM	MC
Fake leptons	$6.9 \pm 0.8 \pm 4.3$	$9.2 \pm 1.2 \pm 3.5$
WZ	$2.7 \pm 0.4 \pm 0.7$	
ZZ	$1.7 \pm 0.6 \pm 1.9$	
$t\bar{t}V$	$0.82 \pm 0.07 \pm 0.27$	
tZ	$0.73 \pm 0.07 \pm 0.42$	
Higgs	$0.11 \pm 0.02 \pm 0.05$	
Tribosons	$0.002 \pm 0.001 \pm 0.001$	
Total background	$13 \pm 1 \pm 5$	$15 \pm 1 \pm 4$
Data	17	
Signal efficiency [$\times 10^{-4}$]	$1.77 \pm 0.06 \pm 0.20$	

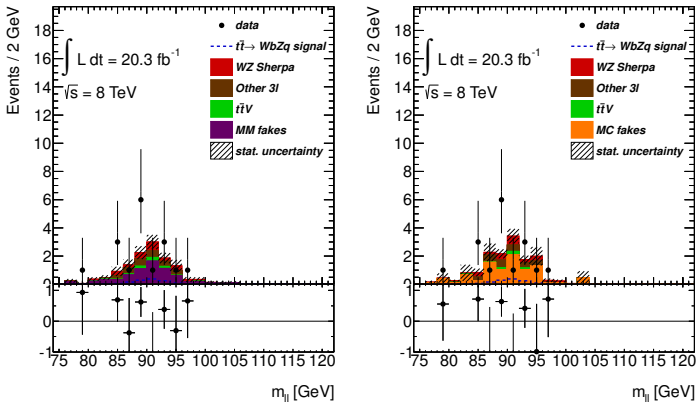

(a) (b)

Figure 5.30: Expected and observed distributions in the fake-lepton CR using the fake-lepton estimation from (a) MM and (b) MC.

MC/DD method is used. This method uses a CR in the ($E_{\mathrm{T}}^{\mathrm{miss}}$, jet multiplicity) plane by selecting events with exactly two opposite-charge electrons or muons for which $|m_Z - m_{\mathrm{reco}}| < 15$ GeV and an additional loose lepton (as defined in Sections 5.2.1 and 5.2.2) not reconstructed as tight, in six different $E_{\mathrm{T}}^{\mathrm{miss}}$ bins from 0 GeV to 60 GeV and seven jet multiplicity bins (taking into account b-tag information). This choice is made in order to normalise the contribution from additional radiation since the $E_{\mathrm{T}}^{\mathrm{miss}}$ and jets are not expected to come from the Z boson. Also, further separation in b-jet multiplicity bins takes into account the heavy flavour component of this background. The Z+jets estimate in each $E_{\mathrm{T}}^{\mathrm{miss}}$/jet bin is then given by:

$$[N_{Z+\mathrm{jets}}^{\mathrm{Data}}]_{\mathrm{SR}} = \left[\frac{N^{\mathrm{Data}} - N_{\mathrm{Other\ backgrounds}}^{\mathrm{Monte\ Carlo}}}{N_{Z+\mathrm{jets}}^{\mathrm{Monte\ Carlo}}}\right]_{\mathrm{CR}} \cdot \left[N_{Z+\mathrm{jets}}^{\mathrm{Monte\ Carlo}}\right]_{\mathrm{SR}} \tag{5.12}$$

For each $E_{\mathrm{T}}^{\mathrm{miss}}$/jet bin considered, the corresponding ratio in the CR is applied to the Z+jets background in the SR in order to evaluate the expected number of Z+jets events in data. The Z+jets normalisation factors obtained with `ALPGEN + PYTHIA`, `ALPGEN + HERWIG` are shown in Table 5.15. The remaining backgrounds with one fake lepton (dileptonic $t\bar{t}$, single-top. $Z\gamma$+jets and WW production) are evaluated using MC simulation samples. To enhance the statistical power of the MC samples in the SR, the lepton selection is loosened and a multiplicative factor to account for the MC probability of the three loose leptons to pass the SR lepton criteria is then applied to the final result. They are derived as the ratio between the number of events using tight leptons and the number of events using loose leptons after the lepton requirements of the SR. These multiplicative factors are shown in Table 5.16.

A comparison between `ALPGEN + PYTHIA` and `ALPGEN + HERWIG` is done. The best agreement is obtained with the `ALPGEN + PYTHIA` samples. This can be seen, for example, looking to the second lepton p_{T}, shown in Figure 5.31; `ALPGEN + PYTHIA` gives a better agreement at the second bin.

Since Z+jets is not a dominant background for the SR, and taking into account the statistical uncertainties associated to the Z+jets samples in the final selection level of the SR, it can be considered that the total SM background yield and shape at the SR are not dependent on the choice of the Z+jets generator after applying the DD normalisation.

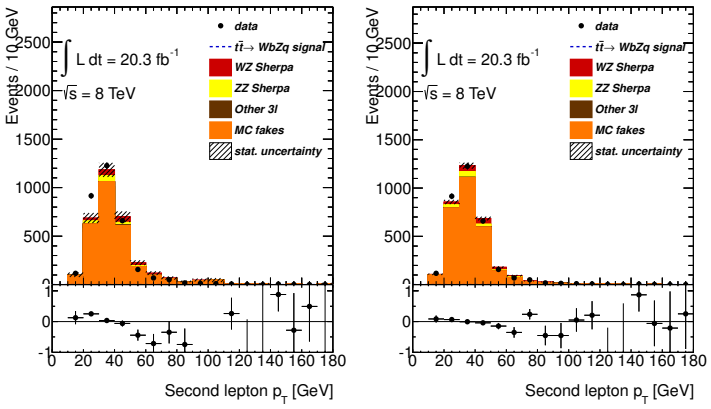

(a) (b)

Figure 5.31: Expected and observed distributions for the second lepton p_{T} with the Z+jets CR for different generators. (a) `ALPGEN` + `HERWIG` and (b) `ALPGEN` + `PYTHIA`. The normalisation is done in bins of jet and b-jet multiplicity and $E_{\mathrm{T}}^{\mathrm{miss}}$.

Table 5.15: Z+jets normalisation factors for six $E_{\mathrm{T}}^{\mathrm{miss}}$ bins from 0 to 60 GeV and 7 jet multiplicity bins, calculated from Equation 5.12 and using ALPGEN + PYTHIA and ALPGEN + HERWIG. The first uncertainty is the statistical one, associated with the number of events in the samples, the second one is systematic and is described in Section 5.5.

$E_{\mathrm{T}}^{\mathrm{miss}}$ region	$= 0j$	$= 1j(0b)$	$= 2j(0b)$	$\geq 3j(0b)$	$= 1j(\geq 1b)$	$= 2j(\geq 1b)$	$\geq 3j(\geq 1b)$
ALPGEN + PYTHIA							
$[0, 10]$	$1.10 \pm 0.12 \pm 0.39$	$0.68 \pm 0.09 \pm 0.18$	$0.26 \pm 0.09 \pm 0.22$	$-0.08 \pm 0.10 \pm 0.10$	$0.23 \pm 0.06 \pm 0.05$	$0.08 \pm 0.08 \pm 0.08$	$0.32 \pm 0.22 \pm 0.22$
$[10, 20]$	$0.97 \pm 0.07 \pm 0.18$	$0.50 \pm 0.05 \pm 0.12$	$0.36 \pm 0.07 \pm 0.12$	$0.76 \pm 0.20 \pm 0.29$	$0.14 \pm 0.03 \pm 0.03$	$0.23 \pm 0.06 \pm 0.05$	$0.24 \pm 0.11 \pm 0.13$
$[20, 30]$	$0.98 \pm 0.07 \pm 0.21$	$0.41 \pm 0.05 \pm 0.07$	$0.42 \pm 0.08 \pm 0.12$	$0.35 \pm 0.11 \pm 0.11$	$0.12 \pm 0.03 \pm 0.03$	$0.23 \pm 0.07 \pm 0.07$	$0.15 \pm 0.11 \pm 0.20$
$[30, 40]$	$0.74 \pm 0.07 \pm 0.21$	$0.55 \pm 0.07 \pm 0.12$	$0.47 \pm 0.11 \pm 0.18$	$0.42 \pm 0.14 \pm 0.30$	$0.12 \pm 0.04 \pm 0.04$	$0.34 \pm 0.09 \pm 0.08$	$0.21 \pm 0.11 \pm 0.14$
$[40, 50]$	$0.69 \pm 0.09 \pm 0.23$	$0.52 \pm 0.08 \pm 0.17$	$0.28 \pm 0.10 \pm 0.17$	$0.42 \pm 0.23 \pm 0.29$	$0.29 \pm 0.08 \pm 0.08$	$0.27 \pm 0.13 \pm 0.17$	$0.29 \pm 0.22 \pm 0.25$
$[50, 60]$	$0.70 \pm 0.15 \pm 0.32$	$0.42 \pm 0.13 \pm 0.23$	$0.29 \pm 0.16 \pm 0.23$	$1.0 \pm 0.4 \pm 1.07$	$-0.07 \pm -0.07 \pm 0.12$	$0.29 \pm 0.19 \pm 0.44$	$0.8 \pm 0.4 \pm 0.6$
ALPGEN + HERWIG							
$[0, 10]$	$1.03 \pm 0.18 \pm 0.44$	$0.74 \pm 0.16 \pm 0.43$	$0.50 \pm 0.23 \pm 0.25$	$-0.14 \pm 0.21 \pm 0.55$	$2.3 \pm 1.2 \pm 1.4$	$0.8 \pm 0.9 \pm 9.5$	$1.4 \pm 1.4 \pm 2.6$
$[10, 20]$	$0.94 \pm 0.12 \pm 0.24$	$0.69 \pm 0.12 \pm 0.14$	$0.40 \pm 0.13 \pm 0.17$	$1.7 \pm 0.9 \pm 1.39$	$1.1 \pm 0.4 \pm 0.4$	$2.7 \pm 1.3 \pm 5.7$	$0.6 \pm 0.4 \pm 1.2$
$[20, 30]$	$0.94 \pm 0.12 \pm 0.25$	$0.68 \pm 0.12 \pm 0.19$	$0.43 \pm 0.12 \pm 0.23$	$1.4 \pm 0.8 \pm 0.88$	$0.9 \pm 0.4 \pm 0.3$	$1.6 \pm 0.8 \pm 1.3$	2.0 ± 2.1
$[30, 40]$	$0.81 \pm 0.17 \pm 0.65$	$0.86 \pm 0.18 \pm 0.28$	$1.0 \pm 0.4 \pm 1.1$	$1.2 \pm 0.8 \pm 5.02$	$1.2 \pm 0.6 \pm 0.6$	$3.2 \pm 1.6 \pm 2.9$	$0.6 \pm 0.4 \pm 10$
$[40, 50]$	$0.78 \pm 0.18 \pm 0.50$	$0.99 \pm 0.27 \pm 0.71$	$1.1 \pm 0.6 \pm 1.7$	$600 \pm 700 \pm 3599$	$6 \pm 4 \pm 4$	2.5 ± 2.0	—
$[50, 60]$	$0.41 \pm 0.17 \pm 0.15$	$0.44 \pm 0.19 \pm 0.53$	$0.44 \pm 0.27 \pm 1.01$	$3.0 \pm 1.9 \pm 13$	$-0.8 \pm -1.0 \pm 1.8$	$3.6 \pm 3.5 \pm 7.1$	4 ± 4

Table 5.16: Factors to account for the MC probability of three loose leptons to enter the SR. The $Z\gamma$+jets scale factor is an order of magnitude larger than for the other samples due to the fake leptons coming from photons and not from jets. The first uncertainty is the statistical one, associated with the number of events in the samples, the second one is systematic and is described in Section 5.5.

Sample	Loose→Tight SF
Z+jets	$0.060 \pm 0.004 \pm 0.010$
$Z\gamma$+jets	$0.354 \pm 0.032 \pm 0.053$
Single top	$0.058 \pm 0.030 \pm 0.030$
$t\bar{t}$ SM	$0.020 \pm 0.004 \pm 0.013$
WW	$0.051 \pm 0.023 \pm 0.044$

5.4.2.3 Sideband control region

A CR to crosscheck both the MM and MC methods is performed inverting the SR window cut on the Z boson mass. Three leptons are required in which one lepton pair must have the same flavour, opposite charge and a reconstructed mass such that $|m_Z - m_{\ell\ell}| > 15$ GeV. Additionally, one b-tagged jet is also required. The results are consistent between both methods, taking into account the uncertainties as can be seen, for example, on Figure 5.32 showing the leading lepton p_{T} and Figure 5.33 showing the second lepton p_{T}. Yields are shown in Table 5.17.

5.4.3 Summary table

The selection requirements of the previously described SR and CRs are summarised in Table 5.18.

Table 5.17: Event yields in the sideband CR using the fake-lepton estimation obtained with the MM and MC. The fake-lepton contribution in the MC is the sum of the $t\bar{t}$ ($19 \pm 3 \pm 5$), single top ($0.62 \pm 0.62 \pm 0.05$), WW ($0.12 \pm 0.09 \pm 0.01$), Z+jets ($1.3 \pm 0.2 \pm 0.7$) and $Z + \gamma$ ($10 \pm 3 \pm 1$) samples. The first uncertainty is the statistical one, associated with the number of events in the samples, the second one is systematic and is described in Section 5.5.

Sample	MM	MC
Fake leptons	$45 \pm 2 \pm 28$	$32 \pm 2 \pm 5$
$t\bar{t}V$	$8.7 \pm 0.2 \pm 2.7$	
WZ	$6.3 \pm 0.7 \pm 1.7$	
Higgs	$2.6 \pm 0.1 \pm 0.4$	
ZZ	$2.5 \pm 0.7 \pm 2.8$	
tZ	$1.52 \pm 0.08 \pm 0.78$	
Tribosons	$0.10 \pm 0.02 \pm 0.02$	
Total background	$67 \pm 3 \pm 28$	$53 \pm 4 \pm 7$
Data	52	
Signal efficiency [$\times 10^{-4}$]	$1.12 \pm 0.04 \pm 0.12$	

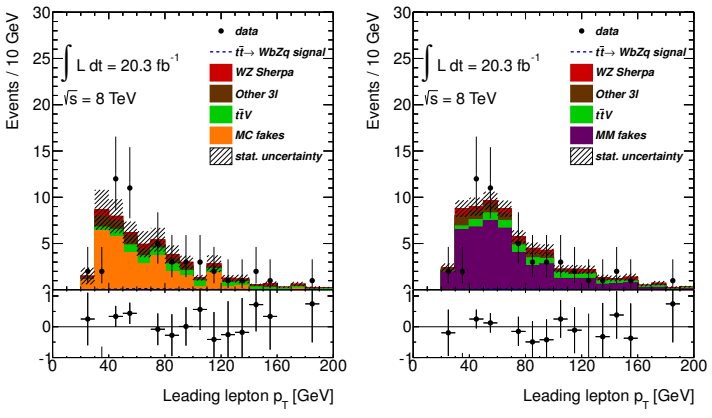

(a) (b)

Figure 5.32: Expected and observed distributions for the leading lepton p_{T} in the sideband CR with (a) MC and (b) MM fake-lepton estimation.

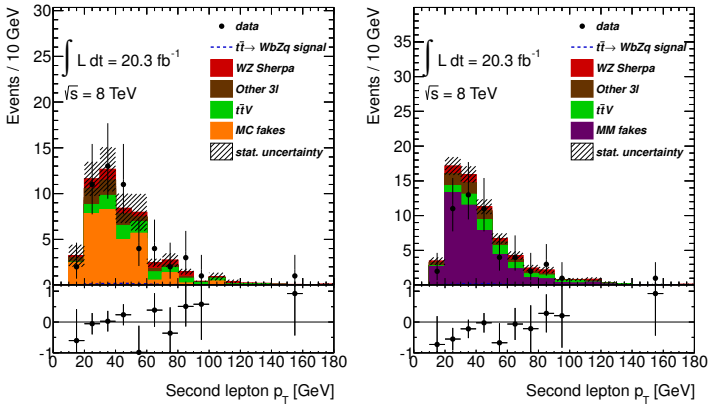

(a) (b)

Figure 5.33: Expected and observed distributions for the second lepton p_{T} with the sideband CR with (a) MC and (b) MM fake-lepton estimation.

Table 5.18: Summary of the selection requirements applied to the SR and CRs, as described in this section. 2T, 3T and 4T refer to 2, 3 and 4 tight leptons, respectively, while 1L corresponds to 1 loose lepton (not tight).

SR	WZ CR	fake-lepton CR	Sideband CR	Z+jets CR	ZZ CR	$t\bar{t}Z$ CR
=3T	= 3T	= 3T	= 3T	= 2T+1L	= 4T	$\geq$ 3T
$\lvert m_Z - m_{\ell\ell}\rvert$ < 15 GeV	$\lvert m_Z - m_{\ell\ell}\rvert$ < 15 GeV	$\lvert m_Z - m_{\ell\ell}\rvert$ < 15 GeV	$\lvert m_Z - m_{\ell\ell}\rvert$ > 15 GeV	$\lvert m_Z - m_{\ell\ell}\rvert$ < 15 GeV	$\lvert m_Z - m_{\ell\ell}\rvert$ < 15 GeV	$\lvert m_Z - m_{\ell\ell}\rvert$ < 15 GeV
$E_{\mathrm{T}}^{\mathrm{miss}} > 20$ GeV	$m_T(W) > 50$ GeV	$E_{\mathrm{T}}^{\mathrm{miss}} < 40$ GeV	—	—	—	—
2 or 3 jets	$\geq$ 1 jet	$\geq$ 1 jet	$\geq$ 1 jet	—	—	$\geq$ 2 jet
1 or 2 b	= 0b	$\geq 1b$	$\geq 1b$	—	—	$\geq 2b$, if $\ell = 3$ $\geq 1b$, if $\ell \geq 4$
$\chi^2 > 6$ (MM) $\chi^2 > 5$ (MC)	—	—	—	—	—	—

5.5 Systematic Uncertainties

Several systematic uncertainties, due to errors and biases in the analysis, can influence the expected number of signal and/or background events, as described in the following sections. The effect of each source of systematic uncertainty is studied by independently varying the corresponding central value by the estimated uncertainty and propagating it through the full analysis chain. For each variation, the total number of expected background events and the signal efficiencies is compared with the reference values. All the detector systematic uncertainties (jets, leptons and $E_{\mathrm{T}}^{\mathrm{miss}}$) are treated as fully correlated between signal and background. The relative impact of each source of systematic uncertainty on the total background and signal is summarised in Table 5.21.

5.5.1 Jet reconstruction

The jet energy scale (JES) systematic uncertainty is derived combining information from single pion test-beam measurements, uncertainties on the material budget of the calorimeter, the description of the electronic noise, the theoretical model used in the MC generation, the comparison of test beam data to the hadronic shower model used in the simulation, and other effects such as a shifted beam spot and the electromagnetic scale uncertainty for the calorimeters. Further sources of uncertainties due to JES calibration are related to jets with larger pseudorapidity, uncertainties due to pile-up, flavour composition of the samples and b-jet response.

The impact of the jet energy resolution (JER) in the analysis is studied by applying a smearing factor to the MC jets from a Gaussian with width,

$$\sigma = \sqrt{(\sigma_{\mathrm{data}} + \Delta\sigma_{\mathrm{data}})^2 - \sigma_{\mathrm{data}}^2}\,, \tag{5.13}$$

with σ_{data} and $\Delta\sigma_{\mathrm{data}}$ the jet resolution and its uncertainty as measured in data. The difference between the nominal and smeared results in MC is taken as a jet resolution uncertainty.

The combined effect of the JES and JER [177, 193] uncertainties are evaluated as 7.7% and 4.9% for the background and signal, respectively.Additional jet uncertainties come from jet reconstruction efficiency and is derived relative to jets built from charged tracks reconstructed in the Inner Detector system. It is defined as the fraction of probe track-jets matched to a calorimeter jet. The jet reconstruction inefficiency is found

to be at most 2.7% for jets with $p_{\mathrm{T}} < 20$ GeV, about 0.2% for jets with p_{T} in range $[20, 30]$ and fully efficient for $p_{\mathrm{T}} > 30$ GeV. This uncertainty is taken into account by randomly dropping jets from the events.

A jet vertex fraction cut of 0.5 is applied to all jets with $p_{\mathrm{T}} < 50$ GeV and $|\eta| < 2.4$ in order to reduce the effect of pile-up. To account for differences between data and MC, a scale factor is applied and uncertainties are derived changing the cut on the jet vertex fraction from the nominal value of 0.5 to 0.53 (up) and 0.47 (down).

5.5.2 Jet tagging

The effects of uncertainties in efficiencies for the heavy flavour identification of jets by the b-tagging algorithm MV1 have been evaluated. Since the corrections are applied separately to b, c, mistag and τ jets, the uncertainties are considered separately for each of these scale factors. Moreover, the τ and charm uncertainties are highly correlated and evaluated as such. They are evaluated by varying the η, p_{T} and flavour-dependent scale factors applied to each jet in the simulation. It is estimated to be 3.9% for the total background and 7.2% for the signal efficiency.

5.5.3 Lepton reconstruction and trigger

The lepton reconstruction, identification and trigger efficiencies, as well as lepton momentum scales and resolutions [170, 175, 194] are considered. The lepton trigger, reconstruction and identification systematics are evaluated redoing the event selection, and varying the scale factors applied to the MC simulation up and down according to the $\pm 1\sigma$ uncertainties. Similarly, the energy scale and resolution systematics are measured by varying the energy corrections by the corresponding uncertainties and the resolution by its uncertainty when smearing the energy on simulation (derived from the Z resonance peak). The overall effect on the total background yield and the signal efficiency is estimated to be 4.7 and 2.9% respectively.

5.5.4 Missing transverse Energy scale and resolution uncertainty

The systematic uncertainty on the value of $E_{\mathrm{T}}^{\mathrm{miss}}$ [182] is a combination of the hard objects and soft terms uncertainties. For the objects, all lepton and jet uncertainties

are propagated to the $E_{\mathrm{T}}^{\mathrm{miss}}$. For the soft terms, the $E_{\mathrm{T}}^{\mathrm{miss}}$ scale and resolution uncertainties are considered. The systematic uncertainty on the $E_{\mathrm{T}}^{\mathrm{miss}}$ resolution is studied by applying a smearing factor to the MC $E_{\mathrm{T}}^{\mathrm{miss}}$ and the energy scale by varying the scale factors (up and down) by the energy scale uncertainties. The $E_{\mathrm{T}}^{\mathrm{miss}}$ scale uncertainty is found to vary the total background yield and the signal efficiency by 3.2 and 1.5%, respectively.

5.5.5 Luminosity

The luminosity uncertainty is derived comparing the number of events of the MC-driven background estimates using the reference value of 20.3 fb^{-1} with the number of events obtained applying a variation of 2.8% up and down of the reference value.

5.5.6 Signal and background modelling

The main uncertainty on the backgrounds comes from their modelling, which has the following two contributions. The level of agreement with data of the reference samples is assessed from the combination of a Poisson uncertainty on the available amount of data with the statistical uncertainty on the expected background yields in the dedicated CRs. The uncertainties are estimated to be 6.3%, 12%, 42% and 62%, for the WZ, ZZ, $t\bar{t}Z$ and fake-lepton backgrounds, respectively. The other contribution comes from the uncertainty on the theoretical prediction in the SR and is estimated using the alternative WZ and ZZ simulated samples. The corresponding uncertainties are 17% and 100%, respectively. A summary of this calculation is shown in Table 5.19. Similarly, for $t\bar{t}Z$, tZ and Higgs samples, conservative values of 30% [195, 196], 50% [190] and 15% [197], respectively, are used in order to account for the theoretical uncertainties; see Table 5.20 for a breakdown of the individual Higgs samples cross-sections. The combination of all these uncertainties gives a 17% effect on the total background estimation.

The effect of the initial and final state radiation is taken into account comparing the reference signal sample with the signal samples with less and more parton showers referenced in Section 5.1.2.1.

The samples with different top-quark mass (see Section 5.1.2.1) are used to compare the number of events using the reference mass of 172.5 GeV with the samples with masses 170 and 175 GeV. The relative differences with respect to the reference are

Table 5.19: ALPGEN and HERWIG relative uncertainties with respect to SHERPA for the WZ and ZZ samples, along with the yields in the SR (after χ^2 cut) and respective CRs, used in the calculation. Only the statistical uncertainty is shown in the yields.

	ALPGEN	HERWIG	SHERPA
WZ SR	1.8 ± 0.4	0.11 ± 0.10	1.3 ± 0.2
WZ CR	393 ± 6	163 ± 6	333 ± 5
WZ SR/CR	0.0046 ± 0.0010	0.0007 ± 0.0006	0.0040 ± 0.0006
WZ relative uncer.	0.17 ± 0.07	-0.83 ± 0.15	—
ZZ SR	0.37 ± 0.13	$(0.9 \pm 0.9) \times 10^{-6}$	0.06 ± 0.06
ZZ CR	189 ± 3	85 ± 4	87 ± 4
ZZ SR/CR	0.0020 ± 0.0006	$(1.0 \pm 1.0) \times 10^{-8}$	0.0007 ± 0.0007
ZZ relative uncer.	1.7 ± 1.6	-1.0 ± 1.9	—

0.4% (0.5%) and -1.8% (-1.5%) for the fake-lepton estimation using the MM (MC), for 175 GeV and 170 GeV, respectively. This uncertainty is not included in the results.

The uncertainty on the $t\bar{t}$ cross section is estimated changing the central value from the theoretical calculation, 253 pb, by the corresponding up and down uncertainties $\delta\sigma_{t\bar{t}} = ^{+13}_{-15}$ pb. The limit on the BR($t \to qZ$) is inversely proportional to the product of the signal efficiency and the $t\bar{t}$ cross section. Since the effect of the variation of the cross section on the limit is equivalent to changing the signal efficiency to yield the same product, the systematic uncertainty is calculated instead for the signal efficiency, as the relative difference between the efficiency for the central value of the $t\bar{t}$ cross section and the corresponding efficiencies for the up and down variations.

5.6 Limit evaluation

A good agreement between data and background yields is observed, as shown in Table 5.8 (before the χ^2 cut) and in Table 5.9 (for the final selection level). No evidence for the $t \to qZ$ decay is found and 95% CL upper limits on the number of signal events are derived using ROOT's TLimit [188] implementation of the modified frequentist likelihood method [198, 199]. A test-statistic, X_d, that compares the number of data events with background and signal expectations, is defined as:

$$X_d = n \ln\left(1 + \frac{s}{b}\right) \tag{5.14}$$

Table 5.20: Higgs samples normalisation uncertainties

Sample	δQCD scale [%]	δ(PDF + α_s) [%]	δBR [%]		Total uncertainty [%]
$t\bar{t}H$	$^{+3.8}_{-9.3}$	$^{+8.1}_{-8.1}$	$H \to cc$	$^{+12.17}_{-12.21}$	$^{+15.10}_{-17.35}$
			$H \to bb$	$^{+3.21}_{-3.27}$	$^{+9.51}_{-12.76}$
			$H \to \gamma\gamma$	$^{+4.98}_{-4.89}$	$^{+10.24}_{-13.27}$
			$H \to gg$	$^{+10.22}_{-9.98}$	$^{+13.58}_{-15.87}$
			$H \to \tau\tau$	$^{+5.71}_{-5.67}$	$^{+10.61}_{-13.57}$
			$H \to WW$	$^{+4.26}_{-4.20}$	$^{+9.91}_{-13.03}$
			$H \to ZZ$	$^{+4.28}_{-4.21}$	$^{+9.92}_{-13.03}$
WH	$^{+1}_{-1}$	$^{+2.3}_{-2.3}$	$H \to ZZ$	$^{+4.28}_{-4.21}$	$^{+4.96}_{-4.90}$
ZH	$^{+3.1}_{-3.1}$	$^{+2.5}_{-2.5}$	$H \to bb$	$^{+3.21}_{-3.27}$	$^{+5.12}_{-5.12}$
			$H \to \tau\tau$	$^{+5.71}_{-5.67}$	$^{+6.96}_{-6.93}$
			$H \to WW$	$^{+4.26}_{-4.20}$	$^{+5.83}_{-5.74}$
ggH	$^{+7.2}_{-7.8}$	$^{+7.5}_{-6.9}$	$H \to ZZ$	$^{+4.28}_{-4.21}$	$^{+11.24}_{-11.23}$

Table 5.21: Summary of the relative impact of each source of uncertainty in the total background events and signal efficiency, with the fake-lepton estimation from MC and MM, after the χ^2 cut. The statistical uncertainty is also shown.

Source	MM background	signal (%)	MC background	signal (%)
statistical	8.1	1.5	7.4	1.5
Jet	7.7	4.9	9.9	5.4
b-tag	3.9	7.2	3.6	7.5
Leptons	4.7	2.9	4.8	2.8
MET	3.2	1.5	4.4	1.8
Signal modelling	—	5.5	—	5.5
Background modelling	17	—	13	—
Luminosity	2.4	—	1.7	—

where n, s and b are the number of data, expected background and signal events, respectively. When data events are more similar to the signal events, the X_d variable takes higher values. The X_d statistical test is then compared to 2×10^5 pseudo-experiments in the hypotheses of signal plus background (X_{s+b}) and background only (X_b). The statistical fluctuations of the pseudo-experiments are performed with Poisson distributions. All statistical and systematic uncertainties of the expected backgrounds and signal efficiencies are taken into account, as described in Section 5.5, and were implemented assuming Gaussian distributions [199]. The confidence level (CL) for a given signal hypothesis s is defined as [198]:

$$1 - CL = \frac{\int_0^{X_d} P_{s+b}(X)\mathrm{d}X}{\int_0^{X_d} P_b(X)\mathrm{d}X}\,, \tag{5.15}$$

where P_{s+b} and P_b are the probability density functions (pdfs) obtained from the pseudo-experiments for the X_{s+b} and X_b values, respectively, and are functions of s and b. The limit on the number of signal events is determined by finding the value of s for which the corresponding CL is 95%. The expected limit is computed by replacing X_d with the median of the statistical test for the background hypothesis (X_b). Figure 5.36 shows the distributions of $-2\ln X$ for the signal plus background hypothesis and for the background-only hypothesis that corresponds to the 95% CL limit, taking into account the systematic uncertainties. The limits on the number of signal events are

converted into upper limits on the corresponding BR fraction using the approximate NNLO calculation, and uncertainty, for the $t\bar{t}$ cross-section ($\sigma_{t\bar{t}} = 253^{+13}_{-15}$ pb), and constraining BR($t \to bW$) = 1−BR($t \to qZ$). Figure 5.34 and 5.35 show the expected and observed limits as a function of a cut on the χ^2 (as defined in Equation 5.3, without the Z term) for the uZ and cZ channels, respectively. The number of observed data events, expected number of total background events and signal efficiency for each of the first 20 bins of the distribution are shown in Table 5.22. The limits for the final selection, with the cut on the χ^2 that yields the best expected limit, are shown in Table 5.23. Ultimately, the limit on the $t\bar{t} \to cZ$ decay is chosen, since it gives a more conservative result than the $t\bar{t} \to uZ$ sample. The smaller b-tagged jet multiplicity of the $t\bar{t} \to uZ$ signal sample leads to a 4% improvement in the limit.

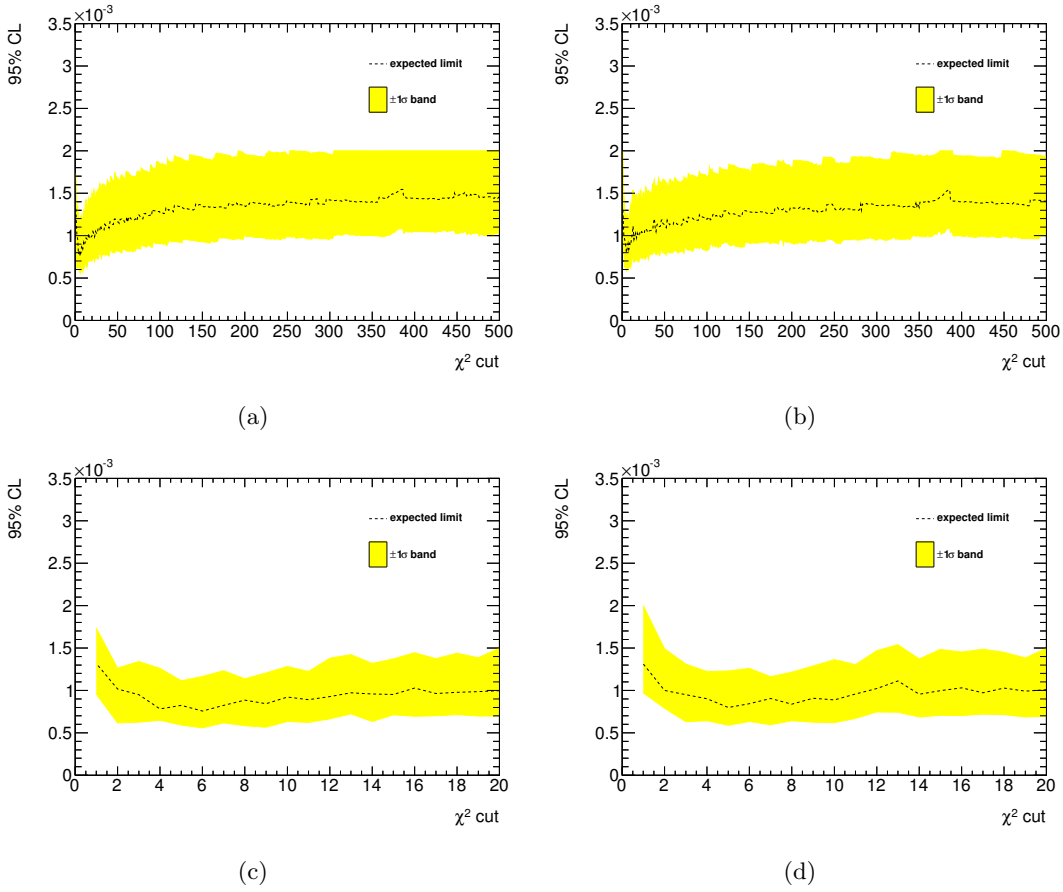

Figure 5.34: Limits for the uZ channel. Expected limit in each bin corresponds to using the χ^2 distribution with a cut in that bin, using the (a) MM and (b) MC samples to estimate the fake-lepton contribution. (c) and (d) show the first 20 bins of the same distributions, using the MM and MC samples to estimate the fake-lepton contribution, respectively.

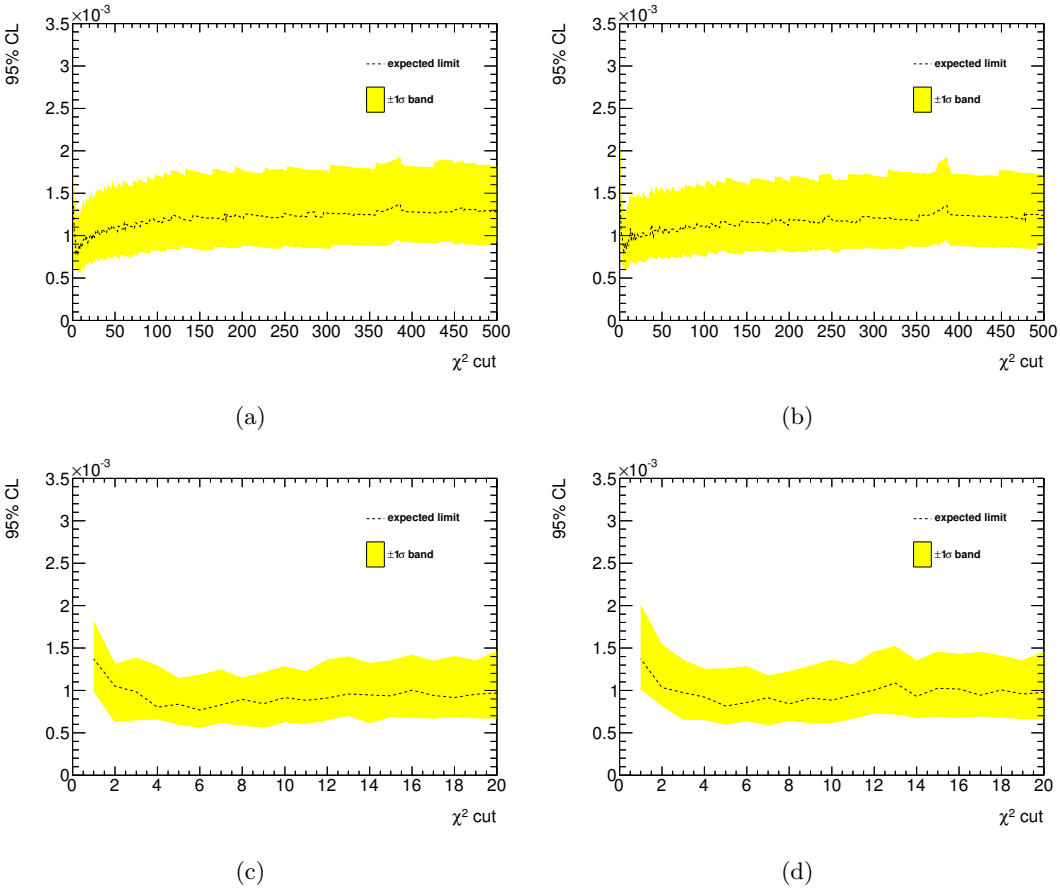

Figure 5.35: Limits for the cZ channel. Expected limit in each bin corresponds to using the χ^2 distribution with a cut in that bin, using the (a) MM and (b) MC samples to estimate the fake-lepton contribution. (c) and (d) show the first 20 bins of the same distributions, using the MM and MC samples to estimate the fake-lepton contribution, respectively.

Table 5.22: Number of selected data events, expected number of background events (using fake-lepton estimation from MC and MM), and signal efficiency for uZ and cZ decays (normalized to all decays of the W and Z bosons), after cutting on χ^2 distribution. The first uncertainty is the statistical one, associated with the number of events in the samples, the second one is systematic and is described in Section 5.5.

χ^2 cut	data	total background (MM)	total background (MC)	signal efficiency (uZ)	signal efficiency (cZ)
20	7	$11.59 \pm 0.70 \pm 2.50$	$11.66 \pm 0.57 \pm 2.43$	$0.0998 \pm 0.0013 \pm 0.0099$	$0.1005 \pm 0.0013 \pm 0.0093$
19	7	$11.27 \pm 0.70 \pm 2.26$	$11.38 \pm 0.57 \pm 2.13$	$0.0992 \pm 0.0013 \pm 0.0098$	$0.0997 \pm 0.0013 \pm 0.0091$
18	7	$10.76 \pm 0.67 \pm 2.22$	$11.00 \pm 0.56 \pm 2.25$	$0.0986 \pm 0.0013 \pm 0.0098$	$0.0987 \pm 0.0013 \pm 0.0089$
17	6	$10.42 \pm 0.66 \pm 2.19$	$10.66 \pm 0.55 \pm 2.18$	$0.0979 \pm 0.0013 \pm 0.0098$	$0.0979 \pm 0.0013 \pm 0.0090$
16	4	$10.01 \pm 0.65 \pm 2.32$	$10.22 \pm 0.53 \pm 2.40$	$0.0970 \pm 0.0013 \pm 0.0097$	$0.0967 \pm 0.0013 \pm 0.0090$
15	3	$9.22 \pm 0.58 \pm 2.06$	$9.79 \pm 0.52 \pm 2.24$	$0.0963 \pm 0.0013 \pm 0.0097$	$0.0957 \pm 0.0013 \pm 0.0090$
14	3	$8.93 \pm 0.58 \pm 1.89$	$9.47 \pm 0.51 \pm 1.96$	$0.0952 \pm 0.0013 \pm 0.0096$	$0.0945 \pm 0.0013 \pm 0.0089$
13	3	$8.36 \pm 0.56 \pm 2.30$	$8.82 \pm 0.49 \pm 2.64$	$0.0940 \pm 0.0013 \pm 0.0094$	$0.0930 \pm 0.0013 \pm 0.0087$
12	3	$7.62 \pm 0.50 \pm 2.21$	$8.34 \pm 0.46 \pm 2.47$	$0.0927 \pm 0.0013 \pm 0.0093$	$0.0913 \pm 0.0013 \pm 0.0085$
11	3	$7.28 \pm 0.50 \pm 1.61$	$7.94 \pm 0.45 \pm 1.67$	$0.0914 \pm 0.0013 \pm 0.0092$	$0.0896 \pm 0.0013 \pm 0.0085$
10	3	$6.85 \pm 0.49 \pm 1.49$	$7.44 \pm 0.43 \pm 1.49$	$0.0897 \pm 0.0012 \pm 0.0090$	$0.0877 \pm 0.0012 \pm 0.0084$
9	3	$6.25 \pm 0.46 \pm 1.31$	$6.90 \pm 0.42 \pm 1.26$	$0.0881 \pm 0.0012 \pm 0.0089$	$0.0858 \pm 0.0012 \pm 0.0083$
8	3	$5.74 \pm 0.45 \pm 1.15$	$6.35 \pm 0.40 \pm 1.07$	$0.0861 \pm 0.0012 \pm 0.0089$	$0.0835 \pm 0.0012 \pm 0.0083$
7	3	$5.18 \pm 0.40 \pm 1.06$	$5.83 \pm 0.38 \pm 1.03$	$0.0833 \pm 0.0012 \pm 0.0084$	$0.0806 \pm 0.0012 \pm 0.0081$
6	3	$4.67 \pm 0.38 \pm 0.94$	$5.25 \pm 0.36 \pm 0.93$	$0.0806 \pm 0.0012 \pm 0.0085$	$0.0776 \pm 0.0012 \pm 0.0084$
5	2	$4.21 \pm 0.36 \pm 0.88$	$4.64 \pm 0.35 \pm 0.84$	$0.0767 \pm 0.0012 \pm 0.0082$	$0.0736 \pm 0.0011 \pm 0.0083$
4	2	$3.65 \pm 0.34 \pm 0.77$	$4.03 \pm 0.33 \pm 0.75$	$0.0711 \pm 0.0011 \pm 0.0078$	$0.0678 \pm 0.0011 \pm 0.0077$
3	2	$2.91 \pm 0.31 \pm 0.76$	$3.15 \pm 0.30 \pm 0.78$	$0.0636 \pm 0.0011 \pm 0.0074$	$0.0603 \pm 0.0010 \pm 0.0075$
2	2	$1.87 \pm 0.26 \pm 0.51$	$2.11 \pm 0.22 \pm 0.53$	$0.0519 \pm 0.0010 \pm 0.0060$	$0.0488 \pm 0.0009 \pm 0.0059$
1	0	$0.92 \pm 0.17 \pm 0.47$	$1.27 \pm 0.20 \pm 0.58$	$0.0339 \pm 0.0008 \pm 0.0047$	$0.0320 \pm 0.0008 \pm 0.0053$

Table 5.23: The expected 95% confidence level limits on the FCNC top quark decay BR, in the absence of signal, are shown for a counting experiment, with and without a cut on the χ^2, for both fake-lepton estimation methods. The central values are represented with the $\pm 1\sigma$ bands, which include the contribution from the statistical and systematic uncertainties.

	observed	(-1σ)	expected	$(+1\sigma)$
Fake-lepton estimation from MM				
no cut on χ^2 (uZ)	1.5×10^{-3}	1.0×10^{-3}	1.4×10^{-3}	2.0×10^{-3}
$\chi^2 < 6$ (uZ)	6.4×10^{-4}	5.4×10^{-4}	7.4×10^{-4}	1.1×10^{-3}
no cut on χ^2 (cZ)	1.3×10^{-3}	9.3×10^{-4}	1.3×10^{-3}	1.8×10^{-3}
$\chi^2 < 6$ (cZ)	6.7×10^{-4}	5.7×10^{-4}	7.7×10^{-4}	1.2×10^{-3}
Fake-lepton estimation from MC/DD Methods				
no cut on χ^2 (uZ)	1.4×10^{-3}	1.0×10^{-3}	1.4×10^{-3}	1.9×10^{-3}
$\chi^2 < 5$ (uZ)	5.7×10^{-4}	5.7×10^{-4}	7.8×10^{-4}	1.2×10^{-3}
no cut on χ^2 (cZ)	1.2×10^{-3}	8.8×10^{-4}	1.2×10^{-3}	1.7×10^{-3}
$\chi^2 < 5$ (cZ)	6.0×10^{-4}	6.0×10^{-4}	8.2×10^{-4}	1.3×10^{-3}

Instead of cutting on the χ^2, it is possible to use other distributions as well. The reconstructed mass of the top quark coming from the FCNC decay, is also a good discriminant variable to improve the signal efficiency. Figure 5.37 shows the expected limits in function of a window cut around 173 GeV. Table 5.24 shows the limits without the window cut and with the best window cut. The expected limit is slightly worse but in agreement with the previous results.

5.7 Conclusions

A search for FCNC decays of top quarks produced in pairs was performed using data collected by the ATLAS experiment at a centre-of-mass energy of $\sqrt{s} = 8$ TeV, corresponding to an integrated luminosity of 20.3 fb^{-1}, recorded in 2012. The search for the $t \to qZ$ decay mode was performed by studying top quark pair production with one top quark decaying according to the SM and the other via FCNC ($t\bar{t} \to bWqZ$). Backgrounds with three real leptons were studied with MC samples and validated in CRs. Other backgrounds with contributions from jets faking leptons were evaluated using the MM, and cross-checked with MC/DD, which produce compatible results. No

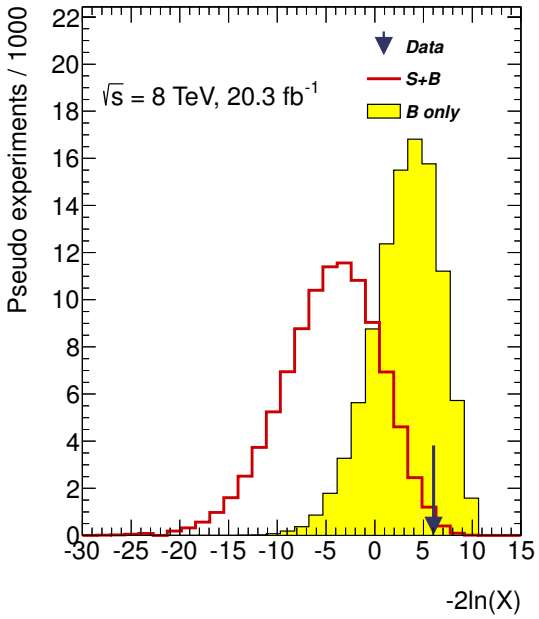

Figure 5.36: Distributions of $-2\ln X$ obtained with 10^5 pseudo-experiments for the background-only hypothesis (filled histogram) and the signal plus background hypothesis with $\mathrm{BR}(t \to qZ) = 7 \times 10^{-4}$. This corresponds to the observed 95% CL limit (full line), taking into account the systematic uncertainties. The value obtained for the data sample is indicated by the arrow.

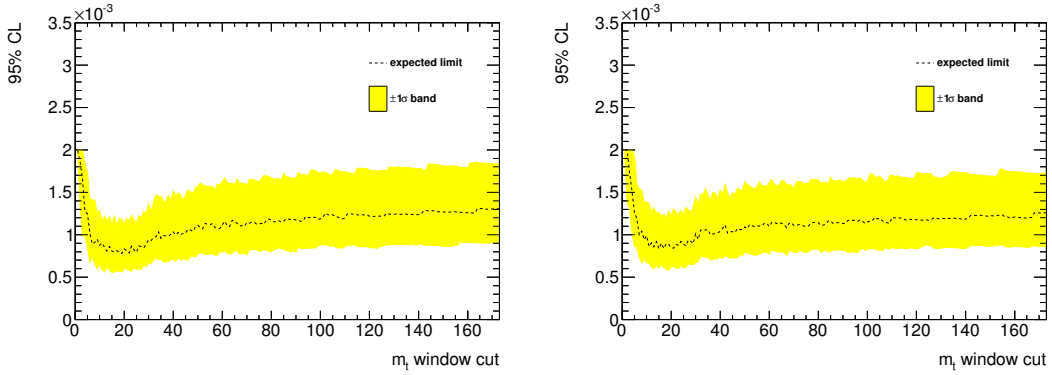

(a) (b)

Figure 5.37: Expected limit in each bin corresponds to applying a window cut around 173 GeV, of such a value, in the reconstructed top quark mass with FCNC decay. (a) using the MM and (b) using the MC samples to estimate the fake-lepton contribution.

Table 5.24: The expected 95% confidence level limits on the FCNC top quark decay BR, in the absence of signal, are shown for a counting experiment, with and without a window cut on the reconstructed mass of the quark top with FCNC decay, for both fake-lepton estimation methods. The central values are represented with the $\pm 1\sigma$ bands, which include the contribution from the statistical and systematic uncertainties.

	observed	(-1σ)	expected	$(+1\sigma)$
Fake-lepton estimation from MM				
no cut on $m_{t_{\mathrm{FCNC}}}$	1.3×10^{-3}	9.3×10^{-4}	1.3×10^{-3}	1.8×10^{-3}
$\chi^2 < 19$	8.8×10^{-4}	5.6×10^{-4}	7.8×10^{-4}	1.2×10^{-3}
Fake-lepton estimation from MC/DD Methods				
no cut on $m_{t_{\mathrm{FCNC}}}$	1.2×10^{-3}	8.8×10^{-4}	1.2×10^{-3}	1.7×10^{-3}
$\chi^2 < 15$	7.5×10^{-4}	6.1×10^{-4}	8.4×10^{-4}	1.3×10^{-3}

evidence for signal events, above the expected background, was found in data. An observed limit at 95% C.L. on the $t \to qZ$ FCNC top quark decay branching fraction was set as $\mathrm{BR}(t \to qZ) < 6.7 \times 10^{-4}$, in agreement with the expected limit of 7.7×10^{-4}, which are one order of magnitude better than the previous ATLAS results.

Figure 5.38 compares the 95% CL observed limit found in this analysis with the results from other FCNC searches performed by the H1, ZEUS, LEP (combined results of the ALEPH, DELPHI, L3 and OPAL collaborations), CDF, DØ and CMS collaborations. The results presented are consistent with the ones from the CMS Collaboration. The present experimental limits on the BRs established by experiments at the LEP [56–61], HERA [62–64], Tevatron [65–69] and LHC [200–206] colliders are shown in Table 5.25.

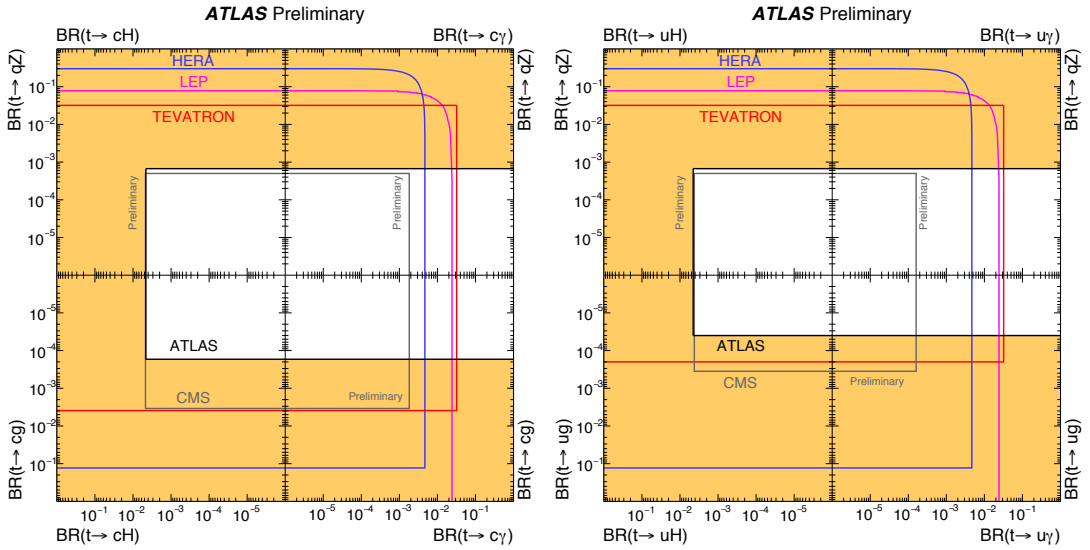

(a) (b)

Figure 5.38: Summary of the current 95% confidence level observed limits on the BRs of the top-quark decays via FCNC to (a) a charm and (b) a up-quark, and a neutral boson $t \to cX$ ($t \to uX$) ($X = g$, Z, γ or H). The coloured lines represent the results from HERA (the most stringent limits obtained by either the H1 and ZEUS collaborations, in blue), LEP (combined ALEPH, DELPHI, L3 and OPAL collaborations result, in magenta), TEVATRON (the most stringent limits obtained by either the CDF and DØ collaborations, in red) and the CMS Collaboration (in grey). The yellow area represents the region excluded by the ATLAS Collaboration. Results made public by CMS in August are not inluded in this figure. Taken from [207, 208].

Table 5.25: Experimental 95% CL upper limits on the BRs of the FCNC top quark decay channels established by experiments at the LEP [56–60, 64] (combination of the ALEPH, DELPHI, L3 and OPAL collaborations), HERA [62–64] (best ZEUS and H1 results), Tevatron [65–69] and LHC [200, 204, 209–213] colliders. ($q = u, c$).

	LEP	HERA	Tevatron		LHC	
			CDF	DØ	ATLAS	CMS
$t \to qZ$	7.8×10^{-2}	3.0×10^{-1} (uZ)	3.7×10^{-2}	3.2×10^{-2}	7×10^{-4}	$2.2 \times 10^{-4} (uZ)$ 4.9×10^{-4} (cZ)
$t \to q\gamma$	2.4×10^{-2}	4.7×10^{-1} $(u\gamma)$	3.2×10^{-2}	—	—	1.3×10^{-4} $(u\gamma)$ 1.7×10^{-3} $(c\gamma)$
$t \to qg$	1.7×10^{-1}	1.3×10^{-1}	3.9×10^{-4} 5.7×10^{-3}	2.0×10^{-4} 3.9×10^{-3}	4.0×10^{-5} (ug) 2.0×10^{-4} (ug)	2.0×10^{-5} (ug) 4.1×10^{-4} (ug)
$t \to qH$	—	—	—	—	4.5×10^{-3} (uH) 4.6×10^{-3} (cH)	5.5×10^{-3} (uH) 4.0×10^{-3} (cH)

6

ATLAS sensitivity at the High Luminosity LHC to FCNC top-quark decays $t \to qZ$ and $t \to q\gamma$

After Run 1 of the LHC (2010 to 2012) and around 30 fb^{-1} of data collected, the first LHC upgrade was performed during the Long Shutdown 1 (LS1) in 2013-1014. During LS1 the detectors also went through a programme of maintenance and improvements in preparation for the new energy frontier. In June 2015, LHC operations resumed with centre-of-mass energies of 13 TeV, which is expected to increase to 14 TeV and reach the design luminosity value of 10^{34} cm^{-2} s^{-1} and a total integrated luminosity of 150 fb^{-1} of data.

After these goals are met, it becomes necessary to improve the luminosity beyond its design value, to reach any significant statistical gains. On 30th May 2013, the updated European Strategy for Particle Physics took this into account and was agreed that *"[...] Europes top priority should be the exploitation of the full potential of the LHC, including the high-luminosity upgrade of the machine and detectors with a view to collecting ten times more data than in the initial design, by around 2030 [...]"*. [214].

It is foreseen for the early 2020's an upgrade to the LHC accelerator and its detectors, to handle high luminosities between 5×10^{34} cm^{-2}s^{-1} and 7×10^{34} cm^{-2}s^{-1} (HL-LHC operation). The total integrated luminosity foreseen to be reached is 3 ab^{-1}.

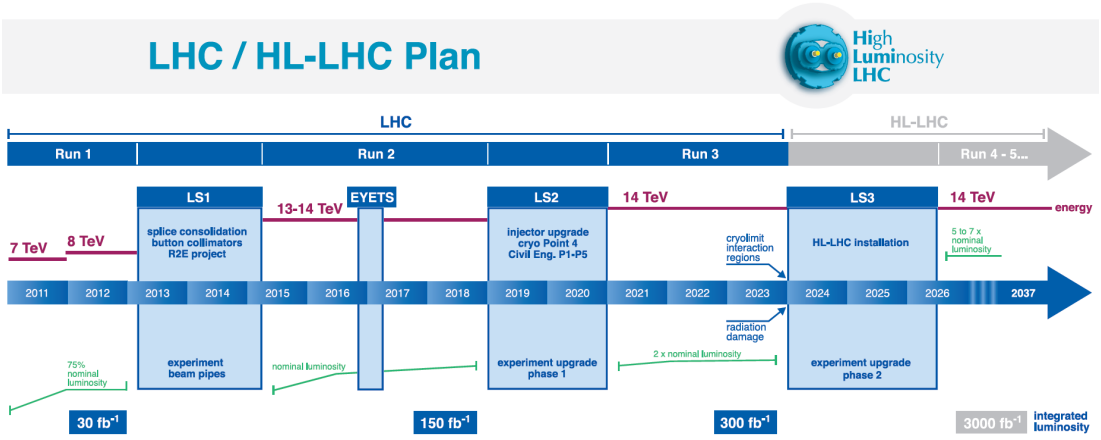

Figure 6.1: LHC/HL-LHC plan, as of 21/07/2015. Taken from [218].

A summary of the LHC upgrade plan is shown in Figure 6.1.

In this chapter, a study of the ATLAS experiment sensitivity to top-quark decays via FCNC ($t \to qX, X = \gamma, Z$ and $q = u, c$ with $Z \to \ell^+\ell^-$), from $t\bar{t}$ production, is done for the expected HL-LHC luminosity of 3 ab^{-1}. Chronologically, this work was done before the analysis described in the previous chapter has started. Therefore, sensitivities are derived at 14 TeV and 3 ab^{-1} following previously published methodologies and results of analysis based on data with centre-of-mass energy of 7 TeV. Sensitivities are derived in two ways. In the first one, a simple extrapolation from 7 TeV results to the 14 TeV centre-of-mass energy and luminosities is performed. In the second one, a dedicated analysis using simulated events is implemented. These initial studies of the ATLAS experiment sensitivity to these FCNC decays have been done in the context of two ATLAS PUB Notes [215] and [216] and explained in more detail in Ref. [217].

6.1 Extrapolations

The extrapolations initially done for the PUB notes [215, 216] were done using the results from the 7 TeV analysis (with luminosities of 2.1 and 0.7 fb^{-1} for qZ [70] and $q\gamma$ [219], respectively). To expand upon those results, an extrapolation based on the 8 TeV $t \to qZ$ analysis described in this thesis is outlined, in this section, following the same methodology used for the 7 TeV extrapolations [217].

Following Equation 3.1, to have a rough estimation on the number of events at

Table 6.1: Luminosities, theoretical cross-sections and event yields for the main backgrounds at 14 TeV and 8 TeV. The ratios are also shown.

	14 TeV	8 TeV	Ratios	Events @ 8 TeV
L_{qZ} [fb^{-1}]	3000	20.3	147.8	—
$t\bar{t}V$ [fb]	1000 [190]	220 [190]	4.5	1.37
σ_{WZ} [pb]	51.8 [220]	20.3 [221]	2.6	1.11
tZ [fb]	640 [190]	160 [190]	4.0	0.90
$\sigma_{Z+\text{jets}}$ [nb]	55 [104]	30 [104]	1.8	0.79
$\sigma_{t\bar{t}}$ [pb]	985 [76–81]	253 [76–81]	3.9	0.30
σ_{ZZ} [pb]	17.7 [220]	7.2 [222]	2.5	0.06

14 TeV, the total number of events obtained by the individual analyses at 7 TeV and 8 TeV can be multiplied by the luminosity, S_L, and the cross-section, S_σ, scale factors:

$$N_{\text{event}}^{14\text{TeV}} = N_{\text{event}}^{8\text{TeV}} S_\sigma S_L, \tag{6.1}$$

with the scale factors calculated as the ratio between values at 14 and 8 TeV. Using the corresponding ratios for the luminosities and the various cross-sections for the main backgrounds (shown in Table 6.1), the extrapolated number of background events from the 8 TeV result is 2275.

In the absence of a FCNC top-quark decay signal hypothesis, expected limits at 95% CL are derived using the CLs [198, 199] method, as explained in Section 5.6. Using the expected SM $t\bar{t}$ production cross-section of 985 pb [76–81], these limits are converted into limits on the BRs. Background's statistical and systematic uncertainties are taken into account as $\sqrt{B}$. Table 6.2 shows the central value of the limit using the extrapolated background events, together with the $\pm 1\sigma$ bands, along with the summary of the limits obtained extrapolating from the 7 TeV analysis. With these rough estimates a BR of around 10^{-5} (10^{-6}) can be reached with HL-LHC at the expected luminosity for the $t \to qZ$ ($t \to q\gamma$) FCNC decay, increasing the sensitivity by a factor ten in relation to the current results.

Table 6.2: The expected 95% confidence level limits on the FCNC top quark decay BR, in the absence of signal, are shown for a luminosity of 3 ab^{-1}. The limits extrapolated from the 7 TeV analyses and described in Ref. [217] and the one derived from the 8 TeV result obtained using the MC estimation for the fake-leptons, described in this thesis. The central values are presented with the $\pm 1\sigma$ bands, which include the contribution from the statistical and systematic background uncertainties as $\sqrt{B}$, as well as the signal uncertainties.

	(-1σ)	expected	(+1σ)
$t \to q\gamma$ (7 TeV)	7.6×10^{-6}	1.1×10^{-5}	1.6×10^{-5}
$t \to qZ$ (7 TeV)	2.5×10^{-5}	3.8×10^{-5}	5.2×10^{-5}
$t \to qZ$ (8 TeV)	3.0×10^{-5}	4.3×10^{-5}	6.0×10^{-5}

6.2 Dedicated analysis

A dedicated Monte Carlo analysis was also implemented, as described in this section. Since no data is available, DD methods for background estimation or control, as used in the analysis described in the previous chapter, are not possible. Only a general approach following the same methodology of the previous published 7 TeV analysis [186, 223] and based on the expected detector performance under the conditions of an high pile-up environment.

6.2.1 Monte Carlo samples

The MC generation of the QCD, $\gamma\gamma$, γ + jets and ZZ backgrounds is performed using `PYTHIA 8` with the CTEQ6L1 PDF and the AU2 set of tuned parameters. The WW and $t\bar{t}$ SM background events are generated using `MC@NLO` + `HERWIG` with the CT10 PDF and the AUET2 set of tuned parameters. Samples with Z+jets events are generated using `ALPGEN` + `HERWIG` with the PDF CTEQ6L1 and the AUET2 set of parameters, while $t\bar{t}Z$ samples are generated using `MADGRAPH` + `PYTHIA`, with the CTEQ6L1 PDF and AU2 set of tuned parameters. W+jets events are generated with `SHERPA` and the CT10 PDF. It should be noted that only leptons with $p_{\mathrm{T}} > 200$ GeV were made available in these centrally produced samples. Since no specific WZ sample was available, its contribution is taken into account by normalising the ZZ sample (which has a shape similar to the WZ) with scale factors taken from the WZ and ZZ samples used in Ref. [219] and [70] for $q\gamma$ for qZ, respectively.

MC samples of the signal corresponding to $t\bar{t}$ FCNC events with one of the top quarks decaying through FCNC to a γ or Z boson and the other top quark with a SM decay, are generated using `TopReX` [224] with the CTEQ6L1 PDF and AUET2B set of tuned parameters. The anomalous couplings in `TopReX` to the γ and Z bosons are set to $\kappa_{tq}^{\gamma,Z} = 0.1$, with $f = 1/\sqrt{2}$ and $|f|^2 + |h|^2 = 1$ at an energy scale of $\Lambda = 1$ TeV. Only the leptonic decays of the Z and W boson are considered. The `TopReX` generator is used instead of `PROTOS` because it was the one used by ATLAS at the time this analysis was done. A comparison between the kinematics of several particles given by both generators is shown in Figures B.14 and B.15 in Appendix B.2 and no significant differences are found between them.

6.2.2 Object definition

No full simulation of the upgraded detector is available, so a fast simulation based on parametrisations of the trigger and detector response is used instead. The functions to describe the resolutions, reconstruction and trigger efficiencies are obtained through extrapolation of the available 7 TeV data and MC simulations that include up to an average number of 69 pp interactions. The expected effects of the ATLAS detector at the HL phase [215, 225] are simulated by smearing the p_{T} and η distributions of the final state particles of the MC generated events.

The electrons and photons considered are required to be within $|\eta| < 2.47$ (excluding the transition region between the barrel and endcap electromagnetic calorimeters at $1.37 < |\eta| < 1.52$). Additionally, electrons are required to have $E_{\mathrm{T}} > 20$ GeV and photons need to have $E_{\mathrm{T}} > 40$ GeV, with the transverse energy calculated as:

$$E_{\mathrm{T}} = E_{\mathrm{cluster}}/\cosh(\eta_{\mathrm{track}}). \tag{6.2}$$

The reconstruction efficiency is taken as $0.85 - 0.19\exp(1 - p_{\mathrm{T}}/20)$ for electrons and $0.80 - 0.30\exp(1 - E_{\mathrm{T}}/25)$ for photons.

Muons are required to have $p_{\mathrm{T}} > 20$ GeV and $|\eta| < 2.5$ with a reconstruction efficiency of 97%.

Jets are reconstructed with the anti-k_t algorithm ($\Delta R = 0.4$). The efficiency to tag a b-quark jet is set at 70%. The probability of jets faking electrons is computed as the ratio between the number of jets passing the electron reconstruction and the number

Table 6.3: Parameters used in the muon momentum smearing functions.

$\lvert\eta\rvert$	a_1	a_2	b_0	b_1	b_2
< 1.05	0.01607	0.000307	0.24	0.02676	0.00012
> 1.05	0.03000	0.000387	0.00	0.03880	0.00016

of truth jets, and is given by $0.0048\exp(-0.035 p_{\mathrm{T}})$. The corresponding value for jets faking photons is fixed at 1.3%.

Moreover, photons, electrons and muons, are required to be isolated from any jet within a cone of size $\Delta R < 0.4$. If there is just one jet within a cone of size $\Delta R < 0.1$ and with an energy of at most 15% of the energy of the object, it is assumed that it is the same object (i.e. the jet algorithm wrongly reconstructed the object).

Finally, the energies of the different objects are smeared to simulate the detector resolution. For the electron and photons, energy resolution is simulated by Gaussian smearing the energy with a $\sigma_E/E = 10\%/\sqrt{E} + 1\%$ for $|\eta| < 1.4$, and $\sigma_E/E = 15\%/\sqrt{E} + 1.5\%$ for $|\eta| > 1.4$. The muon energy is smeared with:

$$\sigma = \frac{\sigma_{\mathrm{ID}}\sigma_{\mathrm{MS}}}{\sqrt{(\sigma_{\mathrm{ID}})^2 + (\sigma_{\mathrm{MS}})^2}}, \tag{6.3}$$

$$\sigma_{\mathrm{ID}}/p_{\mathrm{T}} = \sqrt{a_1^2 + (a_2 p_{\mathrm{T}})^2}, \tag{6.4}$$

$$\sigma_{\mathrm{MS}}/p_{\mathrm{T}} = \sqrt{(b_0/p_{\mathrm{T}})^2 + b_1^2 + (b_2 p_{\mathrm{T}})^2}. \tag{6.5}$$

The parameter values are in Table 6.3. Jets are smeared using

$$\sigma = \sqrt{(A + 150B)^2/p_{\mathrm{T}}^2 + S^2/p_{\mathrm{T}} + C^2}, \tag{6.6}$$

with A, B, S and C values given in Table 6.4. Lastly, the components of the missing transverse energy are smeared with

$$\sigma = (0.4 + 0.09\sqrt{\mu})\sqrt{\Sigma E_{\mathrm{T}} + 20\mu}, \tag{6.7}$$

where μ is the number of pile-up events.

Only events passing a single electron or muon trigger are considered. The trigger is simulated assigning a probability to an electron or muon of activating the trigger. For the electron trigger, an 88% chance is assigned to an electron with energy above

Table 6.4: Parameter values for the jet energy smearing, for the different η coverage.

$\lvert\eta\rvert$	A	B	S	C
$0 - 0.8$	3.16	0.07	0.74	0.055
$0.8 - 1.2$	3.03	0.07	0.85	0.053
$1.2 - 2.8$	3.32	0.08	0.56	0.056
$2.8 - 3.6$	2.84	0.11	0.83	0.054

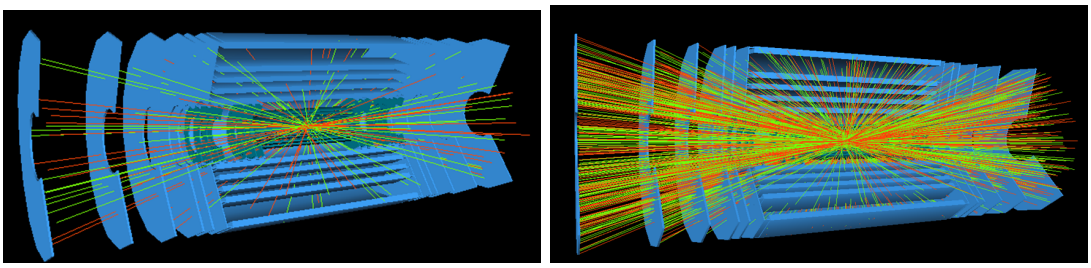

(a) (b)

Figure 6.2: The layout of the Inner Detector, traversed by simulated (a) 23 pile-up events and (b) 230 pile-up events. Taken from [226].

25 GeV and $|\eta| < 2.5$ to activate the trigger. For the muon trigger, at least one muon with an energy above 25 GeV and $|\eta| < 2.4$ is required to pass the trigger, with a 64% efficiency for $|\eta| < 1$ and 86% for $|\eta| > 1$.

For luminosities of 5–7 $\times 10^{34}$ cm^{-2}s^{-1}, around 140–200 events of pile-up are expected, significantly higher than the current average numbers (see Figure 3.5). For a comparison, a simulation of the inner detector with two pileup scenarios is shown in Figure 6.2. Reconstruction is performed assuming 140 pile-up events. To check the impact in the reconstruction, different pile-up values are tested. A summary of the resolutions of the reconstructed Z boson, W boson, top-quark with the FCNC decay and top-quark with the SM decay is shown in Table 6.5, for the qZ channel. No significant impact in the χ^2 reconstruction is observed.

6.2.3 Sequential analyses

The different top-quark FCNC decay modes lead to different final states topologies, according to the number of leptons, jets and photons present in the final state. The different channels assume the dominant SM decay $t \to bW$, where the W boson decays

Table 6.5: Standard deviation of a Gaussian fit, in GeV, to the reconstructed mass distributions of the analysis objects, obtained with the χ^2 minimisations, for different pile-up values.

μ	60	80	140	150	200
t_{FCNC}	14	13	12	13	13
t_{SM}	33	31	31	29	35
W	17	17	17	16	17
Z	2	2	2	2	2

leptonically ($W \to \ell\nu_\ell$, with $\ell = e,\ \mu,\ \tau$) and an FCNC $t \to q\gamma$ or $t \to qZ$ decay, again with a leptonic decay for the Z boson ($Z \to \ell^+\ell^-$). The analyses described in Ref. [186, 223] are used as a starting point. The preselection and final selection requirements of those analyses are summarised in Table 6.6.

The final states of the $q\gamma$ channel are characterised by a topology with one isolated high p_{T} photon, one isolated lepton, missing transverse momentum from the undetected neutrino and two jets (one b-tagged jet from the SM top quark decay, and another jet originated from the c- or u-quark decay of the FCNC top-quark decay). At the preselection exactly one isolated lepton (in a cone of size $\Delta R < 0.4$) is required with $p_{\text{T}} > 25$ GeV and $|\eta| < 2.5$, only one photon with $p_{\text{T}} > 25$ GeV and $|\eta| < 2.5$ and at least two jets with $p_{\text{T}} > 20$ GeV and $|\eta| < 2.5$. A missing transverse momentum greater than 20 GeV is also required.

For the qZ channel, the only topology considered is $t\bar{t} \to b\ell\nu q\ell\ell$, with three charged leptons (two of which reconstruct a Z boson), large missing transverse momentum due to the neutrino, and at least two jets (one of which is b-tagged). For this channel, the preselection requires exactly three isolated leptons (within a cone of size $\Delta R > 0.4$) with $p_{\text{T}} > 25$ GeV for the leading lepton and $p_{\text{T}} > 20$ GeV for the other two with the highest transverse momenta and $|\eta| < 2.5$. Additionally, two of the leptons are required to have opposite charge and their reconstructed masses be within 15 GeV of the known Z boson mass, $m_Z = 91.19$ GeV. Also, at least two jets with $p_{\text{T}} > 25$ GeV and $|\eta| < 2.5$, and missing transverse momentum higher than 20 GeV are required.

6.2.4 Kinematic Reconstruction

As explained in Section 5.3.2, the four-momentum of the neutrino from the top-quark SM decay can be estimated by minimizing a χ^2 function. Equation 5.3 is used for the minimisation in the $t \to qZ$ and $t \to q\gamma$ channels. For the $t \to q\gamma$ channel the Z term is not included in the χ^2 minimization.

In order to reduce the background contributions, further selection cuts are applied. For the $q\gamma$ channel, events are rejected if the reconstructed mass of the lepton and photon is reconstructed within 15 GeV of the Z boson mass and the missing transverse momentum is less than 50 GeV. This requirement allows to remove events from the Z+jets background in which an electron is misidentified as a photon. Also, at the final selection, the photon is required to have $p_{\mathrm{T}} > 60$ (50) GeV if the lepton is an electron (muon).

In the 7 TeV analyses, a mass window cut is applied to the reconstructed objects in both channels in order to further reduce the expected background, instead of a single cut in the χ^2 distribution used in the 8 TeV analysis described in Section 5.3.2. In view of the high pile-up environment, there is $E_{\mathrm{T}}^{\mathrm{miss}}$ and jet energy resolution degradation that leads to worse signal resolution, as shown in Figure 6.3. By applying the same mass cuts, the signal efficiencies drop to 38% (instead of the 79% efficiency seen in the 7 TeV analyses), so these cuts are not applied. Instead, to improve the signal/background ratio, at least one b-tagged jet is required in both channels, mirroring the requirement applied in the 8 TeV analysis.

The number of expected background and signal events at the final selection level is shown in Table 6.7 for a luminosity of 3 ab^{-1}. No QCD, $\gamma\gamma$ and γj events survive the selection, thus they are not included in the table. Relevant distributions after the final selection are shown in Figures 6.4 and 6.5 for the $q\gamma$ channel and in Figures 6.6 and 6.7 for the qZ channel.

6.2.5 Discriminant analysis

Following the final selection, a likelihood-based analysis can be applied. Signal- and background-like probabilities are computed for each event, $\mathcal{P}_i^{Signal}$ and $\mathcal{P}_i^{Back}$ respectively, using pdfs of relevant physical variables: χ^2, mass of the reconstructed top

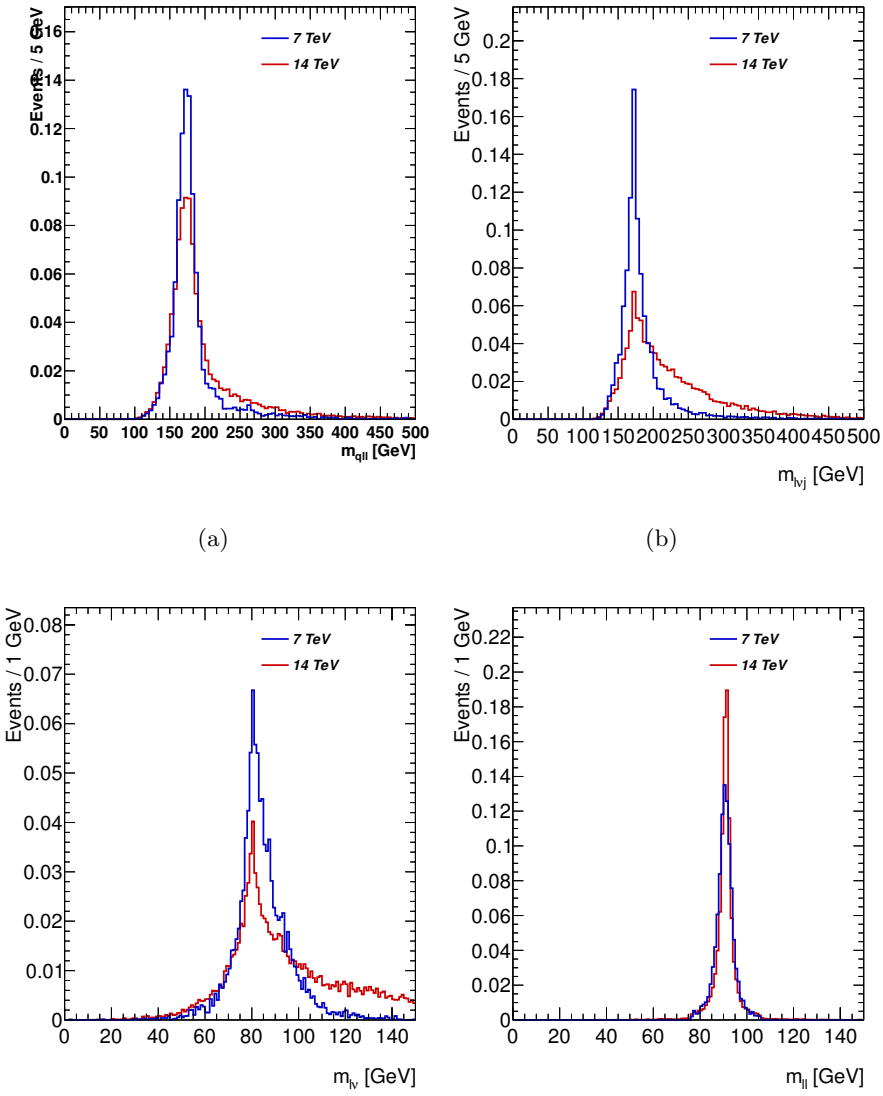

(a) (b)

(c) (d)

Figure 6.3: Reconstructed masses at a centre-of-mass energy of 7 and 14 TeV, of the (a) top-quark with the FCNC decay, (b) top-quark with the SM decay, (c) W boson and (d) Z boson.

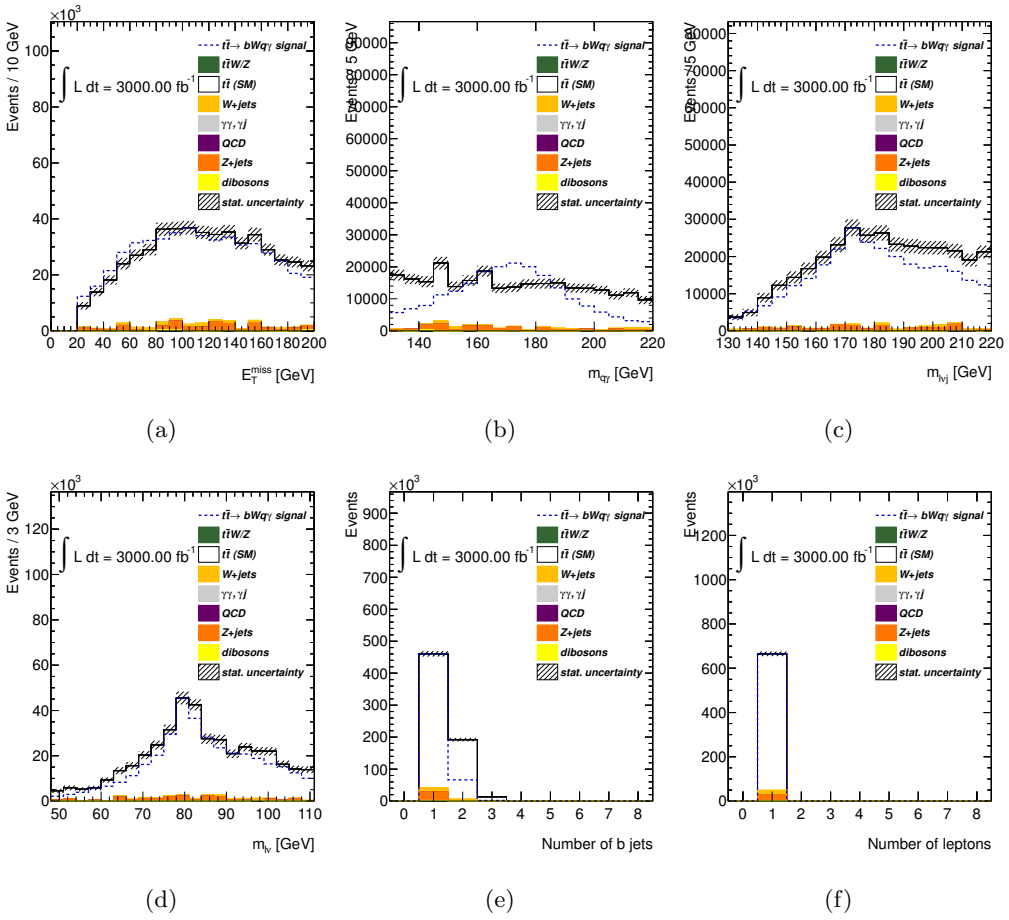

Figure 6.4: Distributions obtained after the final selection of the $t \rightarrow q\gamma$ analysis for the (a) missing transverse momentum, (b) reconstructed mass of the top-quark with the FCNC decay, (c) reconstructed mass of the top-quark with the SM decay, (d) reconstructed mass of the W boson, (e) number of b-tagged jets and (f) number of leptons. The signal distributions have arbitrary normalisation.

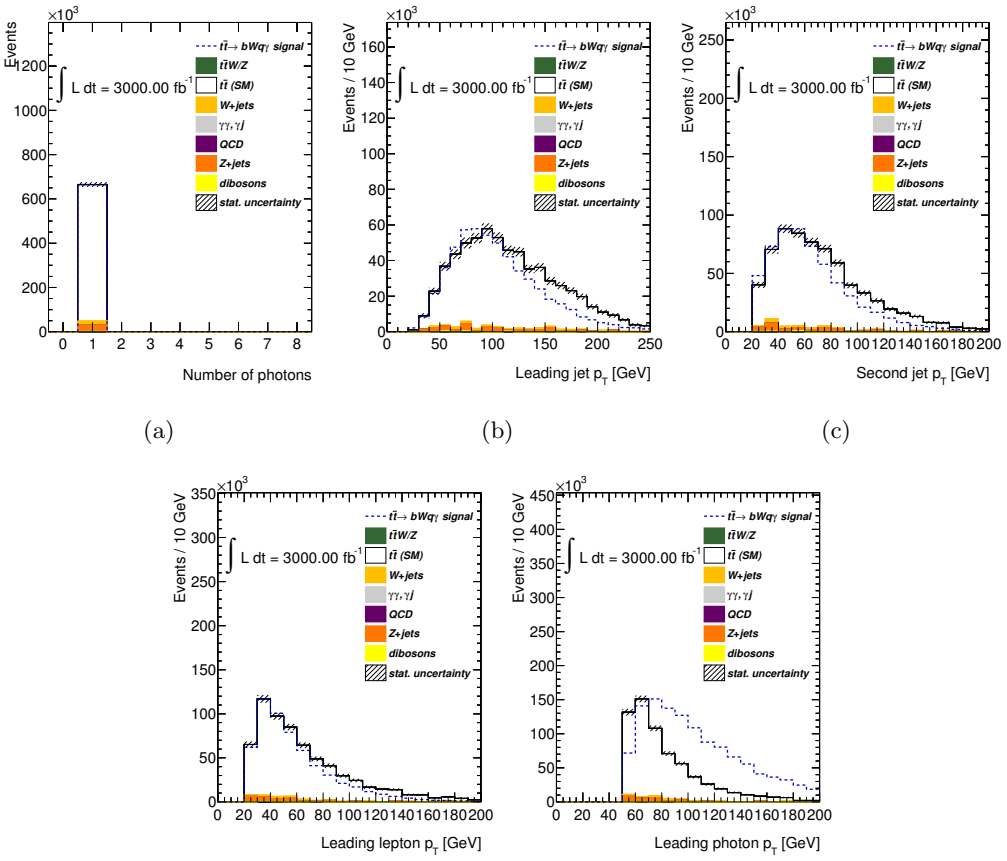

Figure 6.5: Distributions obtained after the final selection of the $t \to q\gamma$ analysis for the (a) number of photons and p_{T} of the (b) leading jet, (c) sub-leading jet, (d) lepton and (e) photon. The signal distributions have arbitrary normalisation.

Table 6.6: Summary of the selection cuts applied in the qZ and $q\gamma$ analyses. Additionally, the leptons, photons and jets are required to have $|\eta|$ <2.5.

channel	$t\bar{t} \to bWq\gamma$	$t\bar{t} \to bWqZ$
Trigger	Single lepton	Single lepton
Pre-selection	$= 1\ell$ ($p_{\mathrm{T}} > 25$ GeV)	$= 3\ell$ ($p_{\mathrm{T}} > 25,\ 20,\ 20$ GeV)
	≥ 2j ($p_{\mathrm{T}} > 20$ GeV)	≥ 2j ($p_{\mathrm{T}} > 25$ GeV)
	$= 1\gamma$ ($p_{\mathrm{T}} > 25$ GeV)	
	$\not{p}_{\mathrm{T}} > 25$ GeV	$\not{p}_{\mathrm{T}} > 25$ GeV
Final selection	≥ 1 b-tagged jet	≥ 1 b-tagged jet
	$p_{\mathrm{T}}^{\gamma} > 60(50)$ GeV, if $\ell = e(\mu)$	

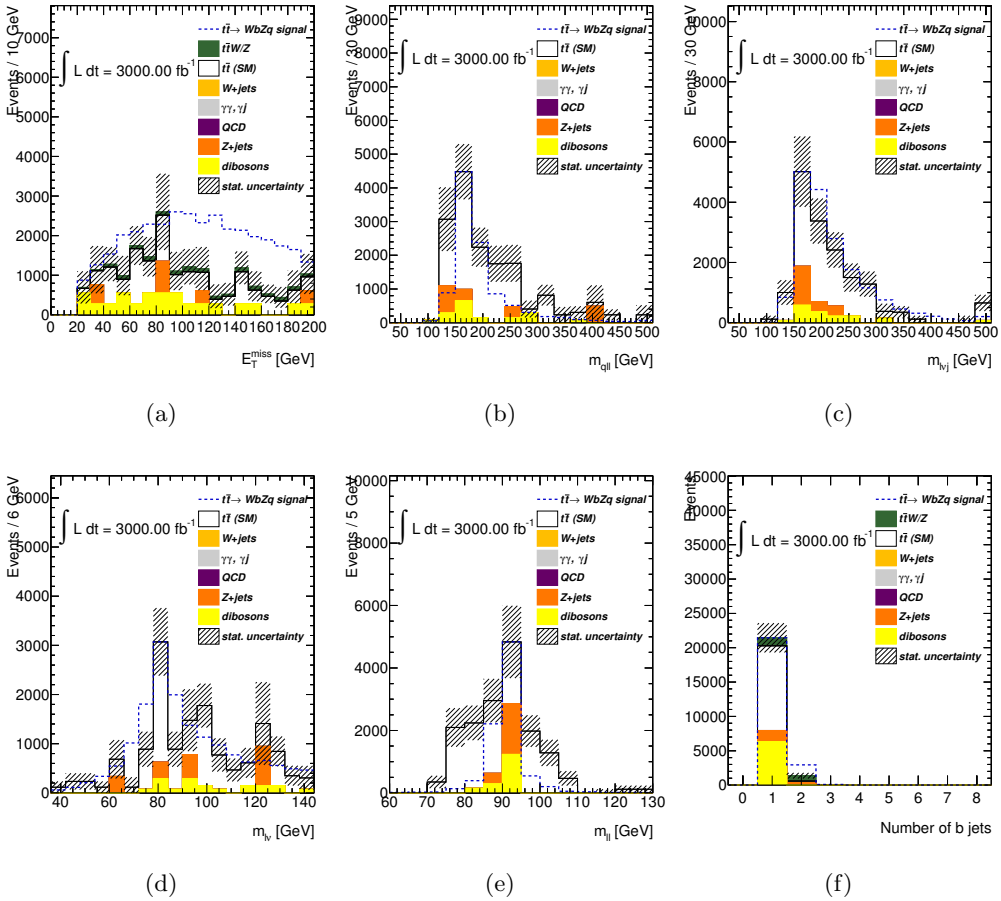

Figure 6.6: Distributions obtained after the final selection of the $t \to qZ$ analysis for the (a) missing transverse momentum, (b) reconstructed mass of the top-quark with the FCNC decay, (c) reconstructed mass of the top-quark with the SM decay, (d) reconstructed mass of the W boson, (e) reconstructed mass of the Z boson and (f) number of b tagged jets. The signal distributions have arbitrary normalisations.

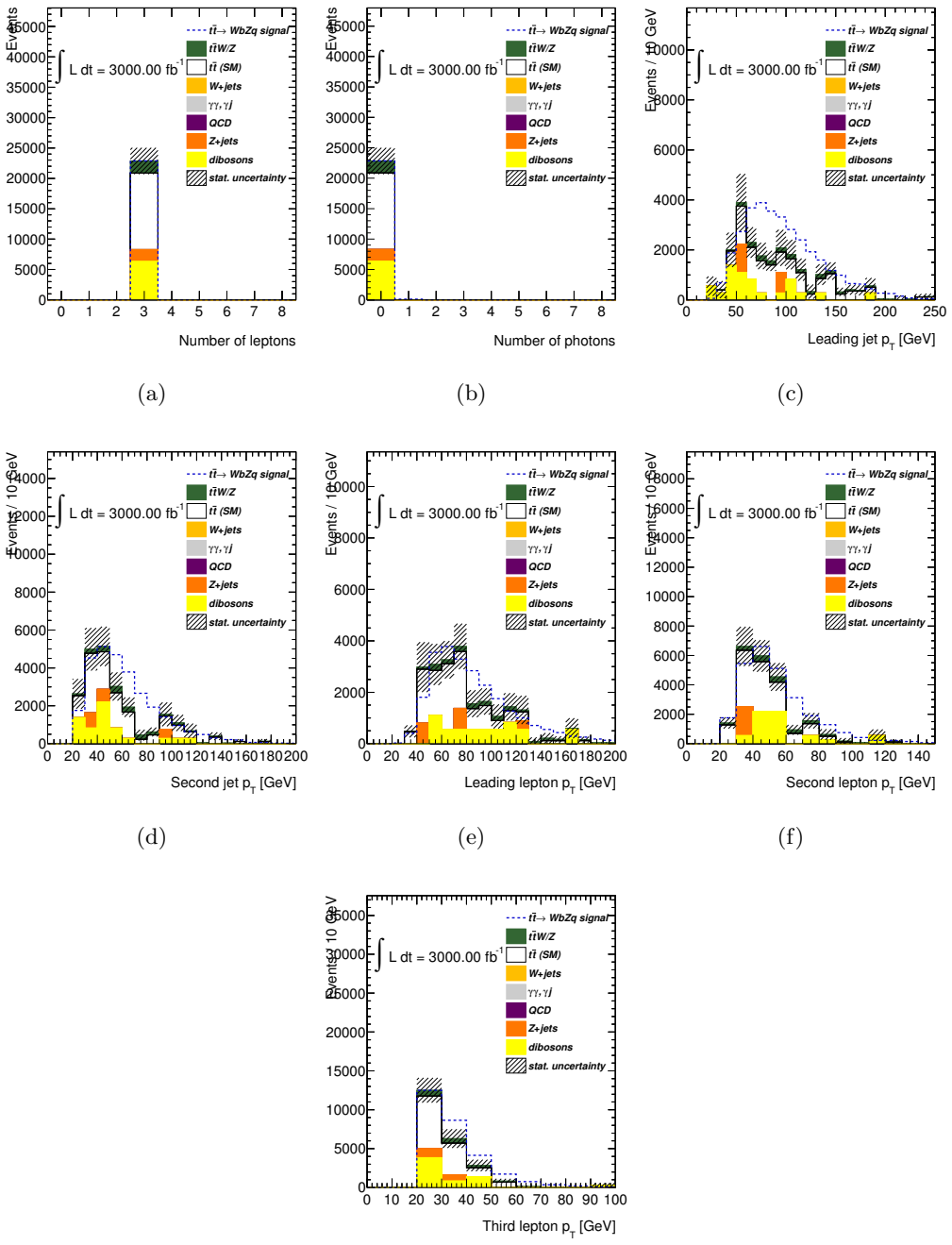

(a) (b) (c)

(d) (e) (f)

(g)

Figure 6.7: Distributions obtained after the final selection of the $t \to qZ$ analysis for the (a) number of leptons, (b) number of photons and p_{T} of the (c) leading jet, (d) sub-leading jet, (e) leading lepton and (f) sub-leading lepton and (g) third highest p_{T} lepton. The signal distributions have arbitrary normalisations.

Table 6.7: The number of selected background events, normalised to $L = 3$ ab^{-1}. Statistical and systematic uncertainties are taken into account as $\sqrt{B}$.

Channel	$t\bar{t} \to bWq\gamma$	$t\bar{t} \to bWqZ$
Dibosons	1773 ± 531	6325 ± 1319
Z+jets	27353 ± 3499	1958 ± 1050
W+jets	19365 ± 1522	—
$t\bar{t}$ (SM)	616122 ± 9614	12576 ± 1368
$t\bar{t}Z$	446 ± 45	2013 ± 96
Total background	665058 ± 10357	22873 ± 2173
Signal efficiency [$\times 10^{-2}$]	1.799 ± 0.014	0.118 ± 0.001

quark from the FCNC decay and transverse momentum of the photon for the $q\gamma$ channel; minimum mass of two out of the three leptons, mass of the three leptons and mass of reconstructed top quark from the FCNC decay for the qZ channel (Figure 6.8).

Then, signal ($\mathcal{L}_S$) and background ($\mathcal{L}_B$) likelihoods are defined as:

$$\mathcal{L}_S = \prod_{i=1}^{n} \mathcal{P}_i^{\text{signal}} \text{ and } \mathcal{L}_B = \prod_{i=1}^{n} \mathcal{P}_i^{\text{back}}, \tag{6.8}$$

with n being the number of pdfs. These likelihoods are used to define a discriminant variable $L_R = \log_{10}(\mathcal{L}_S/\mathcal{L}_B)$. The ratio between these two probabilities discriminates signal-like events from background-like ones, L_R being higher for signal-like events than for background-like events. The distributions of the discriminant variables are presented in Figure 6.9.

The expected limits at 95% CL are derived using the CLs method and then converted into limits on the BR using the SM $t\bar{t}$ production cross-section. Background statistical and systematic uncertainties are taken into account as $\sqrt{B}$. The central values of these limits are shown in Table 6.8 along with the $\pm 1\sigma$ bands.

6.3 Conclusions

Results are about a factor 2.3 (1.3) for $q\gamma$ (qZ) better on the full analysis than on the extrapolated projection. The large factor of the $q\gamma$ can be explained by the fact that simulated samples for some of the main backgrounds in this channel were not available at the time this work was performed, like W+jets with leptons (the ones available only

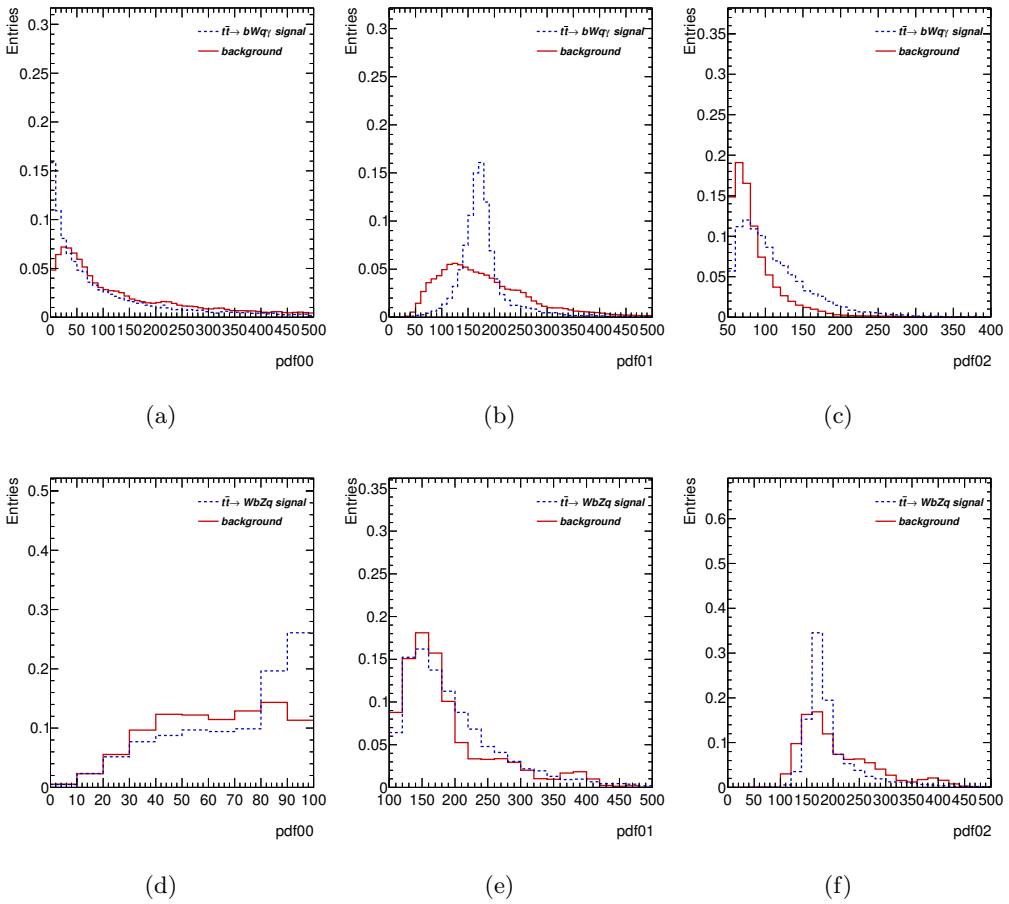

Figure 6.8: The pdfs of the variables used to compute the signal- and background-like probabilities for the $q\gamma$ channel: (a) χ^2 probability, (b) mass of reconstructed top quark from the FCNC decay, (c) transverse momenta of the photon; for the qZ channel: (d) minimum mass of two out of three leptons, (e) mass of the three leptons and (f) mass of reconstructed top quark from the FCNC decay.

Table 6.8: The expected 95% confidence level limits on the FCNC top quark decay BR, in the absence of signal, are shown for a luminosity of $L = 3$ ab^{-1}. The central values are presented with the 1σ bands, which include the contribution from the statistical and systematic uncertainties as $\sqrt{B}$.

	(-1σ)	expected	(+1σ)
$q\gamma$	4.1×10^{-6}	4.7×10^{-6}	6.0×10^{-6}
qZ	2.5×10^{-5}	3.1×10^{-5}	4.4×10^{-5}

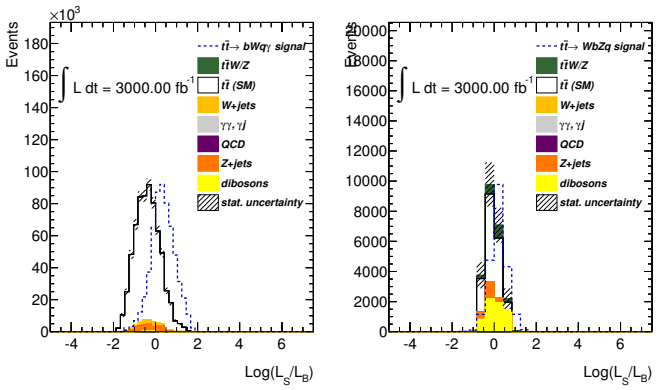

(a) (b)

Figure 6.9: Distributions of the normalized discriminant variables for the expected background and signal for FCNC channels (a) $t \to q\gamma$ and (b) $t \to qZ$.

had leptons with $pT > 200$ GeV). With all the background samples the estimation for the $q\gamma$ channel could be improved and it would be between the values derived with the extrapolation method and the dedicated analysis presented here. A summary of the results as well as previous experimental limits are summarised in Figure 6.10. It is clear that the sensitivity greatly improves with increased luminosity, allowing to probe BRs of the order of $\sim 10^{-5}$ and $\sim 10^{-6}$ on $q\gamma$ and qZ channel, respectively. This sensitivity allows to test and constrain some of the models outlined in Table 2.2.

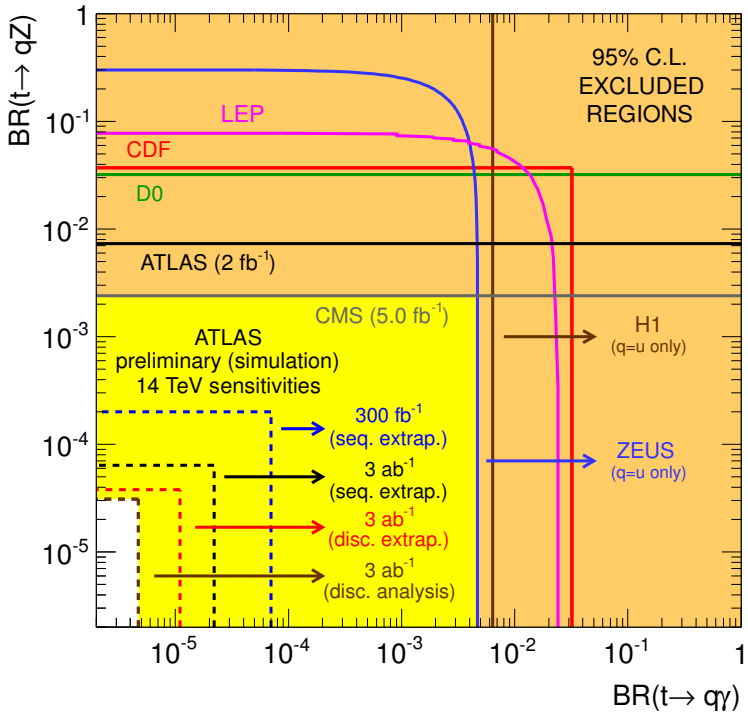

Figure 6.10: The present 95% CL observed limits on the BR($t \to q$) vs. BR($t \to qZ$) plane are shown as full lines for the LEP, ZEUS, H1, D0, CDF, ATLAS and CMS collaborations [2]. The expected sensitivity for ATLAS is also represented by the dashed lines. For an integrated luminosity of $L = 3$ ab^{-1} the limits range from 5.5×10^{-6} to 2.5×10^{-5} (2.5×10^{-5} to 7.2×10^{-5}) for the $t \to q\gamma$ ($t \to qZ$). Limits at $L = 300$ fb^{-1} are also shown. Taken from [215]

7

Conclusions

In the first topic of the doctoral work, a study of the ATLAS hadronic calorimeter (TileCal) PMTs stability and linearity was performed [227], by measuring the signal of each PMT as a function of either time or signal measured by a LASER system PD. A method to monitor the stability of the PMTs between cesium runs and flag them, depending on the χ^2 of the fit, was presented along with a way of identifying specific PMT topological behaviours by correlating them to HV jumps. For the linearity it was described a method to calculate deviations from linearity by fitting a line to the linear range of the PMT, taking into account the ones that reach saturation. Both the stability and linearity methods presented allow to monitor all the PMTs of the TileCal and also to identify the ones deviating from the expected behaviour.

In the second topic of the studies, a search for the FCNC decay $t \to qZ$ was implemented. The signal considered was $t\bar{t}$ production with one top-quark decaying through the FCNC $t \to qZ$ channel and the other through the dominant SM $t \to bW$ mode, using only leptonic decays of the Z and W bosons. The full dataset of 20.3 fb^{-1} was analised, collected from proton–proton collisions with the ATLAS detector in 2012. No evidence of signal was found, therefore an observed (expected) upper limit was set in the BR of 7×10^{-4} (8×10^{-4}) [200]. These results are consistent with the ones from the CMS Collaboration and an order of magnitude better than previous ATLAS results.

In the last topic, the sensitivity for top-quark FCNC decays $t \to qZ$ and $t \to q\gamma$, in the context of the future HL-LHC is estimated, where luminosities of the order of 3 ab^{-1} are expected to be collected. With this luminosity increase, the sensitivity for

these rare decays greatly improves, allowing to probe BRs of the order of 10^{-5} and 10^{-6} on the top-quark decays, $t \to q\gamma$ and $t \to qZ$, respectively [215, 216]. This increased reach will allow to further test or constrain some of the proposed extensions to the SM.

Appendix A

LASER performance distributions

A.1 Example distributions of the PMT stability survey

Figures A.1–A.3 show example distributions of PMTs with stabilities classified respectively as “good”, “bad” and “ugly”.

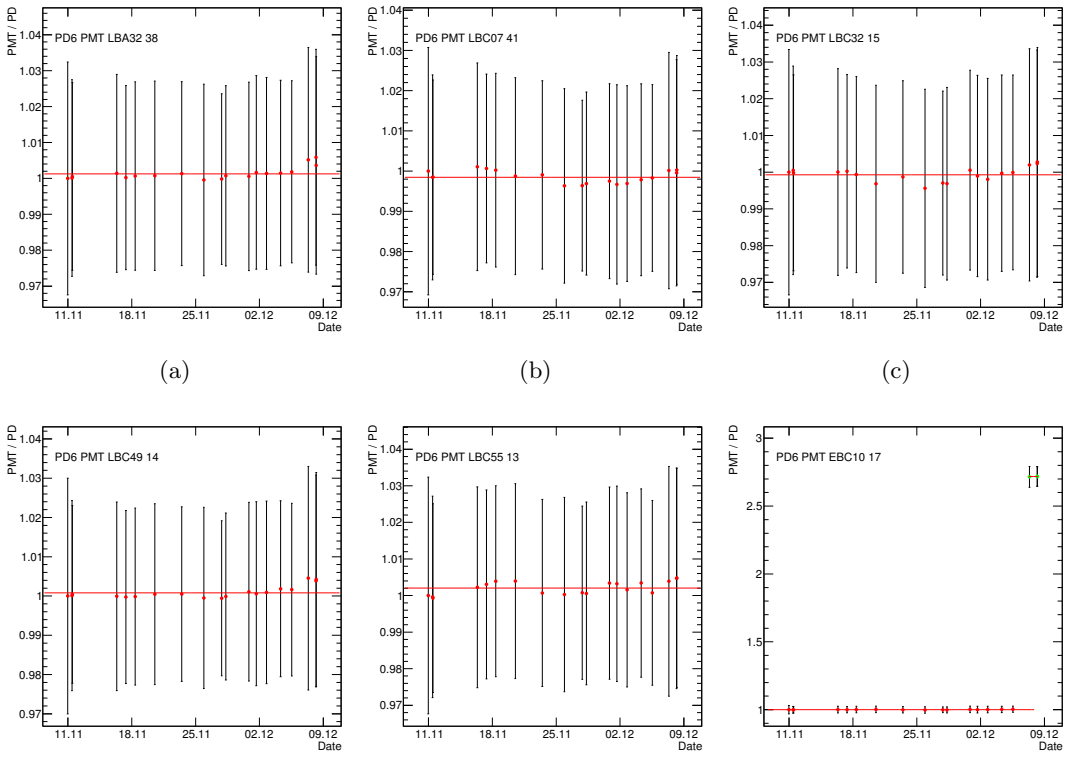

(a) (b) (c)

(d) (e) (f)

Figure A.1: Distribution of the ratio between the signals measured by a PMT and the signals measured by PD 6, as a function of time, for (a) PMT 6 of LBA 32, (b) PMT 41 of LBC 7, (c) PMT 15 of LBC 32, (d) PMT 14 of LBC 49, (e) PMT 13 of LBC 55 and (f) PMT 17 of EBC 10, tagged as good by the method. These PMTs are not tagged in the COOL DB. The red line shows the resulting fit.

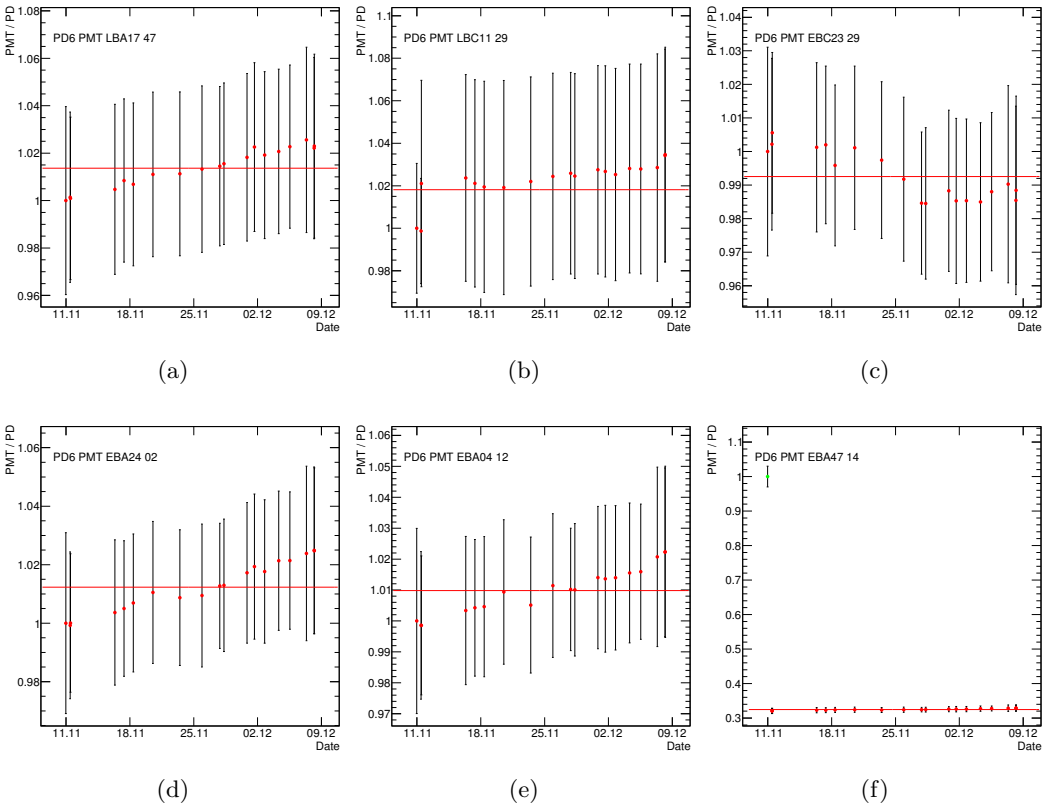

(a) (b) (c)

(d) (e) (f)

Figure A.2: Distribution of the ratio between the signals measured by a PMT and the signals measured by PD 6, as a function of time, for (a) PMT 47 of LBA 17, (b) PMT 29 of LBC 11, (c) PMT 29 of EBC 23 (d) PMT 2 of EBA 24 (e) PMT 12 of EBA 4 and (f) PMT 14 of EBA 47, tagged as bad by the method. The first three PMTs are tagged in the COOL DB respectively as "Bad laser calibration", "Severe stuck bit" and "Bad & ADC masked; Bad CIS calibration", while the last three do not have problems identified there. The red line shows the resulting fit.

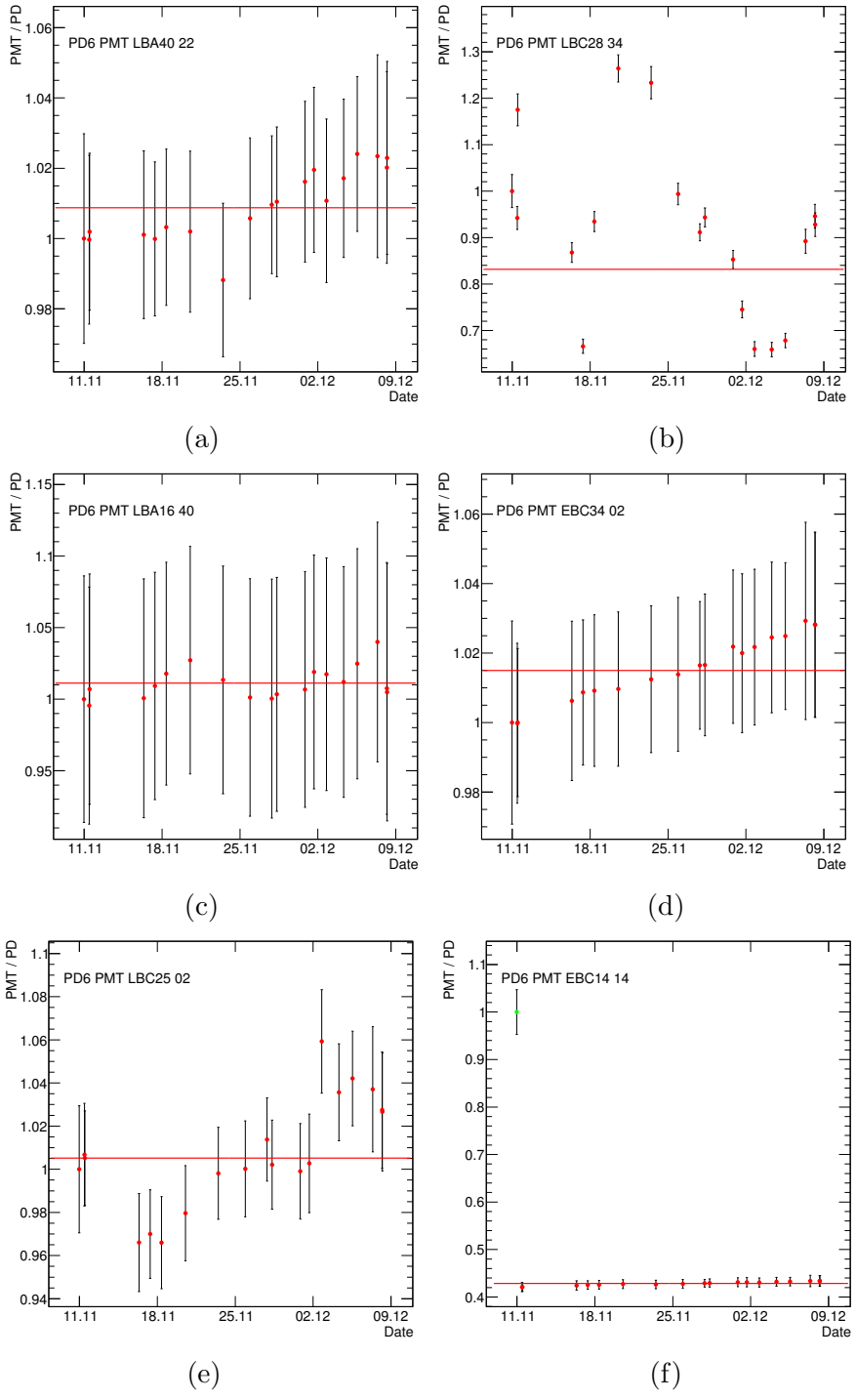

Figure A.3: Distribution of the ratio between the signals measured by a PMT and the signals measured by PD 6, as a function of time, for (a) PMT 22 of LBA 40, (b) PMT 34 of LBC 28, (c) PMT 40 of LBA 16, (d) PMT 2 of EBC 34, (e) PMT 2 of LBC 25 and (f) PMT 14 of EBC 14, tagged as ugly by the method. The first three PMTs are tagged in the COOL DB respectively as "ADC masked; Bad CIS", "Bad laser calibration" and "Severe stuck bit"', while the last three does not have problems identified there. The red line shows the resulting fit.

A.2 Example distributions of the PMT linearity survey

Figures A.4–A.8 show example distributions of PMTs with linearities classified respectively as “good”, “regular”, “bad”, “ugly” and “dwarf”.

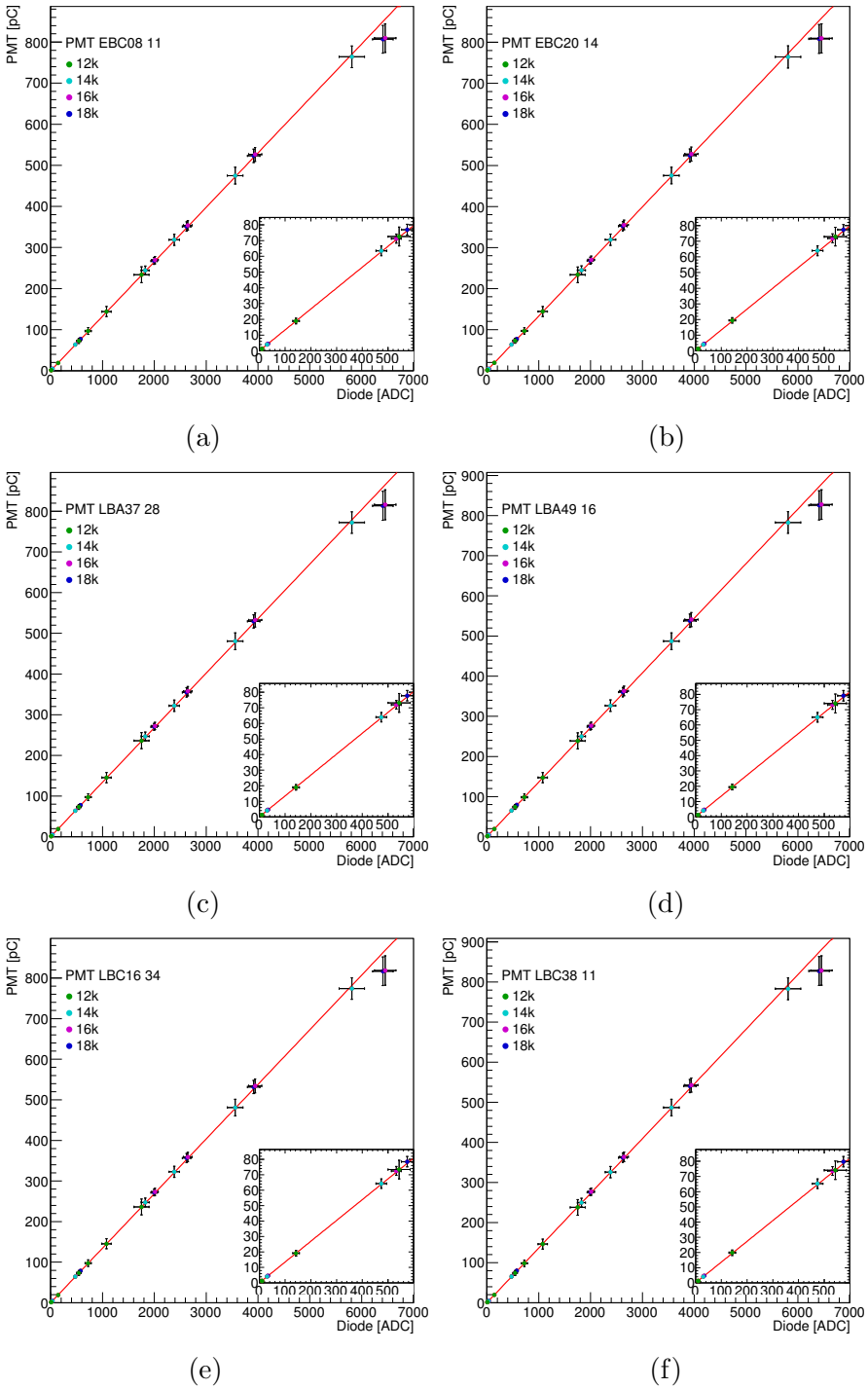

Figure A.4: Distribution of the signals measured by a PMT versus the signals measured by PD 6, for (a) PMT 11 of EBC 8, (b) PMT 14 of EBC 14, (c) PMT 28 of LBA 37, (d) PMT 16 of LBA 49, (e) PMT 34 of LBC 16 and (f) PMT 11 of LBC 38, tagged as good by the method. These PMTs are not tagged in the COOL DB. The red line shows the resulting fit.

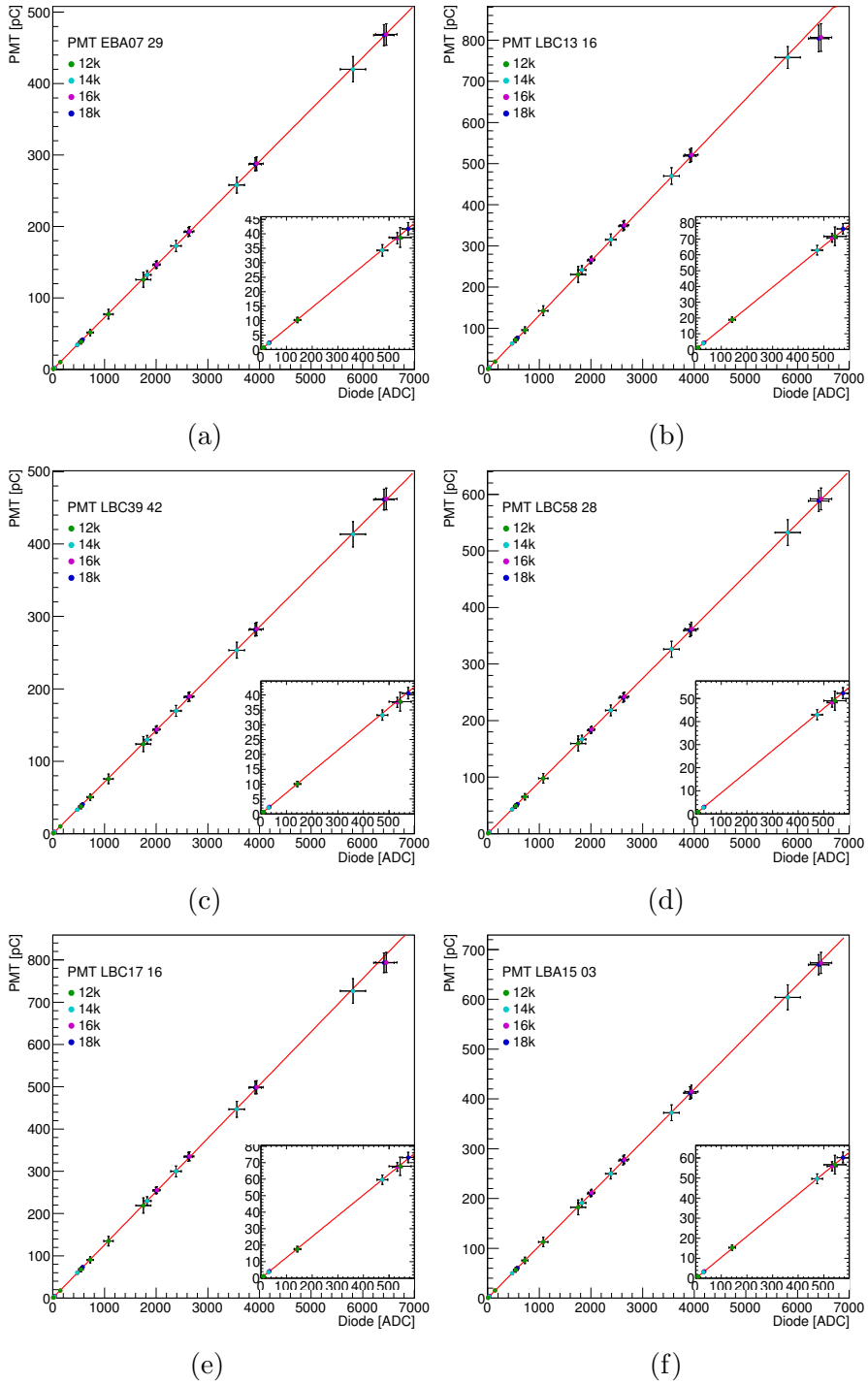

Figure A.5: Distribution of the signals measured by a PMT versus the signals measured by PD 6, for (a) PMT 29 of EBA 7, (b) PMT 16 of LBC 13, (c) PMT 42 of LBC 39, (d) PMT 28 of LBC 58, (e) PMT 16 of LBC 17 and (f) PMT 3 of LBA 15, tagged as regular by the method. The PMTs are tagged in the COOL DB respectively as 'ADC masked; Bad CIS calibration", "Bad timing", "Stuck bit", "ADC masked; Data corruption", "Bad laser calibration" and "ADC masked; Bad timing". The red line shows the resulting fit.

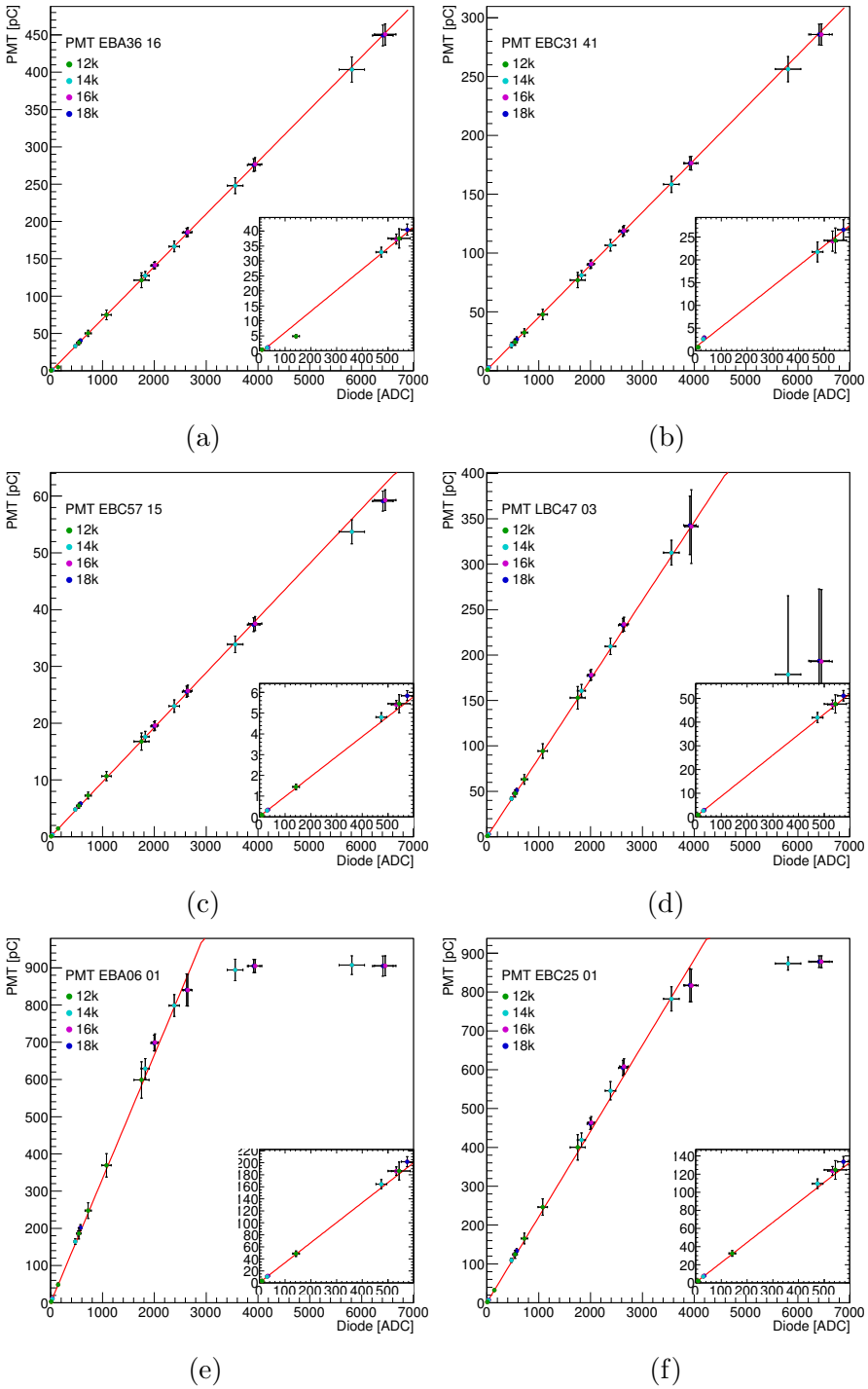

Figure A.6: Distribution of the signals measured by a PMT versus the signals measured by PD 6, for (a) PMT 16 of EBA 36, (b) PMT 41 of EBC 31, (c) PMT 15 of EBC 57, (d) PMT 3 of LBC 47, (e) PMT 1 of EBA 6 and (f) PMT 1 of EBC 25, tagged as bad by the method. The first five PMTs are tagged in the COOL DB respectively as "ADC masked; Bad CIS calibration", "Bad CIS calibration; No cesium calibration", "Bad cesium calibration; Bad laser calibration; Channel masked" and "ADC masked; Bad CIS calibration; Severe stuck bit", while the last two do not have problems identified there. The red line shows the resulting fit.

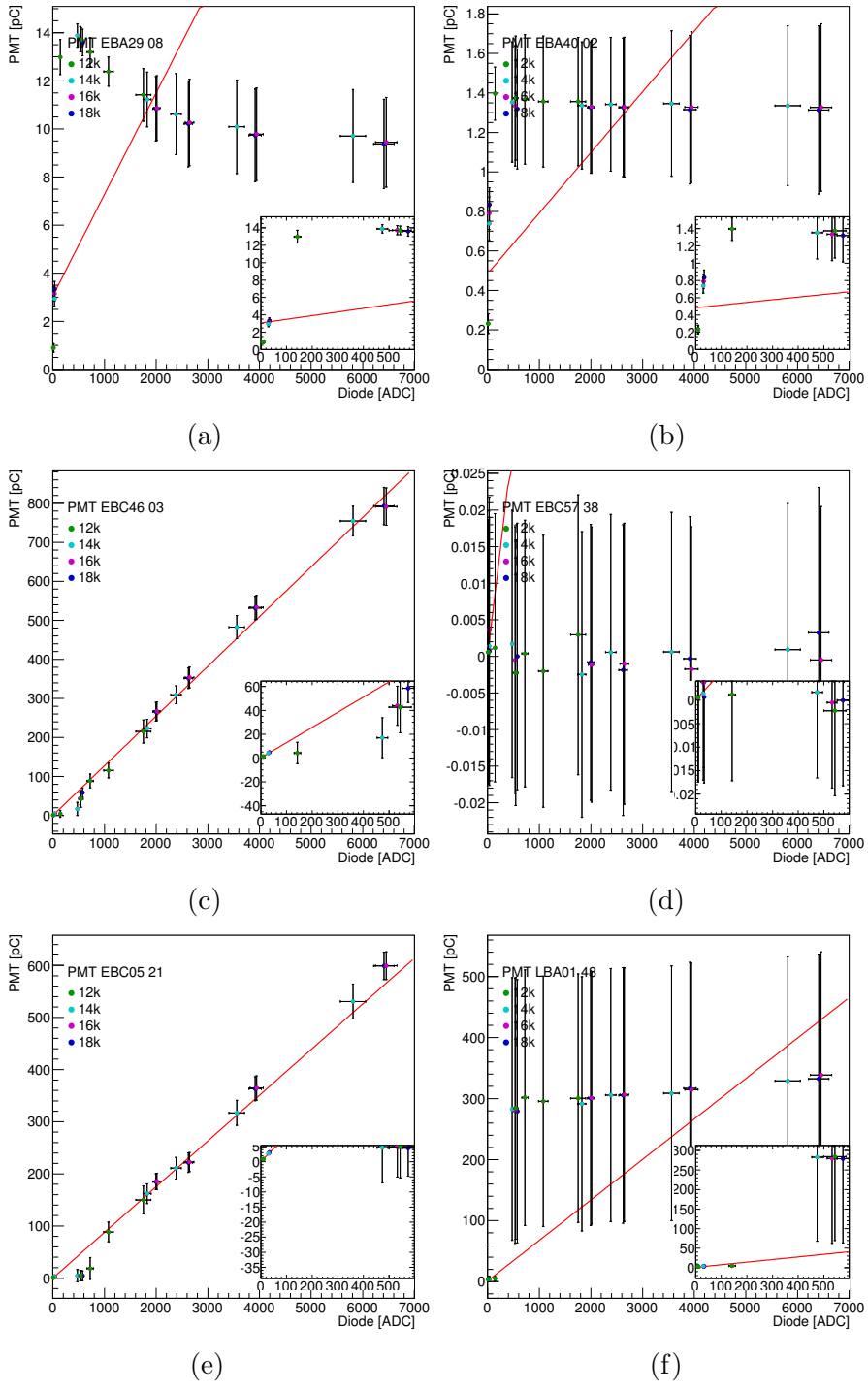

Figure A.7: Distribution of the signals measured by a PMT versus the signals measured by PD 6, for (a) PMT 8 of EBA 29, (b) PMT 2 of EBA 40, (c) PMT 3 of EBC 46, (d) PMT 38 of EBC 57, (e) PMT 21 of EBC 5 and (f) PMT 48 of LBA 1, tagged as ugly by the method. The PMTs are tagged in the COOL DB respectively as "Stuck bit", "ADC masked; Bad CIS calibration", "Severe stuck bit", "Bad CIS calibration; Severe stuck bit" and "Channel masked; No cesium calibration; No laser calibration", while the last one does not have problems identified there. The red line shows the resulting fit.

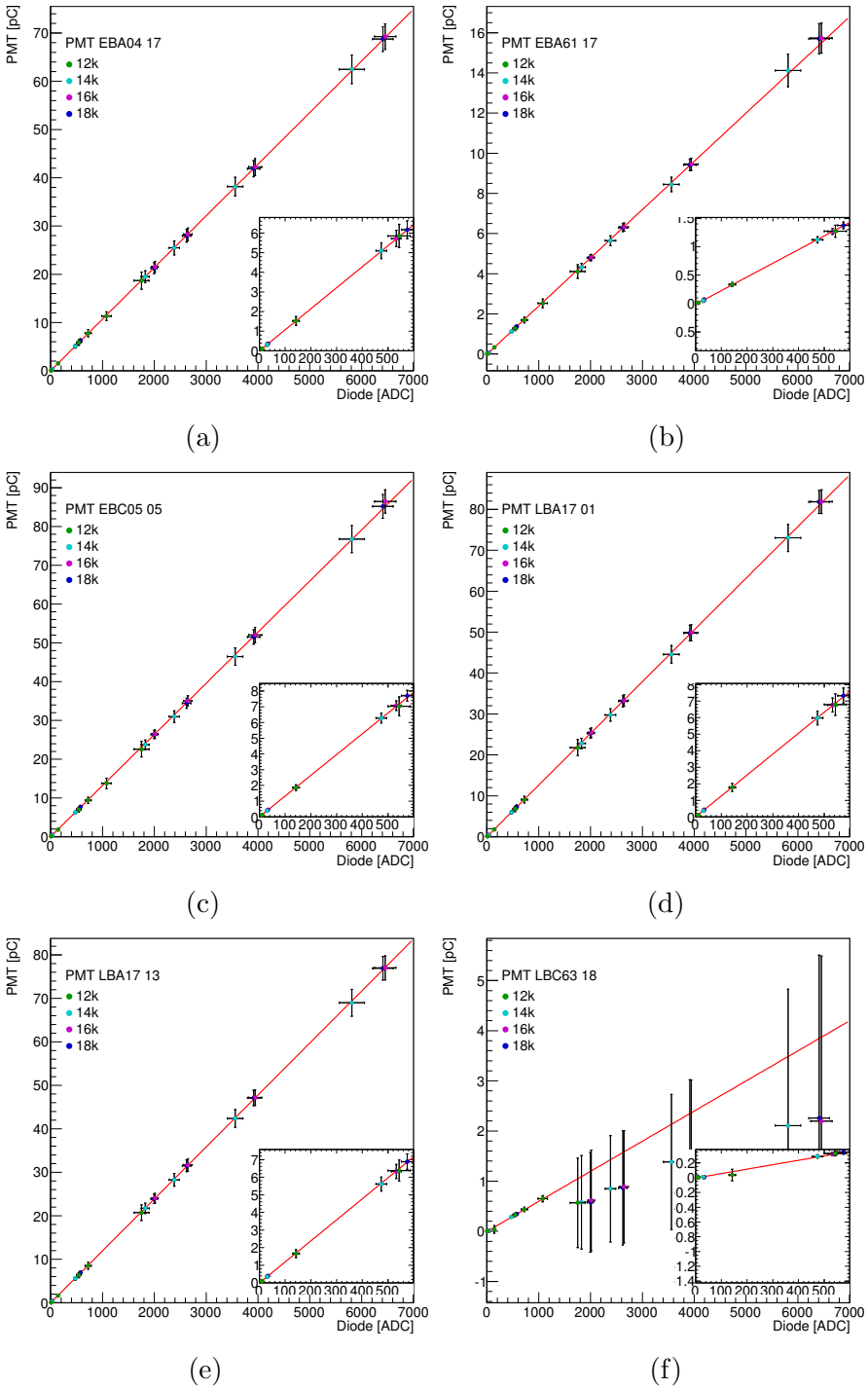

Figure A.8: Distribution of the signals measured by a PMT versus the signals measured by PD 6, for (a) PMT 17 of EBA 4, (b) PMT 17 of EBA 61, (c) PMT 5 of EBC 5, (d) PMT 1 of LBA 17, (e) PMT 13 of LBA 17 and (f) PMT 18 of LBC 63, tagged as dwarf by the method. The PMTs are tagged in the COOL DB respectively as " Bad laser calibration", "Bad cesium calibration; Channel masked; No laser calibration", "Bad cesium calibration; Bad laser calibration; Channel masked", "Bad laser calibration", "Bad laser calibration" and "ADC masked". The red line shows the resulting fit.

Appendix B

PROTOS distributions

B.1 The effect of different coupling values

The following distributions compare the effect of different coupling values in various observables.

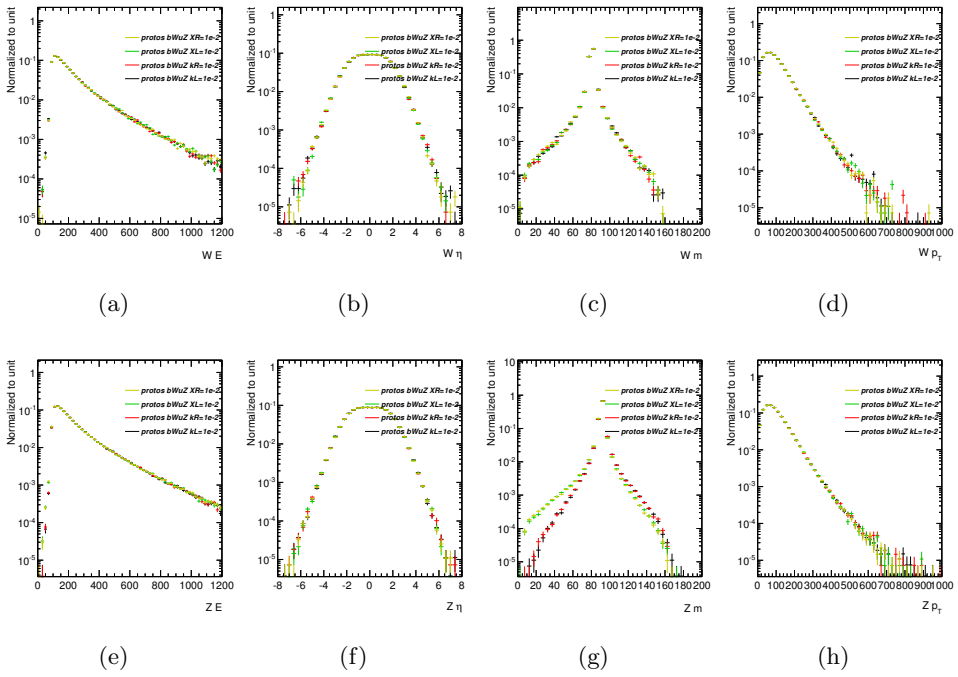

(a) (b) (c) (d)

(e) (f) (g) (h)

Figure B.1: Comparison of the effect of different coupling values on the (a) and (e) energy, (b) and (f) η, (c) and (g) mass and (d) and (h) p_{T} of the W boson and the Z boson, respectively.

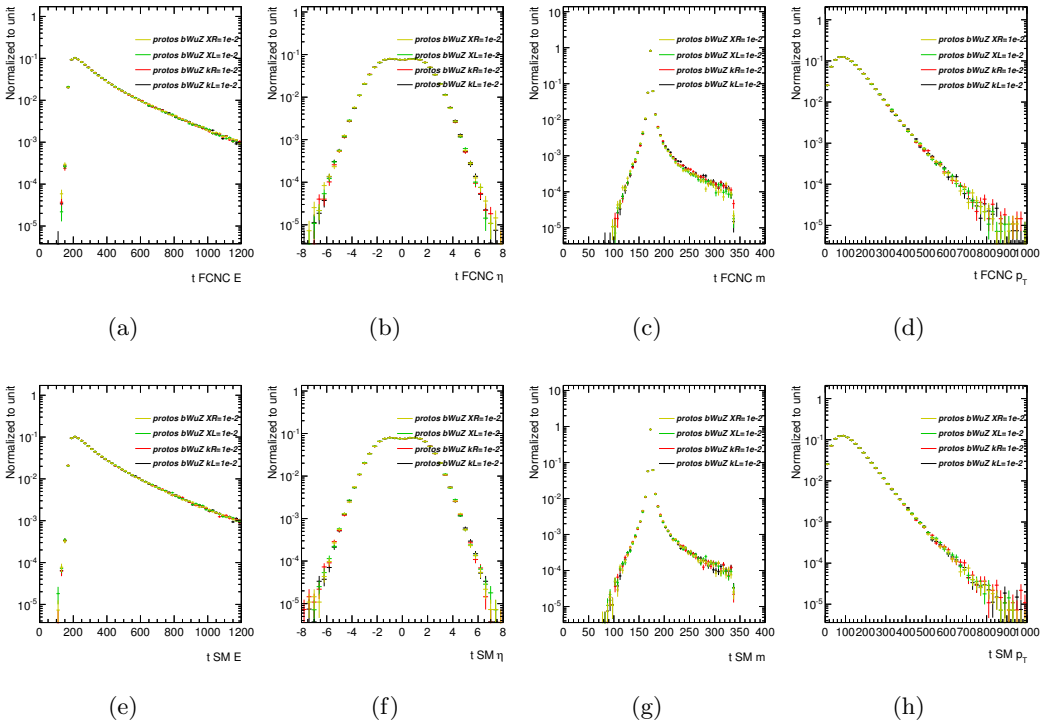

Figure B.2: Comparison of the effect of different coupling values on the (a) and (e) energy, (b) and (f) η, (c) and (g) mass and (d) and (h) p_{T} of the top-quark with the FCNC decay and the top-quark with the SM decay, respectively.

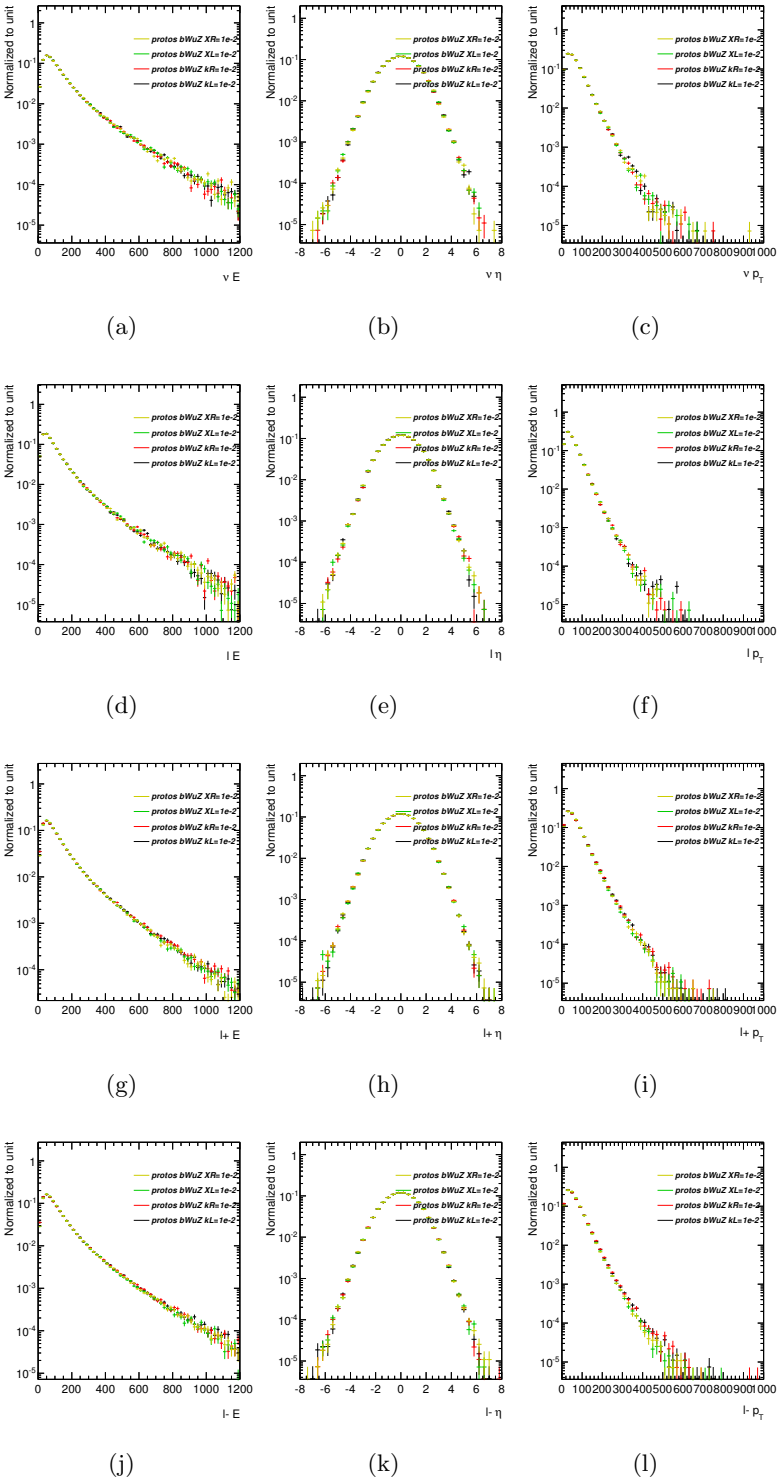

Figure B.3: Comparison of the effect of different coupling values on the (a), (d), (g) and (j) energy, (b), (e), (h) and (k) η and (c), (f), (i) and (l) p_{T} of the neutrino, the lepton from the W boson decay and the positively and negatively charged leptons from the Z boson decay, respectively.

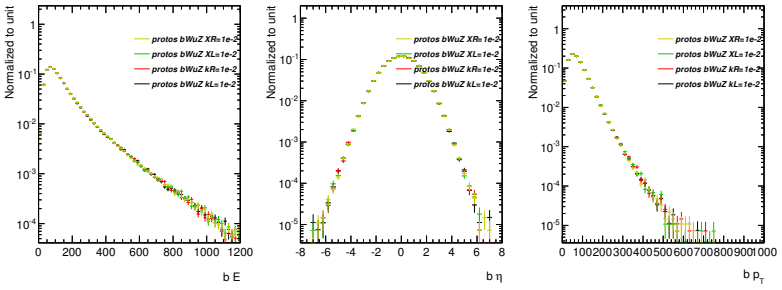

(a) (b) (c)

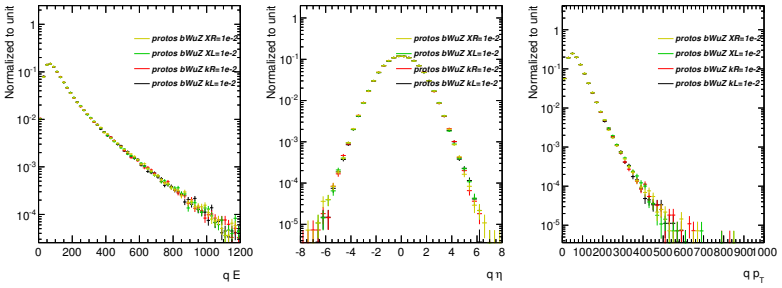

(d) (e) (f)

Figure B.4: Comparison of the effect of different coupling values on the (a) and (d) energy, (b) and (e) η and (c) and (f) p_{T} of the b quark and the light quark, respectively.

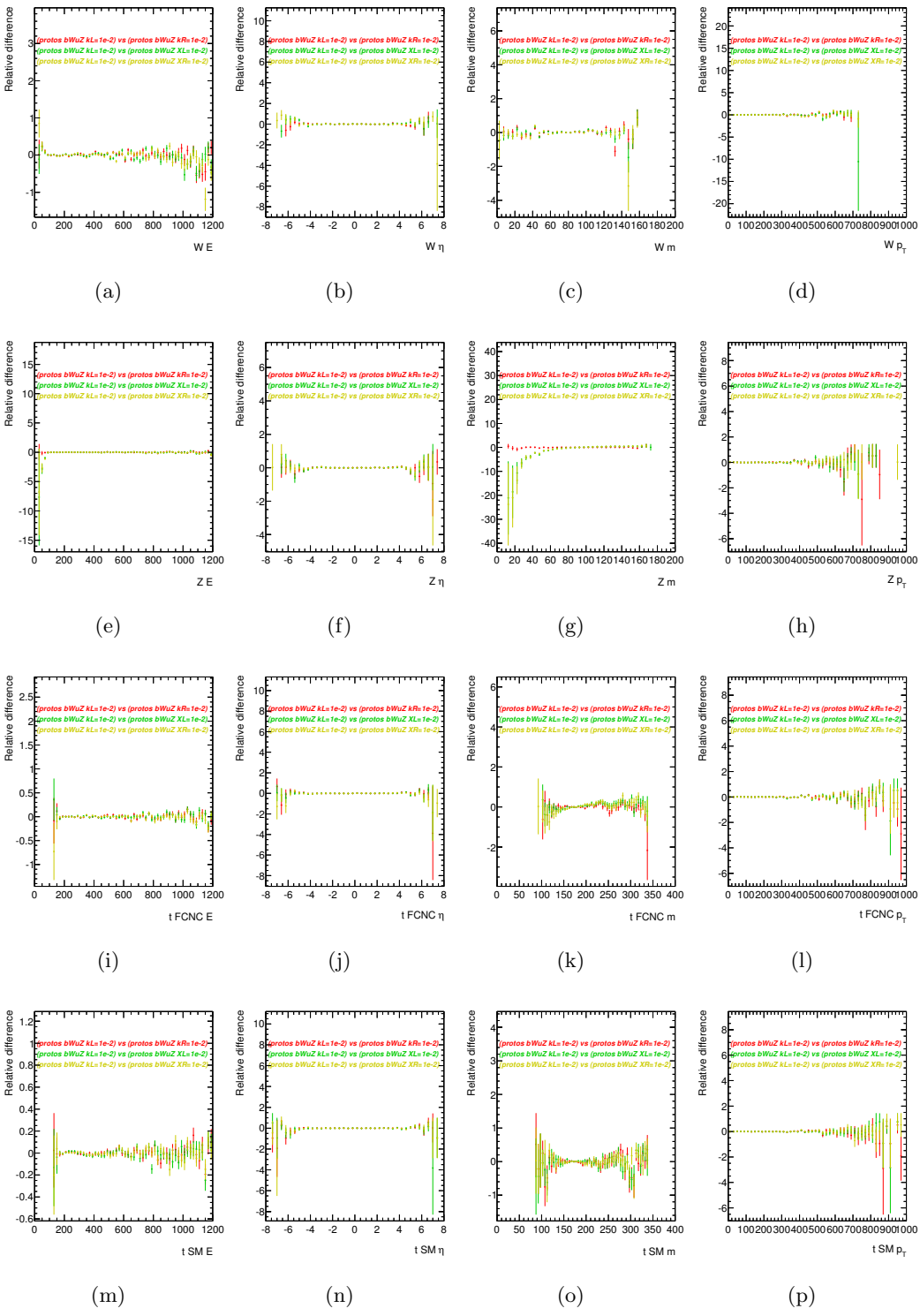

(a) (b) (c) (d)

(e) (f) (g) (h)

(i) (j) (k) (l)

(m) (n) (o) (p)

Figure B.5: Comparison of the ratio between k^{L} and the remaining couplings on the (a), (e), (i) and (m) energy, (b), (f), (j) and (n) η, (c), (g), (k) and (o) mass and (d), (h), (l) and (p) p_{T} of the W boson, Z boson, top-quark with the FCNC decay and top-quark with the SM decay, respectively.

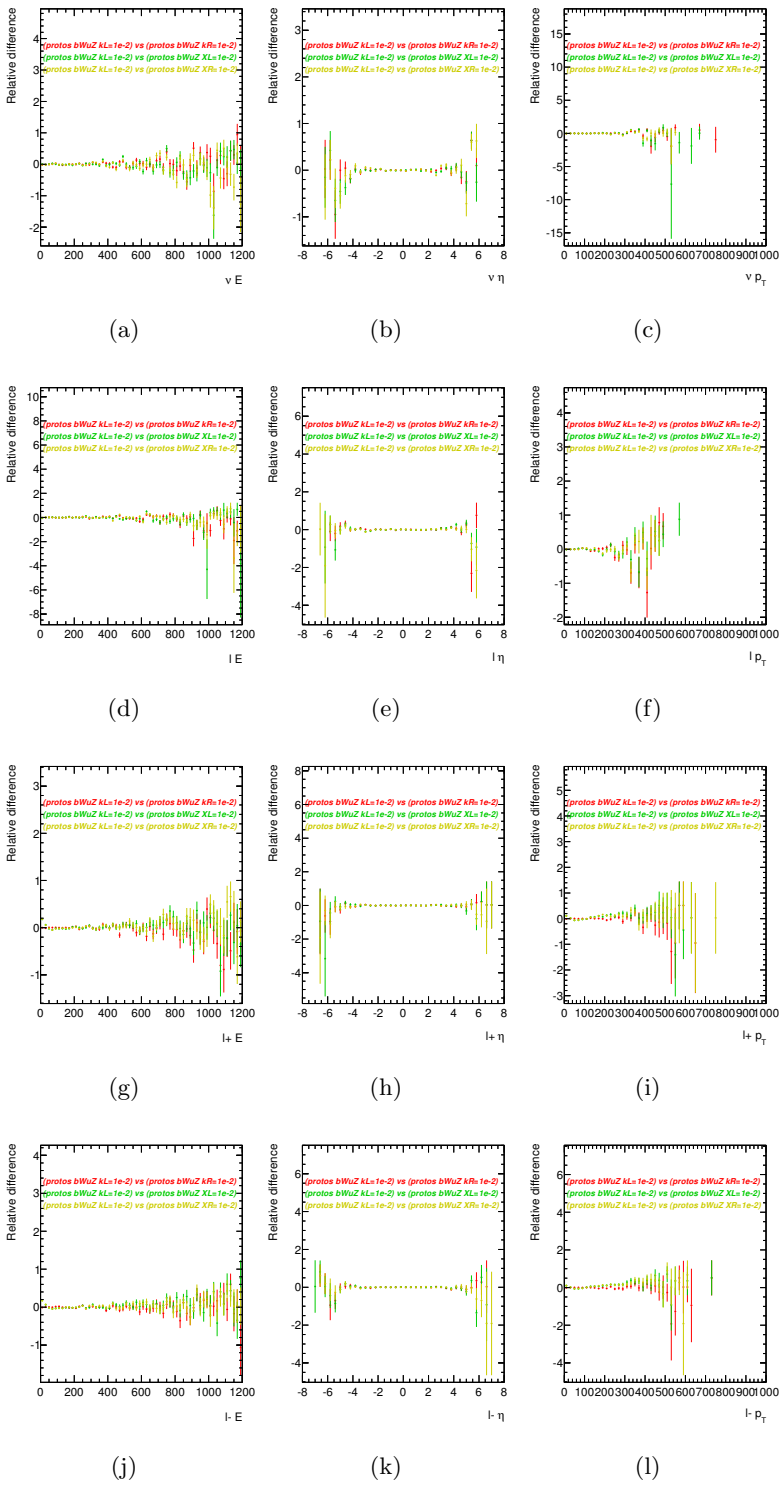

Figure B.6: Comparison of the ratio between k^{L} and the remaining couplings on the (a), (d), (g) and (j) energy, (b), (e), (h) and (k) η and (c), (f), (i) and (l) p_{T} of the neutrino, the lepton from the W boson decay, and the positively and negatively charged leptons from the Z boson decay, respectively.

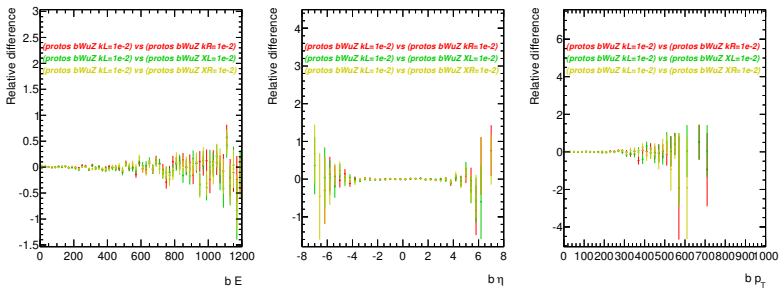

(a) (b) (c)

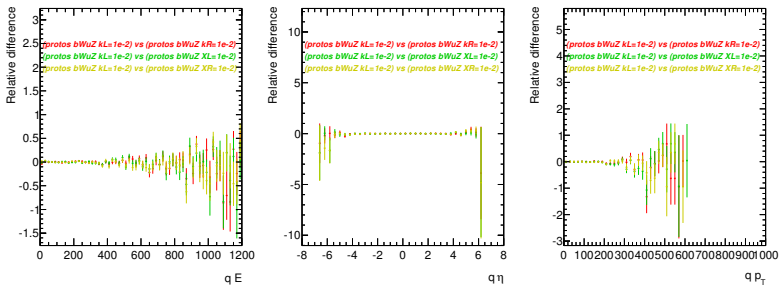

(d) (e) (f)

Figure B.7: Comparison of the ratio between k^{L} and the remaining couplings on the (a) and (d) energy, (b) and (e) η and (c) and (f) p_{T} of the b quark and the light quark, respectively.

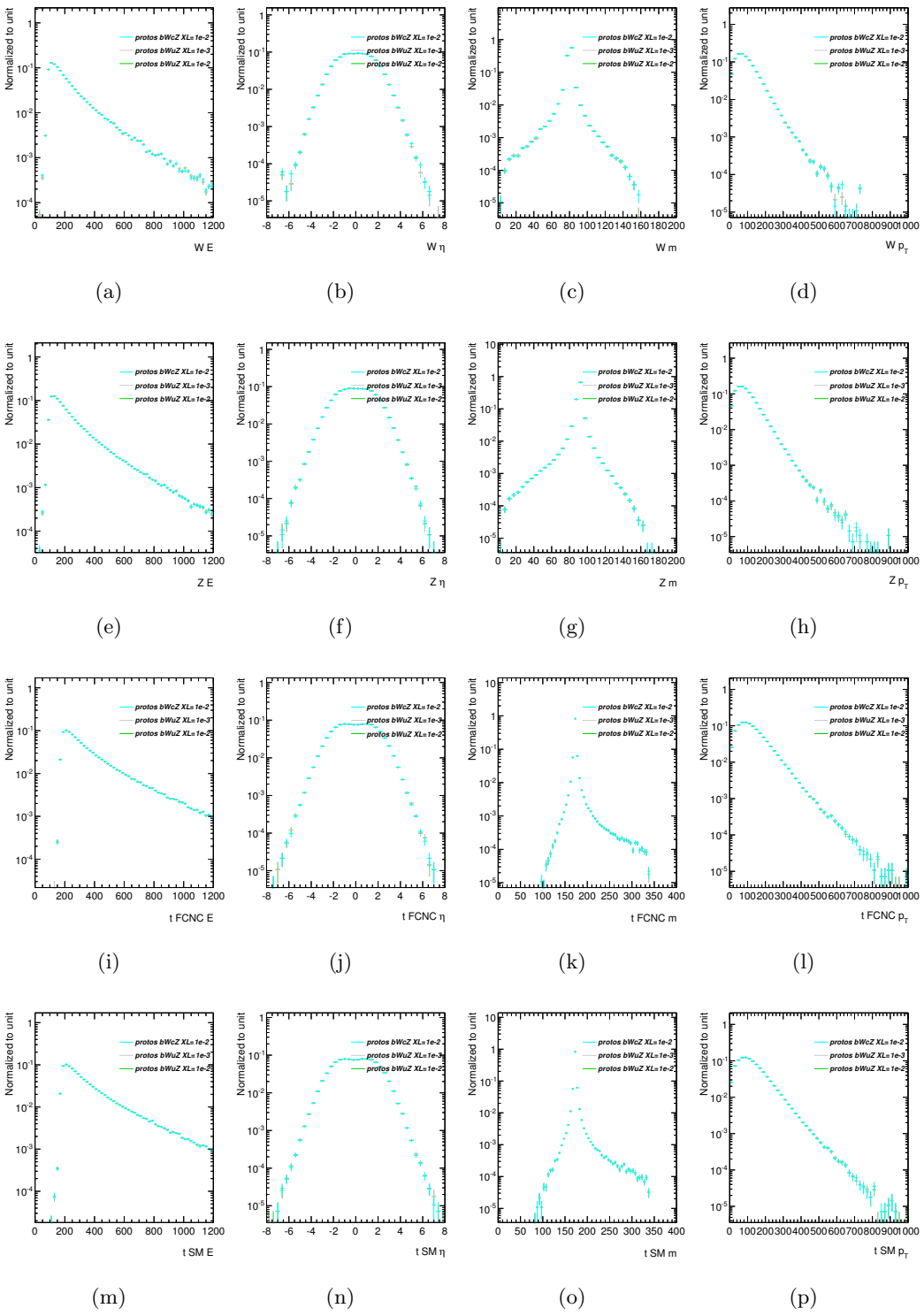

(a) (b) (c) (d)

(e) (f) (g) (h)

(i) (j) (k) (l)

(m) (n) (o) (p)

Figure B.8: Comparison of the effect of different coupling values and the choice of the up-type quark involved in the FCNC decay on the (a), (e), (i) and (m) energy, (b), (f), (j) and (n) η and (c), (g), (k) and (o) mass and (d), (h), (l) and (p) p_{T} of the W boson, Z boson, top-quark with the FCNC decay and top-quark with the SM decay, respectively.

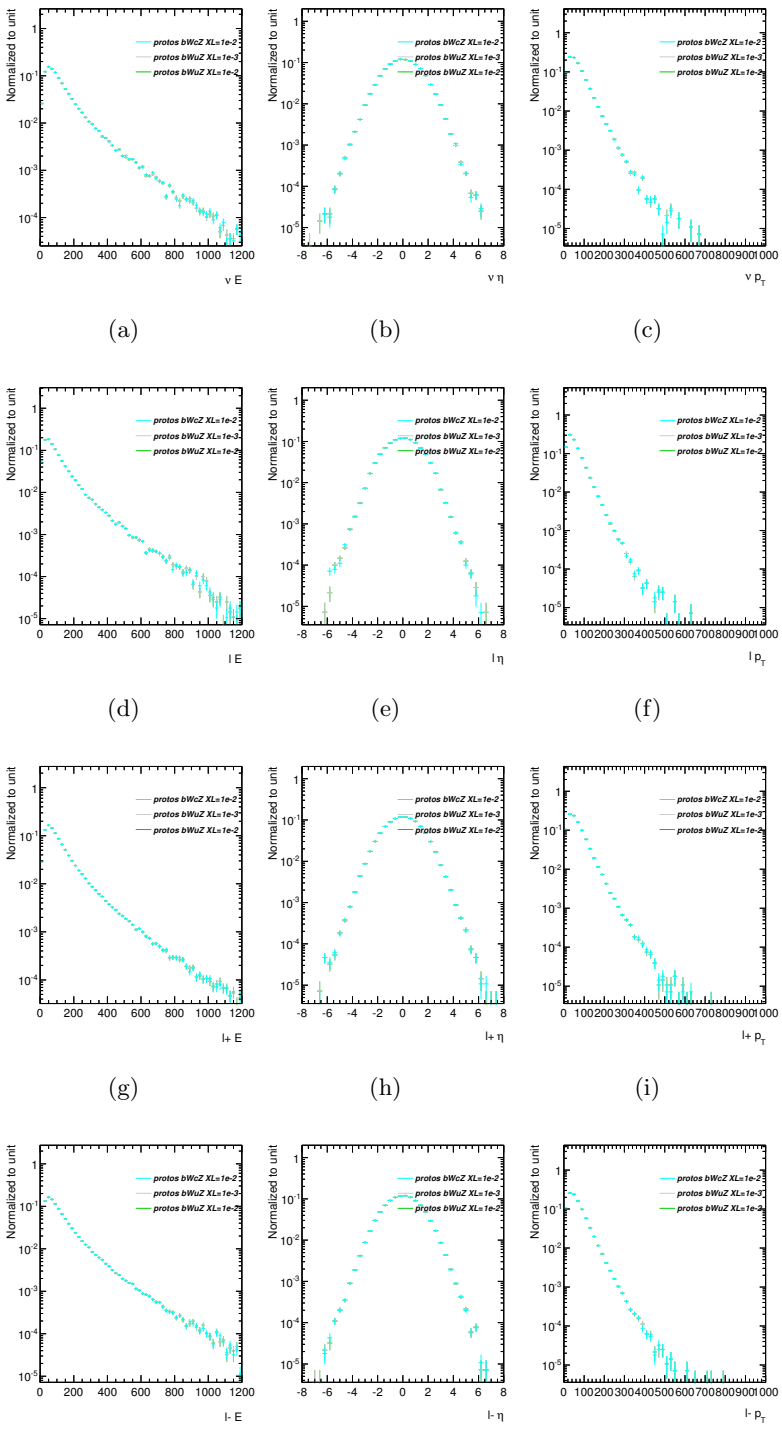

(a) (b) (c)

(d) (e) (f)

(g) (h) (i)

(j) (k) (l)

Figure B.9: Comparison of the effect of different coupling values and the choice of the up-type quark involved in the FCNC decay on the (a), (d), (g) and (j) energy, (b), (e), (h) and (k) η and (c), (f), (i) and (l) p_{T} of the neutrino, the lepton from the W boson decay and the positively and negatively charged leptons from the Z boson decay, respectively.

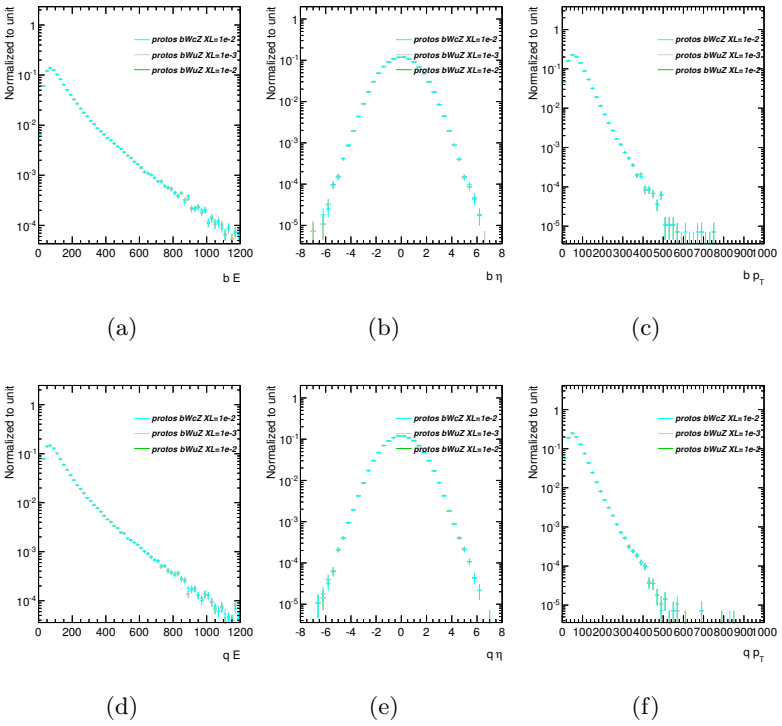

(a) (b) (c)

(d) (e) (f)

Figure B.10: Comparison of the effect of different coupling values and the choice of the up-type quark involved in the FCNC decay on the (a) and (d) energy, (b) and (e) η and (c) and (f) p_{T} of the b quark and the light quark, respectively.

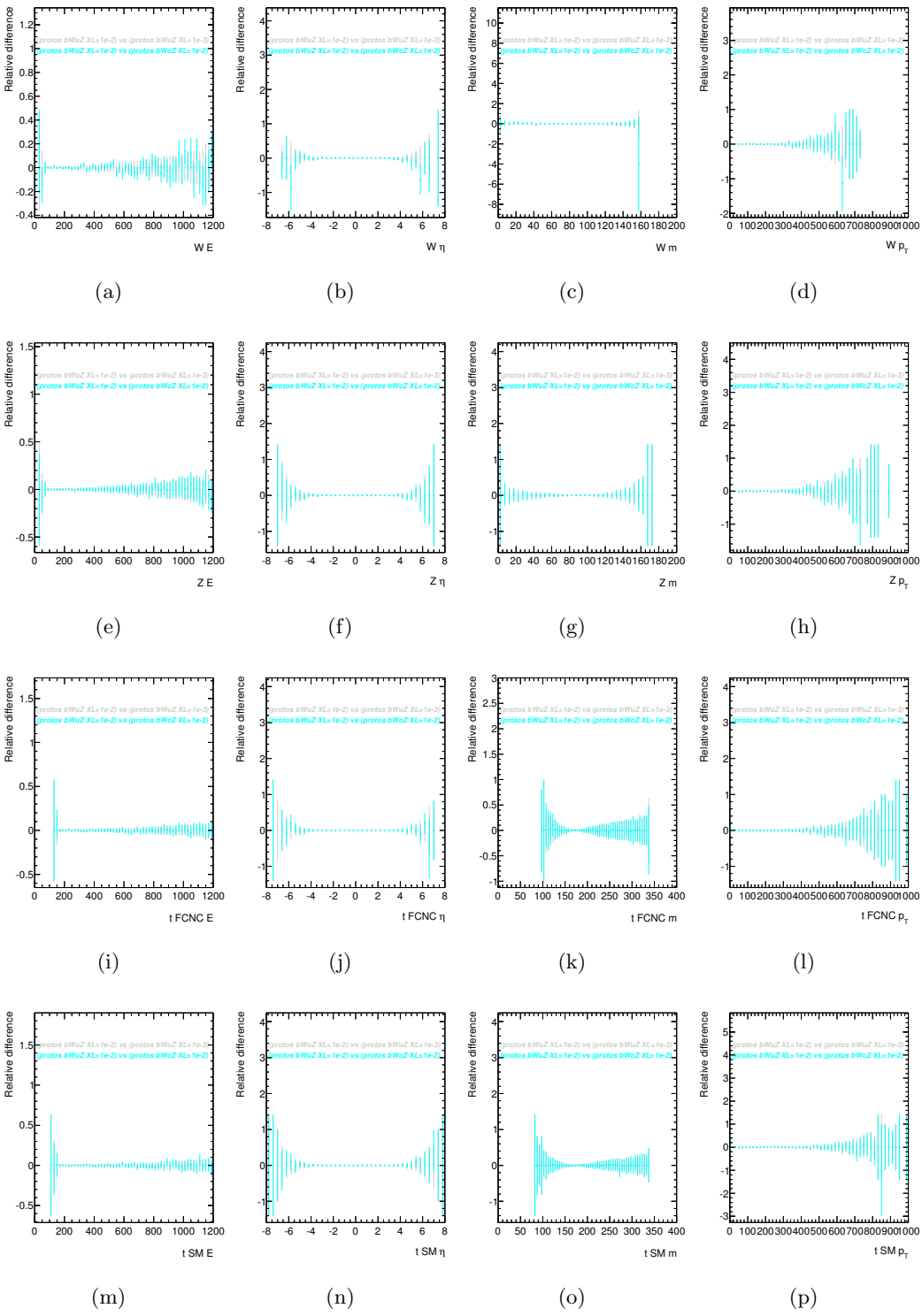

(a) (b) (c) (d)

(e) (f) (g) (h)

(i) (j) (k) (l)

(m) (n) (o) (p)

Figure B.11: Comparison of the ratio between $X^{\mathrm{L}} = 0.01$ and $X^{\mathrm{L}} = 0.001$, and between $bWuZ$ and $bWcZ$ processes on the (a), (e), (i) and (m) energy, (b), (f), (j) and (n) η, (c), (g), (k) and (o) mass and (d), (h), (l) and (p) p_{T} of the W boson, Z boson, top-quark with the FCNC decay and top-quark with the SM decay, respectively.

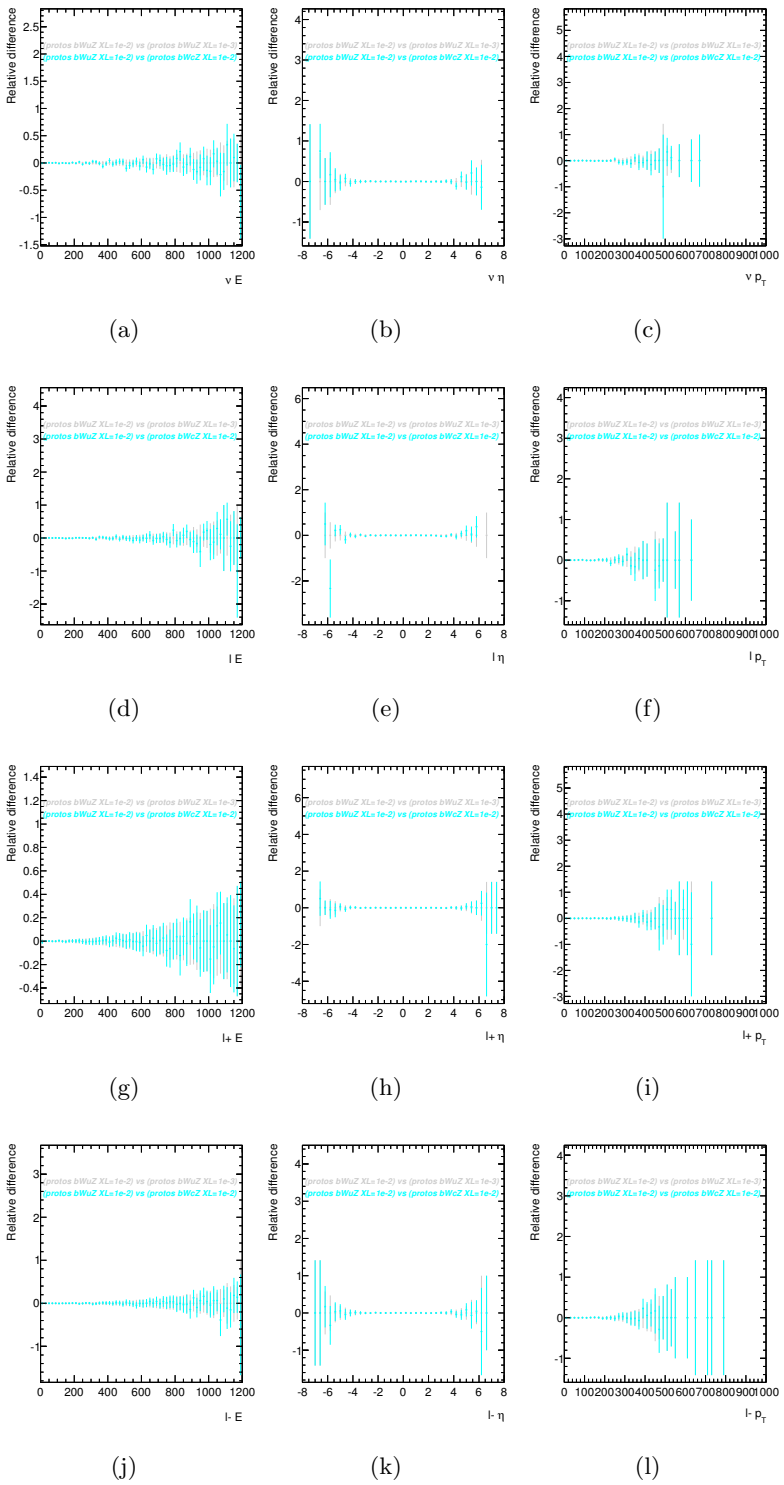

Figure B.12: Comparison of the ratio between $X^{\mathrm{L}} = 0.01$ and $X^{\mathrm{L}} = 0.001$, and between $bWuZ$ and $bWcZ$ processes on the (a), (d), (g) and (j) energy, (b), (e), (h) and (k) η and (c), (f), (i) and (l) p_{T} of the neutrino, the lepton from the W boson decay, and the positively and negatively charged leptons from the Z boson decay, respectively.

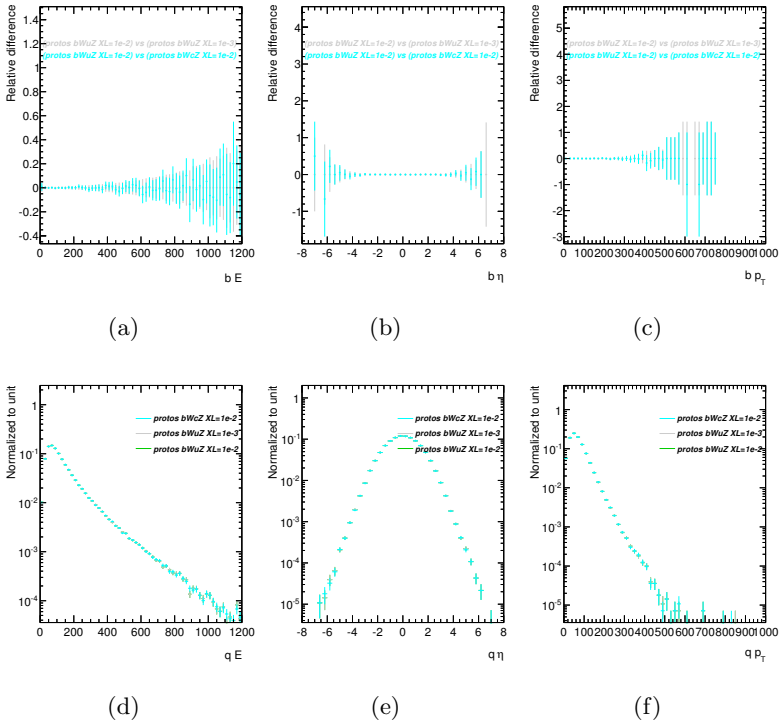

Figure B.13: Comparison of the ratio between$X^{\mathrm{L}} = 0.01$ and $X^{\mathrm{L}} = 0.001$, and between $bWuZ$ and $bWcZ$ processes on the (a) and (d) energy, (b) and (e) η and (c) and (f) p_{T} of the b quark and the light quark, respectively.

B.2 Comparison between the PROTOS and TopReX generators

The following distributions compare the kinematics of several objects from the PROTOS and TopReX generators.

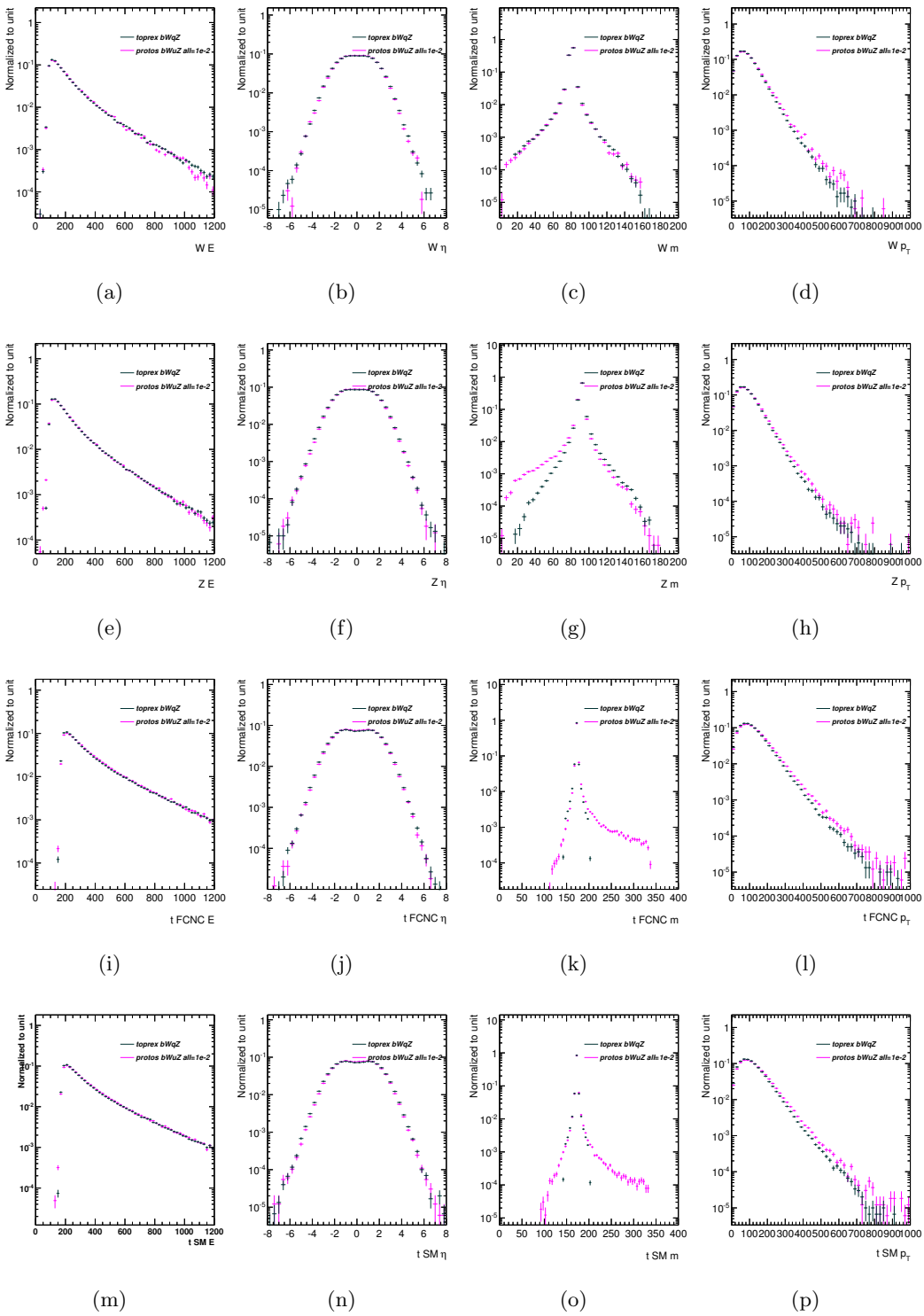

(a) (b) (c) (d)

(e) (f) (g) (h)

(i) (j) (k) (l)

(m) (n) (o) (p)

Figure B.14: Comparison of the (a), (e), (i) and (m) energy, (b), (f), (j) and (n) η, (c), (g), (k) and (o) mass and (d), (h), (l) and (p) p_{T} of the W boson, Z boson, top-quark with the FCNC decay and top-quark with the SM decay, respectively, generated with PROTOS and TopReX.

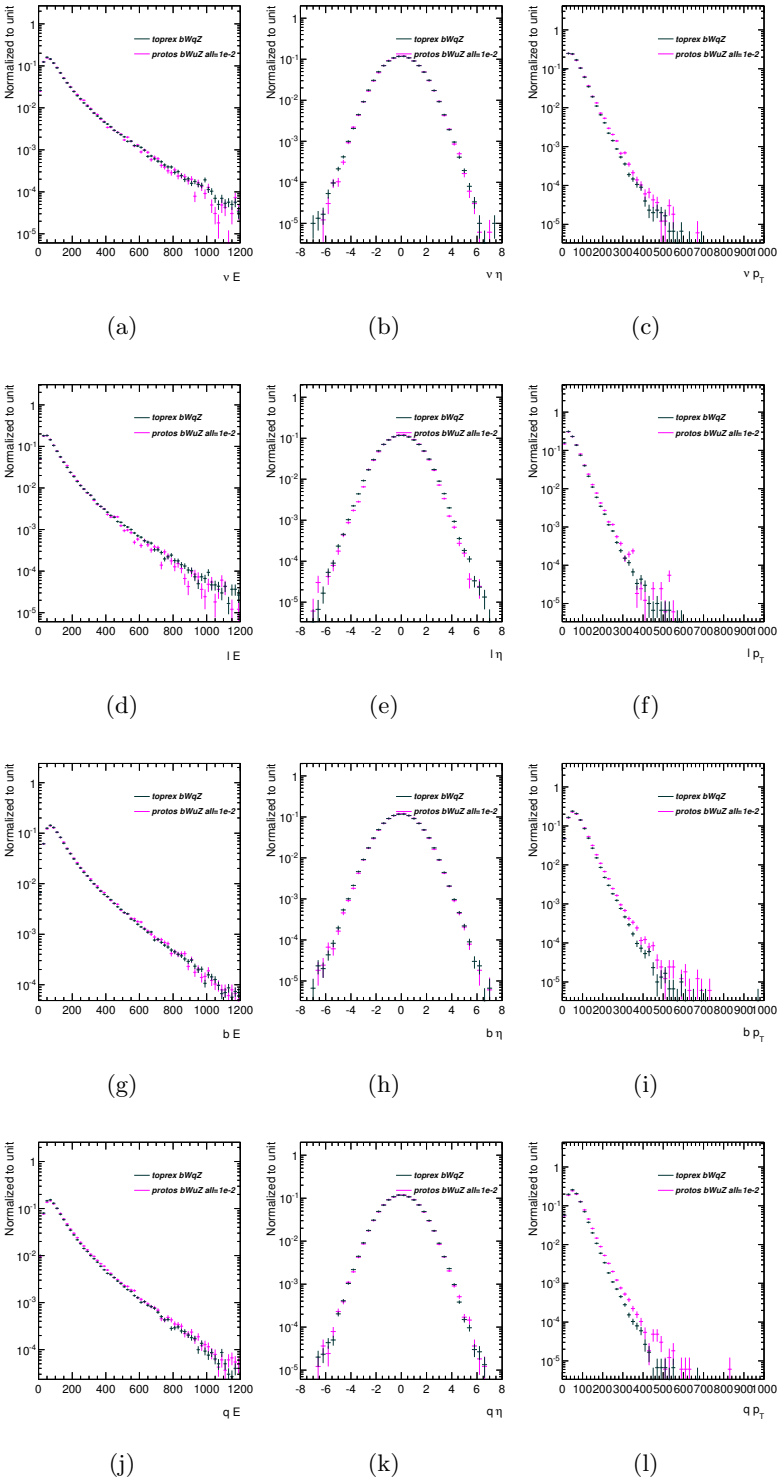

Figure B.15: Comparison of the (a), (d), (g) and (j) energy, (b), (e), (h) and (k) η and (c), (f), (i) and (l) p_{T} of the neutrino, the lepton from the W boson decay, the b-quark and the light-quark generated, respectively, with PROTOS and TopReX.

Appendix C

Collection of the samples used in the analysis

The following tables collect the information about the generated MC samples used in the analysis described in Chapter 5, including those used for comparisons.

Table C.1: The collection of the FCNC $t\bar{t} \to bWuZ$ PROTOS samples. The dataset ID and requested number of reconstructed events are given for each sample.

Samples	DSID	Nominal size
$t\bar{t} \to bWuZ$lep	110600	300000
$t\bar{t} \to bWuZ$lep $m_t = 170$ GeV	110601	300000
$t\bar{t} \to bWuZ$lep $m_t = 175$ GeV	110602	300000
$t\bar{t} \to bWuZ$lep with less parton shower	110603	300000
$t\bar{t} \to bWuZ$lep with more parton shower	110604	300000

Table C.2: The collection of the Diboson SHERPA samples. The dataset ID, requested number of reconstructed events, the cross-section times filter efficiency and the k-factor are given for each sample.

Samples	DSID	Nominal size	F.E.$\times\sigma$ [pb]	k-factor
$WW \to \ell\nu\ell\nu$	177997	8000000	5.2963	1.06
$ZZ \to \ell\ell\ell\ell$	189608	972000	8.6823	1.00
$ZZ \to \ell\ell\nu\nu$	177999	900000	0.49434	1.05
$WZ \to \ell\ell\ell\nu$	179974	2699000	9.7446	1.05

Table C.3: The collection of the Diboson HERWIG samples. The dataset ID, requested number of reconstructed events, the cross-section times filter efficiency and the k-factor are given for each sample.

Samples	DSID	Nominal size	F.E.$\times\sigma$ [pb]	k-factor
WW	105985	2500000	12.416	1.6833
ZZ	105986	495000	0.99244	1.5496
WZ	105987	2000000	3.6666	1.9011

Table C.4: The collection of the Diboson ALPGEN samples. The dataset ID, requested number of reconstructed events, the cross-section times filter efficiency and the k-factor are given for each sample.

Samples	DSID	Nominal size	F.E.$\times\sigma$ [pb]	k-factor
$WW \to \ell\nu\ell\nu$ Np0	107100	255000	2.4970	1.2307
$WW \to \ell\nu\ell\nu$ Np1	107101	125000	1.2491	1.2307
$WW \to \ell\nu\ell\nu$ Np2	107102	60000	0.59200	1.2307
$WW \to \ell\nu\ell\nu$ Np3	107103	35000	0.32847	1.2307
WZ incll Np0	107104	400000	0.80162	1.2785
WZ incll Np1	107105	260000	0.52407	1.2785
WZ incll Np2	107106	150000	0.29484	1.2785
WZ incll Np3	107107	95000	0.18258	1.2785
ZZ incll Np0	107108	610000	0.60660	1.3718
ZZ incll Np1	107109	290000	0.28893	1.3718
ZZ incll Np2	107110	120000	0.11853	1.3718
ZZ incll Np3	107111	60000	0.056223	1.3718
$WW \to qq\ell\nu$ Np0	110829	995000	9.9819	1.2832
$WW \to qq\ell\nu$ Np1	110830	495000	5.0144	1.2832
$WW \to qq\ell\nu$ Np2	110831	235000	2.3658	1.2832
$WW \to qq\ell\nu$ Np3	110832	130000	1.3139	1.2832

Table C.5: The collection of the Z+jets `ALPGEN` + `PYTHIA` samples. The dataset ID, requested number of reconstructed events, the cross-section times filter efficiency and the k-factor are given for each sample.

Samples	DSID	Nominal size	F.E.$\times\sigma$ [pb]	k-factor
$Z \to ee$ Np0	147105	6300000	718.97	1.18
$Z \to ee$ Np1	147106	8200000	175.70	1.18
$Z \to ee$ Np2	147107	3176000	58.875	1.18
$Z \to ee$ Np3	147108	895000	15.636	1.18
$Z \to ee$ Np4	147109	398600	4.0116	1.18
$Z \to ee$ Np5	147110	229700	1.2592	1.18
$Z \to \mu\mu$ Np0	147113	6300000	719.16	1.18
$Z \to \mu\mu$ Np1	147114	8200000	175.74	1.18
$Z \to \mu\mu$ Np2	147115	3176000	58.882	1.18
$Z \to \mu\mu$ Np3	147116	895000	15.673	1.18
$Z \to \mu\mu$ Np4	147117	398200	4.0057	1.18
$Z \to \mu\mu$ Np5	147118	229700	1.2544	1.18
$Z \to \tau\tau$ Np0	147121	19430000	718.87	1.18
$Z \to \tau\tau$ Np1	147122	10680000	175.76	1.18
$Z \to \tau\tau$ Np2	147123	3771000	58.856	1.18
$Z \to \tau\tau$ Np3	147124	1102000	15.667	1.18
$Z \to \tau\tau$ Np4	147125	398800	4.0121	1.18
$Z \to \tau\tau$ Np5	147126	229800	1.2560	1.18

Table C.6: The collection of the Z+jets ALPGEN + PYTHIA samples with bb and cc. The dataset ID, requested number of reconstructed events, the cross-section times filter efficiency and the k-factor are given for each sample.

Samples	DSID	Nominal size	F.E.$\times\sigma$ [pb]	k-factor
$Z \to ee + bb$ Np0	200332	1800000	6.5083	1.18
$Z \to ee + bb$ Np1	200333	700000	3.2927	1.18
$Z \to ee + bb$ Np2	200334	250000	1.2544	1.18
$Z \to ee + bb$ Np3	200335	139500	0.61711	1.18
$Z \to \mu\mu + bb$ Np0	200340	1800000	6.5056	1.18
$Z \to \mu\mu + bb$ Np1	200341	700000	3.2904	1.18
$Z \to \mu\mu + bb$ Np2	200342	250000	1.2601	1.18
$Z \to \mu\mu + bb$ Np3	200343	139500	0.61882	1.18
$Z \to \tau\tau + bb$ Np0	200348	300000	6.5062	1.18
$Z \to \tau\tau + bb$ Np1	200349	100000	3.2935	1.18
$Z \to \tau\tau + bb$ Np2	200350	50000	1.2485	1.18
$Z \to \tau\tau + bb$ Np3	200351	50000	0.61363	1.18
$Z \to ee + cc$ Np0	200432	300000	11.763	1.18
$Z \to ee + cc$ Np1	200433	200000	7.1280	1.18
$Z \to ee + cc$ Np2	200434	100000	3.3603	1.18
$Z \to ee + cc$ Np3	200435	50000	1.7106	1.18
$Z \to \mu\mu + cc$ Np0	200440	300000	11.795	1.18
$Z \to \mu\mu + cc$ Np1	200441	200000	7.1123	1.18
$Z \to \mu\mu + cc$ Np2	200442	100000	3.3708	1.18
$Z \to \mu\mu + cc$ Np3	200443	50000	1.7059	1.18
$Z \to \tau\tau + cc$ Np0	200448	300000	11.760	1.18
$Z \to \tau\tau + cc$ Np1	200449	200000	7.1410	1.18
$Z \to \tau\tau + cc$ Np2	200450	100000	3.3582	1.18
$Z \to \tau\tau + cc$ Np3	200451	50000	1.7046	1.18

Table C.7: The collection of the Z+jets ALPGEN + HERWIG samples for the low mass region. The dataset ID, requested number of reconstructed events, the cross-section times filter efficiency and the k-factor are given for each sample.

Samples	DSID	Nominal size	F.E.$\times\sigma$ [pb]	k-factor
$Z \to ee$ Np0 Excl Mll10to60	146830	1000000	3477.9	1.195
$Z \to ee$ Np1 Excl Mll10to60	146831	300000	108.88	1.195
$Z \to ee$ Np2 Excl Mll10to60	146832	470000	52.651	1.195
$Z \to ee$ Np3 Excl Mll10to60	146833	144500	11.309	1.195
$Z \to ee$ Np4 Excl Mll10to60	146834	36300	2.5743	1.195
$Z \to ee$ Np5 Incl Mll10to60	146835	79620	0.69211	1.195
$Z \to \mu\mu$ Np0 Excl Mll10to60	146840	1000000	3477.8	1.195
$Z \to \mu\mu$ Np1 Excl Mll10to60	146841	300000	108.63	1.195
$Z \to \mu\mu$ Np2 Excl Mll10to60	146842	470000	52.675	1.195
$Z \to \mu\mu$ Np3 Excl Mll10to60	146843	144500	11.283	1.195
$Z \to \mu\mu$ Np4 Excl Mll10to60	146844	36300	2.5690	1.195
$Z \to \mu\mu$ Np5 Incl Mll10to60	146845	79940	0.69425	1.195
$Z \to \tau\tau$ Np0 Excl Mll10to60	146850	1000000	3478.1	1.195
$Z \to \tau\tau$ Np1 Excl Mll10to60	146851	300000	108.85	1.195
$Z \to \tau\tau$ Np2 Excl Mll10to60	146852	470000	52.777	1.195
$Z \to \tau\tau$ Np3 Excl Mll10to60	146853	144500	11.295	1.195
$Z \to \tau\tau$ Np4 Excl Mll10to60	146854	218400	2.5904	1.195
$Z \to \tau\tau$ Np5 Incl Mll10to60	146855	120140	0.69034	1.195

Table C.8: The collection of the $Z\gamma$ SHERPA samples. The dataset ID, requested number of reconstructed events, the cross-section times filter efficiency and the k-factor are given for each sample.

Samples	DSID	Nominal size	F.E.$\times\sigma$ [pb]	k-factor
$Z \to ee + \gamma\ p_{\mathrm{T}} > 10$	145161	16000000	32.298	1.00
$Z \to \mu\mu\gamma\ p_{\mathrm{T}} > 10$	145162	16000000	32.326	1.00
$Z \to \tau\tau\gamma\ p_{\mathrm{T}} > 10$	126854	4000000	32.317	1.00

Table C.9: The collection of the $t\bar{t}$ and single-top samples. The dataset ID, requested number of reconstructed events, the cross-section times filter efficiency and the k-factor are given for each sample.

Samples	DSID	Nominal size	F.E.$\times\sigma$ [pb]	k-factor
$t\bar{t}$	117050	99985000	114.51	1.1992
single-top (s-channel) $W \to e\nu$	108343	200000	0.56395	1.0744
single-top (s-channel) $W \to \mu\nu$	108344	200000	0.56430	1.0737
single-top (s-channel) $W \to \tau\nu$	108345	200000	0.56434	1.0736
single-top (Wt-channel) Incl	108346	2000000	20.666	1.0825
singletop (t-channel) e	117360	300000	8.5878	1.1037
singletop (t-channel) μ	117361	300000	8.5889	1.1035
singletop (t-channel) τ	117362	290000	8.5810	1.1045

Table C.10: The collection of the $t\bar{t}$ $+W$ and $t\bar{t}$ $+Z$ samples, including those with extra jets samples. The dataset ID, requested number of reconstructed events, the cross-section times filter efficiency and the k-factor are given for each sample.

Samples	DSID	Nominal size	F.E.$\times\sigma$ [pb]	k-factor
$t\bar{t}$ W	119353	400000	0.10410	1.170
$t\bar{t}$ Wj	119354	400000	0.093317	1.170
$t\bar{t}$ Z	119355	400000	0.067690	1.350
$t\bar{t}$ Zj	119356	400000	0.087339	1.350
$t\bar{t}$ WW	119583	10000	0.00091901	2.0685

Table C.11: The collection of tZ samples. The dataset ID, requested number of reconstructed events, the cross-section times filter efficiency and the k-factor are given for each sample.

Samples	DSID	Nominal size	F.E.$\times\sigma$ [pb]	k-factor
Wt-channel $Z \to \ell\ell$	179991	100000	0.0041303	1.0
st-channel $Z \to \ell\ell$	179992	100000	0.031161	1.0

Table C.12: The collection of triboson samples. The dataset ID, requested number of reconstructed events, the cross-section times filter efficiency and the k-factor are given for each sample.

Samples	DSID	Nominal size	F.E.$\times\sigma$ [pb]	k-factor
$WWW* \to \ell\nu\ell\nu\ell\nu$	167006	50000	0.0050961	1.0
$ZWW* \to \ell\ell\ell\nu\ell\nu$	167007	50000	0.0015546	1.0
$ZZZ* \to \nu\nu\ell\ell\ell\ell$	167008	50000	0.00033239	1.0

Table C.13: The collection of higgs samples. The dataset ID, requested number of reconstructed events, the cross-section times filter efficiency and the k-factor are given for each sample.

Samples	DSID	Nominal size	F.E.$\times\sigma$ [pb]	k-factor
$t\bar{t}H$, $H \to WW$ inclusive	161305	190000	0.019499	1.4257
$t\bar{t}H$, $H \to b\bar{b}$	161871	500000	0.0055716	1.4053
$t\bar{t}H$, $H \to ZZ$ inclusive	169072	100000	0.0023465	1.4547
$t\bar{t}H$, $H \to \tau\tau \to \ell\ell$	161708	30000	0.00077024	1.3156
$t\bar{t}H$, $H \to \tau\tau \to \ell h$	161719	30000	0.0028600	1.3029
$t\bar{t}H$, $H \to \tau\tau \to hh$	161730	30000	0.0026259	1.3070
$t\bar{t}H$, $H \to gg$	169070	100000	0.0056990	1.9444
$t\bar{t}H$, $H \to \gamma\gamma$	160069	300000	0.00025687	1.1477
$t\bar{t}H$, $H \to c\bar{c}$	169071	100000	0.0030317	1.2411
ZH: $H \to WW$, Z inclusive	161155	20000	0.00947187	1.0
ZH: $H \to \tau\tau$, Z inclusive	161697	500000	0.009471	1.0
ZH: $H \to b\bar{b}$, $Z \to \ell\ell$	161827	300000	0.024185	1.0
WH: $H \to ZZ \to \ell\ell\ell\ell$, W inclusive	160255	100000	0.00018949	1.0
ggH: $H \to ZZ \to \ell\ell\ell\ell$	160155	200000	0.00518234	1.0

References

[1] ATLAS Collaboration, *Event display of the second lowest χ^2 selected event (run=214651, event=20468734)*, 2015. `https://atlas.web.cern.ch/Atlas/GROUPS/PHYSICS/PAPERS/TOPQ-2014-08/figaux_09.png`. [Online; accessed 11-January-2016].

[2] S. L. Glashow, *Partial Symmetries of Weak Interactions*, Nucl. Phys. **22** (1961) 579–588.

[3] A. Salam, *Weak and Electromagnetic Interactions*, Conf. Proc. C **680519** (1968) 367–377.

[4] S. Weinberg, *A Model of Leptons*, Phys. Rev. Lett. **19** (1967) 1264–1266.

[5] G. Zweig, *An SU(3) model for strong interaction symmetry and its breaking. Version 2*, Developments in the Quark Theory of Hadrons, Volume 1. Edited by D. Lichtenberg and S. Rosen. pp. 22-101 (1964) 22–101, `http://inspirehep.net/record/4674/files/cern-th-412.pdf`.

[6] S. Weinberg, *The Quantum theory of fields. Vol. 1: Foundations*. Cambridge University Press, 2005.

[7] J. S. Schwinger, *Quantum electrodynamics. I A covariant formulation*, Phys. Rev. **74** (1948) 1439.

[8] R. P. Feynman, *Space - time approach to quantum electrodynamics*, Phys. Rev. **76** (1949) 769–789.

[9] R. P. Feynman, *Mathematical formulation of the quantum theory of electromagnetic interaction*, Phys. Rev. **80** (1950) 440–457.

[10] S. Tomonaga, *On a relativistically invariant formulation of the quantum theory of wave fields*, Prog. Theor. Phys. **1** (1946) 27–42.

[11] H. D. Politzer, *Reliable Perturbative Results for Strong Interactions?*, Phys. Rev. Lett. **30** (1973) 1346–1349.

[12] LHCb Collaboration, *Observation of $J/\psi p$ resonances consistent with pentaquark states in $\Lambda_b^0 \to J/\psi K^- p$ decays*, Phys. Rev. Lett. **115** no. 7, (2015) 072001, `arXiv:1507.03414 [hep-ex]`.

[13] P. W. Higgs, *Broken Symmetries and the Masses of Gauge Bosons*, Phys. Rev. Lett. **13** (1964) 508–509.

[14] F. Englert and R. Brout, *Broken Symmetry and the Mass of Gauge Vector Mesons*, Phys. Rev. Lett. **13** (1964) 321–323.

[15] G. S. Guralnik, C. R. Hagen and T. W. B. Kibble, *Global Conservation Laws and Massless Particles*, Phys. Rev. Lett. **13** (1964) 585–587.

[16] SNO Collaboration, S. N. Ahmed et al., *Measurement of the total active B-8 solar neutrino flux at the Sudbury Neutrino Observatory with enhanced neutral current sensitivity*, Phys. Rev. Lett. **92** (2004) 181301, `arXiv:nucl-ex/0309004 [nucl-ex]`.

[17] Super-Kamiokande Collaboration, S. Fukuda et al., *Determination of solar neutrino oscillation parameters using 1496 days of Super-Kamiokande I data*, Phys. Lett. B **539** (2002) 179–187, `arXiv:hep-ex/0205075 [hep-ex]`.

[18] KamLAND Collaboration, K. Eguchi et al., *First results from KamLAND: Evidence for reactor anti-neutrino disappearance*, Phys. Rev. Lett. **90** (2003) 021802, `arXiv:hep-ex/0212021 [hep-ex]`.

[19] K2K Collaboration, M. H. Ahn et al., *Indications of neutrino oscillation in a 250 km long baseline experiment*, Phys. Rev. Lett. **90** (2003) 041801, `arXiv:hep-ex/0212007 [hep-ex]`.

[20] S. Verma, *Theoretical and Phenomenological Status of Neutrino Physics: A Brief Review*, Adv. High Energy Phys. **2015** (2015) 385968.

[21] M. Kobayashi and T. Maskawa, *CP Violation in the Renormalizable Theory of Weak Interaction*, Prog. Theor. Phys. **49** (1973) 652–657.

[22] S. L. Glashow, J. Iliopoulos and L. Maiani, *Weak Interactions with Lepton-Hadron Symmetry*, Phys. Rev. D **2** (1970) 1285–1292.

[23] SLD Electroweak Group, DELPHI, ALEPH, SLD, SLD Heavy Flavour Group, OPAL, LEP Electroweak Working Group, L3 Collaboration, S. Schael et al., *Precision electroweak measurements on the Z resonance*, Phys. Rept. **427** (2006) 257–454, arXiv:hep-ex/0509008 [hep-ex].

[24] DELPHI, OPAL, LEP Electroweak, ALEPH, L3 Collaboration, S. Schael et al., *Electroweak Measurements in Electron-Positron Collisions at W-Boson-Pair Energies at LEP*, Phys. Rept. **532** (2013) 119–244, arXiv:1302.3415 [hep-ex].

[25] M. Baak, M. Goebel, J. Haller, A. Hoecker, D. Kennedy, R. Kogler, K. Moenig, M. Schott and J. Stelzer, *The Electroweak Fit of the Standard Model after the Discovery of a New Boson at the LHC*, Eur. Phys. J. C **72** (2012) 2205, arXiv:1209.2716 [hep-ph].

[26] CDF Collaboration, F. Abe et al., *Observation of top quark production in $\bar{p}p$ collisions*, Phys. Rev. Lett. **74** (1995) 2626–2631, arXiv:hep-ex/9503002 [hep-ex].

[27] DØ Collaboration, S. Abachi et al., *Observation of the top quark*, Phys. Rev. Lett. **74** (1995) 2632–2637, arXiv:hep-ex/9503003 [hep-ex].

[28] Particle Data Group Collaboration, K. A. Olive et al., *Review of Particle Physics*, Chin. Phys. C **38** (2014) 090001.

[29] J. F. Donoghue, E. Golowich and B. R. Holstein, *Dynamics of the standard model*, Camb. Monogr. Part. Phys. Nucl. Phys. Cosmol. **2** (1992) 1–540.

[30] Top LHC WG, *Summary of the ATLAS and CMS direct m_{top} measurements*, 2016. https://atlas.web.cern.ch/Atlas/GROUPS/PHYSICS/CombinedSummaryPlots/TOP/mtopSummary_TopLHC/mtopSummary_TopLHC.png. [Online; accessed 26-September-2016].

[31] G. Eilam, J. L. Hewett and A. Soni, *Rare decays of the top quark in the standard and two Higgs doublet models*, Phys. Rev. D **44** (1991) 1473–1484, [Erratum: Phys. Rev.D59,039901(1999)].

[32] B. Mele, S. Petrarca and A. Soddu, *A New evaluation of the $t \to cH$ decay width in the standard model*, Phys. Lett. B **435** (1998) 401–406, arXiv:hep-ph/9805498 [hep-ph].

[33] J. A. Aguilar-Saavedra and B. M. Nobre, *Rare top decays $t \to c\gamma$, $t \to cg$ and CKM unitarity*, Phys. Lett. B **553** (2003) 251–260, arXiv:hep-ph/0210360 [hep-ph].

[34] J. A. Aguilar-Saavedra, *Top flavor-changing neutral interactions: Theoretical expectations and experimental detection*, Acta Phys. Polon. B **35** (2004) 2695–2710, arXiv:hep-ph/0409342 [hep-ph].

[35] F. del Aguila, J. A. Aguilar-Saavedra and R. Miquel, *Constraints on top couplings in models with exotic quarks*, Phys. Rev. Lett. **82** (1999) 1628–1631, arXiv:hep-ph/9808400 [hep-ph].

[36] J. A. Aguilar-Saavedra, *Effects of mixing with quark singlets*, Phys. Rev. D **67** (2003) 035003, arXiv:hep-ph/0210112 [hep-ph], [Erratum: Phys. Rev.D69,099901(2004)].

[37] T. P. Cheng and M. Sher, *Mass Matrix Ansatz and Flavor Nonconservation in Models with Multiple Higgs Doublets*, Phys. Rev. D **35** (1987) 3484.

[38] B. Grzadkowski, J. F. Gunion and P. Krawczyk, *Neutral current flavor changing decays for the Z boson and the top quark in two Higgs doublet models*, Phys. Lett. B **268** (1991) 106–111.

[39] M. E. Luke and M. J. Savage, *Flavor changing neutral currents in the Higgs sector and rare top decays*, Phys. Lett. B **307** (1993) 387–393, arXiv:hep-ph/9303249 [hep-ph].

[40] D. Atwood, L. Reina and A. Soni, *Probing flavor changing top - charm - scalar interactions in e^+e^- collisions*, Phys. Rev. D **53** (1996) 1199–1201, arXiv:hep-ph/9506243 [hep-ph].

[41] D. Atwood, L. Reina and A. Soni, *Phenomenology of two Higgs doublet models with flavor changing neutral currents*, Phys. Rev. D **55** (1997) 3156–3176, arXiv:hep-ph/9609279 [hep-ph].

[42] S. Bejar, J. Guasch and J. Sola, *Loop induced flavor changing neutral decays of the top quark in a general two Higgs doublet model*, Nucl. Phys. B **600** (2001) 21–38, arXiv:hep-ph/0011091 [hep-ph].

[43] S. Bejar, *Flavor changing neutral decay effects in models with two Higgs boson doublets: Applications to LHC Physics*, 2006.

[44] C. S. Li, R. J. Oakes and J. M. Yang, *Rare decay of the top quark in the minimal supersymmetric model*, Phys. Rev. D **49** (1994) 293–298, [Erratum: Phys. Rev.D56,3156(1997)].

[45] G. M. de Divitiis, R. Petronzio and L. Silvestrini, *Flavor changing top decays in supersymmetric extensions of the standard model*, Nucl. Phys. B **504** (1997) 45–60, arXiv:hep-ph/9704244 [hep-ph].

[46] J. L. Lopez, D. V. Nanopoulos and R. Rangarajan, *New supersymmetric contributions to $t \to cV$*, Phys. Rev. D **56** (1997) 3100–3106, arXiv:hep-ph/9702350 [hep-ph].

[47] J. Guasch and J. Sola, *FCNC top quark decays: A Door to SUSY physics in high luminosity colliders?*, Nucl. Phys. B **562** (1999) 3–28, arXiv:hep-ph/9906268 [hep-ph].

[48] D. Delepine and S. Khalil, *Top flavor violating decays in general supersymmetric models*, Phys. Lett. B **599** (2004) 62–74, arXiv:hep-ph/0406264 [hep-ph].

[49] J. J. Liu, C. S. Li, L. L. Yang and L. G. Jin, *$t \to cV$ via SUSY FCNC couplings in the unconstrained MSSM*, Phys. Lett. B **599** (2004) 92–101, arXiv:hep-ph/0406155 [hep-ph].

[50] J. J. Cao, G. Eilam, M. Frank, K. Hikasa, G. L. Liu, I. Turan and J. M. Yang, *SUSY-induced FCNC top-quark processes at the large hadron collider*, Phys. Rev. D **75** (2007) 075021, arXiv:hep-ph/0702264 [hep-ph].

[51] J. M. Yang, B.-L. Young and X. Zhang, *Flavor changing top quark decays in r parity violating SUSY*, Phys. Rev. D **58** (1998) 055001, arXiv:hep-ph/9705341 [hep-ph].

[52] G. Eilam, A. Gemintern, T. Han, J. M. Yang and X. Zhang, *Top quark rare decay $t \to ch$ in R-parity violating SUSY*, Phys. Lett. B **510** (2001) 227–235, arXiv:hep-ph/0102037 [hep-ph].

[53] K. Agashe, G. Perez and A. Soni, *Flavor structure of warped extra dimension models*, Phys. Rev. D **71** (2005) 016002, arXiv:hep-ph/0408134 [hep-ph].

[54] K. Agashe, G. Perez and A. Soni, *Collider Signals of Top Quark Flavor Violation from a Warped Extra Dimension*, Phys. Rev. D **75** (2007) 015002, arXiv:hep-ph/0606293 [hep-ph].

[55] Top Quark Working Group Collaboration, K. Agashe et al., *Working Group Report: Top Quark*, in *Community Summer Study 2013: Snowmass on the Mississippi (CSS2013) Minneapolis, MN, USA, July 29-August 6, 2013*. 2013. arXiv:1311.2028 [hep-ph].

[56] ALEPH Collaboration, A. Heister et al., *Search for single top production in e^+e^- collisions at $\sqrt{s}$ up to 209-GeV*, Phys. Lett. B **543** (2002) 173–182, arXiv:hep-ex/0206070 [hep-ex].

[57] DELPHI Collaboration, J. Abdallah et al., *Search for single top production via FCNC at LEP at $\sqrt{s}$ = 189-GeV to 208-GeV*, Phys. Lett. B **590** (2004) 21–34, arXiv:hep-ex/0404014 [hep-ex].

[58] OPAL Collaboration, G. Abbiendi et al., *Search for single top quark production at LEP-2*, Phys. Lett. B **521** (2001) 181–194, arXiv:hep-ex/0110009 [hep-ex].

[59] L3 Collaboration, P. Achard et al., *Search for single top production at LEP*, Phys. Lett. B **549** (2002) 290–300, arXiv:hep-ex/0210041 [hep-ex].

[60] The LEP Exotica WG, *Search for single top production via flavour changing neutral currents: preliminary combined results of the LEP experiments*, DELPHI-2001-119-CONF-542. CERN-DELPHI-2001-119-CONF-542.

LEP-Exotica-WG-2001-01. ALEPH-2001-055. CERN-ALEPH-CONF-2001-035. L3-2706. OPAL-TN-698, Jul, 2001, https://cds.cern.ch/record/1006392.

[61] M. Beneke et al., *Top quark physics*, in *1999 CERN Workshop on standard model physics (and more) at the LHC, CERN, Geneva, Switzerland, 25-26 May: Proceedings*. 2000. arXiv:hep-ph/0003033 [hep-ph]. http://weblib.cern.ch/abstract?CERN-TH-2000-100.

[62] ZEUS Collaboration, H. Abramowicz et al., *Search for single-top production in ep collisions at HERA*, Phys. Lett. B **708** (2012) 27–36, arXiv:1111.3901 [hep-ex].

[63] H1 Collaboration, F. D. Aaron et al., *Search for Single Top Quark Production at HERA*, Phys. Lett. B **678** (2009) 450–458, arXiv:0904.3876 [hep-ex].

[64] A. A. Ashimova and S. R. Slabospitsky, *The Constraint on FCNC Coupling of the Top Quark with a Gluon from ep Collisions*, Phys. Lett. B **668** (2008) 282–285, arXiv:hep-ph/0604119 [hep-ph].

[65] CDF Collaboration, T. Aaltonen et al., *Search for the Flavor Changing Neutral Current Decay $t \to Zq$ in $p\bar{p}$ Collisions at $\sqrt{s} = 1.96$ TeV*, Phys. Rev. Lett. **101** (2008) 192002, arXiv:0805.2109 [hep-ex].

[66] CDF Collaboration, F. Abe et al., *Search for flavor-changing neutral current decays of the top quark in $p\bar{p}$ collisions at $\sqrt{s} = 1.8$ TeV*, Phys. Rev. Lett. **80** (1998) 2525–2530.

[67] CDF Collaboration, T. Aaltonen et al., *Search for top-quark production via flavor-changing neutral currents in W+1 jet events at CDF*, Phys. Rev. Lett. **102** (2009) 151801, arXiv:0812.3400 [hep-ex].

[68] D0 Collaboration, V. M. Abazov et al., *Search for flavor changing neutral currents in decays of top quarks*, Phys. Lett. B **701** (2011) 313–320, arXiv:1103.4574 [hep-ex].

[69] D0 Collaboration, V. M. Abazov et al., *Search for flavor changing neutral currents via quark-gluon couplings in single top quark production using 2.3 fb^{-1} of $p\bar{p}$ collisions*, Phys. Lett. B **693** (2010) 81–87, arXiv:1006.3575 [hep-ex].

[70] ATLAS Collaboration, *A search for flavour changing neutral currents in top-quark decays in pp collision data collected with the ATLAS detector at* $\sqrt{s} = 7$ *TeV*, JHEP **09** (2012) 139, arXiv:1206.0257 [hep-ex].

[71] CMS Collaboration, *Search for flavor changing neutral currents in top quark decays in pp collisions at* 7 *TeV*, Phys. Lett. B **718** (2013) 1252, arXiv:1208.0957 [hep-ex].

[72] ATLAS Collaboration, *Search for FCNC single top-quark production at* $\sqrt{s} = 7$ *TeV with the ATLAS detector*, Phys. Lett. B **712** (2012) 351, arXiv:1203.0529 [hep-ex].

[73] W. Buchmüller and D. Wyler, *Effective Lagrangian analysis of new interactions and flavour conservation*, Nucl. Phys. B **268** no. CERN-TH-4254-85, (1985) 621–653, https://cds.cern.ch/record/163116.

[74] J. A. Aguilar-Saavedra, *A Minimal set of top anomalous couplings*, Nucl. Phys. B **812** (2009) 181–204, arXiv:0811.3842 [hep-ph].

[75] W. C. Carithers, *Top quark physics at hadron colliders*, NATO Sci. Ser. B **351** (1995) 201–215.

[76] M. Cacciari, M. Czakon, M. Mangano, A. Mitov and P. Nason, *Top-pair production at hadron colliders with next-to-next-to-leading logarithmic soft-gluon resummation*, Phys. Lett. B **710** (2012) 612–622, arXiv:1111.5869 [hep-ph].

[77] P. Bärnreuther, M. Czakon and A. Mitov, *Percent Level Precision Physics at the Tevatron: First Genuine NNLO QCD Corrections to* $q\bar{q} \to t\bar{t} + X$, Phys. Rev. Lett. **109** (2012) 132001, arXiv:1204.5201 [hep-ph].

[78] M. Czakon and A. Mitov, *NNLO corrections to top-pair production at hadron colliders: the all-fermionic scattering channels*, JHEP **12** (2012) 054, arXiv:1207.0236 [hep-ph].

[79] M. Czakon and A. Mitov, *NNLO corrections to top pair production at hadron colliders: the quark-gluon reaction*, JHEP **01** (2013) 080, arXiv:1210.6832 [hep-ph].

[80] M. Czakon, P. Fiedler and A. Mitov, *Total Top-Quark Pair-Production Cross Section at Hadron Colliders Through $O(\frac{4}{S})$*, Phys. Rev. Lett. **110** (2013) 252004, arXiv:1303.6254 [hep-ph].

[81] M. Czakon and A. Mitov, *Top++: A Program for the Calculation of the Top-Pair Cross-Section at Hadron Colliders*, Comput. Phys. Commun. **185** (2014) 2930, arXiv:1112.5675 [hep-ph].

[82] N. Kidonakis, *Top-quark transverse-momentum distributions in t-channel single-top production*, Phys. Rev. D **88** no. 3, (2013) 031504, arXiv:1306.3592 [hep-ph].

[83] N. Kidonakis, *NNLL resummation for s-channel single top quark production*, Phys. Rev. D **81** (2010) 054028, arXiv:1001.5034 [hep-ph].

[84] N. Kidonakis, *Two-loop soft anomalous dimensions for single top quark associated production with a W- or H-*, Phys. Rev. D **82** (2010) 054018, arXiv:1005.4451 [hep-ph].

[85] Top LHC WG, *Summary of measurements of the top-pair production cross-section at 8 TeV*, 2016. https://atlas.web.cern.ch/Atlas/GROUPS/PHYSICS/CombinedSummaryPlots/TOP/tt_xsec_8TeV/tt_xsec_8TeV.png. [Online; accessed 26-September-2016].

[86] Top LHC WG, *Summary of measurements of the single-top production cross-sections as a function of the center of mass energy*, 2016. https://atlas.web.cern.ch/Atlas/GROUPS/PHYSICS/CombinedSummaryPlots/TOP/singletop_allchanvsroots/singletop_allchanvsroots.png. [Online; accessed 26-September-2016].

[87] A. Asner et al., *ECFA-CERN Workshop on large hadron collider in the LEP tunnel, Lausanne and CERN, Geneva, Switzerland, 21-27 Mar 1984: Proceedings. 1.*, http://www.slac.stanford.edu/spires/find/books/www?cl=QCD183:E2:1984.

[88] *Convention for the establishment of a European organization for nuclear research : Paris, 1st July, 1953 : as amended*, https://cds.cern.ch/record/330625.

[89] Gargamelle Neutrino Collaboration, F. J. Hasert et al., *Observation of Neutrino Like Interactions without Muon or Electron in the Gargamelle Neutrino Experiment*, Nucl. Phys. B **73** (1974) 1–22.

[90] UA1 Collaboration, G. Arnison et al., *Further Evidence for Charged Intermediate Vector Bosons at the SPS Collider*, Phys. Lett. B **129** (1983) 273–282.

[91] UA1 Collaboration, G. Arnison et al., *Experimental Observation of Lepton Pairs of Invariant Mass Around 95-GeV/c^2 at the CERN SPS Collider*, Phys. Lett. B **126** (1983) 398–410.

[92] T. Berners-Lee, R. Cailliau, J.-F. Groff and B. Pollermann, *World-Wide Web: the information universe*, Electron. Netw. **2** (1992) 52–58, `https://cds.cern.ch/record/245849`, Reprinted in 2010.

[93] NA48 Collaboration, V. Fanti et al., *A New measurement of direct CP violation in two pion decays of the neutral kaon*, Phys. Lett. B **465** (1999) 335–348, `arXiv:hep-ex/9909022 [hep-ex]`.

[94] ATLAS Collaboration, *Observation of a new particle in the search for the Standard Model Higgs boson with the ATLAS detector at the LHC*, Phys. Lett. B **716** (2012) 1, `arXiv:1207.7214 [hep-ex]`.

[95] CMS Collaboration, *Observation of a new boson at a mass of 125 GeV with the CMS experiment at the LHC*, Phys. Lett. B **716** (2012) 30, `arXiv:1207.7235 [hep-ex]`.

[96] L. Evans and P. Bryant, *LHC Machine*, JINST **3** (2008) S08001.

[97] J. Haffner, *The CERN accelerator complex*, 2013. `https://cds.cern.ch/record/1621894`. [Online; accessed 28-August-2015].

[98] W. Herr and B. Muratori, *Concept of luminosity*, `http://doc.cern.ch/yellowrep/2006/2006-002/p361.pdf`.

[99] M. Lamont, *Status of the LHC*, J. Phys. Conf. Ser. **455** (2013) 012001.

[100] M. Brice, *Cross section of an LHC dipole in the tunnel.*, 2011. https://cds.cern.ch/record/1365795. [Online; accessed 28-August-2015].

[101] ATLAS Collaboration, *The ATLAS Experiment at the CERN Large Hadron Collider*, JINST **3** (2008) S08003.

[102] J. Pequenao, *Computer generated image of the whole ATLAS detector*, 2008. https://cds.cern.ch/record/1095924. [Online; accessed 28-August-2015].

[103] J. Pequenao and P. Schaffner, *An computer generated image representing how ATLAS detects particles*, 2013. https://cds.cern.ch/record/1505342. [Online; accessed 28-August-2015].

[104] J. M. Campbell, J. W. Huston and W. J. Stirling, *Hard Interactions of Quarks and Gluons: A Primer for LHC Physics*, Rept. Prog. Phys. **70** (2007) 89, arXiv:hep-ph/0611148 [hep-ph].

[105] ATLAS Collaboration, *Luminosity determination in pp collisions at $\sqrt{s} = 7$ TeV using the ATLAS detector at the LHC*, Eur. Phys. J. C **71** (2011) 1630, arXiv:1101.2185 [hep-ex].

[106] ATLAS Collaboration, *Number of Interactions per Crossing*, 2012. https://atlas.web.cern.ch/Atlas/GROUPS/DATAPREPARATION/InteractionsperCrossing/muplot/2012/mu_2011_2012-nov.png. [Online; accessed 28-August-2015].

[107] ATLAS Collaboration, *$Z \to \mu\mu$ event with high pileup*, 2012. https://twiki.cern.ch/twiki/pub/AtlasPublic/EventDisplayStandAlone/2012_highPileup.png. [Online; accessed 28-August-2015].

[108] ATLAS Collaboration, *Total Integrated Luminosity in 2011 and 2012*, 2012. https://atlas.web.cern.ch/Atlas/GROUPS/DATAPREPARATION/PublicPlots/2011-2012/Luminosity/intlumivstime2011-2012.png. [Online; accessed 28-August-2015].

[109] ATLAS Collaboration, *ATLAS magnet system: Technical design report*, CERN-LHCC-97-18, 1997.

[110] ATLAS Collaboration, *ATLAS inner detector: Technical design report. Vol. 1*, CERN-LHCC-97-16, ATLAS-TDR-4, 1997.

[111] ATLAS Collaboration, *ATLAS inner detector: Technical design report. Vol. 2*, CERN-LHCC-97-17, 1997.

[112] ATLAS Collaboration, *The ATLAS Inner Detector commissioning and calibration*, Eur. Phys. J. C **70** (2010) 787, arXiv:1004.5293 [hep-ex].

[113] ATLAS Collaboration, *ATLAS calorimeter performance Technical Design Report*, CERN-LHCC-96-40, 1996.

[114] ATLAS Collaboration, *ATLAS liquid argon calorimeter: Technical design report*, CERN-LHCC-96-41, 1996.

[115] ATLAS Collaboration, *Readiness of the ATLAS liquid argon calorimeter for LHC collisions*, Eur. Phys. J. C **70** (2010) 723, arXiv:0912.2642 [hep-ex].

[116] ATLAS Collaboration, *ATLAS tile calorimeter: Technical design report*, CERN-LHCC-96-42, 1996.

[117] ATLAS Collaboration, *Readiness of the ATLAS Tile Calorimeter for LHC collisions*, Eur. Phys. J. C **70** (2010) 1193, arXiv:1007.5423 [hep-ex].

[118] ATLAS Collaboration, *ATLAS muon spectrometer: Technical design report*, CERN-LHCC-97-22, ATLAS-TDR-10, 1997.

[119] ATLAS Collaboration, *Commissioning of the ATLAS Muon Spectrometer with cosmic rays*, Eur. Phys. J. C **70** (2010) 875, arXiv:1006.4384 [hep-ex].

[120] K. Kordas et al., *The ATLAS Data Acquisition and Trigger: Concept, design and status*, Nucl. Phys. Proc. Suppl. **172** (2007) 178–182.

[121] ATLAS Collaboration, *ATLAS first level trigger: Technical design report*, CERN-LHCC-98-14, ATLAS-TDR-12, 1998.

[122] ATLAS Collaboration, *ATLAS high-level trigger, data acquisition and controls: Technical design report*, CERN-LHCC-2003-022, ATLAS-TRD-016, 2003.

[123] ATLAS Collaboration, *Performance of the ATLAS muon trigger in pp collisions at* $\sqrt{s} = 8$ *TeV*, Eur. Phys. J. C **75** (2015) 120, arXiv:1408.3179 [hep-ex].

[124] R. W. L. Jones, *ATLAS computing and the GRID*, Nucl. Instrum. Meth. A **502** (2003) 372–375.

[125] ATLAS Collaboration, *ATLAS computing: Technical design report*, CERN-LHCC-2005-022, ATLAS-TRD-017, 2005.

[126] ATLAS Collaboration, *The ATLAS Tile Calorimeter Calibration and Performance*, EPJ Web Conf. **60** (2013) 20051, arXiv:1310.2945 [physics.ins-det].

[127] ATLAS Collaboration, *Cesium monitoring system for ATLAS Tile Hadron Calorimeter*, Nucl. Instrum. Meth. A **494** (2002) 381–384.

[128] ATLAS Collaboration, *Radioactive source control and electronics for the ATLAS tile calorimeter cesium calibration system*, Nucl. Instrum. Meth. A **508** (2003) 276–286.

[129] ATLAS Collaboration, *LASER monitoring system for the ATLAS tile calorimeter*, Nucl. Instrum. Meth. A **617** (2010) 120–122.

[130] K. Anderson et al., *Design of the front-end analog electronics for the ATLAS tile calorimeter*, Nucl. Instrum. Meth. A **551** (2005) 469–476.

[131] R. Alves et al., *ATLAS tile calorimeter LASER calibration system*, ATL-TILECAL-INT-2010-001, Jan, 2010, https://cds.cern.ch/record/1235180.

[132] LASER Calibration WG, *Diodes linearity and resolution*, 2009. http://atlas-tile-laser.web.cern.ch/atlas-tile-laser/Welcome.php?n=Work.SystemCalibration. [Online; accessed 7-September-2015].

[133] D. Calvet et al., *Commissioning of the ATLAS tile calorimeter LASER calibration system*, ATL-TILECAL-INT-2011-004, Jun, 2011, https://cds.cern.ch/record/1357908.

[134] ATLAS Collaboration, *Upgrade of the Laser Calibration System of the Atlas Hadron Calorimeter*, ATL-TILECAL-PROC-2015-019, Nov, 2015, https://cds.cern.ch/record/2103219.

[135] A. Blanco et al., *Upgrade of the LASER calibration system of the ATLAS Tile Calorimeter*, ATL-COM-TILECAL-2015-088, Dec, 2015, https://cds.cern.ch/record/2117164.

[136] ATLAS Collaboration, *Summary of several Standard Model total production cross section measurements*, 2016. https://atlas.web.cern.ch/Atlas/GROUPS/PHYSICS/CombinedSummaryPlots/SM/ATLAS_a_SMSummary_TotalXsect/ATLAS_a_SMSummary_TotalXsect.png. [Online; accessed 26-September-2016].

[137] A. Heinson, *Beyond-the-Standard-Model Top Processes*, 2011. http://www-d0.fnal.gov/Run2Physics/top/top_public_web_pages/top_feynman_diagrams.html. [Online; accessed 7-September-2015].

[138] ATLAS Collaboration, *Reliability Engineering Analysis of ATLAS Data Reprocessing Campaigns*, J. Phys. Conf. Ser. **513** (2014) 032101.

[139] ATLAS Collaboration, *Updated Luminosity Determination in pp Collisions at $\sqrt{s} = 7$ TeV using the ATLAS Detector*, ATLAS-CONF-2011-011, 2011, https://cds.cern.ch/record/1334563.

[140] T. Gleisberg et al., *Event generation with SHERPA 1.1*, JHEP **02** (2009) 007, arXiv:0811.4622 [hep-ph].

[141] R. P. Feynman, *The behavior of hadron collisions at extreme energies*, Conf. Proc. C **690905** (1969) 237–258.

[142] M. Dittmar et al., *Working Group I: Parton distributions: Summary report for the HERA LHC Workshop Proceedings*, arXiv:hep-ph/0511119 [hep-ph].

[143] V. N. Gribov and L. N. Lipatov, *Deep inelastic e p scattering in perturbation theory*, Sov. J. Nucl. Phys. **15** (1972) 438–450, [Yad. Fiz.15,781(1972)].

[144] L. N. Lipatov, *The parton model and perturbation theory*, Sov. J. Nucl. Phys. **20** (1975) 94–102, [Yad. Fiz.20,181(1974)].

[145] G. Altarelli and G. Parisi, *Asymptotic Freedom in Parton Language*, Nucl. Phys. B **126** (1977) 298.

[146] H1 Collaboration, S. Glazov, *Measurement of DIS cross section at HERA*, Braz. J. Phys. **37** (2007) 793–797.

[147] ZEUS, H1 Collaboration, H. Abramowicz et al., *Combination of Measurements of Inclusive Deep Inelastic $e^{\pm}p$ Scattering Cross Sections and QCD Analysis of HERA Data*, `arXiv:1506.06042 [hep-ex]`.

[148] J. A. Aguilar-Saavedra, *Protos - PROgram for TOp Simulations*, `https://jaguilar.web.cern.ch/jaguilar/protos/`. [Online; accessed 7-September-2015].

[149] J. A. Aguilar-Saavedra, *Zt, gamma t and t production at hadron colliders via strong flavour-changing neutral couplings*, Nucl. Phys. B **837** (2010) 122–136, `arXiv:1003.3173 [hep-ph]`.

[150] J. Pumplin et al., *New generation of parton distributions with uncertainties from global QCD analysis*, JHEP **07** (2002) 012, `arXiv:hep-ph/0201195 [hep-ph]`.

[151] ATLAS Collaboration, *Measurements of normalized differential cross-sections for $t\bar{t}$ production in pp collisions at $\sqrt{s} = 7$ TeV using the ATLAS detector*, Phys. Rev. D **90** (2014) 072004, `arXiv:1407.0371 [hep-ex]`.

[152] T. Sjostrand, S. Mrenna and P. Z. Skands, *PYTHIA 6.4 Physics and Manual*, JHEP **05** (2006) 026, `arXiv:hep-ph/0603175 [hep-ph]`.

[153] P. Z. Skands, *Tuning Monte Carlo Generators: The Perugia Tunes*, Phys. Rev. D **82** (2010) 074018, `arXiv:1005.3457 [hep-ph]`.

[154] S. Jadach, J. H. Kuhn and Z. Was, *TAUOLA: A Library of Monte Carlo programs to simulate decays of polarized tau leptons*, Comput. Phys. Commun. **64** (1990) 275–299.

[155] ATLAS Collaboration, *The ATLAS Simulation Infrastructure*, Eur. Phys. J. C **70** (2010) 823, arXiv:1005.4568 [hep-ex].

[156] W. Lukas, *Fast Simulation for ATLAS: Atlfast-II and ISF*, ATL-SOFT-PROC-2012-065, Geneva, Jun, 2012, https://cds.cern.ch/record/1458503.

[157] ATLAS Collaboration, T. Yamanaka, *The ATLAS calorimeter simulation FastCaloSim*, J. Phys. Conf. Ser. **331** (2011) 032053.

[158] H.-L. Lai et al., *New parton distributions for collider physics*, Phys. Rev. D **82** (2010) 074024, arXiv:1007.2241 [hep-ph].

[159] G. Corcella et al., *HERWIG 6.5 release note*, arXiv:hep-ph/0210213 [hep-ph].

[160] ATLAS Collaboration, *New ATLAS event generator tunes to 2010 data*, ATL-PHYS-PUB-2011-008, 2011, https://cds.cern.ch/record/1345343.

[161] M. L. Mangano, M. Moretti, F. Piccinini, R. Pittau and A. D. Polosa, *ALPGEN, a generator for hard multiparton processes in hadronic collisions*, JHEP **07** (2003) 001, arXiv:hep-ph/0206293 [hep-ph].

[162] J. Alwall, M. Herquet, F. Maltoni, O. Mattelaer and T. Stelzer, *MadGraph 5 : Going Beyond*, JHEP **06** (2011) 128, arXiv:1106.0522 [hep-ph].

[163] T. Sjöstrand et al., *An Introduction to PYTHIA 8.2*, Comput. Phys. Commun. **191** (2015) 159–177, arXiv:1410.3012 [hep-ph].

[164] ATLAS Collaboration, *Summary of ATLAS Pythia 8 tunes*, ATL-PHYS-PUB-2012-003, 2012, https://cds.cern.ch/record/1474107.

[165] S. Frixione, P. Nason and C. Oleari, *Matching NLO QCD computations with Parton Shower simulations: the POWHEG method*, JHEP **11** (2007) 070, arXiv:0709.2092 [hep-ph].

[166] S. Allwood-Spires et al., *Monte Carlo samples used for top physics*, ATL-PHYS-INT-2010-132, Dec, 2010, https://cds.cern.ch/record/1312945.

[167] S. Frixione and B. R. Webber, *Matching NLO QCD computations and parton shower simulations*, JHEP **06** (2002) 029, arXiv:hep-ph/0204244 [hep-ph].

[168] B. P. Kersevan and E. Richter-Was, *The Monte Carlo event generator AcerMC versions 2.0 to 3.8 with interfaces to PYTHIA 6.4, HERWIG 6.5 and ARIADNE 4.1*, Comput. Phys. Commun. **184** (2013) 919–985, arXiv:hep-ph/0405247 [hep-ph].

[169] GEANT4 Collaboration, S. Agostinelli et al., *GEANT4: A Simulation toolkit*, Nucl. Instrum. Meth. A **506** (2003) 250–303.

[170] ATLAS Collaboration, *Electron and photon energy calibration with the ATLAS detector using LHC Run 1 data*, Eur. Phys. J. C **74** (2014) 3071, arXiv:1407.5063 [hep-ex].

[171] ATLAS Collaboration, *Electron performance measurements with the ATLAS detector using the 2010 LHC proton–proton collision data*, Eur. Phys. J. C **72** (2012) 1909, arXiv:1110.3174 [hep-ex].

[172] ATLAS Collaboration, *2012 Electron Identification Efficiency vs. E_T: data and MC*, 2013. https://atlas.web.cern.ch/Atlas/GROUPS/PHYSICS/EGAMMA/PublicPlots/20130926/ATL-COM-PHYS-2013-1287/Fig5a.png. [Online; accessed 11-January-2016].

[173] ATLAS Collaboration, *2011 and 2012 Electron Reconstruction Efficiency vs. E_T*, 2013. https://atlas.web.cern.ch/Atlas/GROUPS/PHYSICS/EGAMMA/PublicPlots/20130926/ATL-COM-PHYS-2013-1287/Fig3.png. [Online; accessed 11-January-2016].

[174] ATLAS Collaboration, *Trigger efficiencies vs. E_T*, 2012. https://twiki.cern.ch/twiki/pub/AtlasPublic/EgammaTriggerPublicResults/SingleElectronTriggerEfficiency2012_et.png. [Online; accessed 11-January-2016].

[175] ATLAS Collaboration, *Measurement of the muon reconstruction performance of the ATLAS detector using 2011 and 2012 LHC proton–proton collision data*, Eur. Phys. J. C **74** (2014) 3130, arXiv:1407.3935 [hep-ex].

[176] K. Rehermann and B. Tweedie, *Efficient Identification of Boosted Semileptonic Top Quarks at the LHC*, JHEP **1103** (2011) 059, arXiv:1007.2221 [hep-ph].

[177] ATLAS Collaboration, *Jet energy measurement and its systematic uncertainty in proton–proton collisions at $\sqrt{s} = 7$ TeV with the ATLAS detector*, Eur. Phys. J. C **75** (2015) 17, arXiv:1406.0076 [hep-ex].

[178] M. Cacciari, G. P. Salam and G. Soyez, *The Anti-k(t) jet clustering algorithm*, JHEP **0804** (2008) 063, arXiv:0802.1189 [hep-ph].

[179] ATLAS Collaboration, *Data-Quality Requirements and Event Cleaning for Jets and Missing Transverse Energy Reconstruction with the ATLAS Detector in Proton–Proton Collisions at a Center-of-Mass Energy of $\sqrt{s} = 7$ TeV*, ATLAS-CONF-2010-038, 2010, https://cds.cern.ch/record/1277678.

[180] ATLAS Collaboration, *Commissioning of the ATLAS high performance b-tagging algorithms in the 7 TeV collision data*, ATLAS-CONF-2011-102, 2011, https://cds.cern.ch/record/1369219.

[181] ATLAS Collaboration, *Calibration of the performance of b-tagging for c and light-flavour jets in the 2012 ATLAS data*, ATLAS-CONF-2014-046, 2014, https://cds.cern.ch/record/1741020.

[182] ATLAS Collaboration, *Performance of missing transverse momentum reconstruction in proton–proton collisions at $\sqrt{s} = 7$ TeV with ATLAS*, Eur. Phys. J. C **72** (2012) 1844, arXiv:1108.5602 [hep-ex].

[183] ATLAS Collaboration, *Performance of Missing Transverse Momentum Reconstruction in ATLAS studied in Proton–Proton Collisions recorded in 2012 at $\sqrt{s} = 8$ TeV*, ATLAS-CONF-2013-082, 2013, https://cds.cern.ch/record/1570993.

[184] ATLAS Collaboration, *Performance of the ATLAS Electron and Photon Trigger in pp Collisions at $\sqrt{s} = 7$ TeV in 2011*, ATLAS-CONF-2012-048, 2012, https://cds.cern.ch/record/1450089.

[185] ATLAS Collaboration, *Monitoring and data quality assessment of the ATLAS liquid argon calorimeter*, JINST **9** (2014) P07024, arXiv:1405.3768 [hep-ex].

[186] F. Veloso, *Study of ATLAS sensitivity to FCNC top quark decays*, 2008. http://weblib.cern.ch/abstract?CERN-THESIS-2008-106.

[187] N. Castro, *Study of the Wtb vertex structure at the ATLAS experiment*, 2008. http://weblib.cern.ch/abstract?CERN-THESIS-2008-083.

[188] R. Brun and F. Rademakers, *ROOT: An object oriented data analysis framework*, Nucl. Instrum. Meth. A **389** (1997) 81–86.

[189] G. Aad et al., *Invariant Mass Studies for the $H \to bb$ Measurements for LHCP*, ATL-COM-PHYS-2013-449, Apr, 2013.

[190] J. Campbell, R. K. Ellis and R. Röntsch, *Single top production in association with a Z boson at the LHC*, Phys. Rev. D **87** (2013) 114006, arXiv:1302.3856 [hep-ph].

[191] O. Bessidskaia Bylund, H. Khandanyan, J. McFayden, J. Sjölin and K. Suruliz, *Measurements of the $t\bar{t}Z$ and $t\bar{t}W$ production cross sections in final states with three-leptons or two same-sign leptons with* 20.3fb^{-1} *of* $\sqrt{s} = 8$ *TeV pp collision data collected by the ATLAS detector*, ATL-COM-PHYS-2013-1131, Aug, 2013.

[192] ATLAS Collaboration, *Estimation of non-prompt and fake lepton backgrounds in final states with top quarks produced in proton–proton collisions at* $\sqrt{s} = 8$ *TeV with the ATLAS Detector*, ATLAS-CONF-2014-058, 2014, https://cds.cern.ch/record/1951336.

[193] ATLAS Collaboration, *Jet energy resolution in proton–proton collisions at* $\sqrt{s} = 7$ *TeV recorded in 2010 with the ATLAS detector*, Eur. Phys. J. C **73** (2013) 2306, arXiv:1210.6210 [hep-ex].

[194] ATLAS Collaboration, *Electron reconstruction and identification efficiency measurements with the ATLAS detector using the 2011 LHC proton–proton collision data*, Eur. Phys. J. C **74** (2014) 2941, arXiv:1404.2240 [hep-ex].

[195] J. M. Campbell and R. K. Ellis, *$t\bar{t}W^{\pm}$ production and decay at NLO*, JHEP **07** (2012) 052, arXiv:1204.5678 [hep-ph].

[196] M. V. Garzelli, A. Kardos, C. G. Papadopoulos and Z. Trocsanyi, *$t\bar{t}W^{\pm}$ and $t\bar{t}Z$ Hadroproduction at NLO accuracy in QCD with Parton Shower and Hadronization effects*, JHEP **11** (2012) 056, arXiv:1208.2665 [hep-ph].

[197] LHC Higgs Cross Section Working Group Collaboration, J. R. Andersen et al., *Handbook of LHC Higgs Cross Sections: 3. Higgs Properties*, arXiv:1307.1347 [hep-ph].

[198] A. L. Read, *Presentation of search results: the CL_s technique*, J. Phys. G **28** no. 10, (2002) 2693–704.

[199] T. Junk, *Confidence level computation for combining searches with small statistics*, Nucl. Instrum. Meth. A **434** (1999) 435–443, arXiv:hep-ex/9902006 [hep-ex].

[200] ATLAS Collaboration, *Search for flavour-changing neutral current top-quark decays to qZ in pp collision data collected with the ATLAS detector at $\sqrt{s} = 8$ TeV*, Eur. Phys. J. C **76** (2016) 12, arXiv:1508.05796 [hep-ex].

[201] ATLAS Collaboration, *Search for single top-quark production via FCNC in strong interactions in $\sqrt{s} = 8$ TeV ATLAS data*, ATLAS-CONF-2013-063, 2013, https://cds.cern.ch/record/1562777.

[202] ATLAS Collaboration, *Search for top quark decays $t \to qH$ with $H \to \gamma\gamma$ using the ATLAS detector*, JHEP **06** (2014) 008, arXiv:1403.6293 [hep-ex].

[203] CMS Collaboration, *Search for flavor-changing neutral currents in top-quark decays $t \to Zq$ in pp collisions at $\sqrt{s} = 8$ TeV*, Phys. Rev. Lett. **112** (2014) 171802, arXiv:1312.4194 [hep-ex].

[204] CMS Collaboration, *Search for anomalous single top quark production in association with a photon in pp collisions at $\sqrt{s} = 8$ TeV*, JHEP **04** (2016) 035, arXiv:1511.03951 [hep-ex].

[205] CMS Collaboration, *Search for anomalous Wtb couplings and top FCNC in t-channel single-top-quark events*, https://cds.cern.ch/record/1702400.

[206] CMS Collaboration, *Searches for heavy Higgs bosons in two-Higgs-doublet models and for $t \to ch$ decay using multilepton and diphoton final states in pp collisions at $\sqrt{s} = 8$ TeV*, Phys. Rev. D **90** (2014) 112013, arXiv:1410.2751 [hep-ex].

[207] ATLAS Collaboration, *Summary of the current 95% confidence level observed limits on the branching ratios of the top-quark decays via FCNC to a charm quark and a neutral boson*, 2015. https://atlas.web.cern.ch/Atlas/GROUPS/PHYSICS/CombinedSummaryPlots/TOP/fcnc_tXc/fcnc_tXc.png. [Online; accessed 16-November-2015].

[208] ATLAS Collaboration, *Summary of the current 95% confidence level observed limits on the branching ratios of the top-quark decays via FCNC to a up quark and a neutral boson*, 2015. https://atlas.web.cern.ch/Atlas/GROUPS/PHYSICS/CombinedSummaryPlots/TOP/fcnc_tXu/fcnc_tXu.png. [Online; accessed 16-November-2015].

[209] ATLAS Collaboration, *Search for single top-quark production via flavour-changing neutral currents at 8 TeV with the ATLAS detector*, Eur. Phys. J. C **76** (2016) 55, arXiv:1509.00294 [hep-ex].

[210] ATLAS Collaboration, *Search for flavour-changing neutral current top quark decays $t \to Hq$ in pp collisions at $\sqrt{s} = 8$ TeV with the ATLAS detector*, JHEP **12** (2015) 061, arXiv:1509.06047 [hep-ex].

[211] CMS Collaboration, *Search for associated production of a Z boson with a single top quark and for tZ flavour-changing interactions in pp collisions at $\sqrt{s} = 8$ TeV,*.

[212] CMS Collaboration, *Search for anomalous Wtb couplings and flavour-changing neutral currents in t-channel single top quark production in pp collisions at $\sqrt{s} = 7$ and 8 TeV*, arXiv:1610.03545 [hep-ex].

[213] CMS Collaboration, *Search for top quark decays via Higgs-boson-mediated flavor changing neutral currents in pp collisions at $\sqrt{s} = 8$ TeV,*.

[214] T. Radford et al., *Accelerating science and innovation: societal benefits of European research in Particle Physics*, May, 2013.

[215] ATLAS Collaboration, *Physics at a High-Luminosity LHC with ATLAS*, ATL-PHYS-PUB-2012-001, 2012, `https://cds.cern.ch/record/1472518`.

[216] ATLAS Collaboration, *Physics at a High-Luminosity LHC with ATLAS (Update)*, ATL-PHYS-PUB-2012-004, 2012, `https://cds.cern.ch/record/1484890`.

[217] J. Araque, N. Castro, M. C. N. Fiolhais, B. Galhardo, A. Onofre and F. Veloso, *Study of ATLAS sensitivity at the High Luminosity LHC to FCNC top decays $t \to qZ$ and $t \to q\gamma$*, ATL-COM-PHYS-2013-472, Apr, 2013, `https://cds.cern.ch/record/1543218`.

[218] CERN, *LHC/HL-LHC Plan*, 2015. `http://hilumilhc.web.cern.ch/about/hl-lhc-project`. [Online; accessed 7-September-2015].

[219] J. Carvalho et al., *A search for Flavour Changing Neutral Currents in Top Quark Decays $t \to qZ$ at $\sqrt{s} = 7$ TeV in 0.70 fb^{-1} of pp collision data collected with the ATLAS Detector*, ATLAS-COM-CONF-2011-111v3, Jun, 2011.

[220] J. M. Campbell, R. K. Ellis and C. Williams, *Vector boson pair production at the LHC*, JHEP **07** (2011) 018, `arXiv:1105.0020 [hep-ph]`.

[221] ATLAS Collaboration, *A Measurement of $W^{\pm}Z$ Production in Proton–Proton Collisions at $\sqrt{s} = 8$ TeV with the ATLAS Detector*, ATLAS-CONF-2013-021, 2013, `https://cds.cern.ch/record/1525557`.

[222] ATLAS Collaboration, *Measurement of the total ZZ production cross section in proton–proton collisions at $\sqrt{s} = 8$ TeV in 20 fb^{-1} with the ATLAS detector*, ATLAS-CONF-2013-020, 2013, `https://cds.cern.ch/record/1525555`.

[223] ATLAS Collaboration, *Expected Performance of the ATLAS Experiment - Detector, Trigger and Physics*, `arXiv:0901.0512 [hep-ex]`.

[224] S. R. Slabospitsky and L. Sonnenschein, *TopReX generator (version 3.25): Short manual*, Comput. Phys. Commun. **148** (2002) 87–102, arXiv:hep-ph/0201292 [hep-ph].

[225] ATLAS Collaboration, *Performance assumptions for an upgraded ATLAS detector at a High-Luminosity LHC*, ATL-PHYS-PUB-2013-004, 2013, https://cds.cern.ch/record/1527529.

[226] P. Vankov, *ATLAS Upgrade for the HL-LHC: Meeting the challenges of a five-fold increase in collision rate*, EPJ Web Conf. **28** (2012) 12069, arXiv:1201.5469 [physics.ins-det].

[227] A. Blanco et al., *Performance of the upgraded LASER calibration system of the ATLAS Tile Calorimeter*, in preparation.